dortmund
university

astroparticle
physics

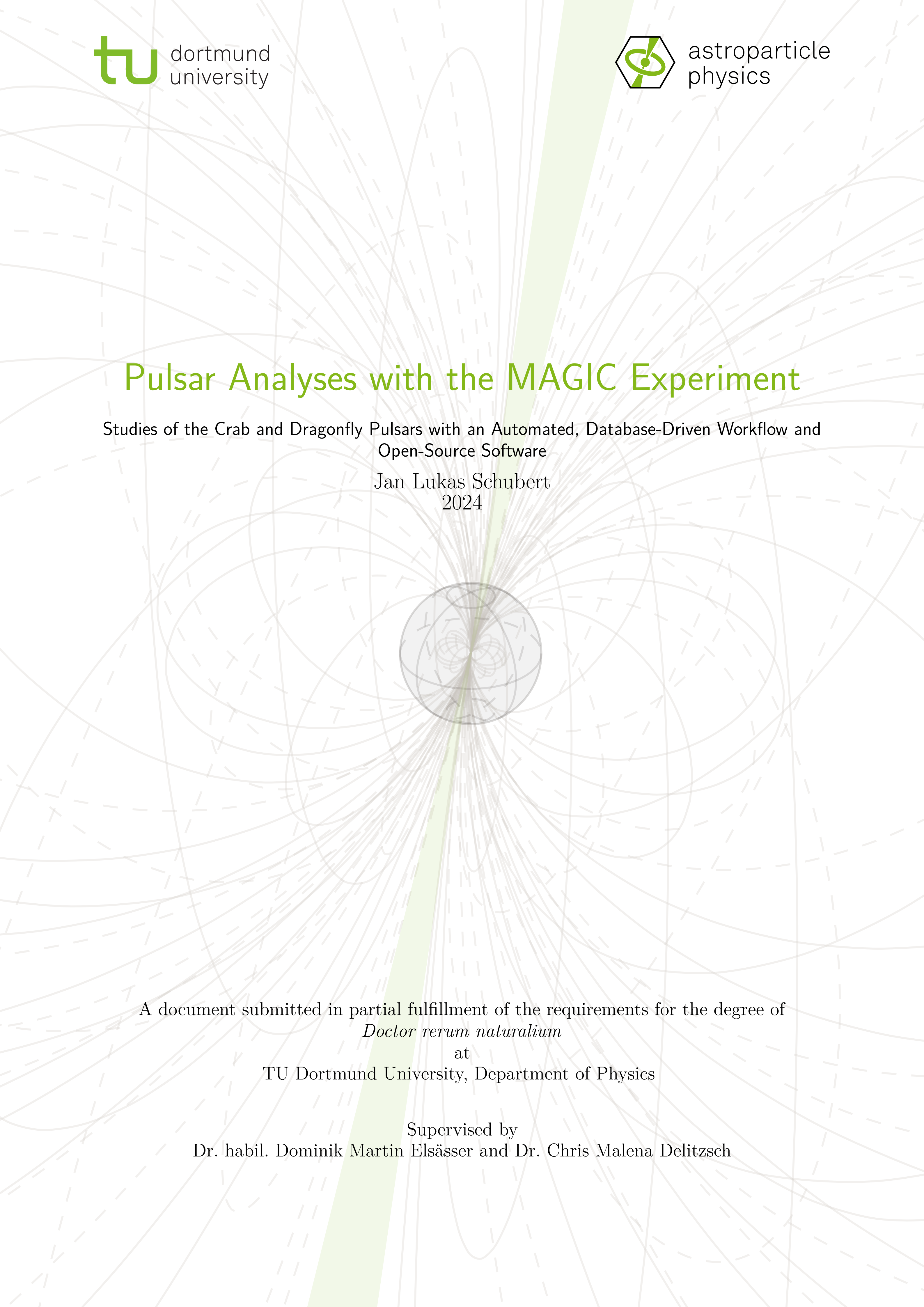

Pulsar Analyses with the MAGIC Experiment

Studies of the Crab and Dragonfly Pulsars with an Automated, Database-Driven Workflow and Open-Source Software

Jan Lukas Schubert
2024

A document submitted in partial fulfillment of the requirements for the degree of
Doctor rerum naturalium
at
TU Dortmund University, Department of Physics

Supervised by
Dr. habil. Dominik Martin Elsässer and Dr. Chris Malena Delitzsch

You're never going to learn
something as profoundly as when
it's purely out of curiosity.

Christopher Nolan

This thesis is set in Latin Modern (Serif, Sans and Math),
typeset using LaTeX with LuaTeX from TeX-Live 2023.
Title graphic based on Graphic by Tomasz M. Trzeciak.

Kurzfassung

Pulsare sind schnell rotierende Neutronensterne, die gepulste, elektromagnetische Strahlung aussenden. Insbesondere die Entdeckung von Pulsen mit Energien von über 100 GeV wirft neue Fragen zu den zugrundeliegenden Emissionsmechanismen auf. Bisher sind nur drei Pulsare in diesem Energiebereich bekannt. Die MAGIC Teleskope sind ab etwa 50 GeV sensitiv, können ihre Energiegrenze jedoch mit optimierten Triggerkriterien (dem Sum-Trigger-II) bis auf 20 GeV senken und werden somit geeignete Messinstrumente für hochenergetische Pulsare. In dieser Arbeit werden der Krebs- und der Dragonflypulsar studiert. Aufgrund der großen Datenmengen, aufgenommen über mehr als zehn Jahre, wird die Analyse automatisiert. Grundlage dafür ist `autoMAGIC`, ein datenbankgestütztes Werkzeug, das reproduzierbare Analysen mit minimaler menschlicher Interaktion ermöglicht. Die speziellen Anforderungen einer Pulsaranalyse werden in `autoMAGIC` implementiert und somit ein standardisierter Datensatz zur anschließenden Produktion physikalischer Ergebnisse erzeugt. In den letzten Jahren wurden in der Gammaastronomie große Anstrengungen unternommen, um die Daten verschiedener Teleskope zu standardisieren und anschließend mit der gleichen Software zu analysieren. In diesem Rahmen ist das Open-Source-Projekt `Gammapy` entstanden. Im Rahmen dieser Arbeit wurde das `Python`-Paket `magicpulsar` entwickelt, das das Pulsar-Timing und große Teile der `Gammapy` Analyse basierend auf dem standardisierten Datensatz aus `autoMAGIC` übernimmt. Der Krebspulsar wird basierend auf ~480 h Messzeit mit 15,47 σ für den Peak P1, 24,30 σ für den Peak P2 und 8,85 σ für die Bridge klar detektiert. Außerdem werden die Energiespektren für diese Peaks und weitere physikalisch interessante Phasenbereiche erstellt. Dabei wird ein abnehmendes P1/P2-Verhältnis zwischen ~20 GeV und ~800 GeV festgestellt. Das gepulste Signal von Dragonfly kann basierend auf 27 h Messzeit nicht mit MAGIC detektiert werden.

Abstract

Pulsars are fast-rotating neutron stars that emit pulsed electromagnetic radiation. In particular, the discovery of pulses with energies above 100 GeV raises new questions about the underlying emission mechanisms. So far, only three pulsars in this energy regime are known. The MAGIC telescopes are sensitive from approximately 50 GeV, but can lower their enery threshold down to 20 GeV with optimized trigger criteria (the Sum-Trigger-II) and thus become suitable instruments for the observation of high-energy pulsars. In this work, the Crab and Dragonfly Pulsars are studied. Due to the large amount of data recorded over more than ten years, the analysis is automated. The basis for this is `autoMAGIC`, a database-supported tool that enables reproducible analyses with minimal human interaction. The special requirements of pulsar analyses are implemented in `autoMAGIC` and a standardized dataset for the subsequent production of physical results is generated. In recent years, great efforts have been made in gamma astronomy to standardize the data across different telescopes and to analyze them using unified software. In this context, the open-source project `Gammapy` was developed. As part of this work, the `Python` package `magicpulsar` was developed, which computes the pulsar timing and large parts of the `Gammapy` analysis based on the standardized dataset from `autoMAGIC`. The Crab Pulsar is clearly detected based on ~480 h observation time with 15.47 σ for peak P1, 24.30 σ for peak P2, and 8.85 σ for the bridge. The energy spectra for these peaks and other physically interesting phase ranges are generated and agree with the *Fermi*-LAT results. A decreasing P1/P2 ratio between ~20 GeV and ~800 GeV is observed. The analysis of 27 h of Dragonfly data delivers no pulsed signal.

Contents

1

Introduction

> No matter what people tell you, words and ideas can change the world.
>
> Robin
> Inception

Since the discovery of cosmic rays by Victor Hess in 1912 [90], the huge field of astroparticle physics has developed in various sub-fields that each fascinate scientists as well as the general public. Cosmic rays are classified into several messengers such as protons, neutrons, electrons, neutrinos, gravitational waves, and photons at different wavelengths, each of which contain information about the physical processes in the cosmic sources they are produced in, based on their characteristics. By combining the information from different instruments, the nature of the highly complex objects that the cosmos holds can be revealed. With increasing knowledge, financial support, and workforce, more complex scientific experiments could be realized and numerous new, exotic objects could be discovered within the last century.

For this work, the most important discovery is the somewhat accidental first detection of pulsars in 1967 by Jocelyn Bell Burnell and Antony Hewish [92]. They observed surprisingly periodic radio signals while searching for new radio sources. These sources could soon be associated with magnetized neutron stars and many more pulsars were found in already existing radio data [147]. Since 1967, thousands more pulsars have been observed spanning from radio to gamma-ray wavelength most of which have proven to be the most exact clocks in the universe. Although the theoretical description of pulsars has made enormous progress in the last 50 years, the emission mechanisms and the orientation of the observed pulsars with regard to Earth are largely unknown. While the emission mechanisms in the radio regime are still controversial, the gamma-ray emission is partly understood, which is not least owed to the extensive gamma-ray observation of pulsars that were made possible by the Large Area Telescope (LAT) on the *Fermi* satellite [160]. In fact, since its launch, gamma-ray pulsars experience a golden era, multiplying the previously known sources by a factor of around ten [81].

Some of the pulsars observed by *Fermi*-LAT can also be detected with ground-based gamma-ray telescopes, such as Imaging Air Cherenkov Telescopes (IACTs). IACTs exploit the Cherenkov effect to indirectly measure gamma rays in the energy range from tens of GeV to tens of TeV. Hence, the pulsar energies are in the low-energy range of the ground-based gamma-ray telescopes. One of the four major currently operating Earth-bound gamma-ray observatories are the Major Atmospheric Gamma-Ray Imaging Cherenkov (MAGIC) telescopes. So far, the MAGIC telescopes have detected two pulsars, the Crab Pulsar and

Geminga [11, 115], in the Very High Energy (VHE) regime. The MAGIC telescopes are equipped with a special low-energy trigger, called Sum-Trigger-II, that is mainly used for pulsar observations. The Sum-Trigger-II data analysis poses some additional challenges but rewards with a high performance in the energy range of few tens of GeV [63]. With the MAGIC telescopes (and IACTs in general), the high-energy tail of the spectrum of gamma-ray pulsars can be observed, constraining the possible emission mechanisms and therefore helping to understand these powerful objects. As the number of measured events in the VHE gamma-ray regime is comparably low, especially long-term analyses can deliver reliable spectra.

The goal of this work is to design an automatized workflow for the MAGIC pulsar analysis of Sum-Trigger-II data, as well as of Standard Trigger data. With the new approach to use the gamma-ray astronomy standard data format `DL3` in the MAGIC pulsar analysis, compatibility with other experiments is ensured. The automatization enables the analyzer to perform long-term pulsar analyses with MAGIC data, which is exploited by performing a low-energy analysis of all available Crab Sum-Trigger-II Data and by analyzing 12 years of Crab Pulsar Standard Trigger data. Additionally, a low-energy analysis of all available MAGIC Sum-Trigger-II Dragonfly data is done.

In **Chapter 2**, the basic physics properties of pulsars are summarized and the two target sources, namely the Crab and the Dragonfly, are introduced. Further, ground-based gamma-ray astronomy is briefly explained, and an overview of the MAGIC telescopes and their observation process is given.

Chapter 3 deals with the MAGIC data analysis. The theoretical background is established and the implementation of the analysis chain is described. Furthermore, recent changes, such as the automatization of the analysis chain and new standard data formats, are described.

Chapter 4 describes MAGIC's dedicated low-energy trigger system, called Sum-Trigger-II, and the required modifications in the data analysis, as well as their implementation in the automatized analysis pipeline.

Chapter 5 discusses the calculation of the pulsar phase, which is essential in time-resolved pulsar analysis. Various time systems and transformations that occur in a pulsar analysis, as well as pulsar models and statistical tests for periodic signal are described. Finally, the software used in this work for pulsar analysis is presented and its application explained.

Chapter 6 shows the results of a pulsar analysis of approximately 120 h of MAGIC Sum-Trigger-II data which is afterward complemented by a pulsar analysis of more than 400 h of Standard Trigger data in different zenith distance (zd) ranges. A combined analysis is then performed to benefit from the joint statistics of both datasets.

In **Chapter 7**, a search for pulsed signal in Sum-Trigger-II data of the Dragonfly Pulsar is presented.

Finally, in **Chapter 8** the results are summarized and conclusions are drawn. Further, the results are placed in the wider context and future prospects are addressed.

Gamma-Ray Astronomy

2

> We're pioneers. We've barely begun.
>
> Cooper
> Interstellar

Gamma-ray astronomy is a broad field in which different experiments observe various source types to understand the most energetic processes in the universe. The work at hand studies pulsars which are among the most energetic persistent sources in our galaxy. This chapter focuses on the pulsar structure and emission mechanisms. Further, detection methods of gamma-ray emission are explained.

Firstly, the main properties of pulsars are discussed, and the mechanisms for the gamma-ray emission are introduced. Then, their environments, so-called Pulsar Wind Nebulae (PWNe), are described briefly. The characteristics and the current state of knowledge for the Crab Nebula and the Crab Pulsar are summarized and the current status of research on the Dragonfly Pulsar is described. Afterward, the detection of gamma rays with space-based and ground-based telescopes is discussed and the MAGIC telescopes are introduced.

2.1 Pulsars

Pulsars are fast-rotating neutron stars with a strong magnetic field that emit radiation from radio to gamma rays periodically. They emit beams of radiation that sweep the universe as the pulsar rotates rapidly. Every time the beam sweeps the telescope's line of sight, a light pulse is observed – that is the name-giving characteristic of these exotic astrophysical objects. These light pulses can serve as extremely accurate clocks, comparable to the most precise human-made atomic clocks. Hence, since their discovery, they have fascinated astronomers and have been studied extensively. Nevertheless, the scientific understanding of pulsars is far from complete.

The population of pulsars is usually divided into two classes: "normal" pulsars have larger rotational periods (and lower frequencies) and typically higher magnetic field strengths. Millisecond pulsars, on the other hand, have rotational periods as low as few milliseconds and in general lower magnetic field strengths. While normal pulsars obtain their rotational energy from the preceding supernova and usually occur without companion stars, millisecond pulsars are expected to be old neutron stars that reabsorb rotational energy through the accretion of mass from a companion star in a binary system. This chapter focuses on normal pulsars. For a review of millisecond pulsars, the interested reader is referred to [120]. Here, only the main properties of pulsars and the currently favored models to explain the observations are summarized. [118]

2.1.1 Neutron Stars

Neutron stars are remnants of supernovae of progenitor stars with a mass range from approximately 8 to 20 $M_\odot$ [118]. At the end of their lifetime, when they run out of material for the fusion, the radiation pressure decreases, leading the star to collapse due to the high gravitational pressure. A huge amount of the star's initial mass is ejected into space as the shell of the star falls onto the core and is reflected. The core itself collapses into a neutron star in which the gravitational pressure and the degeneration pressure are in equilibrium. The radius of the star collapses from 10^6 km to 10^7 km to around 10 km within seconds. As the rotational momentum and the magnetic flux are conserved, the newly emerged neutron star has a much higher rotational frequency and a much higher magnetic field at the surface. A high percentage of the star's mass is ejected into space, while the remaining neutron star has only few solar masses.

Neutron stars reach the density of atomic nuclei in the order of magnitude of 10^{14} g/cm^3. The main component of a neutron star is a neutron superfluid mainly consisting of neutrons and a small fraction of electrons and protons. On top of the fluid, there is a crystalline crust formed out of heavy nuclei such as iron and also other cores that are hypothesized to be neutron-rich isotopes that cannot exist anywhere else [140]. According to current models, the angular momentum of the crust can be decoupled from the angular momentum of the neutron fluid in the core. [118]

Pulsars are neutron stars with a strong magnetic field typically between 10^7 T and 10^9 T whereas the magnetic field axis is significantly misaligned with the rotation axis. The orthogonal component of the magnetic field then causes an electromagnetic wave at the rotation frequency of the pulsar, leading to the emission of radiation and consequently to the slowdown of the pulsar caused by the energy loss. The electrons and protons in the neutron fluid located in the pulsar core lead to a strong coupling of the fluid to the magnetic field. [118]

Typical pulsars have masses between 0.8 and 3 $M_\odot$ [189]. Below this mass, the gravitational pressure is not large enough to form a neutron star, and above this mass, the Tolman-Oppenheimer-Volkoff limit [102] is exceeded at which the gravitational pressure exceeds the degeneration pressure leading the star to collapse into a black hole. Typical rotational periods of pulsars are milliseconds to seconds whereas a slowdown of the rotation can be observed. This can be explained as the conversion of angular momentum into the emitted radiation. This pulsar spin-down (i. e. the decrease in the pulsar's rotational frequency) is usually very uniform and small. Sometimes, however, so-called glitches can occur, during which the pulsar suddenly increases its rotation frequency and deviates from the uniform spin-down. The most probable reason is the coupling of the internal superfluid of the pulsar to the crust. Usually, they are decoupled, leading the surface to lose angular momentum. When the superfluid and the crust recouple, angular momentum stored in the superfluid can be transferred to the crust, resulting in an increase in the observable pulsar frequency. This frequency increase can then be observed as a glitch. [190]

2.1.2 Pulsar Measurements

Pulsars leave a unique signature in detectors, making them comparably easy to identify as such. The very stable pulsed signal cannot be seen in any other object in the universe. By comparing the amount of measured signal to the pulsar's rotational phase, even weak excess signal for certain rotational phases sums up to visible peaks in the so-called phasogram. Each pulsar phasogram is as unique as a fingerprint and contains important information about the physics processes in the neutron star. For most of the pulsars, two peaks separated by between 0.15 and 0.5 rotational phases can be observed. However, there are also pulsars with only one observable pulse per rotational phase. [118]

Pulsed signal is measured from the radio regime up to the VHE gamma rays. However, in the different wavelengths, different characteristics of the pulsars can be observed. Approximately 7 % of the pulsars can be detected in gamma-ray frequencies [5]. In the gamma-ray band, an excess of radiation between the two pulses called bridge emission can be observed [23, 135].

In the VHE (>100 GeV) gamma-ray range, there are only few known pulsars. So far, only the Crab Pulsar, Geminga, and Vela could be observed above energies of 100 GeV with IACTs [11, 14, 28, 55]. Recently, pulsed emission of the Vela Pulsar could be measured to energies as high as 20 TeV by the High Energy Stereoscopic System (H. E. S. S.) [70].

2.1.3 The Pulsar Magnetosphere

A pulsar alone cannot explain the observed characteristics such as the VHE gamma-ray emission. The pulsar is surrounded by the so-called magnetosphere which is dominated by the strong magnetic field of the pulsar. As it rotates, the magnetic field sweeps its surroundings. Since the magnetosphere contains many ionized particles, it co-rotates with the pulsar. The inner magnetosphere extends up to the so-called light cylinder with the radius R_{LC} at which the co-rotation with the pulsar at its equator reaches the vacuum velocity of light:

$$R_{\mathrm{LC}} = \frac{cT}{2\pi}\,. \tag{2.1}$$

The light cylinder orientation is aligned with the rotational axis of the pulsar and extends up to R_{LC}. By definition, the magnetic field lines are closed up to the radius R_{LC}. Beyond this point, they are open as a co-rotation would require a faster movement than the speed of light. This region is also referred to as the outer magnetosphere. The charged particles in the magnetosphere travel along the magnetic field lines. Consequently, they are trapped in the equatorial region where the magnetic field lines are closed but they can escape the light cylinder on the magnetic field lines starting at the poles. Compensating the outflow at the poles, a return flow of charged particles from outside the magnetosphere emerges which is confined in a Y-shaped equatorial current sheet. At the light cylinder, all magnetic field components change their sign, so in this area magnetic reconnection takes place. [144] A schematic depiction of the pulsar magnetosphere can be found in Figure 2.1.

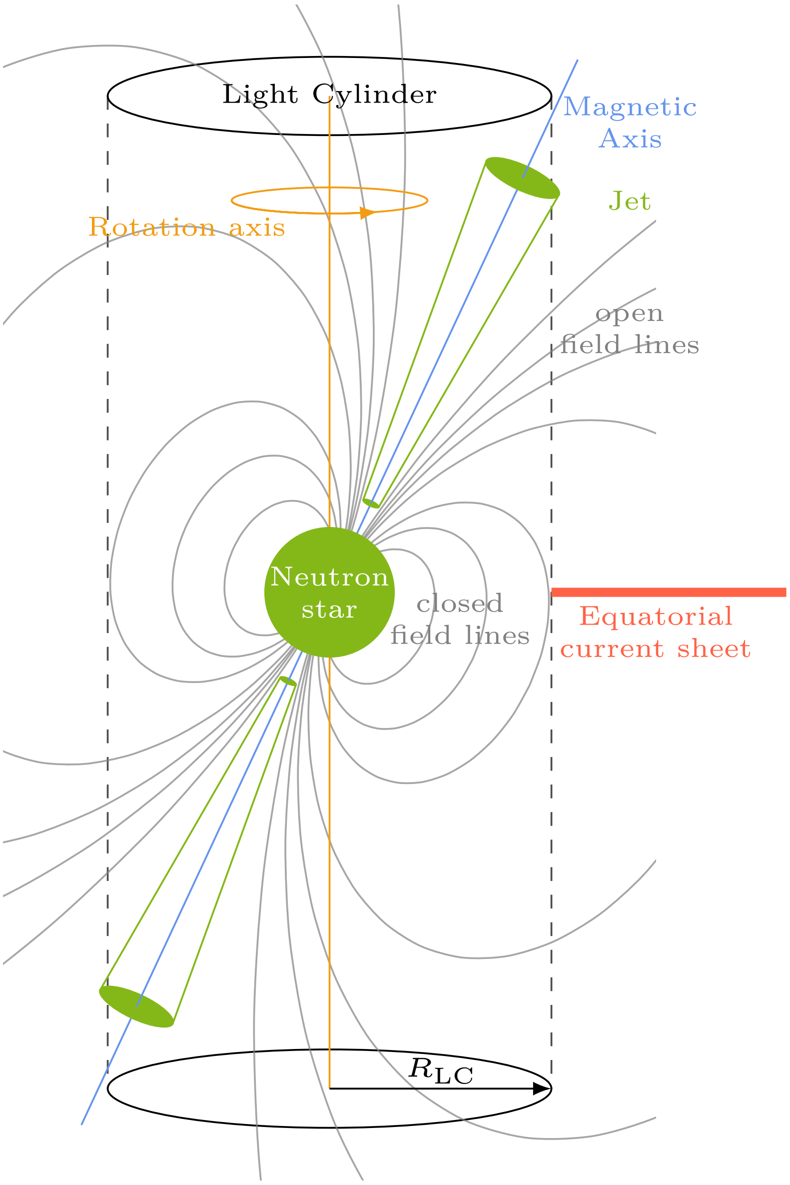

Figure 2.1: Schematic depiction of a pulsar and its surroundings. The neutron star rotates around the rotation axis which is not aligned with the magnetic axis. Up to the light cylinder, the magnetic field lines are closed. Beyond the light cylinder, the magnetic field lines cannot co-rotate and hence the field lines reaching beyond the light cylinder remain open. Along these field lines, charged particles escape the light cylinder. A return flow of charged particles emerges at the equator and is confined in the equatorial current sheet by the reconnecting field lines in this area. Graphic adapted from [106].

2.1.4 Pulsar Emission

Understanding the cause of the characteristic pulsar signals is still a major challenge in astrophysics. Because the pulsation in the signal is seen, it can be concluded that the particle acceleration must take place inside or very near the light cylinder which already restricts the possible emission mechanisms.

There are different models for explaining the pulsed signals that emerged over time. Three older models, namely the polar gap model, the slot gap model, and the outer gap model all assume the pulsed emissions originating from a pulsar beam of the fast-rotating neutron star which sweeps across the telescope's line of sight and is powered by emission mechanisms in different areas inside the light cylinder. A newer approach to explain the high-energy radiation is the equatorial current sheet which is located just at the edge of the light cylinder. All models have in common that they assume electric fields to accelerate charged particles up to high energies, causing the charged particles to emit curvature or synchrotron radiation. Further, pair production is assumed to occur in the polar caps and in the outer magnetosphere as well as in the equatorial current sheet. It should be noted that the origin of radiation in pulsars is still subject to current research. In the following, the most common models for the generation of radiation are presented briefly, focusing on the explanation of gamma emission. For a more detailed overview, the interested reader is referred to [85, 144].

Polar Gap: The polar gap model was first introduced in [167] and developed further in numerous works such as [62, 152]. In this model, the radiation originates at the open magnetic field lines above the pulsar's poles. Here, charged particles are accelerated along open field lines to high energies and emit curvature and synchrotron radiation up to gamma rays of few GeV. In the strongly magnetic environment of the pulsar poles, electron-positron pairs are formed from the high-energy photons and result in a superexponential cut-off[1] at energies of few GeV [40]. Further, this model results in gamma-ray beams with a small opening angle.

Slot Gap: The slot gap model was firstly described in [35] to explain the high-energy emission that was observed in the X-ray and low-energy gamma-ray range. Further research on this model has been published in various articles such as [33, 34, 129, 130]. The slot gap is located at the rim of the polar cap and extends up to the last open magnetic field line. The electric field is weak near the last open magnetic field line so that no high-energy radiation can be emitted at low altitudes (i. e. close to the pulsar). Instead, the particle acceleration is continued up to high altitudes (multiple times the radius of the neutron star) and high-energy radiation is emitted at high altitudes only. In the outer magnetosphere, the gamma-ray absorption is dominated by photon-photon collisions, which result in an exponential cut-off at energies of tens of GeV. In this model, gamma rays are expected to be emitted in a broader beam.

---

[1] A superexponential cut-off describes an exponential decrease in the flux at high energies that is faster than a simple exponential cut-off. This can be described mathematically as $F(E) \sim E^{-\Gamma} \exp\left(-\left(\frac{E}{E_0}\right)^{\beta}\right)$

Outer Gap: The outer gap model was introduced in [57] as an alternative explanation for the high-energy emission of pulsars. Further discussions can be found (amongst others) in [169]. The outer gap occurs outside the last field line of the equatorial region. In this region, charge depletion causes an electric field that can accelerate charged particles. As the acceleration takes place in the outer magnetosphere, an exponential cut-off at few tens of GeV and a wide opening angle of the pulsar beam are expected.

Equatorial Current Sheet: The equatorial current sheet as a Multi Wavelength (MWL) photon emitter was firstly hypothesized in [119] although the current sheet itself was already described much earlier [184]. The emission theories in the current sheet were further developed in numerous works, for example, in [56]. In the current sheet, the magnetic reconnection causes a high energetization of particles leading to pair production and high-energy photon emission through synchrotron and curvature radiation [143, 144]. With this model, a much higher luminosity in the gamma-ray regime can be explained. In this scenario, the observation of pulses is explained by a caustic effect, i. e. with photons emitted at different times, that accumulate in one observable pulse due to the geometry of the current sheet. The signal along the observer's line of sight is accumulated and a pulse can be seen when the observer's line of sight crosses the current sheet.

The beams in the polar gap model are too narrow to explain the pulse profiles that are not separated by half a phase. Further, the super-exponential cut-off at few GeV prohibits a VHE gamma-ray pulsed signal. The slot gap and the outer gap model can explain two peaks separated by less than half a phase since the emission beams in these models are larger. With both models, it is difficult to explain the measured flux in the VHE gamma-ray regime. The high measured flux and the high radiative efficiencies in gamma-ray pulsars can be explained best with the equatorial current sheet. In this region, most of the high-energy photons are expected to be produced. [144]

2.2 Pulsar Wind Nebulae

PWNe occur in Supernova Remnants (SNRs) that have a pulsar as a central compact object and a surrounding nebula that can be visible in the entire electromagnetic spectrum. The central pulsar powers the emissions of the PWN through an exchange of energy via the so-called pulsar wind. The pulsar wind is the stream of particles that are strongly accelerated in the pulsar's magnetic field as described in the last chapter.

While the pulsar wind propagates into the surrounding interstellar medium and collides with dust and gas, it creates a shock front (also called forward shock front). At this shock front, material accumulates and the charged particles are decelerated creating the termination shock. [108]

Due to the material accumulation in front of the forward shockwave and the resulting particle deceleration, a reverse shock evolves which propagates back into the supernova ejecta. The reverse shock heats the gas in the nebula, causing it to emit radiation from radio to gamma rays. Pulsar winds are expected to be mainly composed of electrons and positrons. These relativistic charged particles can emit synchrotron radiation up to X-ray energies. They can also upscatter low-energy photons up to higher energies, enabling the emission of higher-energy photons. In this inverse Compton scattering, even VHE gamma rays can be produced. [159]

2.3 Crab Nebula and Pulsar

The Crab Nebula is a supernova remnant in the constellation of Taurus at a distance of approximately 2 kpc from Earth [51, 173] which is powered by the Crab Pulsar. The corresponding supernova was observed by Chinese astronomers in 1054 as a "guest star" which was visible even during the day for some weeks [138]. It has two bright stars in its direct surroundings, Zeta Tauri, with a visible brightness of 3.0 mag and o Tauri with a visible brightness of 4.88 mag [96]. Although it is not visible by the naked eye anymore, the Crab Nebula is still the brightest PWN and therefore a popular target for hobby astronomers and scientists. In VHE gamma rays, it is the brightest stable source on the night sky and hence it acts as a standard candle for gamma-ray astronomy.

2.3.1 The Crab Nebula

The Crab Nebula itself was discovered by the amateur astronomer John Bevis in 1731 [36, 44, 101]. Since then, it has been a very popular target for hobby astronomers as it is visible with relatively small telescopes and in the optical range. The Crab Nebula is also the first object in the very popular Messier catalog that Charles Messier published in 1771, aiming to exclude nebula-like static objects in the sky for his search for comets [101, 123]. Further, it was the first object that could be classified as a supernova remnant by Edwin Hubble in 1928 based on its expansion [99].

Later on, the Crab Nebula was observed from radio to VHE gamma rays, impacting the understanding of SNRs and especially PWNe. In 1989, TeV gamma rays from the Crab Nebula were detected with an IACT by the Whipple experiment [178]. This opened up a broad field of investigations that have since then been done with different IACTs in the VHE gamma-ray regime and are still done today with multiple telescope arrays, such as MAGIC [19, 21], H. E. S. S. [15, 97], Very Energetic Radiation Imaging Telescope Array System (VERITAS) [121] or the prototypes of the Cherenkov Telescope Array (CTA) [7].

Recently, the Large High Altitude Air Shower Observatory (LHAASO) has observed PeV emissions from the Crab Nebula [53, 54] opening up an energy range in which smoking gun evidence for a hadronic contribution could be found.

The Crab Nebula is well visible all over the electromagnetic spectrum, as visible in Figure 2.2, due to its proximity to Earth and its high luminosity. It spans around 11 ly (depending on the wavelength it is observed in) and is further expanding with around 1500 km/s [45]. The Crab Nebula's measured signal is nearly constant in the high-energy gamma-ray regime, justifying its role as standard candle in high-energy gamma-ray astronomy [124]. Therefore, it is also used as a target for test analyses and is observed frequently.

Despite being the number one calibration source for IACTs, the space-based gamma-ray observatories *Fermi* and Astro-Rivelatore Gamma a Immagini Leggero (AGILE) have observed multiple flares in the low-energy gamma-ray regime [31, 166, 170]. However, those flares could not be observed in the VHE gamma-ray band (as observed by IACTs) [9, 27].

Though it is one of the most studied astronomical objects in the universe, there are still many open questions concerning the Crab Nebula. For example, the particle acceleration inside the nebula and the composition of the pulsar wind are still not fully understood.

(a) The Crab Nebula as seen in X-ray, Ultra Violet (UV), optical, infrared and radio. Image taken from [183].

(b) The Crab Nebula as seen in X-ray, optical, and infrared. Here, the Crab Pulsar and its jet structure can be seen. Image taken from [182].

Figure 2.2: MWL observations of the Crab Nebula.

2.3.2 The Crab Pulsar

The Crab Pulsar was first theoretically proposed by Pacini in 1967 [136] and about one year later, it was detected in radio observations of the Crab Nebula [164]. The Crab Pulsar was the object for which the pulsed radio signal could be associated with neutron stars due to its very short pulse intervals.

The Crab Pulsar has a low rotational period of approximately 33.6 ms and a high power of $\dot{E} = 5 \cdot 10^{31}$ J/s. Following Equation (2.1), the radius of the light cylinder is ∼1500 km. The radius of the Crab Pulsar itself is assumed to be 14 km to 15 km. [185]

The Crab Pulsar is one of the (if not *the*) best observable pulsars and consequently of huge interest for research on pulsar physics but also for research on more basic physics processes, such as particle acceleration or relativistic shocks that also occur in different astronomical objects. It is the object with the broadest measured emission spectrum ranging from 20 MHz up to TeV energies [30, 74]. The first detection of the Crab Pulsar with an IACT was achieved by MAGIC in 2008 [29] and the first detection in the VHE gamma-ray band soon followed by VERITAS in 2011 [28]. Since then, it has been also detected above 100 GeV with MAGIC [25] and more groundbreaking discoveries, such as the discovery of TeV pulses [30] and the discovery of a bridge emission [23] have been achieved.

A crucial characteristic to further understand the Crab Pulsar and the surrounding Nebula is the pulse profile (also called phasogram). It describes the measured signal within one rotational period of the pulsar. The peak P1 is (per definition) at the phase 0. Contrary to some other pulsars, the Crab Pulsar has a second peak P2, located at a phase of ∼0.4. Both pulses are visible from radio to VHE gamma rays and have an approximately constant position in the pulse profile. The width and the amplitude of the pulses however differ largely in the different wavelength bands. While P1 is dominant in the low-energy range from radio to lower-energy gamma rays, P2 becomes dominant at high energies ($\gtrsim$50 GeV) [23]. Further, so-called bridge emission between both pulses can be observed from ∼10 GeV to ∼150 GeV. While the spectrum of P1 could be measured up to 600 GeV, the spectrum of P2 extends up to more than one TeV [30]. In Figure 2.3, an exemplary MWL phasogram of the Crab Pulsar is shown.

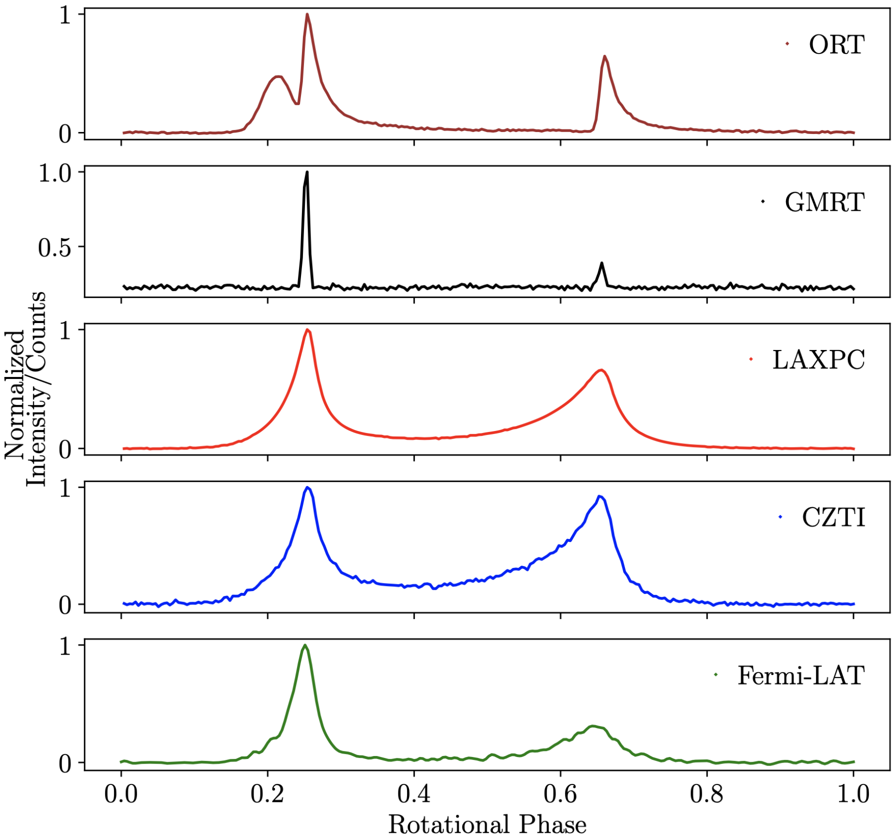

Figure 2.3: MWL pulses of the Crab Pulsar. The ORT and GMRT are radio telescopes observing at 334.5 MHz and 1390 MHz, respectively. LAXPC and CZTI are X-ray observatories with energy boundaries of ∼3 keV to 80 keV and ∼20 keV to 380 keV, respectively. *Fermi*-LAT covers the gamma-ray range from MeV to GeV energies. Graphic adapted from [41].

Although it is one of the most studied pulsars in the universe, there are still numerous unknown features of the Crab Pulsar:

- To which energies does the spectrum extend and which mathematical function describes the spectrum best?

- Which acceleration mechanisms are active in the Crab Pulsar at which wavelengths and which model describes the emission in the different wavelengths best?
- At which angle do we see the Crab Pulsar and what is the opening angle of the pulsar beam in the different wavelengths?

A more detailed summary of the properties of the Crab Pulsar can be found in [185].

2.4 Dragonfly

Dragonfly is a PWN in the Cygnus constellation, located at a distance of approximately 2 kpc [105] to Earth. With its estimated age of around 17 kyr, it still counts to the population of young PWNe. It is powered by the Dragonfly Pulsar (also referred to as PSR J2021+3651) which features a rotational period of ∼104 ms and a total spindown luminosity of $\dot{E} \sim 3.4 \cdot 10^{30}$ J/s. [149]

The Dragonfly Pulsar was first observed in the radio band in 2002 [149] and later, pulsed signal could also be observed in X-ray [91], optical [105], and gamma rays [4, 84]. *Fermi*-LAT could observe pulsed signal up to energies of few GeV, so it might also be observable with IACTs whose thresholds lie around tens of GeV [52]. A study of VERITAS using approximately 58 h of data, however, did not find pulsed signal [32] and neither did MAGIC in a standard analysis using roughly 27 h of data [161]. The Dragonfly Nebula, however, was observed by MAGIC up to TeV energies [188]. A recent study based on MWL data in the X-ray and gamma-ray regime suggests the Dragonfly Nebula to likely be a PeVatron [180].

2.5 Detection of Gamma Rays

There are different approaches for the detection of gamma rays. The direct approach is performed by measuring the gamma photons beyond Earth's atmosphere with a space-based telescope such as the LAT on the *Fermi* satellite. The LAT can detect the charged particles created by pair production in a calorimeter with high-precision trackers when a high-energy photon between ∼20 MeV and ∼300 GeV arrives. The LAT has a field of view of 2.4 sr which allows the simultaneous observation of around 20 % of the sky. Hence, it is used for surveys in the low-energy gamma-ray regime [37]. Further, *Fermi* is equipped with the Gamma-Ray Burst (GRB) monitor [122] which allows for GRBs to be firstly detected and then observed with the LAT directly afterward. It has detected numerous beforehand unknown sources [5, 12, 13], amongst them several gamma-ray pulsars [145, 160], and it has observed the two until now (as of 2024) most powerful GRBs [3, 110]. Further, it discovered gamma-ray emission perpendicular to the galactic plane, the so-called Fermi bubbles [168].

However, there are two main disadvantages of the LAT and of space-based gamma-ray detectors in general. Firstly, they are much more expensive and complex than ground-based experiments. Further, the maintenance and potential repairs or upgrades on a satellite are costly and highly complicated. Another problem for space-based gamma-ray observatories is that the detector volume on satellites is limited by their carrier's size, which in turn determines the upper energy limit of the measured particles. Larger calorimeters that can detect VHE gamma rays could in principle be built and installed on a satellite, however, the costs for this would be astronomical. Since ground-based IACTs represent a good alternative for VHE gamma-ray astronomy that is much cheaper, this is the favored approach.

The detection of gamma rays on Earth's surface is only possible indirectly since the atmosphere is not transparent for gamma photons. As soon as a gamma photon hits the atmosphere, it produces an electron-positron pair, while transferring parts of its momentum to an atom of Earth's atmosphere. These secondary particles emit Bremsstrahlung which can in turn create more electron-positron pairs. All the secondary particles can produce more secondary particles until the entire energy of the initial photon is deposed in a cascade of particles. This cascade is also referred to as an Extensive Air Shower (EAS). A depiction of the development of an EAS is presented in Figure 2.4. [65]

As the charged particles of the EAS pass through the atmosphere, dipoles align and relax again. Each moving dipole emits electromagnetic radiation. If a charged particle moves faster than the speed of light in the medium, the radiation of the different dipoles interferes constructively and Cherenkov radiation is emitted at a material-dependent angle

$$\Theta_{\mathrm{c}} = \cos^{-1}\left(\frac{1}{n\beta}\right) = \cos^{-1}\left(\frac{c}{n v_{\mathrm{p}}}\right) , \tag{2.2}$$

where n is the refractive index of the medium, c is the vacuum speed of light and v_{p} is the velocity of the particle. The geometry of this process is illustrated in Figure 2.5. The emitted photons range from the ultraviolet to the visible spectrum and reach their intensity maximum at 420 nm. If the particle moves slower than the speed of light in the medium, the radiation interferes destructively and no Cherenkov radiation is emitted. This Cherenkov radiation can be measured on Earth by IACTs. [128]

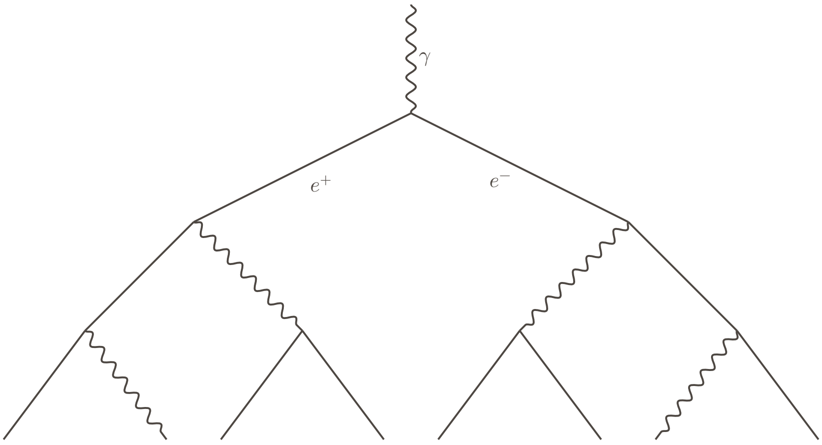

Figure 2.4: Schematic depiction of the development of an electromagnetic air shower as firstly introduced in [89]. An initial photon γ produces an electron-positron pair. The electrons and positrons emit Bremsstrahlung which in turn again creates electron-positron pairs.

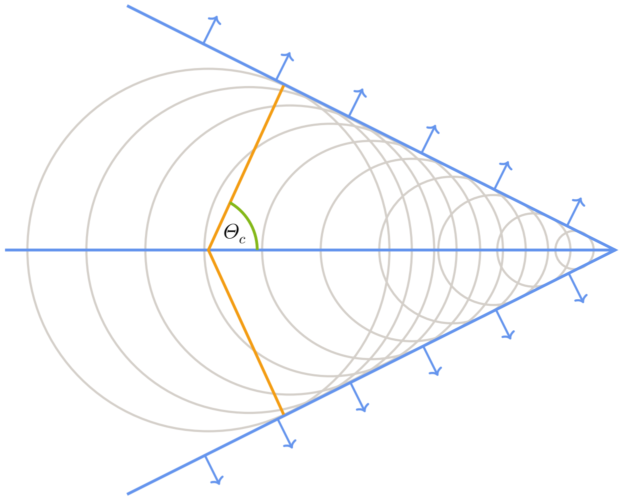

Figure 2.5: Depiction of the emission of Cherenkov radiation. The charged particle moves from the left to the right on the horizontal blue line which causes dipoles to align and relax again afterward. These dipoles emit radiation in all directions, as shown by the grey circles. The envelope of these wavefronts is the emitted Cherenkov radiation shown in blue. The arrows show the direction the wavefront is moving in which is given by $90° - \Theta_\mathrm{c}$ concerning the direction of the initial charged particle.

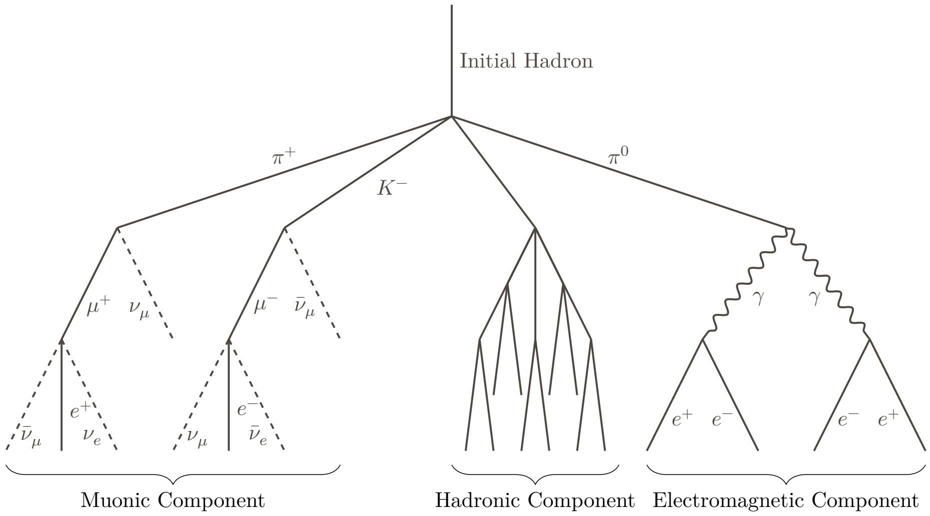

Figure 2.6: Schematic depiction of a hadronic shower. Apart from the electromagnetic component that can also be measured by IACTs, hadronic showers also possess a muonic and a hadronic component. Please note that electrons produced in the muonic or hadronic component also contribute to the electromagnetic component and there is no clear distinction of the components. Here, the components are only split for clarity.

Not only gamma rays create EASs in the atmosphere but also high-energy hadrons (mostly protons). Air showers initiated by hadrons consist of three components, the electromagnetic component, the muonic component, and the hadronic component. The electromagnetic component is initiated by neutral pions that most likely decay into a gamma pair. These photons develop into a shower component via pair production and bremsstrahlung, which is similar to the showers initiated by primary gamma radiation. The muonic component emerges mostly from charged pions or kaons that are created during the nuclear interaction of the shower particles with the atmosphere. The kaons and pions can then decay into (anti) muons and (anti) muon neutrinos. The muons themselves can decay into electrons and positrons afterward but they often reach Earth's surface without decaying. In the hadronic component, more hadronic particles (mostly pions and kaons) are created which can further scatter or decay. An illustration of this process can be found in Figure 2.6. [65]

The Cherenkov radiation created in the electromagnetic component of those hadron-induced showers is also detected by IACTs and builds the main background for the analysis with a factor of around 10^5 more background showers than gamma-induced showers. However, their signature in the camera differs (in most cases) from the signature gamma-induced showers leave in the camera. Therefore, it is possible to distinguish between those particles, as will be further described in Chapter 3.

2.6 The MAGIC Telescopes

The MAGIC telescopes are a stereoscopic IACT pair sensible to the GeV to TeV gamma-ray range. They are located on the Roque de los Muchachos on La Palma (Canary Islands, Spain) at an altitude of 2200 m. They observe the high-energy gamma sky with their 17 m dish consisting of 247 mirrors which reflect Cherenkov light into the camera. The cameras consist of 1039 Photo Multiplier Tubes (PMTs) pixels each which can detect even single Cherenkov photons. The PMTs have a diameter of 25.4 mm each and are topped with a hexagonal Winston cone, maximizing the collected light. The PMTs produce an electric output signal proportional to the energy of the initial Cherenkov photon using the photoelectric effect. [26] The MAGIC telescopes are shown in Figure 2.7.

The first MAGIC telescope (called M1 in the following) started observations in 2004 [39]. In 2009, the second MAGIC telescope (M2) followed [60], and in 2012 both underwent a major upgrade to modernize and unify both telescopes in order to allow for stereoscopic measurements [20, 26]. Still, M1 and M2 are not completely identical and consequently have different parameters and performance. The stereoscopic observation allows for an improved reconstruction of the events.

They are equipped with the Light Detection and Ranging (LIDAR) laser that fires pulses into the atmosphere whose reflections are measured. This allows for measuring the aerosol transmission of the atmosphere in real-time. The transmission serves as a measure for the amount of Cherenkov-light-obscuring dust in the atmosphere and is a value between 0 and 1, denoting the fraction of the light that is transmitted. [154] Further, the MAGIC telescopes are equipped with a pyrometer monitoring the cloudiness at the target position by measuring the thermal radiation of the sky in the line of sight to the target position [80].

Figure 2.7: The MAGIC telescopes on La Palma with M1 on the left, M2 in the center, and the counting house with the LIDAR dome on the right. The Gran Telescopio Canarias (GTC) can be seen in the background.

Analysis of MAGIC Data 3

> The only way humans have ever figured out of getting somewhere is to leave something behind.
>
> Cooper
> Interstellar

The data acquired by IACTs consist of time series of currents in each of the PMTs, while most of the triggered signal is hadron-induced. On this level, the data do not yet allow for drawing conclusions about the EAS or even the gamma-ray source. Instead, the measured data must first undergo a complex data analysis in order to provide physics results. This chapter describes the (stereo) analysis chain that calculates physics information such as the energy spectrum or the light curve of the gamma source from the pixel information of individual showers recorded by the MAGIC detector. Additionally, new tools for the data analysis are introduced which represent a new analysis approach and go one step towards reproducible and open science. It is one of the main goals of this thesis to further strengthen the use of these tools.

In the following, different types of data as well as the data-taking process itself are described. Afterward, an overview of the calculations performed in the standard analysis chain is presented. Then, the new gamma-astronomy standard data format `DL3` is introduced and the implementation of the standard analysis chain up to `DL3` is described. In the end, the MAGIC tool for automatic analyses `autoMAGIC` as well as the open-source `Python` package `Gammapy` are presented.

3.1 MAGIC Data

In this section, the data-taking procedure as well as the different data types are described. In the MAGIC analysis chain, three different types of data appear:

On data: Data of the source to be analyzed.

Off data: Data containing few to no gamma rays used to train models for the gamma-hadron separation.

Monte Carlo (MC) data: Simulated gamma-ray data containing the true, simulated properties of the primary particle.

In the following, the data-taking procedure is presented and afterward, these three data types are shortly presented and distinguished from one another.

3.1.1 Data Taking

During data taking, the PMTs in both cameras detect the incoming Cherenkov photons. The PMTs are connected to Domino Ring Sampler 4 (DRS4) chips reading out the PMT signals with a measured bandwidth of ∼650 MHz [26]. If the signal exceeds the trigger thresholds (see also Chapter 4), the signal of all pixels is recorded for the duration of around 30 ns. The trigger criteria include that both telescopes measure enough signal and they stereoscopically record the data.

In the data, a signal that does not originate from the gamma source is expected. On the one hand, it consists of diffuse gamma rays and on the other hand also of hadrons that were incorrectly identified as photons. This background should fall homogeneously into the camera. Due to the radially symmetric acceptance of the camera, the background can be expected to be the same in regions with the same distance to the camera center. For the signal extraction, the excess of the signal over the background has to be measured, which is achieved by defining a so-called On region in which the source is expected and so-called Off regions from which the background signal is extracted.

Standardly, IACTs take data in the so-called *wobble* mode, introduced in [77]. This means that instead of pointing exactly at the source position, the telescopes point next to the source position with a certain offset, enabling the possibility to take data for the On and Off regions simultaneously. The position the telescope points at during this procedure is called wobble position.

During the observation of a source, the wobble positions are changed to prevent systematic errors due to different telescope responses for different positions of the source in the camera. Usually, observations at four wobble positions at 0°, 90°, 180°, and 270° are performed. In special cases, however, the wobble positions can differ both in the angle and in the offset to the source. During the analysis of the data, for each wobble position, one or more Off regions can be defined in which the background is evaluated. They are taken equidistantly around the wobble position with the same distance to it as the On region. In Figure 3.1, an overview of the wobble mode is presented.

The data is organized in a structure of so-called runs and subruns. For each observation of a source at a certain wobble position, a run with a length of typically 20 min is recorded. In order to limit the size of individual data files, the run is divided into typically tens of subruns.

At the beginning of each observation of a source, calibration and pedestal runs are taken. For long observations (multiple hours), a pedestal and calibration run are also taken in between. The pedestal runs are taken with a random trigger and are used to measure the noise. For the calibration runs, a calibration laser located at the center of the dish emits short light pulses with constant light intensity and wavelength in the direction of the camera. A dedicated calibration trigger is applied. This is necessary to compute the conversion factor from readout counts to photo electrons (p. e.).

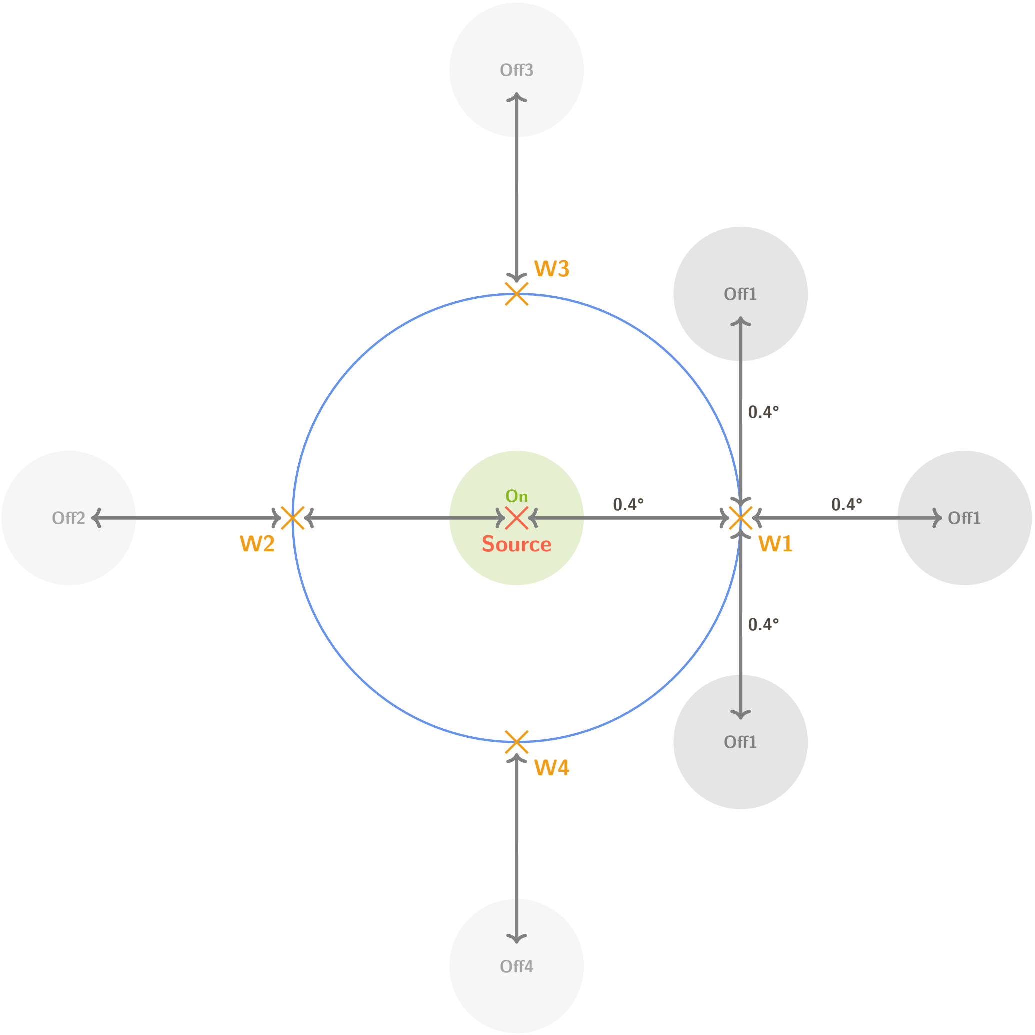

Figure 3.1: Overview of the wobble mode. The assumed source position is marked in red and lies in the defined On region. Usually, the wobble positions are chosen with a wobble distance of 0.4° at wobble angles 0°, 90°, 180°, and 270°. With a distance of 0.4° around the wobble position, one or multiple Off regions are chosen. For clarity, multiple Off regions are only shown for the first wobble position W1 here.

3.1.2 On Data

On data is the data from observations of the source itself from which the analyzer wants to extract physics information. Models based on the Off and the MC data have to be trained in order to perform the gamma-hadron separation in the On data which is crucial for the success of the analysis. The MC data is further used to estimate the energy of the initial particle and the direction it came from.

3.1.3 Off Data

Off data is taken from dim sources where no significant gamma signal is expected. Consequently, it mostly contains hadronic events and is therefore used together with the MC data to train a Random Forest (RF) for the gamma-hadron separation. The observation conditions of the Off data have to match the observation conditions of the On data in terms of observation angle, moon condition, and the telescope's response to the gamma-ray showers to minimize the risk of systematic errors. As long as the telescopes observe many faint sources in the hope of being able to detect them, the Off data comes 'for free' since much of all measured data can also be used as Off data in other analyses.

For some sources that require a special analysis, dedicated Off data is measured. This is for example sometimes the case for Sum-Trigger-II observations (see Chapter 4). Furthermore, some dark areas in the sky (so-called *dark patches*) are observed which only serve as Off data and for specific tests.

3.1.4 Monte Carlo Data

MC simulations of photons with known energies and direction are performed in order to draw conclusions about the properties of the primary particle from the properties of the shower images. This is essential for the analysis since by the MC data, the RF can learn in which parameter range typical gamma events are and how they differ from hadronic data (the Off data). With machine learning algorithms, the gamma-hadron separation (see also Section 3.2.6) can be performed and physics information can be extracted from the data.

For the gamma-ray simulation, all the secondary particles and their propagation and ray tracing are computed. Further, the telescope's response in terms of the reflection of the photons in the telescope's mirrors and the response of the camera, including trigger patterns and readout electronics, is simulated. The simulation is done for a high number (mostly a few million) of events for different particle input parameters such as different energies and different angles.

The gamma-ray simulation is performed with Cosmic Ray Simulations for Kascade (`CORSIKA`) [87, 88]. It was first published in 1989 and originally developed at the Karlsruhe Institute of Technology (KIT). Since then, multiple versions have been published, enhancing the physics performance and reducing the computation time. The MAGIC collaboration uses a modified version of `CORSIKA` 6.5.0.0 and 6.9.9 called MAGIC Monte Carlo Software (`MMCS`) [162] for the shower simulation and the simulation of the Cherenkov photon generation.

The telescope's response to the events is simulated in the MAGIC internal programs `reflector` and `camera`. While `reflector` computes the atmospheric absorption of the

Cherenkov photons and the reflection in the mirrors, `camera` simulates the data-taking process in the camera, considering trigger, readout, etc.

MC data is usually split into a training and a test sample. The training sample is used to train the RF for the gamma-hadron separation together with the Off data and to train the RFs for the event reconstruction, whereas the test sample is used to calculate true particle flux from the measured one. For this step, the telescope's performance is computed in the form of so-called Instrument Response Functions (IRFs).

Since the telescope's response to the gamma-ray shower changes over time due to parameters such as dust on the mirrors or varying hardware, there are so-called MC periods in which the telescope's response to the gamma-ray showers is similar. A list of the MC periods that were used in this work is shown in Table 3.1. For each period, a dedicated MC set taking into account the varying telescope response is produced and has to be used for the analysis. For each period the two parameters `axis deviation` and `mirror fraction` are adapted based on information from muon runs.[1] While the `mirror fraction` is a measure for the reflectivity of the mirrors and therefore related to the observed brightness of the events, the `axis deviation` is a measure for the scattering of the photons and therefore for the directional resolution.

Diffuse and ringwobble MC simulations are produced. The ringwobble MC simulations are used in standard analyses where the position of the source is known and the source is point-like, meaning its apparent extension is negligible compared to the telescope's resolution. Here, the events are simulated only on a thin ring of 0.4° distance to the camera center because this is where the gamma events are expected. Each of the MC sets consists of multiple (usually a few thousand) MC runs, which each contain typically 1000 gamma events.

---

[1] Muon runs are special runs taken in mono mode for each telescope during which a special trigger is applied, aiming to record the Cherenkov light emitted by muons. Since the amount of light and the narrow ring shape can be predicted theoretically, the measurement of those can serve as a measure for the smearing as well as the mirror reflectivity. Hence, the `axis deviation` and the `mirror fraction` can be calculated from the muon runs.

Table 3.1: MAGIC MC analysis periods. These are periods in which the telescope's response to signal is relatively constant. Only the periods of interest for this work are listed. For ST.03.09 and ST.03.16, the telescope response is nearly the same as for previously produced MC simulations and hence they are reused.

Period Name	Start Date	Stop Date	MC Production
ST.03.01	2012-09-01	2013-01-17	ST.03.01
ST.03.01	2013-01-18	2013-07-26	ST.03.02
ST.03.03	2013-07-27	2014-08-05	ST.03.03
ST.03.05	2014-08-31	2014-11-22	ST.03.05
ST.03.06	2014-11-24	2016-04-28	ST.03.06
ST.03.07	2016-04-29	2017-08-02	ST.03.07
ST.03.08	2017-08-02	2017-11-02	ST.03.08
ST.03.09	2017-11-10	2018-06-29	ST.03.07
ST.03.10	2018-06-30	2018-10-30	ST.03.10
ST.03.11	2018-11-01	2019-09-15	ST.03.11
ST.03.12	2019-09-16	2020-02-22	ST.03.12
ST.03.13	2020-02-26	2020-03-13	ST.03.13
ST.03.14	2020-05-14	2020-09-14	ST.03.14
ST.03.15	2020-09-15	2020-10-18	ST.03.15
ST.03.16	2020-10-24	2021-09-29	ST.03.12
ST.03.17	2021-12-30	2022-06-09	ST.03.17
ST.03.18	2022-06-10	2023-01-06	ST.03.18
ST.03.20	2023-03-10	to be defined	ST.03.20

3.2 Theoretical Description of the Data Analysis

As the detection process of the VHE gamma rays with IACTs is indirect, the recorded data has to undergo a complex analysis chain to deliver physics results. The main tasks in the analysis are:

1. Calibrating the camera images
2. Extracting arrival time information and charge
3. Extracting of the pixels contributing to the shower image (“image cleaning”)
4. Parameterizing the shower
5. Joining the data of both telescopes and calculating stereo parameters
6. Separating the gamma-induced showers from the hadron-induced showers
7. Estimating the direction and energy of the events
8. Computing the IRFs
9. Obtaining physics results (significances, spectra, light curves, etc.)

These steps are each described in detail in the following.

3.2.1 Signal Calibration

The PMTs measure a certain current per pixel, depending on the number of incoming photons and the noise. Since the output current for a given signal is not exactly equal for all PMTs, the data has to be calibrated. Firstly, the baseline has to be estimated so that it can be subtracted from the light pulse. For this, the time slices from pedestal events are taken and their mean is calculated. The baseline is then subtracted from the signal. Afterward, the signal can be extracted using the so-called sliding window method [17]. A window of six neighboring time bins over the time series is defined and the current within the window is summed up. The position of the window is chosen so that it maximizes the summed signal. In Figure 3.2 the signal extraction is visualized.

In the next step, the obtained signals are converted from readout counts to p. e.. This is done by using the F-Factor method (also called excess-noise method) [125]: one readout count is assumed to correspond to an unknown number C of p. e.. Following [79], a light pulse containing N p. e. will on average create a signal

$$\mu = \frac{N}{C}\,, \tag{3.1}$$

where μ is the averaged signal. Assuming a Poissonian response of the PMT, the Root Mean Square (RMS) (i. e. the fluctuations of the signal) is given by

$$RMS = \frac{\sqrt{N}}{C}\,. \tag{3.2}$$

Combining Equation (3.1) and Equation (3.2) delivers

$$N = \left(\frac{\mu}{RMS}\right)^2\,. \tag{3.3}$$

Now, a correction factor F^2 for the non-Poissonian response of the PMT has to be applied, and further, the pedestal fluctuations RMS^2_{ped} have to be subtracted from the signal fluctuations RMS^2_{sig}. Considering this, the number of p. e. becomes

$$N = F^2 \frac{\mu^2}{RMS^2_{\text{sig}} - RMS^2_{\text{ped}}} \,. \tag{3.4}$$

By this, the number of p. e. can be calculated. [20]

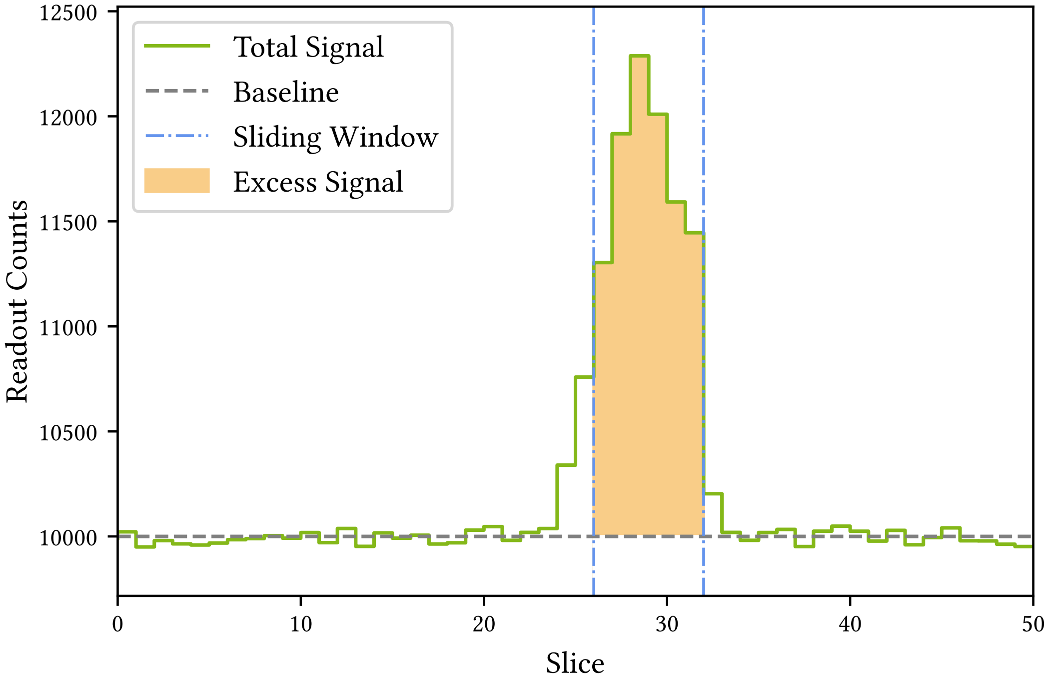

Figure 3.2: The sliding window method for the signal extraction.

3.2.2 Arrival Time Extraction

The pixel-wise arrival times of the signal are calculated by averaging the times of the six time slices of the chosen window, weighted by their signal:

$$t_{\text{arr}} = \frac{\sum_{i=1}^{n} t_i s_i}{\sum_{i=1}^{n} s_i} \,. \tag{3.5}$$

Here, t_{arr} is the arrival time, t_i is the time of the ith bin and s_i is its signal. [20]

3.2.3 Image Cleaning

In the image cleaning, only the pixels in the camera that contribute to the shower image are selected. For the image cleaning, in standard analyses, the so-called sum cleaning algorithm, further described in [20], is used. Here, the sum of all possible combinations of two, three, or four Nearest Neighbors (NN) (see Figure 3.3) in the camera is calculated and a NN-number-specific charge threshold as well as a NN-number-specific time window are applied to the sum of the signal whereas the thresholds for lower multiplicities are stricter than the ones for higher multiplicities. If the summed signal is above the threshold and within the time window, it is considered part of the shower image. In the second step, for the remaining pixels, boundary pixels within a certain, lower charge threshold and within a wider time range are searched. If the signal in the pixel is above the threshold and within the time range, the pixel is considered part of the shower image. In Figure 3.4, images of both an uncleaned and a cleaned camera image are presented.

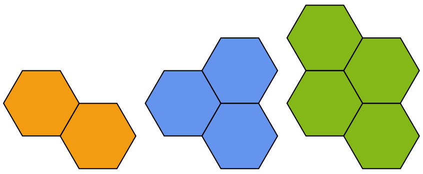

Figure 3.3: Visualization of 2, 3, and 4 NN.

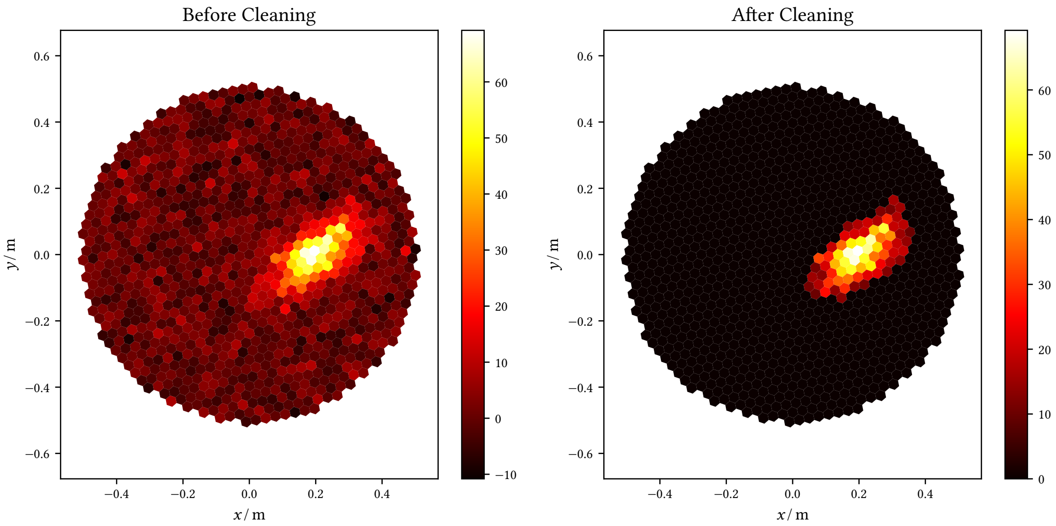

Figure 3.4: Visualization of the image cleaning. On the left, an uncleaned camera image is presented. On the right, a cleaned camera image with only the pixels considered as contributing to the shower image is depicted. The rest of the pixels is discarded (black).

For non-standard analyses, a different cleaning algorithm called MaTaJu cleaning can be used which is described further in Section 4.2.1.

3.2.4 Image Parameterization and Hillas Parameters

The projection of the particle shower recorded by an IACT has approximately the shape of an ellipse in the camera. Using a Principal Component Analysis (PCA), the Hillas parameters characterize and parameterize the camera images. There are six “original” Hillas parameters as introduced by Hillas in [93]:

length: The first component of the PCA or, more graphically speaking, half the length of the major axis of the ellipse.

width: The second component of the PCA or, more graphically speaking, half the length of the minor axis of the ellipse.

frac(2): Fraction of the signal in the two brightest pixels in the shower and the signal in the entire shower.

cog: Center of gravity of the shower, computed by calculating the position of the weighted mean signal along the x and y axis.

dist: Distance of the `cog` to the source position.

alpha: Angle between the major shower axis and the vector spanned by the `cog` and the source position in the camera.

By now, more parameters have been developed, improving the overall performance of the image parameterization and thus the event reconstruction. The most important ones for the scope of this thesis are:

size: Number of p. e. in the entire shower image. This is nearly proportional to the energy of the primary particle.

theta: Distance between the true and the reconstructed source position.

disp: Distance between the Hillas image centroid and the reconstructed source position.

In Figure 3.5, some of the Hillas parameters are visualized. For all measured showers, the Hillas parameterization is performed based on the cleaned images.

3.2.5 Stereo Reconstruction

Since both telescopes see the showers from different perspectives, the showers and thus the shower ellipses have different orientations. The long shower axis of a gamma-induced shower is pointing in the direction of the source, which means that in stereo mode, the shower direction can be reconstructed geometrically based on the shower orientations in the camera. For this, the intersection of the extended long half axes of both shower ellipses is calculated, as shown in Figure 3.6. [59, 114]

Based on the reconstructed shower direction, several other parameters are calculated:

Shower Core Impact on the Ground: The point of impact of the shower axis on the ground, calculated from the two projections of the shower axis in the camera images.

Impact Parameter: The distance of the telescope position projected vertically in a plane that is perpendicular to the shower axis.

Height of the Shower Maximum: Height in which the shower reaches its maximum brightness. It is calculated as the altitude that minimizes the distance between the shower axis and the direction lines originating from both telescopes.

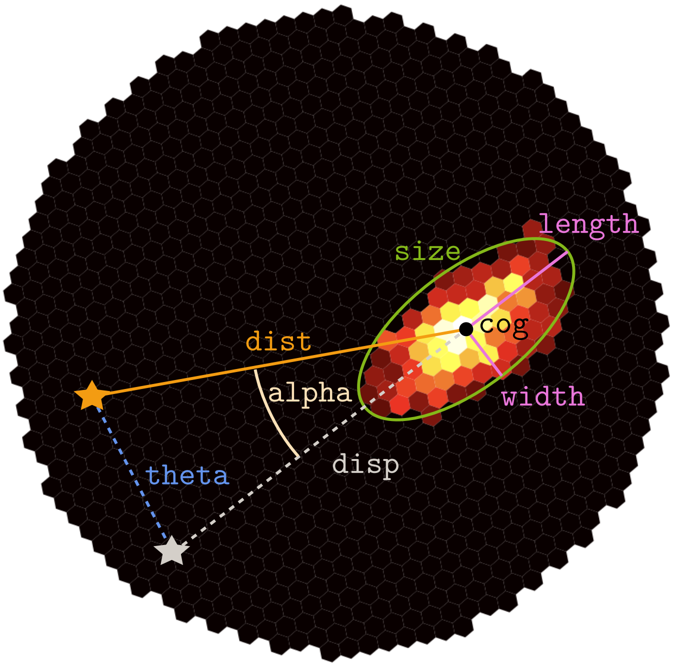

Figure 3.5: Visualization of some selected Hillas parameters. The minor and major half axes are shown in violet and characterize the parameters `length` and `width`. The orange star represents the true source position while the grey star shows the reconstructed source position. The blue dashed line represents the parameter `theta`. The orange line from the `cog` to the true source position is the `dist` and the grey line from the `cog` to the reconstructed source position is the `disp`. The angle between both lines (shown in yellow) is the parameter `alpha`.

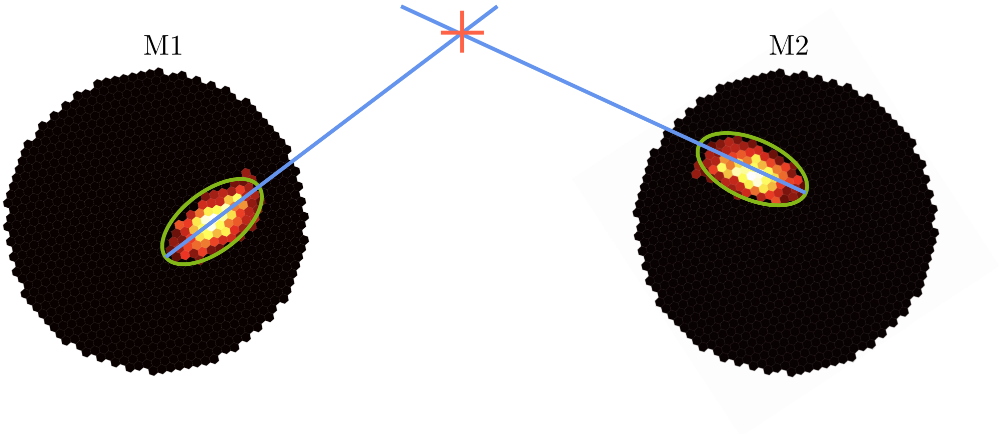

Figure 3.6: Illustration of the direction reconstruction with the Hillas ellipses. The long half-axis of the Hillas ellipses of the events in both telescopes is prolonged (marked in blue) and the intersection of them can be used as reconstructed shower position (marked as a red cross).

Cherenkov Radius: The radius at the ground (where the telescopes stand) of a Cherenkov ring produced by an electron with an energy of 86 MeV at the height of the shower maximum. The energy is assumed because this is the critical energy for an electron to produce Cherenkov radiation in the air.

Cherenkov Density: The light density at ground level in a plane perpendicular to the shower axis caused by a 1 m long track of a 86 MeV electron at the height of the shower maximum.

3.2.6 Gamma-Hadron Separation

For the gamma-hadron separation, each event is assigned a value called *hadronness*, specifying how hadron-like the event is. The hadronness is a value between 0 and 1, whereas events with a hadronness near 0 are most likely gamma-induced events, and events with values near 1 are most likely hadron-induced. In higher analysis steps, gamma-like events can be extracted by cutting on a certain hadronness value. The hadronness is calculated using a RF that is trained on Off data as hadronic background and MC data as gamma signal.

3.2.7 Source Position and Energy Reconstruction

A widely accepted approach for reconstructing the source position using IACTs is the so-called `disp` method [71, 111] which estimates the reconstructed source position with a RF trained with MC data. It delivers more reliable results than the pure geometric reconstruction described in Section 3.2.5. The `disp` describes the distance of the `cog` to the reconstructed source position which is located on the extrapolation of the long half-axis of the Hillas ellipse. It can be reconstructed well by a RF due to its correlation to multiple Hillas parameters such as the impact parameter and the `length`. In the stereo analysis, the `disp` of both camera images is calculated separately and then the average direction of both is taken as reconstructed source position.

With an additional RF, also trained with MC data, the energy reconstruction is performed whereas the `size` parameter is the most important one as it is approximately proportional to the energy.

3.2.8 Calculation of Instrument Response Functions

The IRFs are used to characterize the telescope's response to the incoming signals. Instead of measuring the quantity of interest directly, the measured data always consists of a convolution of the quantity of interest and the detector response, characterized by the so-called IRFs. The characteristic of interest in gamma-ray astronomy is the energy- and time-dependent flux $F(E, t)$ of a source at a position x. What the telescopes measure, however, is a number of counts given by

$$N(\hat{E}, \hat{\boldsymbol{x}}) = \int_{t_0}^{t_1} \mathrm{d}t \int_{\Omega} \int_{E} \frac{\mathrm{d}^2 F(E, \boldsymbol{x}, t)}{\mathrm{d}E \, \mathrm{d}\boldsymbol{x}} R(\hat{E}, \hat{\boldsymbol{x}} \mid E, \boldsymbol{x}, t) \, \mathrm{d}E \, \mathrm{d}\boldsymbol{x} + b(\hat{E}, \hat{\boldsymbol{x}}) \, . \tag{3.6}$$

Here, $N(\hat{E}, \hat{\boldsymbol{x}})$ denotes the number of measured counts, $\hat{E}$ denotes the reconstructed energy, and $\hat{\boldsymbol{x}}$ is the reconstructed position. The true flux $F(E, \boldsymbol{x}, t)$ is convoluted with the detector response $R(\hat{E}, \hat{\boldsymbol{x}} \mid E, \boldsymbol{x}, t)$, and background counts $b(\hat{E}, \hat{\boldsymbol{x}})$ are added. By characterizing the telescope response with the IRFs, the true flux can be reconstructed by deconvoluting the number of counts. The IRFs are:

Point Spread Function (PSF): The $\mathrm{PSF}(\hat{\boldsymbol{x}}|E, \boldsymbol{x})$ is a measure for the smearing of the reconstruction of the direction. It describes the spatial probability distribution of reconstructed events belonging to a source that is seen by the telescopes as a point source.

Effective Area: The effective area $A_{\mathrm{eff}}(E, \hat{\boldsymbol{x}})$ describes the telescope efficiency multiplied by the real detection area:

$$A_{\mathrm{eff}} = A\,\frac{N_{\mathrm{det}}}{N_{\mathrm{sim}}}\,. \tag{3.7}$$

Here, N_{det} denotes the number of detected events, N_{sim} is the number of simulated events, and the ratio denotes the efficiency. A is the area in which events were simulated. The effective area accounts for the detector imperfection.

Energy Dispersion: The energy dispersion $E_{\mathrm{disp}}(\hat{E}|E, \boldsymbol{x})$ is a measure for how well the particle's energy can be reconstructed. It describes the probability of a particle with a true energy E to be reconstructed with an energy E_{reco}.

The telescope response can be written as the product of the IRFs

$$R(\hat{\boldsymbol{x}}, \hat{E} \mid \boldsymbol{x}, E) = A_{\mathrm{eff}}(E, \boldsymbol{x}) \cdot \mathrm{PSF}(\hat{\boldsymbol{x}} \mid E, \boldsymbol{x}) \cdot E_{\mathrm{disp}}(\hat{E} \mid E, \boldsymbol{x})\,. \tag{3.8}$$

The IRFs are computed run-wise, i. e. in time intervals of approximately 20 min to characterize the time-dependency in the detector. The detector response is assumed to be constant within these time intervals.

For point sources at a known position, the spatial component x does not have to be considered. An On region around the estimated source position is defined and the number of events in this region is summed. By also summing the number of the events in the Off regions (see also Section 3.1.1), the background can be eliminated. The measured number of counts simplifies in this case to

$$N(\hat{E}) = t_{\mathrm{obs}} \int_E \frac{\mathrm{d}F(E)}{\mathrm{d}E} \cdot A_{\mathrm{eff}}(E) \cdot E_{\mathrm{disp}}(\hat{E} \mid E)\,\mathrm{d}E\,. \tag{3.9}$$

For counting experiments, such as IACTs, the discrete form applies:

$$\boldsymbol{N} = \boldsymbol{R} \cdot \boldsymbol{F}. \tag{3.10}$$

Here, the flux $\boldsymbol{F}$ and the telescope response $\boldsymbol{R}$ in the corresponding time interval are expressed as matrices with discrete entries in energy bins.

3.2.9 Obtaining Physics Results

After the events have been fully reconstructed and the telescope response has been characterized, finally physics information can be extracted from the data. This includes the calculation of significances and the estimation of flux points which is described in the following.

Significance Calculation

In the high-level analysis, the terms of the On region and the Off region (not to confuse with the On and Off data) are differentiated. They are both contained in the On data.

On region: This is the region where the source is expected and consequently where one expects a gamma-ray excess. For point-like analyses (meaning the source is smaller than the resolution of the telescope), this region has the size of the telescope's PSF (see Section 3.2.8).

Off region: In order to eliminate the remaining background, one or more Off regions are specified. Usually, when observing in wobble mode, the Off regions are defined equidistantly to the camera center with the same offset to the camera center as the On position.

For significance calculations, the excess of the events in the On region over the events in the Off region, weighted by their sizes, is computed, as done by Li&Ma (17) [112]:

$$S = \sqrt{2\left(N_{\mathrm{On}} \cdot \ln\left(\frac{1+\alpha}{\alpha} \cdot \frac{N_{\mathrm{On}}}{N_{\mathrm{On}} + N_{\mathrm{Off}}}\right) + N_{\mathrm{Off}} \cdot \ln\left((1+\alpha) \cdot \frac{N_{\mathrm{Off}}}{N_{\mathrm{On}} + N_{\mathrm{Off}}}\right)\right)}\,. \tag{3.11}$$

Here, N_{On} is the number of events in the On region, N_{Off} is the number of events in the Off region and $\alpha = {}^{t_{\mathrm{On}}}/{t_{\mathrm{Off}}}$ is the ratio of the observation times for the On and Off regions.

Flux Estimation

The flux in gamma-ray astronomy is defined as counts per time and area

$$F = \frac{\mathrm{d}^2 N}{\mathrm{d}A_{\mathrm{eff}}\,\mathrm{d}t_{\mathrm{eff}}}\,. \tag{3.12}$$

With the ideal values of the effective observation time t_{eff} and the effective area of the instrument A_{eff} (see also Section 3.2.8). In the analysis, two types of flux are particularly interesting: The Spectral Energy Distribution (SED) and the light curve. While the SED is the flux with respect to energy

$$\frac{\mathrm{d}F}{\mathrm{d}E} = \frac{\mathrm{d}^3 N}{\mathrm{d}A_{\mathrm{eff}}\,\mathrm{d}t_{\mathrm{eff}}\,\mathrm{d}E}\,, \tag{3.13}$$

the light curve is the flux in time bins for a given energy range

$$F_{\mathrm{int}} = \int_{E_{\mathrm{min}}}^{E_{\mathrm{max}}} \frac{\mathrm{d}F}{\mathrm{d}E}\,\mathrm{d}E\,. \tag{3.14}$$

There are different methods for the flux point estimation whereas the most common and most easy one is the method of forward folding. Here, a hypothetical source model characterized by an assumed spectral shape is folded with the IRFs to obtain a distribution of gamma rays in dependence of the estimated energy $N_{\mathrm{Pred}}(\hat{E})$ which is then compared to observations. A Poisson-statistics-based likelihood model is maximized to compute the model parameters that describe the observations best. [131]

The Poissonian distribution

$$p(k|\lambda) = \frac{e^{-\lambda}\lambda^k}{k!} \tag{3.15}$$

is used where $k = N_i$ are the observed counts and $\lambda = R_i F_i$ are the predicted counts in the corresponding energy bin i.

An energy-bin-wise minimization of the negative logarithmic likelihood $-\log(\mathcal{L}(F))$ delivers the best-fit value for the flux normalization parameter $\hat{F}$ in the corresponding energy bin. A test statistic is defined, comparing the Null hypothesis of no signal to the hypothesis given by the best-fit value:

$$TS = -2\log\left(\frac{\mathcal{L}(F)}{\mathcal{L}(\hat{F})}\right) . \tag{3.16}$$

The TS value is χ^2 distributed and hence underlies the relation to the significance of the flux points

$$\sigma = \begin{cases} \sqrt{TS} & \text{for } TS \geq 0 \\ -\sqrt{-TS} & \text{for } TS < 0 \end{cases} \tag{3.17}$$

3.3 MARS - MAGIC Analysis and Reconstruction Software

The data analysis chain for the MAGIC telescopes is implemented in the MAGIC Analysis and Reconstruction Software (MARS) [126, 186], making use of `C++` and `ROOT` [49]. The standard data analysis chain contains seven programs that have to be executed in a row. An overview of the complete analysis structure is presented in Figure 3.7. In the beginning, the data of both telescopes is treated separately, but in the course of the data analysis, the data is merged. A standard analysis of MAGIC data starts on `superstar` data that are centrally preprocessed with standard settings. For special analyses, however, a start on lower data levels may be necessary. In the following, the analysis steps are described briefly:

`sorcerer` calibrates the raw data and obtains the charge (in p. e.) and the Time Of Arrival (TOA) of the signal for each pixel. On raw level, the data describes readout counts per time in 60 time bins of 0.5 ns each. The signal is in this case an excess of the readout counts over the baseline, which describes the averaged number of readout counts if no signal arrives. From this information, the charge and the arrival time have to be extracted.

`merpp` merges the subsystem reports of the telescopes that contain meta information about the telescopes with the data.

`star` is responsible for the image cleaning and the calculation of the mono Hillas parameters.

`superstar` joins the data of both telescopes and performs the stereo reconstruction.

`selectmc` splits up the MC set into a training sample and a test sample and joins thousands of MC files into one file for each sample. Further, it can select the needed events from a diffuse MC production by cutting out a ring of events within a defined distance range of the event to the camera center.

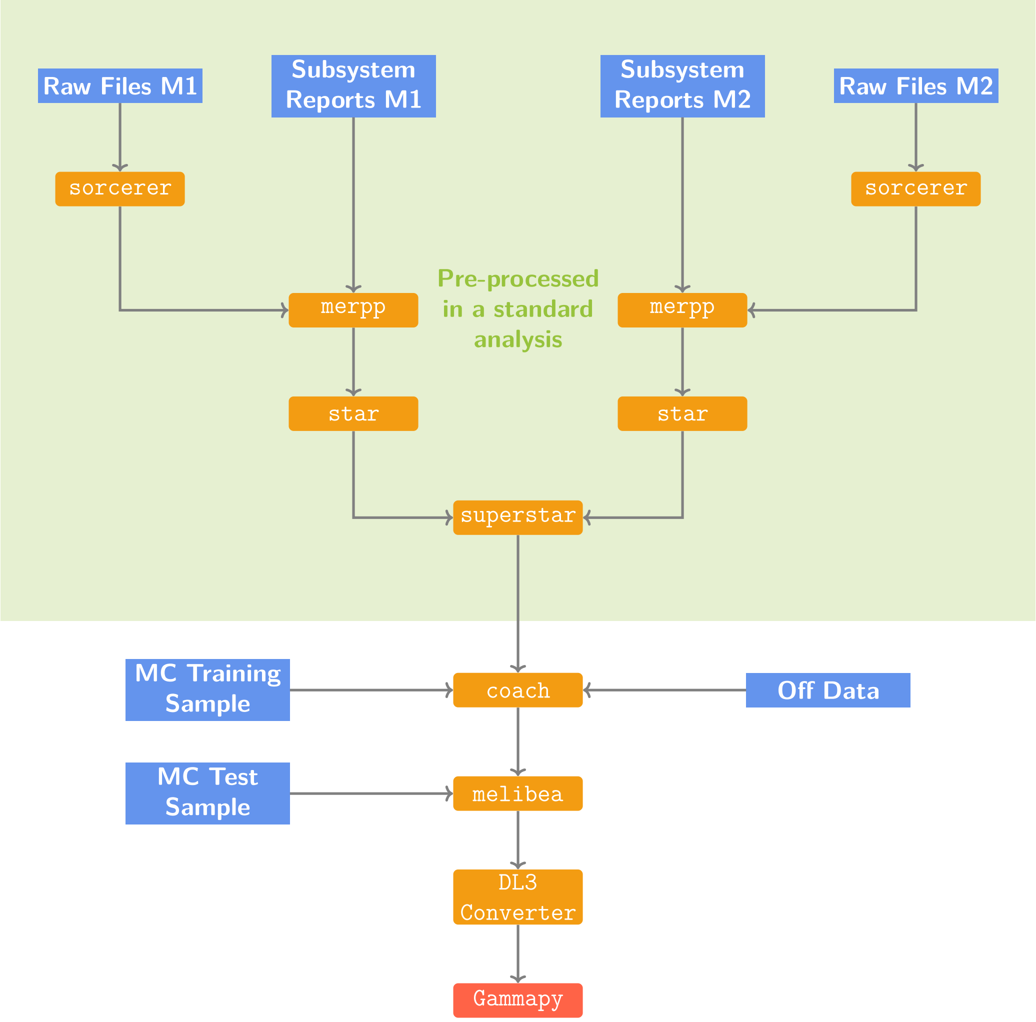

Figure 3.7: Visualization of the MAGIC analysis procedure. The blue boxes show the data that is inserted into the MARS executables, which are shown in yellow. All the analysis steps in the green box are pre-processed in a standard analysis.

`coach` trains models for the gamma-hadron separation as well as for the energy and position reconstruction based on the MC training sample and the Off data. Usually, for the gamma-hadron separation and the direction reconstruction, a corresponding RF is trained. For the energy estimation, the analyzer can choose between Look Up Tables (LUTs) and a RF. The implementation is further described in [18, 47, 153].

`melibea` applies the trained models to the On data. In this step, the hadronness of the events is computed, the energy is estimated and the reconstruction of the direction is performed. Further, the models are applied to the MC test sample. This is important for the `DL3 Converter` to calculate the IRFs.

`DL3 Converter` converts the `melibea` output into a `DL3` file (see also Section 3.4) and calculates the IRFs while making cuts on the hadronness (for only taking gamma-like events) and on the Hillas parameter `theta`, also referred to as θ^2 cut (for only taking well-reconstructed data originating from the source position). This `DL3` data can afterward be analyzed with `Gammapy`.[2]

For fast analyses and preliminary results of the observations, MAGIC performs the so-called MAGIC Online Analysis (MOLA) as real-time analysis [171]. Its results are not as exact as the results of a dedicated analysis but they can serve as a rough estimate of the results. Here it is noteworthy, that the MOLA does not apply any special analysis settings, so it will not deliver reliable results for certain observations.

3.4 `DL3` - Standard Data Format for Gamma Astronomy

As described in the last section, the final step of the MARS pipeline is the conversion of the data into `DL3`. `DL3` is a unified data level in gamma astronomy that is used across different experiments. In the last decades, different gamma-ray observatories have taken and analyzed data with telescope-specific software (such as MARS for MAGIC). Up to the high-level physics results, the data formats of the telescopes were not compatible. In 2016, the gamma-ray astronomy community laid the foundation for more uniform data and analysis software by creating the Gamma Astronomy Data Format (GADF) [67, 69], agreeing on the standard data formats in gamma-ray astronomy. This allows for the possibility to join efforts and deliver more comparable results.

Amongst others, the `DL3` format was established as data consisting of event lists and IRFs. This is fully reconstructed data of events surviving the gamma-hadron separation and angular cuts. In addition to the event list and the IRFs, `DL3` data contains some meta information such as the observation time, the observed target, and the experiment name. In the event list, for each event, an ID of the event, the arrival time, the reconstructed direction, and the reconstructed energy are stored. There is more information that can be added, such as the gammaness (value between 0 and 1 describing how gamma-like a particle is, defined as $1 -$ hadronness) but this is only optional and not required in general for `DL3`

---

[2] The original MARS workflow contains three more executables that calculate flux maps, θ^2 cuts, and flux points. As in this thesis, only the newer approach based on `DL3` is used, the other MARS executables are not further discussed here.

data. Here it is noteworthy, that the phase information for pulsar data is not contained in standard `DL3` files.

For compatibility reasons, the `DL3` data is stored as Flexible Image Transport System (FITS) files, which is used for the transport, analysis, and storage of scientific data and developed to a long-time standard data format in astronomy [22, 76, 179]. FITS data consists of multi-dimensional arrays or tables which are each assigned a human-readable header, containing metadata. The data format is continuously further developed and expanded to new needs such as high-precision storage of time coordinates [151] which is relevant for this work. For a complete overview of all data levels, the interested reader is referred to [134].

The main advantage of using `DL3` is that the unified analysis software `Gammapy` can be used for the production of high level results. MAGIC uses the so-called `DL3 Converter` [133] for obtaining `DL3` files. It converts the data from `melibea` to `DL3` data and therefore enables MAGIC to use `Gammapy`.

Documentation: `https://gitlab.pic.es/magic_dl3/magic_dl3/-/wikis/home`
`DL3 Converter` **GitLab**: `https://gitlab.pic.es/magic_dl3/magic_dl3`

3.5 `Gammapy` - A Standardized Open-Source `Python` Package for Gamma Astronomy

The full potential of `DL3` can only be exploited by using a unified analysis software for the standardized data format. This software is realized in `Gammapy`. `Gammapy` [68, 72, 73, 132] is an open-source `Python` package for high-level analyses in gamma-ray astronomy which is developed mainly for the upcoming CTA but also as a standard analysis tool for existing IACTs such as MAGIC. It is already widely used to obtain physics information such as spectra, flux maps, and light curves from `DL3` files.

`Gammapy` is written in `Python` and is built upon multiple widely used `Python` packages such as `numpy` [86, 177], `scipy` [176] and `astropy` [146, 150].

Gammapy Documentation: `https://gammapy.org`
Gammapy GitHub: `https://github.com/gammapy/gammapy`

3.6 `autoMAGIC` - Automatic Analysis of MAGIC Data

The new gamma-ray science standards `DL3` and `Gammapy` are not only important for the upcoming generation of IACTs but also for the existing IACTs such as the MAGIC telescopes. However, reprocessing the existing data to `DL3` is a time and resource-consuming task. As a solution for this problem, `autoMAGIC` was developed.

The `autoMAGIC` project is a database-driven framework with the humble aim to automatize the entire MAGIC analysis and was first presented in [113]. It was developed with the goal of creating the so-called MAGIC *legacy*. This term refers to the idea of processing all the MAGIC data up to `DL3` so that the data can still be used in the future i. e. for long-term analyses or multi-messenger analyses. It can also help to establish a FAIR[3] high level data preservation, as introduced in [156], for MAGIC. With only the standard analysis software MARS this goal would require an immense amount of workforce if it is achievable at all. However, with the automatized analysis pipeline `autoMAGIC`, the MAGIC collaboration is one step closer to producing its legacy data. Currently, `autoMAGIC` is only used for massive data processing and complex analyses, but in the future, it is most certainly going to be used to produce the MAGIC legacy.

The core concept of `autoMAGIC` is the use of a relational Structured Query Language (SQL) [58, 61] database storing analysis-related information and thus managing the workflow. For each analysis step in the MAGIC standard analysis chain, a wrapper in `Python` [175] is created, calling the original executable with the desired input parameters and managing the output and the interactions with the database. The computations are done on the cluster of the Port d'Informació Científica (PIC) server in Barcelona, where all the MAGIC data is stored.

In Figure 3.8, the basic idea of the workflow is presented. For each execution of one of the MARS executables, a dedicated job is created in the database. The jobs can then be submitted to the cluster and their outputs can be stored in the file system.

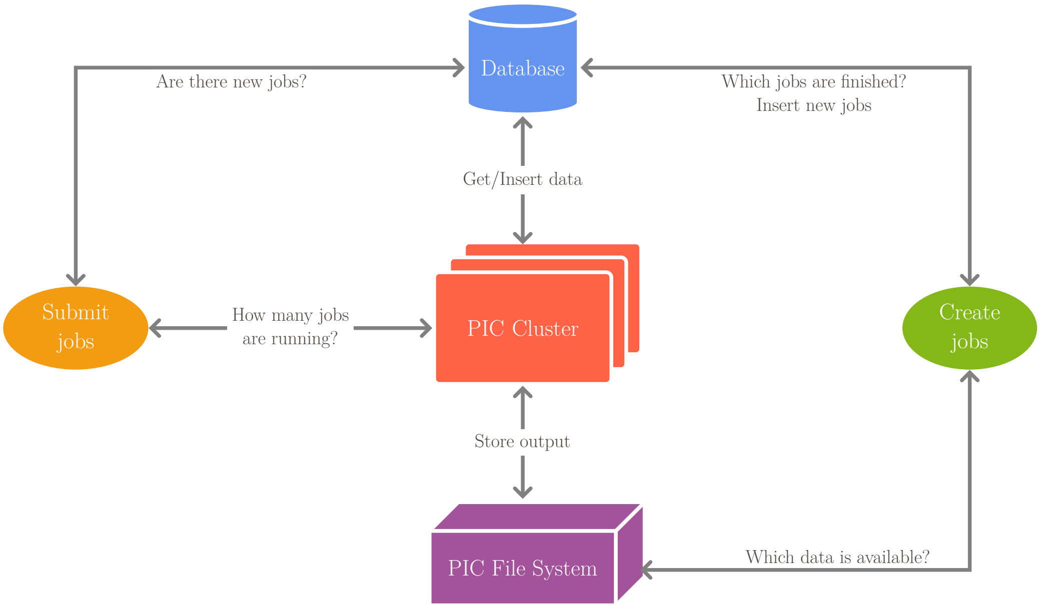

Figure 3.8: Sketch of the basic working principle of `autoMAGIC`. A database stores analysis-related information such as jobs for each of the MARS executables. Depending on the available data in the file system and in the database, new jobs can be created if no job with the exact same settings already exists and existing jobs can be submitted to the PIC cluster to be processed. The output files are then stored in the PIC file system. This graphic is adapted from [113].

---

[3] The FAIR data preservation sets goals for scientific data preservation: Findable, Accessible, Interoperable and Re-usable.

`autoMAGIC` is implemented in `Python` [175], communicating with the PostgreSQL [165] database via `sqlalchemy` [42] and making use of several commonly used python packages such as `numpy` [86, 177], `scipy` [176], and `astropy` [146, 150]. The job submission is handled by `htcondor` [98, 172] and database upgrades are applied using `alembic` [43].

Since its first productions, `autoMAGIC` has developed a lot, enabling the possibility to not only perform standard analyses but also more special analyses such as moon data analyses, the analysis of Sum-Trigger-II data, the analysis of Standard Trigger data with the MaTaJu cleaning and analyses of sources with multiple wobble offsets. A performance study of `autoMAGIC` with standard data and moon data is presented in [8].

It has become one of my main works to implement the analysis of Sum-Trigger-II data in `autoMAGIC` with the goal to produce a long-term pulsar analysis and to be able to analyze Sum-Trigger-II data that has not been analyzed properly yet due to the extraordinarily time-consuming analysis this data requires. More details about the Sum-Trigger-II and the implementation of the analysis of Sum-Trigger-II data are described in Section 4.2.4. A more detailed description of the `autoMAGIC` workflow can be found in Appendix A.1.

`autoMAGIC` **Documentation**:
https://gitlab.pic.es/magic/automatic_analysis/-/wikis/home
`autoMAGIC` **GitLab**: https://gitlab.pic.es/magic/automatic_analysis

4 The MAGIC Sum-Trigger-II

> You have to start looking at the world in a new way.
>
> Priya
> Tenet

For many of the modern experiments in physics, it is essential to use triggers for the data-taking procedure because there is a huge background that is not of interest for the observations. Recording all data would in these cases often lead to an unfeasibly high amount of data and hence, a mechanism to select the events of interest is required.

The MAGIC telescopes are designed for the detection of gamma-ray events. However, in addition to gamma-ray-induced events, the telescopes detect a huge background consisting of hadronic showers, the Night Sky Background (NSB), moonlight, and bright stars in the Field of View (FoV) of the telescope [139]. Consequently, the telescopes require an online mechanism for data selection, i. e. a trigger system to only record events of interest.

Usually, this is done with the MAGIC Standard Trigger that delivers reliable results if the observations require no special settings. Apart from the Standard Trigger system, the MAGIC telescopes are equipped with the Sum-Trigger-II, aiming especially for low-energy data, enabling MAGIC to observe low-energy sources such as pulsars, Active Galactic Nuclei (AGN) under high redshifts, and GRBs. Hence, the Sum-Trigger-II is of special interest for pulsar analyses.

Since the Sum-Trigger-I which was installed at M1 in 2007 [148] was very successful by enabling MAGIC to first observe pulsed emission from the Crab Pulsar [24] with an IACT, the stereo Sum-Trigger-II has been developed, as presented in [78, 83]. It was later installed at both MAGIC telescopes in 2013 [64]. In this chapter, the hardware of both the Sum-Trigger-II and the Standard Trigger is described. Afterward, the specialties arising in the analysis of Sum-Trigger-II data are presented. Finally, the implementation of the automatized pipeline for the analysis of Sum-Trigger-II data in `autoMAGIC` is described, which represents one of the major results achieved in the scope of this thesis.

4.1 Hardware

The MAGIC telescopes are equipped with multiple stereo trigger systems that pre-select the data during the observations based on the output signals of the PMT pixels. The most important ones for this work are the Standard Trigger and the Sum-Trigger-II. Both have three trigger levels, which all have to trip for an event to be recorded by the telescopes. These trigger levels are called `L0`, `L1`, and `L3` and they differ for Standard Trigger and

Sum-Trigger-II.

4.1.1 Standard Trigger

The Standard Trigger system is used for most of the MAGIC observations and delivers good results above energies of ∼100 GeV. The `L0` trigger is an amplitude discriminator for each individual pixel. The `L0` outputs are forwarded to the `L1` trigger. It applies close compact patterns of 2, 3, 4, or 5 NN, and the signal only passes if the summed output current of the pixels is above a certain, NN-number-specific, threshold. Only one trigger pattern can be used at once, and the default is the 3 NN pattern. Up to this point, the trigger process is done separately for both telescopes. Now, the `L1` trigger outputs are forwarded to the `L3` stereo trigger. It triggers in case of coincidence, i. e. if an event is recorded by both telescopes in a narrow time interval. For this, the times are artificially delayed depending on the zd[1] and azimuth orientation of the telescopes to consider the differences arising due to the light travel time from the shower to the telescopes. [26]

4.1.2 Sum-Trigger-II

The Sum-Trigger-II is a stereoscopic analog trigger system designated to take low-energy data, especially improving observations below 100 GeV. Taking low-energy data with IACTs is challenging since the resulting EASs are comparably small. Consequently, only few Cherenkov photons are emitted in a small volume resulting in smaller shower images and a worse signal-to-noise ratio than for higher-energy showers. Hence, the Cherenkov radiation of low-energy showers can easily be misinterpreted as background fluctuations by triggers which only take few pixels into account for the trigger decision. [63]

The Sum-Trigger-II solves this problem by subdividing the trigger area into macrocells of 19 pixels each with a line of the width of one pixel separating the macrocells. There are three layers of macrocells so that small showers in the camera can (almost) always be located in only one macrocell instead of being split into multiple cells. The arrangement of the macrocells is visualized in Figure 4.1. [83]

For the `L1` trigger decision, the summed signal of all pixels in each macrocell is computed analogously and a threshold is applied to the summed signal. In comparison to the Standard Trigger, more pixels are taken into account for the `L1` trigger decision. This causes an improvement in the signal-to-noise ratio. The `L0` and `L3` triggers are the same as in the standard observation. [63, 64]

The Sum-Trigger-II is the preferred trigger for observing sources for which the gamma-ray emission is expected to be mainly in the low-energy regime. Since the simultaneous use of both trigger systems would increase the data volume by about a factor of two while not gaining more scientific information, only one trigger is used at a time and the decision on the trigger is made dependent on the target source. [63]

---

[1] The zd is the angle between the object and the zenith, i. e. 90° minus the angle of the object above the horizon. Low zd angles correspond to a telescope pointing close to the zenith and high zd angles correspond to a telescope pointing close to the horizon.

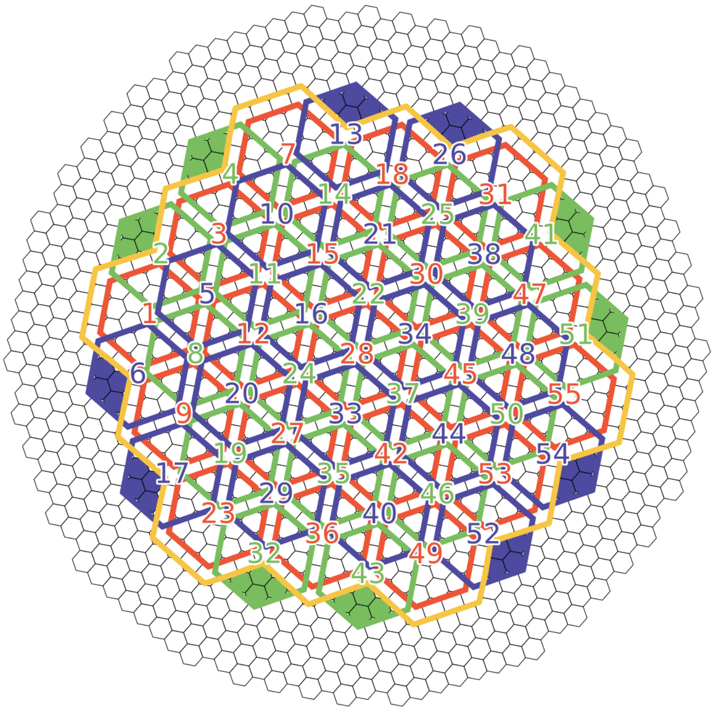

Figure 4.1: Arrangement of the macrocells for the Sum-Trigger-II. The three layers of macrocells are shown in blue, red, and green. The Standard Trigger area is shown in yellow. The pixels filled with color are excluded from the trigger decision to ensure compatibility to the Standard Trigger. Graphic adapted from [63].

4.2 Analysis of Sum-Trigger-II Data

After the low-energy gamma-ray sources (e.g. pulsars) have been observed with the Sum-Trigger-II, their data has to be analyzed to obtain physics results. In contrast to the standard analysis chain described in Chapter 3, some adaptions have to be made when analyzing Sum-Trigger-II data in order to lower the energy threshold for the data analysis as well. The most important one is using a different image cleaning, the so-called MaTaJu cleaning. The analysis of data while applying the MaTaJu cleaning is later referred to as MaTaJu analysis. In the following, the MaTaJu cleaning algorithm and the exclusion of bright stars in the FoV for MaTaJu-cleaned data, as well as the lowering of analysis thresholds, are explained. Finally, the implementation of the MaTaJu analysis in `autoMAGIC` is presented.

4.2.1 The MaTaJu Cleaning Algorithm

While the standard cleaning algorithm does not exploit all the information that can be taken into account, the MaTaJu[2] cleaning algorithm exploits the timing information that is available for the data which results in better image cleaning especially for low-energy events. This is possible because the parabolic shape of the reflector conserves the time structure of the recorded showers. Due to the increased computational effort, it is not commonly used for all analyses.

As described before, during data taking, a time series of 30 ns is recorded in case the telescope triggers an event. This time is comparably large, considering that the shower signal in a given pixel is only around 3 ns to 5 ns. The standard analysis (see Chapter 3) separates the two steps of signal extraction and image cleaning. In the step of the signal extraction, the highest pulse in the PMT time series is selected and converted into a charge Q. At the same time, the arrival time t_{arr} is calculated. This can cause problems, especially for pixels at the edge of the shower image. Since the deposited energy at the edge of the shower can be very low, there might be NSB fluctuations within the 30 ns time series that are higher than the actual signal. Thus, the NSB fluctuation can unintentionally be extracted from the PMT time series instead of the real signal pulse. [157, 158]

To solve this problem, an image cleaning algorithm, executed at the same time as the calibration, i. e. on time series of the individual pixels, can be applied. This allows for the possibility to fully exploit the time information and to apply more narrow constraints on the expected arrival time of the event within the PMT time series. Similar to the standard cleaning, explained in Section 3.2.3, the MaTaJu cleaning also relies on firstly searching for bright so-called core pixels and later searching for boundary pixels that are adjacent to core pixels. The MaTaJu cleaning algorithm works as follows [55]:

Trigger Time Calculation: In the first step, the standard signal extraction (as described in Section 3.2.1) is done for only a small subset of the data. For these events, the trigger time is calculated as the mean of the calibrated arrival times of very bright

---

[2] The name originates from the first names of the three main developers of this cleaning method: Maxim Shayduk, Takayuki Saito, and Julian Sitarek.

pixels ($Q > 20\,$p. e.). This allows for the calculation of a time t_{trig} at which the event is expected.

Modified Signal Extraction: Afterward, the charge Q for each pixel of each event is calculated using the sliding window method. In contrast to the standard signal extraction (where the whole PMT time series is searched) however, here only a small time range $\varDelta T_{\mathrm{sig}}$ centered around the expected time of the event t_{trig} is considered. This prevents the algorithm from extracting spikes or NSB fluctuations and thus allows to increase the probability of having only real signal in the core pixels of the shower.

Core Pixel Search: Next, core pixels forming groups of either 2NN, 3NN or 4NN are searched. Their charge has to be above a NN-number-specific threshold $Q_{k\mathrm{NN}}$ and the arrival time of the signal in all of the pixels has to be in a NN-number-specific time window $\varDelta t_{k\mathrm{NN}}$.

Signal Re-Extraction for Boundary Pixels: The signal of all the pixels that are adjacent to at least one of the core pixels (also called first cleaning ring) is re-extracted, exploiting the time information of the core pixels. For each boundary pixel, the expected arrival time is calculated by taking the average arrival time of the adjacent core pixels, and the signal extraction window in the PMT time series is set to a very narrow time interval $\varDelta t_{\mathrm{bound}}$ centered around the expected arrival time. Then, the signal is extracted only in this time interval and the pixel is taken if its charge lies above a boundary pixel threshold Q_{bound}. By this, especially the edges of the shower images can be cleaned much more reliably since the risk of mistaking a NSB fluctuation as signal is reduced significantly.

Iterative Boundary Pixel Search: The last step of the algorithm is the iterative search for boundary pixels. As described before, the first cleaning ring contains all the boundary pixels adjacent to one of the core pixels. In the higher iterations, the extraction of the next boundary pixel rings and their signal extraction is performed. The boundary pixels of a higher iteration are all pixels that are adjacent to at least one of the boundary pixels of the previous iteration. The calculation of the expected arrival time works as described before with the only difference that now the arrival times of the adjacent boundary pixels of the previous iteration are averaged. The default number for the maximum N_{rings} of cleaning rings is 3, since the contribution of higher iterations is negligible.

The MaTaJu cleaning focuses on the improvement of the separation between NSB and the shower signal. Hence, the cleaning of low-energy showers and here mostly the search for boundary pixels is improved. As low-energy events are quite small in the camera and only around 4-10 pixels (with the standard cleaning) contribute to the image, the additionally found boundary pixels can improve the Hillas reconstruction a lot. Further, around 20 % more events below 100 GeV survive the cleaning. This energy range is crucial for pulsar analyses with MAGIC.

Essentially, the MaTaJu cleaning can be fully characterized by ten parameters for each telescope, whereas some of them are identical for M1 and M2 and others differ. These parameters are [55]:

The signal extraction time interval $\mathit{\Delta}T_{\text{sig}}$ in which the signal is searched, centered around the trigger time t_{trig}.

The three cleaning thresholds $Q_{k\text{NN}}$ defining the NN-number-specific threshold for the charge Q in each pixel. There are two sets of cleaning parameters: Galactic cleaning parameters with a higher threshold and extragalactic parameters with a lower threshold.[3] These values differ for M1 and M2.

The three time constraints $\mathit{\Delta}t_{k\text{NN}}$ in which the signal of the core pixels has to be.

The charge threshold Q_{bound} for the boundary pixels.

The time interval $\mathit{\Delta}t_{\text{bound}}$ for the boundary pixels.

The number of cleaning rings N_{rings} in which boundary pixels are searched iteratively.

A full list of the parameters and their values for both telescopes can be found in Table 4.1.

Table 4.1: List of the MaTaJu cleaning parameters for galactic and extragalactic targets. A set of ten parameters fully characterizes the MaTaJu cleaning. For extragalactic sources, there is a special set of cleaning parameters that take into account the lower background in extragalactic observations.

	Galactic		Extragalactic	
Parameter	M1	M2	M1	M2
$\mathit{\Delta}T_{\text{sig}}/\text{ns}$	12	12	12	12
$Q_{2\text{NN}}/\text{p. e.}$	7.3	8.4	6.21	6.72
$Q_{3\text{NN}}/\text{p. e.}$	4.2	4.6	3.57	3.68
$Q_{4\text{NN}}/\text{p. e.}$	3.3	3.6	2.81	2.88
$\mathit{\Delta}t_{2\text{NN}}/\text{ns}$	2.31	2.31	2.31	2.31
$\mathit{\Delta}t_{3\text{NN}}/\text{ns}$	2.81	2.81	2.81	2.81
$\mathit{\Delta}t_{4\text{NN}}/\text{ns}$	3.14	3.14	3.14	3.14
$Q_{\text{bound}}/\text{p. e.}$	2.3	2.5	1.96	2.00
$\mathit{\Delta}t_{\text{bound}}/\text{ns}$	3.5	3.5	3.5	3.5
N_{rings}	3	3	3	3

4.2.2 Exclusion of Bright Stars in the Field of View

The data processed with the MaTaJu cleaning contains more low-energy events than standard cleaned data. However, because the algorithm is designed to find small showers and searches for correlated signal between few pixels, bright stars in the FoV might be misinterpreted as a shower. Consequently, the bright stars in the FoV of the telescopes have to be removed in the On data and the Off data. Therefore, a batch of pixels within a certain radius, around

---

[3] It has to be noted that the extragalactic cleaning levels are not yet properly optimized and are only a downscaling of the galactic cleaning thresholds to a factor of 0.85 for M1 and 0.8 for M2.

the star is excluded from the analysis. The radius depends on the brightness of the star. There is a set of recommended parameters by MAGIC which are presented in Table 4.2. It should be noted that these values are rather educated guesses than properly optimized parameters. However, experience has proven them to be reliable estimates.

Table 4.2: Values of radii excluded in the MaTaJu Analysis due to bright stars, depending on their brightness m.

Brightness/mag	Exclusion Radius/mm
$m > 6$	0
$5 < m \leq 6$	30
$4 < m \leq 5$	60
$3 < m \leq 4$	90
$m \leq 3$	Dedicated Analysis

In order to avoid mismatches for the effective area, the exclusion of stars has to be simulated in the MC test set. To do so, a batch of pixels within the same radius around a point with the same distance to the camera as the star in the On data has to be discarded in the MC test set.

This is not trivial since the position of the star in the camera changes with time. There are two superposing effects: Firstly, the positions of the stars in the camera at the same time of the night change throughout the year due to Earth's movement around the Sun. Secondly, because of Earth's self-rotation, a change in the position of the star in the camera during the night arises. An example for the movement of stars in the camera for both cases is shown in Figure 4.2.

For each wobble position in the On data, the stars in the FoV have a different distance to the camera center, and further, the number of stars in the FoV can change. Consequently, for each wobble position, a designated MC test set with the corresponding exclusion of pixels has to be produced.

4.2.3 Lowering Analysis Thresholds

In the standard analysis chain, many of the cuts (i. e. threshold values for different parameters used in the analysis chain) that are made are rather conservative and chosen comparably cautious even for the standard trigger, so that low-energy events are usually just cut away. For the analysis of Sum-Trigger-II data or the MaTaJu analysis of Standard Trigger data, some of these cutting parameters have to be lowered in order to not lose the low-energy events obtained with the Sum-Trigger-II and/or the MaTaJu analysis.

Most of the cuts that have to be adapted are on the Hillas parameter `size` which, as described in Section 3.2.4, is a measure for the entire shower size and therefore also for the energy. It is obvious that the cuts on this parameter have to be lowered for a low-energy analysis.

The adaption of the cut on the maximal `disp` (see Section 3.2.4) is less obvious. For low

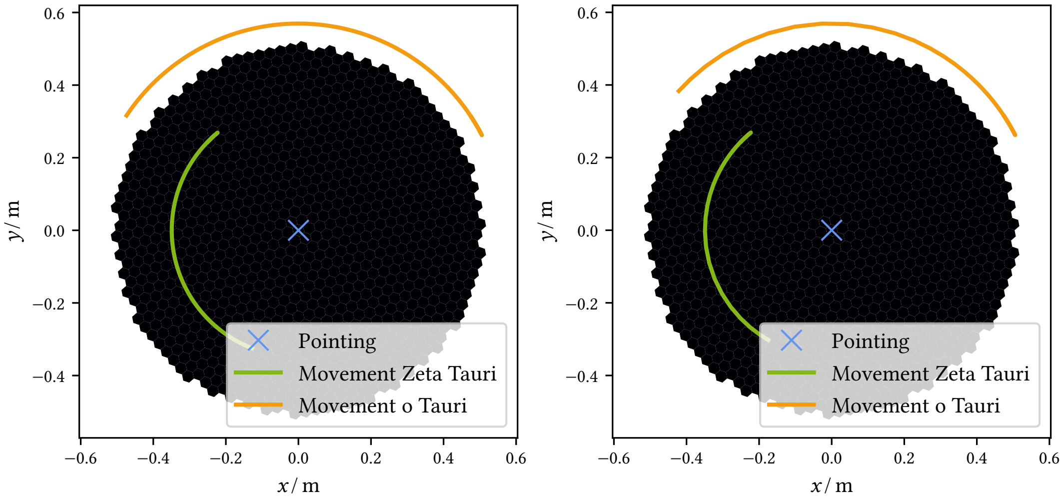

(a) Movement in 6 hours for the first wobble position.

(b) Movement in 90 days for the first wobble position.

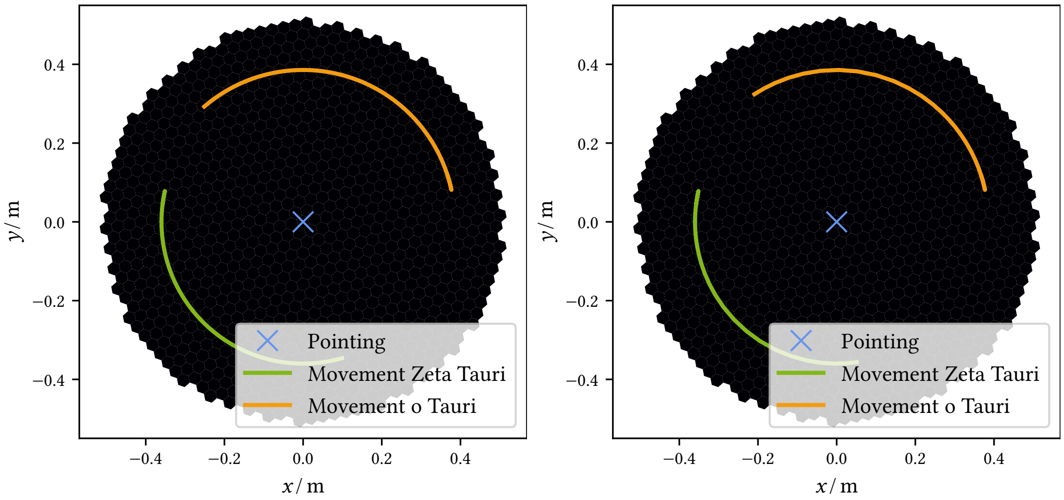

(c) Movement in 6 hours for the second wobble position.

(d) Movement in 90 days for the second wobble position.

Figure 4.2: Star movement in the camera for both wobble positions of the Crab Nebula for a six-hour time window on a fixed date (left) and within 90 days at a fixed time of the night (right).

energies, the showers in the camera are small, so the energy and especially the direction reconstruction are worse than for high-energy showers. Consequently, the cut on the angular resolution (the `disp` parameter) has to be lowered.

4.2.4 The MaTaJu Analysis in `autoMAGIC`

The manual analysis of larger sets of Sum-Trigger-II data is a challenging and time-consuming task. Hence, the Sum-Trigger-II analysis chain was implemented in `autoMAGIC` to save computation time, to reduce human effort, and to enable the possibility of delivering entirely reproducible results. The groundwork for this was done in [155]. It has become one of the major tasks for this work to fine-tune and optimize the workflow. Here, a short overview of the automatic analysis of Sum-Trigger-II data as presented in [155] is shown:

`sorcerer` and MaTaJu Cleaning: The MARS executable is implemented in `autoMAGIC` for the calibration of the data and for performing the MaTaJu cleaning. The MaTaJu cleaning is implemented only with standard (galactic) MaTaJu cleaning levels. Further, since the last steps of the MaTaJu cleaning are done by `star`, this also has to be specified in `star` by setting the `UseMaxim` parameter to `Yes`.

Exclusion of Stars: The removal of stars is implemented for the On data and the MC test set. For the On data, this is achieved by enabling the `ExcludeStar` option in case a bright star is found in the FoV. The search for bright stars is done with `ctapipe` [107], based on the yale bright star catalog [96]. Depending on the number of bright stars in the FoV, the parameter `ExcludeStarN` is set to the number of stars N and with `MStarPosCalc`K`.SourceRaDec` and `MStarPosCalc`K`.StarRadius`, the star position and the exclusion radii are set. Here, K denotes the star index which ranges from 1 to N.

In the MC data this is simulated by excluding a set of pixels with the same exclusion radius around a point with the same distance to the camera center as the star in the On data. For this, dedicated pixel exclusion files have to be generated beforehand, specifying the pixels to exclude and later they are handed to `star` by setting `BadPixelsUpdate` to `Yes` and `BadPixelsFile` to the pixel exclusion file. For each MC run, a random rotation of the camera is taken into account to avoid systematic effects due to asymmetries in the telescope response. For each wobble position, a designated MC test set is generated. If there is no bright star in the On data, MC data without excluded pixels is taken for the analysis.

Consequently, the MC analysis structure gains some levels of complexity since multiple MC test sets have to be produced and distinguished in the database and in the analysis. An independent MaTaJu analysis chain is set up with independent database tables managing these additional levels of complexity.

Relaxing Cuts: In the entire analysis chain, several cuts have to be reduced in order not to cut the low energy events gained by using the MaTaJu cleaning. Firstly, the `size` cuts are lowered in the entire analysis chain due to the lower energy of the showers and the resulting lower `size` parameter. In `star`, the `minSize` parameter is set to

0 p. e., in `coach` the parameters `MHillas_1.fSize` and `MHillas_2.fSize` are both set to < 20 *p. e.* and in the `DL3 Converter`, the `minSize` parameter is set to 20 p. e..[4] Further, since the energy reconstruction is worse for low-energy events, the parameter `StereoDispCalc.MaxDispDiff2` in `melibea` is increased from 0.05 $\deg^2$ to 0.20 $\deg^2$.

In Table 4.3, an overview of all the parameters applied in the MaTaJu analysis as presented in [155] is shown.

The following implementations in the MaTaJu analysis pipeline were done in the scope of this work and presented in the following for the first time:

Star Exclusion without pre-defined Bad Pixel Set: Before, it was necessary to generate a set of pixel exclusion files beforehand and to give it to `autoMAGIC`. Since this is inconvenient for the user, a new solution automatizing the generation of the pixel exclusion files is implemented. Once they are generated for a certain pointing position, they are stored and can later be reused. This increases the reproducibility and the accessibility of the analysis workflow.

Filling the Database from `superstar` Files: Since MAGIC decided in 2021 to not store all files on calibrated level directly on the PIC server anymore, it became necessary to implement a way to fill the database starting on the files on `superstar` level. This was already implemented for the standard analysis, but had to be adapted for the MaTaJu analysis pipeline since here more information is needed in the database to perform the analysis. The algorithm for adding data was therefore adapted to fill the additionally needed information such as the paths to the raw files of all the subruns of one run, the paths to the calibration and pedestal runs, and the linking of the calibration and pedestal runs to the data runs they are valid for.

Inserting Missing L3 Table Information: In many cases, the L3 table information which is used to distinguish Standard Trigger data from Sum-Trigger-II data, is missing in the `superstar` files. This is a major problem for the analysis of Sum-Trigger-II data since the trigger information is crucial for `autoMAGIC` to know which data to use for which analysis. Therefore, it is essential to fill this missing information into the `autoMAGIC` database. For this, a function updating the `autoMAGIC` database, relying on a file that is generated with the MAGIC observations database, is implemented. The MAGIC observations database contains information about the trigger and therefore, a list of runs taken with this trigger can be extracted.

One `coach` Job with All Possible Off Data: For the standard analysis, it is reasonable to train two RFs at once, so that for each analysis in the same MC period with the same analysis settings, an RF already exists and the total computation time can be reduced. For MaTaJu analyses, however, and especially for the analysis of Sum-Trigger-II data, this is not reasonable since the availability of Off data is poor. Consequently, all the available Off data should be used for one RF for this particular analysis instead of wasting it for another RF which might not even be used since analyses of Sum-Trigger-II data are rather rare. By now, this is implemented in `autoMAGIC`. For all MaTaJu analyses, only one RF is produced.

---

[4] Standard values for the `size` cut in the standard analysis are ranging from 50 p. e. to 70 p. e..

Table 4.3: Overview of all the analysis parameters modified in the MaTaJu analysis. For `sorcerer` only the parameters that are not already listed in Table 4.1 are listed here. The parameters listed in Table 4.1 are also specified in the `sorcerer` configuration file. In `star` for the On data, the `size` cut is set to 0 p. e., the MaTaJu cleaning is enabled with the `UseMaxim` parameter and the number of rings for the MaTaJu cleaning is set with `MImgCleanAdv.CleanRings`. With the remaining four parameters, the exclusion of bright stars in the On data is handled. In `star` for the MC data, the settings for the exclusion of pixels are done with the `BadPixelsUpdate` and `BadPixelsFile`, specifying one of the beforehand generated pixel exclusion files randomly. In `coach` and the `DL3 Converter`, the size cuts are set to 20 p. e.. The angular cut on the `disp` in `melibea` is lowered to 0.20 deg^2.

Executable	Parameter	Entry
`sorcerer`	`UseMaximClean`	Yes
	`MSearchNN.CleanMethod`	Absolute
`star`	`minSize`	0 p. e.
	`UseMaxim`	Yes
	`MImgCleanAdv.CleanRings`	3
	`ExcludeStar`	Yes/No
	`ExcludeStarN`	number of stars
	`MStarPosCalc`K`.SourceRaDec`	star position
	`MStarPosCalc`K`.StarRadius`	exclusion radius
`star` (MC)	`minSize`	0 p. e.
	`UseMaxim`	Yes
	`MImgCleanAdv.CleanRings`	3
	`BadPixelsUpdate`	Yes/No
	`BadPixelsFile`	`bad_pixels.rc`
`coach`	`MHillas_1.fSize`	< 20 p. e.
	`MHillas_2.fSize`	< 20 p. e.
`melibea`	`StereoDispCalc.MaxDispDiff2`	0.20 deg^2
`DL3 Converter`	`minSize`	20 p. e.

Galactic and Extragalactic Analysis: So far, only the galactic cleaning parameters were supported by `autoMAGIC`. Now, `autoMAGIC` can also distinguish between a galactic and an extragalactic MaTaJu analysis. This starts in `sorcerer` where the MaTaJu cleaning is applied. Depending on whether a source is galactic or extragalactic, the corresponding MaTaJu cleaning levels are applied automatically. Later in the analysis chain, during the search for Off data, only data with the same MaTaJu cleaning levels is considered.

For galactic data, if there is not enough Off data, extragalactic data is taken as Off data and processed with the galactic MaTaJu cleaning levels. This is reasonable since by using the higher galactic cleaning levels, the lower-energy events get lost and consequently, the extragalactic data processed with galactic MaTaJu cleaning levels is very similar to galactic data processed with the galactic MaTaJu cleaning levels.

Starting on Calibrated or `superstar` Data: Since the low-level processing is very computation time intensive, it is reasonable to use existing data that have already been processed with the MaTaJu cleaning. To do so, several adjustments in the MaTaJu analysis pipeline had to be made so that the database structure still allows the unique assignment of jobs.

Forcing to use Off Data from Different MC Period: In some MC periods, only very little Sum-Trigger-II Off data is available, which leads to poorly trained RFs and therefore to unreliable results. To prevent this, one can use Off data from different MC periods with very similar properties to enlarge the Off data set.

Using MC Extensions: For some analyses, the usage of MC extensions is crucial. Since the standard MC simulations are only performed in a limited energy range, for special low- or high-energy analyses, a designated MC extension has to be used so that sufficient statistical power is reached also for the non-standard energy range that this analysis exploits. The usage of MC extensions is now implemented in `autoMAGIC` and is highly important for analyzing low-energy Sum-Trigger-II data. They can also be of interest for the analysis of Very High Zenith (VHZ) Standard Trigger data, where the high-energy MC extension can be used.

Massive MaTaJu Processing: A pipeline for the massive processing of MaTaJu data is now set up in `autoMAGIC` to enable the possibility to process not only the needed data for one analysis but an even larger amount of data at once. With this, the data from entire MC periods can be processed automatically, enabling new possibilities for the MAGIC collaboration to handle the MaTaJu analysis. By now, `autoMAGIC` is used as standard tool for MaTaJu processings.

5

Pulsar Analysis

> We need to think of time as a resource.
>
> Dr. Brand
> Interstellar

The pulsar analysis in VHE gamma-ray astronomy relies on the timing information of the measured events in order to associate each event with a rotational phase of the pulsar. This poses some challenges to the analysis since the telescopes are located in a complex moving system. Another challenge is the low number of counts in gamma-ray astronomy, especially when compared to the very short rotational period of some pulsars. In fact, for many gamma-ray pulsars not even one event per rotational period can be measured. In consequence, in the gamma regime, only information integrated over many pulsar periods can be obtained. Further, an important constraint, especially for the VHE gamma astronomy, is that a model for the pulsar's rotation has to be known beforehand because otherwise no relation between the arrival time of the events and the pulsar's rotational phase can be established.

The core concept of a pulsar analysis in VHE gamma-ray astronomy is to assign each event a rotational phase of the pulsar. This is a complex task that requires a precise knowledge of Earth's rotation, the dynamics in the solar system, the interstellar propagation of light, and the pulsar dynamics itself. For this, the TOAs of the events at the telescopes are transformed into the Solar System Barycenter (SSB) since this system can be nearly regarded as an inertial frame with respect to the pulsar. Afterward, a pulsar ephemeris containing information about the pulsar's rotation is used to compute the pulsar phase for each event. Since the rotational periods are often in the order of magnitude from milliseconds to seconds, it is crucial to know the TOAs and the pulsar rotation with a high accuracy. Further, the computations have to be very precise as already small deviations in the time can lead to a completely miscalculated phase.

In this chapter, the specialties of the pulsar analysis and the methods used in the MAGIC pulsar analysis are briefly described. Firstly, different time systems are discussed. Secondly, the time transformations that have to be performed for a pulsar analysis are explained and pulsar ephemerides are introduced. Statistical tests for periodic signals are described and finally, the `Python` package `PINT` is not `tempo3` (`PINT`) and the package `magicpulsar`, which is developed as a part of the thesis at hand, are presented.

5.1 Time Systems

For the detailed discussion of the calculation of the pulsar phases, it is necessary to first introduce different time scales. There are several time scales which differ slightly from one another. The time systems are used to describe the time as precisely as possible in various environments and each serves a specific purpose. For the calculation of the pulsar timing, switching between time systems is crucial, so some time systems are presented in the following:

Temps Atomique International (TAI): The TAI is the average time of more than 600 atomic clocks all over the world. [82]

Coordinated Universal Time (UTC): The UTC (French: “Temps Universel Coordonné”) has the same definition for a second as TAI but is corrected for Earth’s rotation by inserting leap seconds if needed. Currently, the UTC is behind the TAI by 37 seconds. It is designed for practical timekeeping and everyday use. [100, 137]

Terrestial Time (TT): The TT also relies on the same definition for a second as the TAI and is mainly used for astronomical observations from Earth’s surface. For historical reasons, the TT is defined as 32.184 s ahead of TAI. [104, 141]

Barycentric Coordinate Time (TCB): The TCB (French: “Temps-coordonnée Barycentrique”) is the time as experienced by an observer co-moving to the SSB, taking into account all the movements the SSB does but not the gravitational time dilation. It is thought to replace the older TDB which is by now defined as a linear transformation of the TCB. [142]

Barycentric Dynamical Time (TDB): The TDB (French: “Temps Dynamique Barycentrique”) refers to the SSB and is a linear transformation of the TCB whereas the TCB progresses faster by about 0.5 s/yr. In contrast to the TCB, it is very close to the TT and differs from it only by up to 2 ms. [127]

MAGIC measures its events in UTC with a precision of about 200 ns. In the scope of a pulsar analysis, these measured TOAs have to be transformed into one of the SSB time systems TCB or TDB. Internally, the programs performing the pulsar timing often transform the UTC timing firstly into TAI and then into TT before the transformation into one of the barycentric time systems is performed. [116]

5.2 Time Transformations in the Pulsar Analysis

Before the data can be properly analyzed and associated with the pulsar, it has to undergo some time transformations. The telescope frame is not even closely an inertial frame with respect to the pulsar system: Earth rotates once a day and moves around the Sun once per year so that not only the distance to the pulsar but also the relative velocity to the pulsar system changes with time. Further, there are atmospheric delays and general relativistic delays. Especially for measurements that have to be correct to the order of magnitude of microseconds or even nanoseconds, this poses severe problems. The solution is to transform the measured TOAs to the SSB which can be regarded nearly as an inertial frame with respect to the pulsar system.

For the transformation of the TOAs to the SSB, multiple timing corrections have to be applied. The time t_{SSB} in the SSB is given by

$$t_{\mathrm{SSB}} = t_{\mathrm{UTC}} + \mathit{\Delta} t_{\text{Römer}} + \mathit{\Delta} t_{\mathrm{Einstein}} + \mathit{\Delta} t_{\mathrm{Shapiro}} \,, \tag{5.1}$$

where t_{UTC} is the time for the TOA measured by the telescopes on Earth and the terms $\mathit{\Delta} t_{\text{Römer}}$, $\mathit{\Delta} t_{\mathrm{Einstein}}$, and $\mathit{\Delta} t_{\mathrm{Shapiro}}$ are correction terms that are explained in the following [118]:

Römer Delay: This is the sum of all delays caused by the TOA difference due to the classical geometry of the solar system. It covers the timing difference induced by the light travel time from Earth to the SSB, taking into account Earth's rotation as well as the elliptic shape of Earth's orbit. The movement of the SSB due to the movement of the Sun and the planets is also taken into account. The Römer delay can be expressed as

$$\mathit{\Delta} t_{\text{Römer}} = -\frac{\mathbf{r}_{\mathrm{tb}} \cdot \hat{\mathbf{s}}}{c} \,, \tag{5.2}$$

where c is the speed of light, $\hat{\mathbf{s}}$ is the unit position vector of the source and $\mathbf{r}_{\mathrm{tb}}$ is the distance of the telescope to the SSB. The unit position vector of the source is given by

$$\hat{\mathbf{s}} = \begin{pmatrix} \cos(\lambda)\cos(\beta) \\ \sin(\lambda)\cos(\beta) \\ \sin(\beta) \end{pmatrix} \,, \tag{5.3}$$

where λ and β are the ecliptic longitude and latitude of the assumed source position, respectively. The distance of the telescope to the SSB can be described as

$$\mathbf{r}_{\mathrm{tb}} = \mathbf{r}_{\mathrm{oe}} + \mathbf{r}_{\mathrm{es}} + \mathbf{r}_{\mathrm{sb}} \,. \tag{5.4}$$

Here, $\mathbf{r}_{\mathrm{oe}}$ denotes the vector from Earth's center to the telescope, $\mathbf{r}_{\mathrm{es}}$ is the vector from Earth's center to the Sun's center, and $\mathbf{r}_{\mathrm{sb}}$ is the vector from the Sun's center to the SSB which is depending on the vector positions $\mathbf{r}_i$ and masses m_i of the ith object of the list of Sun and planets:

$$\mathbf{r}_{\mathrm{sb}} = \frac{1}{1 + \sum_i m_i^{-1}} \sum_i \left(\mathbf{r}_i m_i^{-1} \right) \,. \tag{5.5}$$

Einstein Delay: The Einstein delay $\mathit{\Delta} t_{\mathrm{Einstein}}$ covers delays induced by general relativity. Namely, these are the gravitational redshift and the gravitational time dilation. During its movement around the Sun, a clock on Earth will experience an annual variation. The relation between the time S a clock on Earth experiences and the coordinate time t measured by a clock that is not trapped in a gravitational potential is given by

$$\frac{\mathrm{d}t}{\mathrm{d}S} = \left(\frac{1}{r} - \frac{1}{4a} \right) \frac{2GM_{\odot}}{c^2} \,, \tag{5.6}$$

where r is the distance between Earth and the Sun, a is the semimajor axis of Earth's orbit, G is the gravitational constant, $M_{\odot}$ is the solar mass and c is the light velocity. There are different approximations (see for example [46]) for computing the accumulating difference between t and S that can hence approximate the Einstein delay.

Shapiro Delay: This is the delay induced by the curvature of spacetime due to a massive object. Here, especially the Sun, but also planets are taken into account. The Shapiro delay can be approximated by

$$\Delta t_{\text{Shapiro}} = -\frac{2GM_{\odot}}{c^3} \ln\left(1 + \cos\left(\theta\right)\right) \, . \tag{5.7}$$

Here G is the gravitational constant, $M_{\odot}$ is the solar mass, c is the vacuum speed of light, and θ is the angle between the vectors from the Sun to the pulsar and from the Sun to Earth. Please note that in this equation only the influence of the Sun is described. Modern pulsar timing packages also take the planet's movement into account.

After these computations, the TOAs in the SSB are known. Now a precise model of the pulsar is required to assign each event a rotational phase of the pulsar.

5.3 Pulsar Ephemerides

For the pulsar timing in the VHE gamma-ray astronomy, it is crucial to have a precise model of the pulsar's rotation beforehand. This information is given in the form of a pulsar ephemeris. Since a high precision in the pulsar timing up to micro or even nanoseconds is required, new ephemerides have to be calculated regularly to allow for a high-precision pulsar phase calculation. For the Crab Pulsar, these ephemerides are provided by the Jodrell Bank Observatory which provides monthly ephemerides. For other pulsars, for example for the Dragonfly Pulsar, *Fermi* provides ephemerides.

A pulsar ephemeris contains information about the pulsar name, the rotation frequency, and its first and second derivatives. Further, it contains the time period the ephemeris is valid for. The number of rotations N since a reference time t_0 is described as a Taylor expansion of the pulsar's rotation frequency, which is the inverse of the pulsar's period $f = T^{-1}$ [118]:

$$N = f_0(t - t_0) + \frac{\dot{f}_0}{2}(t - t_0)^2 + \frac{\ddot{f}_0}{6}(t - t_0)^3 + \ldots \tag{5.8}$$

Here, t is the arrival time in the SSB. The number of rotations itself is not of huge interest for the analysis, but the fractional part of it (i. e. $N \bmod 1$) gives information about the pulsar's rotational phase. This means that all events that have the same fractional part in the number of rotations have been emitted by the pulsar in the very same rotational phase, allowing for studying the pulsar peaks.

5.4 Statistical Tests for Periodic Signals

The main information in a pulsar analysis is the phase which is associated with the rotation angle of the pulsar. This data is measured on a circular scale and therefore also referred to as circular data. Since usual statistical tests cannot properly test for circular data, special tests have been developed. The most important ones for the analysis of pulsars are the Z_n^2 test and the H test which both base on the Rayleigh test. In the following, the tests are briefly introduced and their concept, as well as their advantages and disadvantages, are described.

5.4.1 The Rayleigh Test

The Rayleigh test forms the basis for other tests for the search for periodic signals. Hence, although the Rayleigh test is not used for the search of pulsed signals, it is going to be introduced shortly. The Rayleigh test is often used to determine whether a circular dataset is uniformly distributed or whether it contains clustering in certain angles, as introduced in [187]. In its currently used form it is described in [48]. It uses a uniform distribution as the null hypothesis and the test statistic is given by

$$Z = 2NR^2 \,, \tag{5.9}$$

where N is the number of events in the data and R^2 is the length of the mean vector of the data given by

$$R^2 = \frac{1}{N^2}\sqrt{\left(\sum_j^N \cos(2\pi\varphi_j^2)\right)^2 + \left(\sum_j^N \sin(2\pi\varphi_j^2)\right)^2} \,. \tag{5.10}$$

The resulting test statistic is then given by

$$Z^2 = \frac{2}{N}\left(\left(\sum_j^N \cos(2\pi\varphi_j)\right)^2 + \left(\sum_j^N \sin(2\pi\varphi_j)\right)^2\right) \,. \tag{5.11}$$

Although the Rayleigh test performs well when it comes to finding one cluster in circular data, it reaches its limits when there are multiple clusters as the mean vector is not enough anymore to distinguish between the clusters. In the extreme case of two clusters with the exact same size at the exact opposite positions on the circle, the Rayleigh test statistic returns zero, although the data is clearly clustered.

5.4.2 The Z_n^2 Test

The Z_n^2 test is based on the Rayleigh but solves its problem that multiple clusters on a circular scale cannot be recognized properly. This is achieved by multiplying the arguments of the sine and cosine with a constant integer number k and summing over all k in a range from 1 to n. The integer numbers are also called harmonics and represent integer multiples of the fundamental frequency. [38, 50]

The modified test statistic is then given by

$$Z_n^2 = \frac{2}{N}\sum_{k=1}^{n}\left(\left(\sum_{j=1}^N \cos(2\pi k\varphi_j)\right)^2 + \left(\sum_{j=1}^N \sin(2\pi k\varphi_j)\right)^2\right) \,. \tag{5.12}$$

In the absence of signal, it follows a χ^2 distribution with $2n$ degrees of freedom. The p-value can be calculated by

$$p_Z = 1 - \mathrm{CDF}(Z_n^2)\,, \tag{5.13}$$

where $\mathrm{CDF}(Z_n^2)$ is the Comulative Density Function (CDF) of the χ^2 distribution evaluated at the value of Z_n^2.

The significance is given by

$$S_Z = \frac{Z_n^2 - \mu}{\sigma}\,, \tag{5.14}$$

where μ is the mean of the null distribution (in this case 0) and σ is the standard deviation of the null distribution.

5.4.3 The H Test

The H test is derived from the Z_n^2 in [38, 66]. It is a combination of multiple Z_n^2 tests but normalized for reasons of better comparability

$$H = \max_{n \leq 20} \left(Z_n^2 - 4n\right) + 4\,. \tag{5.15}$$

It estimates the most appropriate harmonic n in the range from 1 to 20 to describe the pulse shape. Currently, it is used as a standard tool for blind pulsar searches since it is more sensitive than the previously described tests. For large sample sizes, the p-value can be approximated as

$$p_H(H > h) \approx \exp(-0.4h)\,. \tag{5.16}$$

The significance is given by

$$S_H = \mathrm{ISF}\left(p(H > h)\right)\,, \tag{5.17}$$

where $\mathrm{ISF}\left(p(H > h)\right)$ is the Inverse Survival Function (ISF) of a standard normal distribution at $p(H)$.

5.5 `PINT` - A `Python` Package for Pulsar Timing

Since the pulsar timing computations are highly complex, there is special software that performs the calculations. The long-time standard for this was `tempo2` [95] which was originally developed for pulsar analyses in the radio regime but was also used in the gamma-ray community. Though being a standard in the field of pulsar timing analyses, over the years the `tempo2` package was poorly maintained and so were the extensions of `tempo2` for dedicated analyses of data taken with special telescopes.

The `Python` package `PINT` [103, 116] follows an open-source approach and aims to become a new standard for pulsar analyses. It is a new implementation for pulsar-related computations (i. e. not based on `tempo2`) making use of standard libraries such as `numpy` [86, 177] and `astropy` [146, 150]. It delivers timing results compatible with `tempo2`, while `tempo2` is using TCB for its calculations and `PINT` uses TDB.

`PINT` **Documentation**: `https://nanograv-pint.readthedocs.io/en/latest/`
`PINT` **GitHub**: `https://github.com/nanograv/PINT`

5.6 `magicpulsar` - Automatic Pulsar Analysis for MAGIC Data

`magicpulsar` is a `Python`-based tool for the automatic analysis of MAGIC pulsar data which is developed as part of the presented thesis as a modern alternative to the usage of the MAGIC `tempo2` plugin. It makes use of `PINT` to compute the pulsar timing and produces a phasogram, a phase-resolved map, a phase-resolved spectrum, and a light curve using `Gammapy`.

The goal is to establish it as an alternative for `tempo2` which was so far used in the MAGIC collaboration in a modified version. It was known as a poorly maintained, hard-to-install, and difficult-to-handle tool. Further, it is working on `melibea` files and computes the pulsar timing for all the events still available in the files. Since in the `melibea` files, there is still a factor of around five[1] more events than in usual `DL3` files, it is obvious that this approach is much more computation time-intensive than `magicpulsar` which is working on `DL3` files.

`magicpulsar` has a pipeline for the pulsar analysis starting on the standardized `DL3` data. Based on the `DL3` files and pulsar ephemerides, firstly a timing file containing the TOAs of the events is created for each run and the ephemerides for the suiting time period are extracted from the ephemerides file. Then, `PINT` is called to calculate the arrival time for each event and the results are written into the `DL3` file and the high-level analysis can be performed. Here, a phasogram, a light curve, and a spectrum are calculated with the help of `Gammapy`. Further, the Li&Ma significance for the pulses is specified and a Z_n^2 as well as a H test are performed. The workflow of `magicpulsar` is visualized in Figure 5.1. It is already used by multiple researchers within the MAGIC collaboration. A more detailed description of the `magicpulsar` package can be found in Appendix A.2.

`magicpulsar` **GitLab**: `https://gitlab.pic.es/jschuber/MAGIC_Pulsar_Analysis`

---

[1] Of course the factor highly depends on the applied cuts and on the observation conditions. For low-zd Sum-Trigger-II data however, this value is decent.

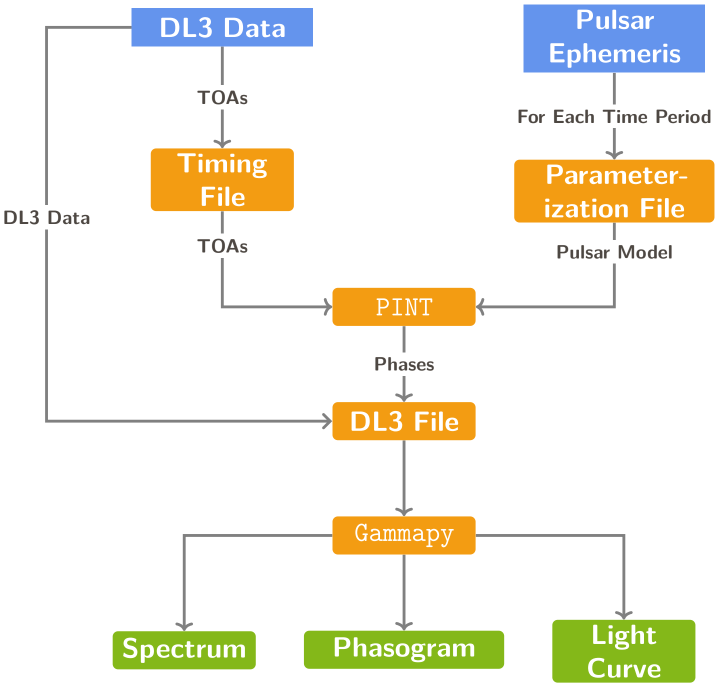

Figure 5.1: Workflow of the `magicpulsar` package. The input data are shown in blue, the analysis steps are marked in yellow and the science results are shown in green. Starting on a `DL3` file and an ephemeris file, the TOAs and the time-dependent ephemeris files are created. Those are then handed to `PINT` to compute the pulsar phases. The phases are stored in a dedicated column in the `DL3` files. Afterward, the high-level analysis can be performed with `Gammapy`.

6

Long-Term Crab Pulsar Analyses

> You mustn't be afraid to dream a little bigger, darling.
>
> Eames
> Inception

In this chapter, multiple analyses of the Crab Pulsar are performed. As already described in Section 5.6, the new approach is the usage of `DL3` data for the MAGIC pulsar analysis. This ensures compatibility with other experiments and also lowers the computational effort. These analyses are the first ever MAGIC pulsar analyses performed on `DL3` data. Setting up a workflow that allows for the possibility to use `DL3` data in the MAGIC pulsar analysis was one of the major projects of the thesis at hand.

Firstly, the analysis workflow which is very similar for all of the analyses is described. Then, three individual analyses of the Crab Pulsar with different data types are presented: A Sum-Trigger-II analysis, a Standard Trigger analysis, and a VHZ Standard Trigger analysis. As the data and also the analysis procedure for these data differs, the analyses are firstly handled separately to take into account the differences that occur in the analysis pipeline. As the main work of this thesis, an analysis of the Crab Pulsar based on approximately 120 h data taken with the low-energy Sum-Trigger-II is presented. It gives special insights into the low-energy pulsed emission below 200 GeV since in this regime, the sensitivity of the Sum-Trigger-II exceeds the one of the Standard Trigger. However, Standard Trigger data is valuable since, as MAGIC uses the Crab Nebula as standard candle, a vast amount of Crab Pulsar data is available. Afterward, an analysis of the Crab Pulsar with approximately 360 h Standard Trigger data is done, giving insights into the higher-energy pulsed emission above 200 GeV. Finally, a pulsar analysis of approximately 100 h of VHZ data is performed to test for VHE pulsed emission above 10 TeV.[1] The possibility of the VHZ data showing a better performance in the VHE regime above 10 TeV arises from a boost in sensitivity for VHE showers that MAGIC experiences in VHZ observations [10].[2] The Standard Trigger results are compared to the Sum-Trigger-II results and, in another step, a joint analysis is

---

[1] So far, pulsed emission could only be found to up to around 1 TeV in [30]. The detection of pulsed emission in a higher energy regime might give new insights into the underlying emission mechanisms. From the Vela Pulsar and its 20 TeV pulsed emission [70] it is clear that this high-energy pulsed emission is possible.

[2] In VHZ observations, the energy threshold is higher as the light of low-energy showers does not reach the telescopes due to the longer path the light has to travel in the atmosphere before reaching the telescopes. Additionally, larger showers can be observed (without exceeding the camera size) as the detected showers are further away. For a more detailed description, the interested reader is referred to [10, 163].

done, representing the most extensive analysis of the Crab Pulsar in the VHE regime to date.

6.1 Analysis Workflow

The general workflow for all of the later described analyses is the same and hence explained once for all analyses here. Deviations from this standard workflow are described in the chapters of the respective analyses. The workflow contains three major steps: Generating `DL3` files with `autoMAGIC`, computing the pulsar timing with `magicpulsar`, and in the end obtaining physics results with `Gammapy`. The detailed procedure for all these steps is described in the following.

6.1.1 Generation of `DL3` Files

The generation of `DL3` files is done automatically with `autoMAGIC`. For each of the analyses, a dedicated `autoMAGIC` configuration file is prepared and the data is processed with the corresponding settings.

In the scope of this work, several improvement opportunities in the `DL3 Converter` were identified and reported to the maintainers and have been addressed in the current version:

Leap Seconds: The `DL3 Converter` was not taking into account the leap seconds, leading the pulsar timing to be incorrect as the events were associated with a wrong pulsar phase due to the wrong TOA.

Event Association: The event association was malfunctioning, assigning the events their subrun id which is not unique per run so that no clear event assignment could be done.

6.1.2 Pulsar Timing

The pulsar timing is done with the package `magicpulsar` based on ephemerides provided by the Jodrell Bank Observatory. A more detailed description of the `magicpulsar` workflow can be found in Appendix A.2. In Appendix B, the pulsar ephemerides are described more in detail and a list of the ephemerides and their values used in this analysis can be found. By executing `magicpulsar`, the phase information for each event is added to the `DL3` files so that the high-level pulsar analysis becomes possible.[3]

6.1.3 `Gammapy` Analysis

In the `Gammapy` analysis, multiple pulsar characteristics are computed. All `Gammapy` analyses are done with `Gammapy` version 1.2. Many of the pulsar characteristics are computed phase-range-wise. The phase ranges for the Crab Pulsar are defined as listed in Table 6.1, based on previous measurements of the Crab Pulsar. While the peak regions P1 and P2 as well as

---

[3] Although `magicpulsar` provides the possibility to also obtain physics results to get a first glimpse at the data, the high-level analysis is done manually for this work so that more exact results than with the automatized `Gammapy` analysis in `magicpulsar` can be obtained.

the Off region OFF and the bridge region BE are chosen as in previous MAGIC analyses [23, 25], for P1, P2, and the bridge, leading and trailing phase ranges are defined. The chosen phase ranges are similar to the phase ranges defined by *Fermi*-LAT in [1] but fewer phase regions are chosen as in the VHE gamma-ray regime, fewer statistics is available. The intervals [0.455, 0.520) and [0.870, 0.950) are not used in this work as no excess is expected in these intervals. They could, in principle, be added to the OFF phase region but this is not done here to ensure compatibility in the choice of the OFF phase region with previous MAGIC analyses.

A specialty of the pulsar analysis in general is that the On and Off regions are not taken spatially (as described in Section 3.2.9) but with respect to the pulsar phase. This means that only events from the On region are taken but the timing decides whether they are used as On or Off event.

Table 6.1: Phase ranges for the Crab Pulsar analysis.

Phase Range Name	Phase Interval	Description
L1	[0.950 - 0.983)	P1 Leading
P1	[0.983 - 0.026)	P1
T1	[0.026 - 0.040)	P1 Trailing
LB	[0.040 - 0.140)	Bridge Leading
BE_n	[0.140 - 0.250)	Bridge Emission
TB	[0.250 - 0.320)	Bridge Trailing
L2	[0.320 - 0.377)	P2 Leading
P2	[0.377 - 0.422)	P2
T2	[0.422 - 0.455)	P2 Trailing
OFF	[0.520 - 0.870)	Off

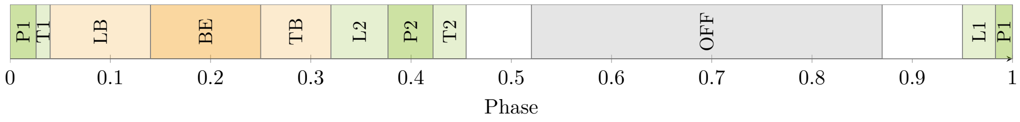

Figure 6.1: Visualization of the defined phase ranges.

Phasograms

A phasogram organizes the phase information of the events in a histogram. By this, potential excess in certain phase ranges can be visualized and quantified. The Li&Ma significance (Equation (3.11)) is calculated while counting the events in pre-defined On and Off phase regions. For P1 and P2, the corresponding phase ranges listed in Table 6.1 are used and as Off region the phase range OFF is taken. For the bridge, however, there are different phase range definitions. While in VHE gamma astronomy, the common definition is the whole range between P1 and P2 (i.e. the phase range $[0.026, 0.377)$, hereafter called BE_w), often also computations for the narrower definition of the bridge in the phase interval $[0.140, 0.250)$ (hereafter $\mathrm{BE_n}$) are performed. The narrower bridge definition is mostly used in the lower-energy regime and was introduced in [75]. The latter one corresponds to the definition as shown in Table 6.1 while the first one aggregates the phase ranges T1, DB, BE, BF, and L2. For both $\mathrm{BE_w}$ and $\mathrm{BE_n}$, the significances are calculated.

Phasograms with 100 bins are calculated and the significances for P1, P2, and the bridge are calculated. Additionally, a Z_n^2 test (Equation (5.12)) with $n = 10$ and an H test (Equation (5.15)) for periodic signal are applied to the data to give a measure for the periodicity.

Both a joint phasogram for the entire energy range and energy-dependent phasograms in the reconstructed energy bins are produced. For the energy-dependent phasograms, the peaks are fitted with a triple Gaussian in order to quantify the height, width, and position of the pulses. This makes it possible to quantify changes in the pulse position and width that might occur with changing energy.

For this, a cyclic Gaussian, defined as

$$G(\varphi, A, \mu, \sigma) = A \sum_{k=-\infty}^{\infty} \exp\left(\frac{1}{2}\left(\frac{\varphi - k + \mu}{\sigma}\right)^2\right) \tag{6.1}$$

is used. Here, φ is the pulsar phase, A is the amplitude, μ is the mean, and σ is the standard deviation. k is a parameter used for enforcing the cyclic behavior. This is important to ensure continuity at the borders of the definition range. A sum of the background counts and three cyclic Gaussians, modeling P1, P2, and the bridge, is fitted to the phasogram:

$$G_{\mathrm{triple}}(\varphi, \ldots) = N_{\mathrm{bkg}} + G(\varphi, A_{\mathrm{P1}}, \mu_{\mathrm{P1}}, \sigma_{\mathrm{P1}}) + G(\varphi, A_{\mathrm{BE}}, \mu_{\mathrm{BE}}, \sigma_{\mathrm{BE}}) + G(\varphi, A_{\mathrm{P2}}, \mu_{\mathrm{P2}}, \sigma_{\mathrm{P2}}) \tag{6.2}$$

This function has 10 free parameters that are determined by fitting the function to the phasogram using the least-squares algorithm. Start values that are close to the expected results are chosen for the fit. The fits are only done in energy bins showing an excess signal in at least one of the phase ranges. Further, some constraints are put on the fit parameters:

Positive Amplitudes: Positive Amplitudes A_{P1}, A_{BE}, and A_{P2} are required to ensure only excess signal is fitted as a peak.

Mean in Phase Range: Mathematically, means beyond the interval [0,1) are possible, but they do not contain physics information, so the possible range for the means μ_i is constrained to [0,1).

Positive Standard Deviation: The standard deviation σ is required to be positive as a negative solution would be unphysical.

Positive Background: The background counts N_{bkg} are required to be positive.

Minimum Width for Bridge: A minimum standard deviation of $\sigma_{\mathrm{BE}} = 0.1$ is set for the bridge to prevent fitting statistical fluctuations.

From the standard deviations σ, the Full Width at Half Maximum (FWHM) of each Gaussian is calculated as

$$\mathrm{FWHM} = 2\sigma\sqrt{2\ln(2)}\,. \tag{6.3}$$

Energy-dependent phase regions are calculated for P1, P2, and the bridge with a width of the FWHM centered around the mean μ and their Li&Ma significances are calculated.

Based on both the fit and the counts of the phasograms, the P1/P2 ratio is obtained in the reconstructed energy bins. For the fit-based P1/P2 ratio, the amplitudes of the fits are divided, as done for example in [55], while for the counts-based P1/P2 ratio, the excess counts in the P1 and P2 regions are used, as done for example in [6]. The P1/P2 ratio is only calculated in the energy bins in which an excess signal can be found.

Spectra

For the phase-resolved spectra, the `Gammapy PhaseBackgroundMaker` is used, calculating the spectral flux points based on the On and Off counts taken from the corresponding On and Off phase ranges. The flux points are calculated by a forward-folding algorithm, assuming a power-law spectrum for each of the phase ranges:

$$F(E) = F_0 \left(\frac{E}{E_0}\right)^{-\Gamma}\,. \tag{6.4}$$

This spectral shape is chosen since previous analyses ([30, 55]) have shown that it describes the VHE tail of the Crab Pulsar peaks well. The best fit for the spectral parameters is calculated while as starting parameters, a reference model is specified. For P1, P2, and the bridge, results from previous MAGIC publications are used while for the other phase ranges, there are no VHE results yet. For these spectra, a simple power-law with spectral index 3 and a reference energy of 100 GeV is used. The reference spectral parameters are summarized in table Table 6.2. For the Standard Trigger and the Sum-Trigger-II analysis, different reference spectra are used as the previous MAGIC results deviate slightly for the different types of analyses. While the Sum-Trigger-II reference spectra most likely better describe the low-energy regime, as they are derived from data in an energy range between 30 GeV and 200 GeV, the Standard Trigger spectra can most likely better describe the higher-energy regime as they originate from data in the energy range between 70 GeV and 1.5 TeV. At this point, it is noteworthy that these reference spectra base on the assumption that the pulsed emission components have a constant SED over time. This underlying assumption does not necessarily have to be true, which should be taken into account when interpreting the following results. Further, it has to be noted that the uncertainties on the parameters are the statistical uncertainties and do not yet consider systematic effects of the MAGIC telescope system which is estimated to be roughly 30%.

In contrast to the standard procedure of `Gammapy`, the spectral index for the energy-bin-wise fits during the flux point calculation is set to 2 instead of the local spectral index in this energy bin. Setting the spectral index to 2 is a common standard in the field of gamma-ray astronomy, especially established by *Fermi*-LAT [181].

Table 6.2: Crab Pulsar reference spectra used for P1, P2, and the bridge.

Name	E_0/GeV	$F_0/\mathrm{TeV^{-1}\,cm^{-2}\,s^{-1}}$	$\mathit{\Gamma}$	Reference
$\mathrm{P1_{sum}}$	59.86	$(3.83 \pm 0.42) \cdot 10^{-10}$	3.49 ± 0.25	[55]
$\mathrm{P2_{sum}}$	70.33	$(3.66 \pm 0.23) \cdot 10^{-10}$	3.18 ± 0.11	[55]
$\mathrm{P1_{standard}}$	150.00	$(1.1 \pm 0.3) \cdot 10^{-11}$	3.2 ± 0.4	[30]
$\mathrm{P2_{standard}}$	150.00	$(2.0 \pm 0.3) \cdot 10^{-11}$	2.9 ± 0.2	[30]
$\mathrm{BE_n}$	100.00	$(3.7 \pm 1.1) \cdot 10^{-11}$	3.51 ± 0.97	[23]
$\mathrm{BE_w}$	100.00	$(12.2 \pm 3.3) \cdot 10^{-11}$	3.35 ± 0.79	[23]

For each phase range, the decorrelation energy E_d, as described in [2] and defined as

$$E_d = E_0 \exp\left(\frac{\mathrm{cov}(F_0, \mathit{\Gamma})}{F_0(\mathit{\Delta\Gamma})^2}\right) , \tag{6.5}$$

is computed, whereas E_0, F_0, and $\mathit{\Gamma}$ are the corresponding items from the used spectral model, which is in this case the power-law spectral model shown in Equation (6.4), and $\mathit{\Delta\Gamma}$ is the uncertainty of the spectral index. The decorrelation energy describes the energy at which the spectral shape is the least uncertain.

A test statistic value threshold of 2 is set for upper limits (corresponding to $\sqrt{2}\,\sigma$ flux points) and 95 % confidence level upper limits are calculated. To account for the lower observation time induced by the selection of a phase range, the flux point results are divided by the length of the corresponding phase range afterward.[4]

In the end, the flux points are compared to *Fermi*-LAT flux points for each phase range, taken from [160] and calculated in the phase ranges defined in table Table 6.1 with `Fermipy` [181]. The *Fermi*-LAT upper limits cannot be directly compared to the MAGIC values since the statistics of *Fermi*-LAT and MAGIC deviate strongly. A test statistic value of 4 is chosen as threshold for the *Fermi*-LAT data.

In addition, the phase-resolved integrated flux is computed. Similar to a phasogram, it shows the phase-resolved flux in dependence of the phase. For this, the integrated flux in the energy range that shows pulsed emission is calculated in all phase ranges and plotted against the phase.

In the end, phase-resolved light curves for P1 and P2 are computed showing the integrated flux in the energy range the pulsed spectra are computed in. The light curves are calculated with a night-wise binning as for run-wise binning the statistical power in the On phase ranges is insufficient.

---

[4] There is no clear consensus on whether or not to rescale the flux by the inverse phase region length. While MAGIC mostly did not do it in the past, *Fermi*-LAT does it by default. For this work, I decide to rescale the flux. This should be kept in mind when comparing different results.

6.2 Sum-Trigger-II Analysis

The Sum-Trigger-II analysis of the Crab Pulsar represents the main work of this thesis. It exploits especially the low-energy part of the Crab Pulsar and gives special insights to the energies below 200 GeV. This energy range is usually hardly accessible for both IACTs due to their higher energy threshold and space-based observatories due to their limited detector volume and hence low statistics in this regime. Though, this energy range is of scientific interest as it is the connecting link between the space-based gamma observatories, such as *Fermi*-LAT and other IACTs, such as VERITAS. Especially the phase regions apart from P1 and P2 are hardly accessible to IACTs but a confirmation of the *Fermi*-LAT results with a different observation technique is scientifically valuable.

This analysis represents the most extensive low-energy analysis of the Crab Pulsar with an IACT to date. The analysis is presented as follows. Firstly, the data selection is described, followed by the selection of MC data. Afterward, the phasogram-related results are shown and discussed. Then, the spectra for different phase ranges are presented and the light curves of P1 and P2 are shown. The Crab Nebula validation for this analysis is presented in Appendix E.1.

6.2.1 Data Selection

For this analysis, all available good-quality Sum-Trigger-II data of the Crab Pulsar are selected.[5] The entire dataset was already processed with MaTaJu galactic settings before. As the data availability for old raw data is inconvenient, I decided to start the analysis on `superstar` level in order to save computation time and human resources.[6] The only disadvantage of this approach is that the data selection cannot be done independently since only the available `superstar` files can be used. Especially for the ST.03.10 and the ST.03.12 MC periods, only very little pre-processed Off data is available.

In `autoMAGIC`, quality cuts are applied to the data which are listed in table Table 6.3. The transmission characterizes the transparency of the atmosphere between 0 and 1. While values close to zero are associated with no transmission, values close to 1 represent nearly perfect conditions. In case the transmission is not available, the cloudiness is taken as a measure for the atmospheric conditions. Here, a value close to zero is desired for good observation conditions. The Dark Current (DC) is the direct current measured at the PMTs and it is correlated to the amount of moonlight reaching the camera. With a value below 2200 nA (for M1), it is ensured that only dark data without any moonlight is selected. The MOLA threshold influences the Off-data search. Only observations with a MOLA significance below $3\,\sigma$ are considered suitable as Off data.

The total amount of On data that survives the cuts is 122.8 h. A full list of the Sum-Trigger-II On Data can be found in Appendix F.1.

---

[5] Sum-Trigger-II data are usually only taken under very good observation conditions and hence, only little data has to be discarded due to bad data quality.

[6] The amount of data is huge on this level and hence the data is not stored permanently on the PIC server and moved to tapes instead. These tapes are only accessible by the administrators of the server and providing the data requires human effort.

Table 6.3: Cuts used for the data selection in the Sum-Trigger-II analysis.

Parameter Name	Cut Value
start date	2014-11-24
stop date	2020-02-22
transmission (On data)	0.9
transmission (Off data)	0.8
maximum cloudiness (On data)	10
maximum cloudiness (Off data)	20
minimum zd	5°
maximum zd	35°
minimum DC	0 nA
maximum DC	2200 nA
MOLA threshold (Off data)	$3\,\sigma$

As MC data, dedicated Sum-Trigger-II MC simulations have to be used. Since the analysis of Sum-Trigger-II data is non-standard, only few of the necessary MC simulations were already done. One specialty of this analysis is further that the low-energy regime is explored, requiring the use of a low-energy extension for the MC simulations in addition to the standard MC simulations. This extension contains a large number of low-energy events ranging from 10 GeV to 200 GeV. The number of simulated events amounts to 120 million events, exceeding the usually used number of events by a factor of 60. This is necessary to get enough statistics in the low-energy regime in which many more events are measured than in the higher-energy regime. Most of the Sum-Trigger-II MC simulations were produced by me for this analysis with the official MAGIC Sum-Trigger-II MC parameters. In Table 6.4, a list of the used MC simulations can be found. It has to be noted at this point, that, so far, no major MAGIC analysis has used the low-energy standard MC simulations and this is the first analysis in which they are used. Hence, this analysis can also be regarded as a test for the Sum-Trigger-II MC parameters.

6.2.2 Data Processing

The `DL3` data is processed with `autoMAGIC` with the configuration file shown in Appendix G.1. A hadronness cut of 90 % MC efficiency and a θ^2 cut of 75 % MC efficiency are chosen in 20 logarithmic reconstructed energy bins between 5 GeV and 50 TeV while for the true energy, 25 logarithmic bins between 5 GeV and 50 TeV are used. Three `autoMAGIC` processings are done for the three different source names that the Crab Nebula was recorded with during the Sum-Trigger-II observations: `CrabNebula`, `Crab`, and `CrabNebula-0`.[7]

As previously mentioned, there is only very little Off data available for ST.03.10 and

---

[7] During observations with MAGIC, it can happen that the shifters accidentally enter a non-standard name for the source, resulting in the data to be stored under that name. MAGIC does not correct these names but treats them as independent source names.

Table 6.4: MC sets used for the long-term Crab Pulsar analysis. All of them are produced in ringwobble mode and for Sum-Trigger-II data.

Analysis Period Name	MC extension	Newly Produced
ST.03.06	None	Yes
ST.03.07	None	No
ST.03.10	None	Yes
ST.03.11	None	Yes
ST.03.12	None	Yes
ST.03.06	low-energy	Yes
ST.03.07	low-energy	No
ST.03.10	low-energy	Yes
ST.03.11	low-energy	Yes
ST.03.12	low-energy	Yes

ST.03.12. Hence, Off data from similar periods is taken instead:

ST.03.10: This period is quite short and only contains few hours of On data. Further, the change in the telescope parameters occurred gradually, leading to a more ST.03.11-like telescope response at the end of ST.03.10. As the On data was taken at the end of ST.03.10, this data is processed with Off data from ST.03.11 but with MC data for ST.03.10.

ST.03.12: This period is relatively long and contains around 20 hours of Crab Pulsar data. Almost no Off data is pre-processed and the data availability for the raw data is inconvenient. As the MC parameters of this period are very similar to the ones of ST.03.06, Off data from this period is used together with ST.03.12 MC data for the analysis.[8]

During the phase assignment with `magicpulsar`, in this analysis, no runs have to be excluded due to pulsar glitches.

The analysis is performed with MARS version 3-0-1, `DL3 Converter` version 0.1.12, and `autoMAGIC` version 0.5.

---

[8] The values for the `mirror fraction` ranges from 0.48 to 0.68 for M1 and from 0.54 to 0.72 for M2. The `axis deviation` ranges from 3 to 8 for M1 and from 0 to 6 for M2. The values for ST.03.06 and ST.03.12 are very similar: The M1 `mirror fractions` are 0.63 for ST.03.06 and 0.61 for ST.03.12 while the M2 `mirror fractions` are both 0.69. The `axis deviations` for M1 are both 5.5 and for M2 5.5 in ST.03.06 and 5.0 in ST.03.12. Hence, both periods show a similar telescope response.

6.2.3 Phasogram

Based on the phased `DL3` data, firstly, a phasogram of the entire energy range above 20 GeV is produced using energy-dependent hadronness and θ^2 cuts. The result is shown in Figure 6.2. The phasogram shows a strong pulsed signal for both P1 and P2 with Li&Ma significances of $S_{\mathrm{P1}} = 12.32\,\sigma$ and $S_{\mathrm{P2}} = 19.13\,\sigma$, respectively. The joint P1+P2 significance amounts to $S_{\mathrm{P1+P2}} = 21.14\,\sigma$. The excess signal is located precisely in the pre-defined phase regions and is not shifted. The significance for the bridge emission is $S_{\mathrm{BE_w}} = 8.38\,\sigma$ with the wide bridge definition and $S_{\mathrm{BE_n}} = 5.39\,\sigma$ with the narrow definition, representing a clear detection. The statistical tests for periodicity deliver significances of $S_Z = 20.54\,\sigma$ and $S_H = 20.63\,\sigma$ clearly stating a periodic signal. The counts and significances are summarized together with the energy-dependent phasogram results in Table 6.5 and further results of the statistical tests can be found in Table 6.6.

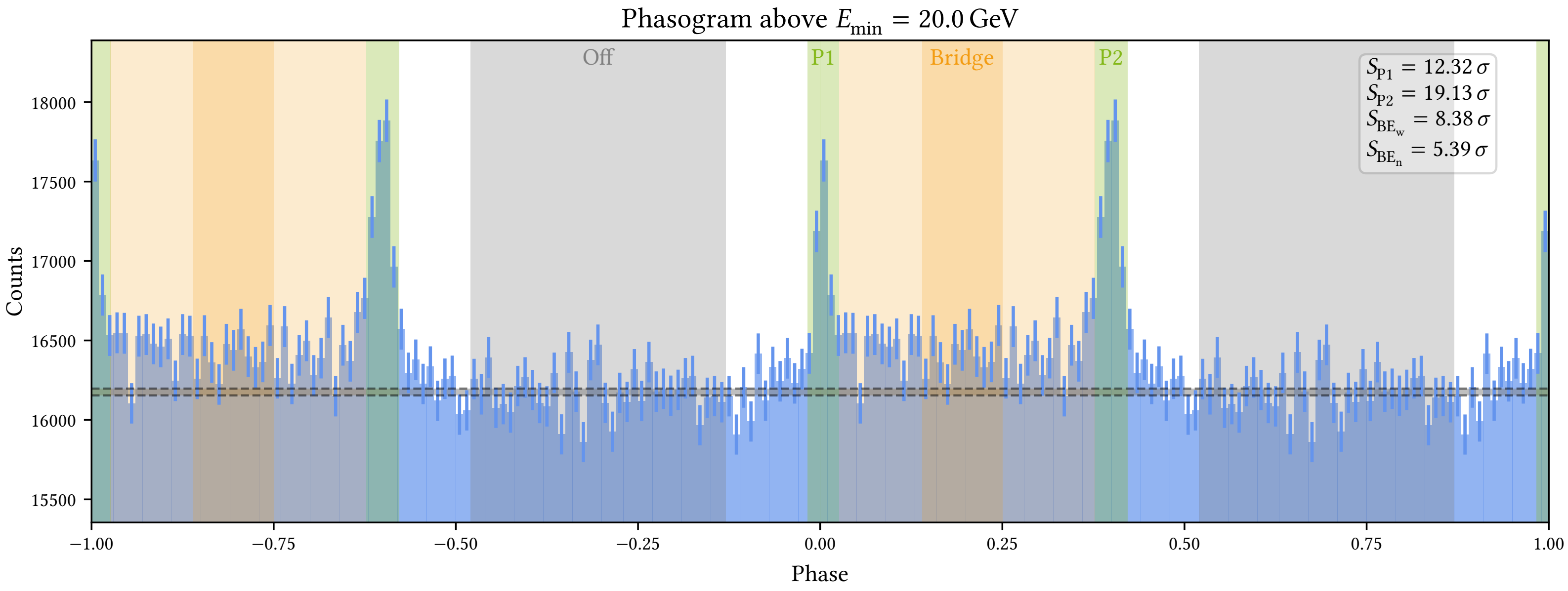

Figure 6.2: Phasogram of the Crab Pulsar in the Sum-Trigger-II analysis above 20 GeV. The entire orange area illustrates the wide definition of the bridge $\mathrm{BE_w}$, whereas the dark orange part of this area depicts the narrow definition of the bridge $\mathrm{BE_n}$. The mean background counts extracted from the Off region are shown as a grey horizontal band.

Energy-dependent phasograms between 19.90 GeV and 792.45 GeV are produced in each energy bin to investigate the energy dependence of the pulsed signal. Above these energies, no pulsation can be found in this dataset (as shown in Appendix C). The phasograms are shown in Figure 6.3 and Figure 6.4. The Li&Ma significance results are listed in Table 6.5 and results of the statistical tests for periodicity can be found in Table 6.5. For the lowest energy bin, a pulse for P1 can be seen while P2 is not clearly visible which is most likely because this energy bin is at the edge of the trigger threshold and hence its signal might have a worse performance than the data in the energy range of better trigger sensitivities. Though, an accumulation of excess counts in the range around P2 is visible. In combination with the wider peaks in the next two energy bins, this is interpreted as a hint of signal.

It can be seen that, while for P1, a signal can only be measured up to ∼300 GeV, P2 remains visible up to ∼500 GeV. The bridge emission is mainly measured below ∼125 GeV. For all features, the highest significances for the pulsed emission can be measured in the low-energy regime, emphasizing the importance of the use of the low-energy Sum-Trigger-II. The statistical tests find pulsed emission only up to ∼300 GeV. In the two highest energy bins, no significant pulsation can be found anymore, although in the second highest energy bin, P2 still is found with a Li&Ma significance of 1.92 σ. Though, looking at the corresponding phasogram, it becomes clear that there are statistical fluctuations higher than the signal in P2 so that no clear pulsed signal can be claimed in this energy bin anymore.

The triple Gaussian (Equation (6.2)) is fitted to the energy-dependent phasograms whereas, for the two highest-energy bins, the fit does not deliver physical results due to the lack of pulsed signal. Hence, the fit is discarded in these two energy bins. The resulting curves are shown in the phasograms in Figure 6.3 and Figure 6.4 in red. The fit results and the FWHM are listed in Table 6.7.

It can be seen that the peak widths based on the fit results are in almost all cases narrower than the pre-defined phase regions. Only for the two lowest-energy bins, the fitted peaks are wider than the pre-defined phase regions, while for the lowest-energy bin, the phasogram suffers from little statistics in general as this bin is at the edge of the MAGIC sensitivity.

From ∼30 GeV to ∼300 GeV, the phasograms can be well described by the triple Gaussian, whereas the fit for the peaks P1 and P2 is more precise than the fit for the bridge. This is intuitively clear since the approximation of the bridge signal as a Gaussian is not ideal. In the joint phasogram in Figure 6.2 where a significant bridge emission is measured, the bridge does not have the shape of a Gaussian but looks like a uniform distribution summed to the background between P1 and P2. The triple Gaussian is just an easy model used especially for evaluating the peak positions, heights, and widths. There are studies approximating the phasogram with different functions such as Lorentzians or asymmetric Lorentzians [1, 25]. So far, no consensus on which function describes the pulses best exists. In the energy range from from ∼30 GeV to ∼300 GeV, some trends of the height and width of P1 and P2 can be observed: while the height ratio of P1 over P2 decreases with increasing energy, the widths of both peaks tend to decrease with increasing energy. The position of the peaks is stable in the given energy range.

From the fit parameters for the standard deviation σ for each of the three Gaussians for P1, P2, and the bridge, the corresponding FWHM is computed using Equation (6.3). The Li&Ma significances for P1, P2, and the bridge are calculated again using the fit-based phase range defined by the interval of the width of the FWHM around the mean. It has to be noted that these fit-based significances have the strong limitation that the phase ranges can overlap. This is especially problematic for the bridge which in some cases contains the P1 and P2 regions, which artificially increases the significance. For P1 and P2 however, these values can indicate that a more significant detection of pulsed signal can be found if the phase ranges are adjusted to the actual peak position and width. For comparability reasons, the most meaningful parameter remains the significance calculated in the pre-defined phase regions. The results of the fit-based significance calculations are shown in Table 6.7. For P1 and P2, the significances calculated with both methods are similar. This shows that the pre-defined phase regions describe the peak positions and widths well. For the bridge, the significances are overestimated by the fit-based approach due to the overestimation of the phase-range width that results from a bad fit of the bridge emission.

A rough estimate of the size of the emission region of the pulsed signal can be derived from the width of the peaks under the assumption that the region emitting the pulsed signal allows for a causal relationship. The FWHM of P1 reaches values below two percent of the phase, while the P2 width reaches values between 2 and 3 percent of the phase. With the rotation period of the Crab Pulsar being approximately 33.6 ms, this corresponds to times between 500 µs and 1 ms. The maximum size of the emission region still allowing for a causal relationship is given by the distance light can travel within this time. This leads to emission regions with a diameter in the order of magnitude of 150 km to 300 km. This is one order of magnitude smaller than the diameter of the light cylinder of the Crab Pulsar which amounts to approximately 3000 km. This finding disfavors models explaining the pulsed emission by beams with a wide opening angle, such as the slot gap or the outer gap model. As the polar gap model cannot produce gamma rays with tens or even hundreds of GeV, three of the four models presented in Section 2.1.4 can be disfavored. The observed pulsed emission is compatible with the model of the equatorial current sheet, which is also the widely favored model for the explanation of the gamma-ray pulsed emission [144].

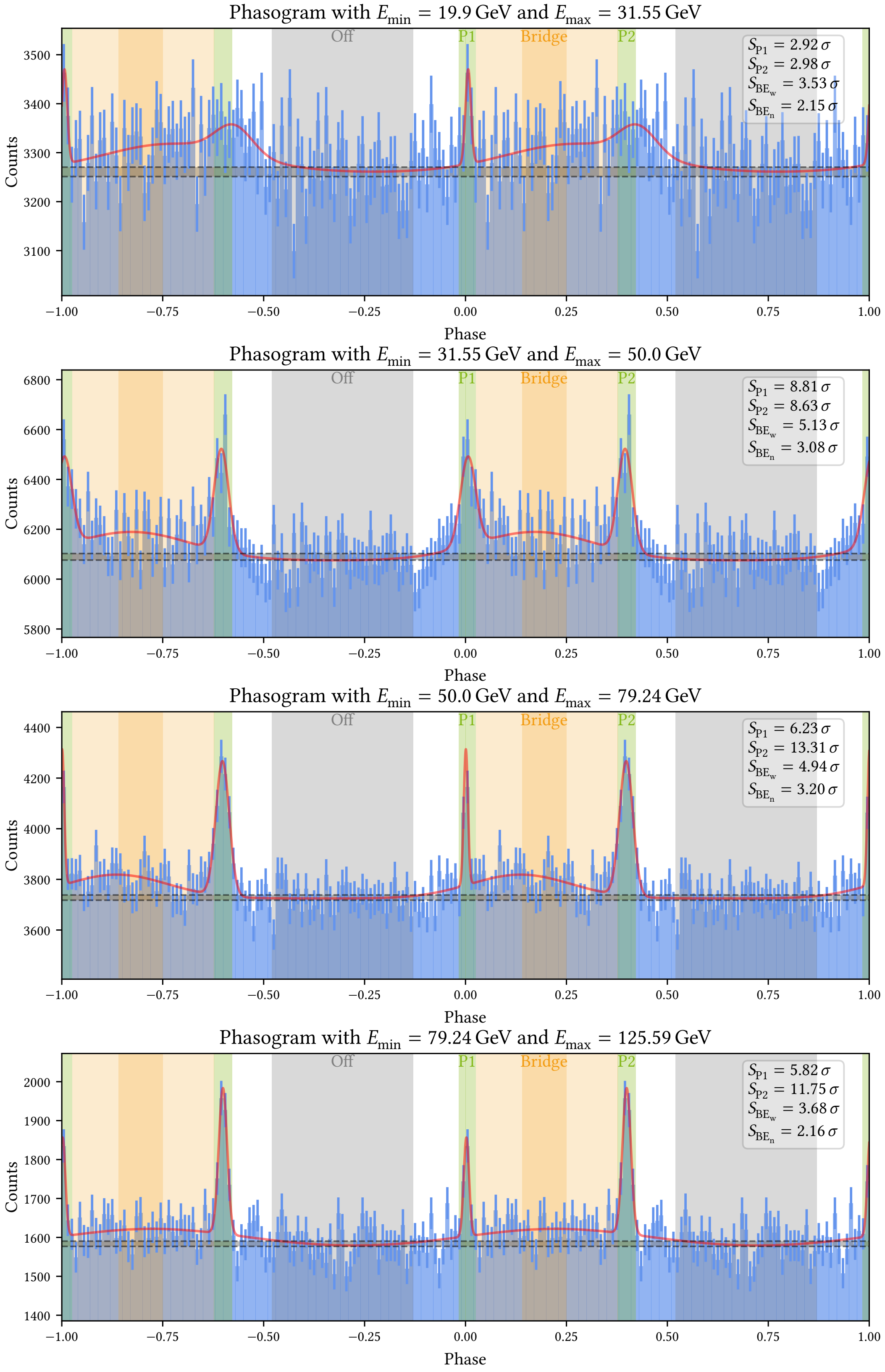

Figure 6.3: Energy bin-wise phasograms for the Sum-Trigger-II analysis. The triple Gaussian fit is shown in red.

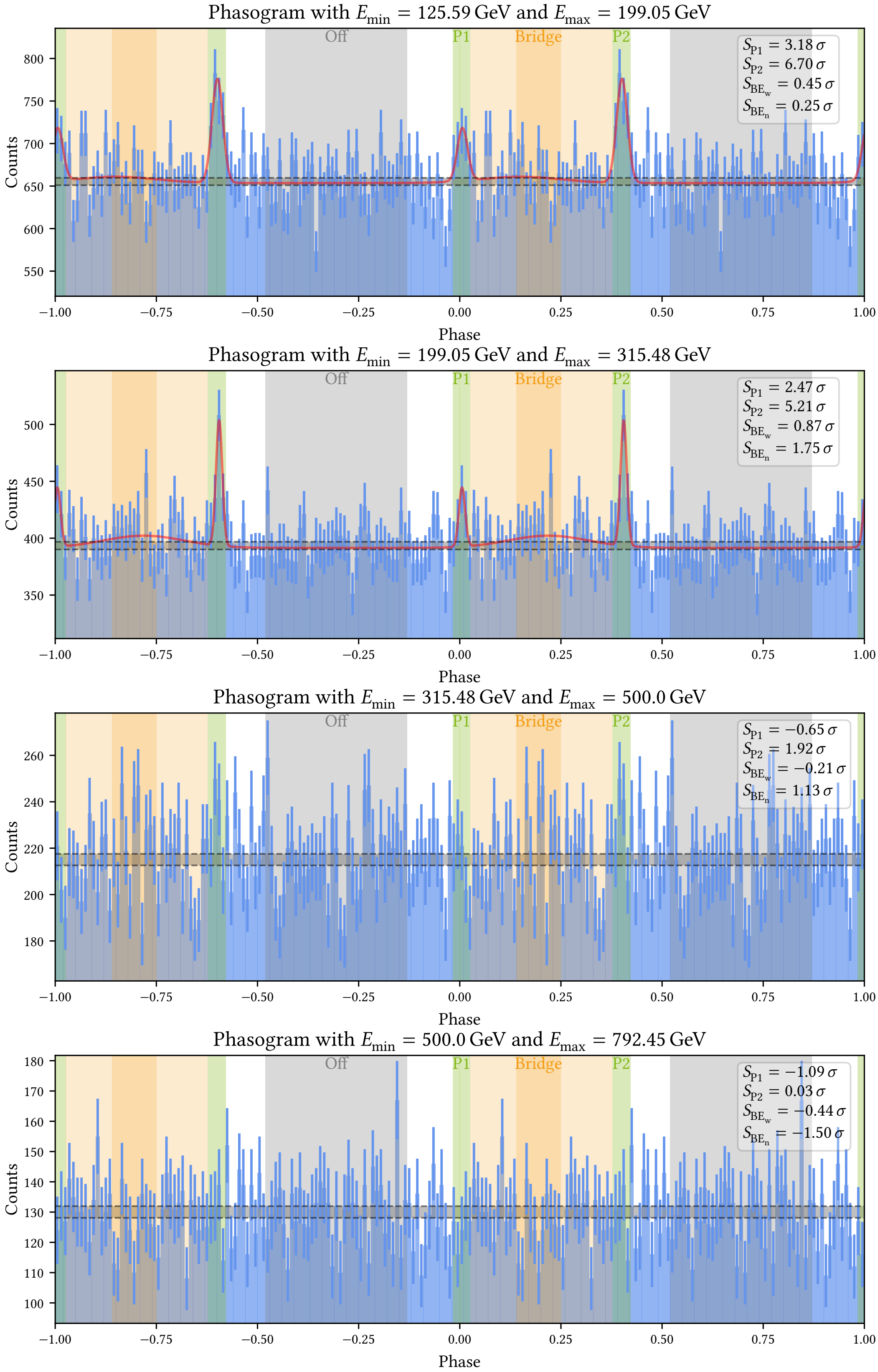

Figure 6.4: Energy bin-wise phasograms for the Sum-Trigger-II analysis (continuation). The triple Gaussian fit is shown in red.

Table 6.5: Li&Ma Significances and counts for the energy-dependent phasograms for the Sum-Trigger-II analysis. The corresponding values for the weighting factor α are $\alpha_{\mathrm{P1}} = 0.123$ for P1, $\alpha_{\mathrm{P2}} = 0.129$ for P2, and $\alpha_{\mathrm{BE_w}} = 1.003$ and $\alpha_{\mathrm{BE_n}} = 0.314$ for the bridge.

E_{min}/GeV	E_{max}/GeV	N_{Off}	N_{P1}	N_{P2}	$N_{\mathrm{BE_w}}$	$N_{\mathrm{BE_n}}$	S_{P1}/σ	S_{P2}/σ	$S_{\mathrm{P1+P2}}/\sigma$	$S_{\mathrm{BE_w}}/\sigma$	$S_{\mathrm{BE_n}}/\sigma$
20.00	-	566144	73028	78350	576737	180544	12.32	19.13	21.14	8.38	5.39
19.90	31.55	114128	14389	15059	116150	36336	2.92	2.98	3.95	3.53	2.15
31.55	50.00	213131	27712	28936	217109	67901	8.81	8.63	11.69	5.13	3.08
50.00	79.24	130481	16875	18645	133394	41754	6.23	13.31	13.18	4.94	3.20
79.24	125.59	55426	7325	8209	56818	17747	5.82	11.75	11.84	3.68	2.16
125.59	199.05	22937	2999	3345	23099	7233	3.18	6.70	6.66	0.45	0.25
199.05	315.48	13771	1801	2009	13955	4461	2.47	5.21	5.18	0.87	1.75
315.48	500.00	7527	904	1032	7523	2429	-0.65	1.92	0.89	-0.21	1.13
500.00	792.45	4551	532	586	4522	1366	-1.09	0.03	-0.70	-0.44	-1.50

Table 6.6: Statistical test results for the energy-dependent phasograms for the Sum-Trigger-II analysis.

E_{min}/GeV	E_{max}/GeV	Z_n^2	p_Z	S_Z/σ	n_Z	H	p_H	S_H/σ	n_H
20.00	-	503.75	$4.77 \cdot 10^{-94}$	20.54	10	541.96	$7.10 \cdot 10^{-95}$	20.63	20
19.90	31.55	37.44	$1.04 \cdot 10^{-2}$	2.31	10	18.49	$6.13 \cdot 10^{-4}$	3.23	1
31.55	50.00	174.05	$1.41 \cdot 10^{-26}$	10.60	10	138.05	$1.04 \cdot 10^{-24}$	10.19	10
50.00	79.24	228.26	$2.67 \cdot 10^{-37}$	12.71	10	211.90	$1.54 \cdot 10^{-37}$	12.75	16
79.24	125.59	153.09	$1.61 \cdot 10^{-22}$	9.69	10	171.46	$1.64 \cdot 10^{-30}$	11.42	20
125.59	199.05	64.19	$1.57 \cdot 10^{-6}$	4.66	10	33.44	$1.55 \cdot 10^{-6}$	4.66	16
199.05	315.48	43.55	$1.73 \cdot 10^{-3}$	2.92	10	13.14	$5.21 \cdot 10^{-3}$	2.56	13
315.48	500.00	26.79	$1.41 \cdot 10^{-1}$	1.08	10	0.31	$8.82 \cdot 10^{-1}$	-1.19	1
500.00	792.45	6.43	$9.98 \cdot 10^{-1}$	-2.91	10	0.49	$8.22 \cdot 10^{-1}$	-0.92	1

Table 6.7: Results of the triple Gaussian fit to the energy-dependent phasograms for P1, P2, and the bridge. The background is only listed once for P1 and is the same for P2 and the bridge.

E_{min}/GeV	E_{max}/GeV	N_{bkg}	A	μ	σ	FWHM	S_{LiMa}/σ
P1							
19.90	31.55	$(3.260 \pm 0.015) \cdot 10^{3}$	$(1.93 \pm 0.45) \cdot 10^{2}$	$(6.7 \pm 2.0) \cdot 10^{-3}$	$(6.8 \pm 1.8) \cdot 10^{-3}$	$(1.61 \pm 0.42) \cdot 10^{-2}$	3.05
31.55	50.00	$(6.075 \pm 0.013) \cdot 10^{3}$	$(3.56 \pm 0.41) \cdot 10^{2}$	$(6.3 \pm 2.4) \cdot 10^{-3}$	$(1.90 \pm 0.27) \cdot 10^{-2}$	$(4.46 \pm 0.63) \cdot 10^{-2}$	8.73
50.00	79.24	$(3.7246 \pm 0.0067) \cdot 10^{3}$	$(5.4 \pm 1.9) \cdot 10^{2}$	$(8.3 \pm 7.6) \cdot 10^{-4}$	$(5.2 \pm 2.1) \cdot 10^{-3}$	$(1.22 \pm 0.48) \cdot 10^{-2}$	7.70
79.24	125.59	$(1.568 \pm 0.057) \cdot 10^{3}$	$(2.54 \pm 0.34) \cdot 10^{2}$	$(2.17 \pm 0.99) \cdot 10^{-3}$	$(6.7 \pm 1.1) \cdot 10^{-3}$	$(1.57 \pm 0.26) \cdot 10^{-2}$	7.01
125.59	199.05	$(6.535 \pm 0.030) \cdot 10^{2}$	$(6.2 \pm 1.7) \cdot 10^{1}$	$(6.7 \pm 3.9) \cdot 10^{-3}$	$(1.27 \pm 0.44) \cdot 10^{-2}$	$(3.0 \pm 1.0) \cdot 10^{-2}$	3.57
199.05	315.48	$(3.915 \pm 0.019) \cdot 10^{2}$	$(5.2 \pm 1.3) \cdot 10^{1}$	$(5.6 \pm 2.4) \cdot 10^{-3}$	$(7.8 \pm 2.2) \cdot 10^{-3}$	$(1.84 \pm 0.51) \cdot 10^{-2}$	2.87
P2							
19.90	31.55		$(5.8 \pm 2.5) \cdot 10^{1}$	$(4.27 \pm 0.18) \cdot 10^{-1}$	$(4.6 \pm 2.4) \cdot 10^{-2}$	$(1.08 \pm 0.56) \cdot 10^{-1}$	4.40
31.55	50.00		$(4.11 \pm 0.41) \cdot 10^{2}$	$(3.955 \pm 0.020) \cdot 10^{-1}$	$(1.80 \pm 0.22) \cdot 10^{-2}$	$(4.23 \pm 0.52) \cdot 10^{-2}$	8.83
50.00	79.24		$(5.32 \pm 0.28) \cdot 10^{2}$	$(3.9810 \pm 0.0099) \cdot 10^{-1}$	$(1.67 \pm 0.10) \cdot 10^{-2}$	$(3.93 \pm 0.24) \cdot 10^{-2}$	13.49
79.24	125.59		$(3.75 \pm 0.25) \cdot 10^{2}$	$(3.9920 \pm 0.0079) \cdot 10^{-1}$	$(1.046 \pm 0.083) \cdot 10^{-2}$	$(2.46 \pm 0.20) \cdot 10^{-2}$	12.44
125.59	199.05		$(1.22 \pm 0.16) \cdot 10^{2}$	$(4.010 \pm 0.020) \cdot 10^{-1}$	$(1.35 \pm 0.21) \cdot 10^{-2}$	$(3.18 \pm 0.49) \cdot 10^{-2}$	6.34
199.05	315.48		$(1.10 \pm 0.13) \cdot 10^{2}$	$(4.052 \pm 0.011) \cdot 10^{-1}$	$(7.8 \pm 1.0) \cdot 10^{-3}$	$(1.84 \pm 0.24) \cdot 10^{-2}$	5.46
BE							
19.9	31.55		$(5.9 \pm 1.9) \cdot 10^{1}$	$(0.7 \pm 5.9) \cdot 10^{-2}$	$(1.72 \pm 0.78) \cdot 10^{-1}$	$(4.1 \pm 1.8) \cdot 10^{-1}$	4.62
31.55	50.0		$(1.15 \pm 0.17) \cdot 10^{2}$	$(1.9 \pm 2.7) \cdot 10^{-2}$	$(1.49 \pm 0.39) \cdot 10^{-1}$	$(3.50 \pm 0.92) \cdot 10^{-1}$	6.10
50.0	79.24		$(9.4 \pm 1.1) \cdot 10^{1}$	$(0.5 \pm 1.7) \cdot 10^{-2}$	$(1.25 \pm 0.21) \cdot 10^{-1}$	$(2.95 \pm 0.50) \cdot 10^{-1}$	6.42
79.24	125.59		$(5.4 \pm 5.4) \cdot 10^{1}$	$(0.7 \pm 3.2) \cdot 10^{-2}$	$(2.4 \pm 1.9) \cdot 10^{-1}$	$(5.6 \pm 4.5) \cdot 10^{-1}$	6.34
125.59	199.05		7.4 ± 6.3	$(0.1 \pm 1.1) \cdot 10^{-1}$	$(1.0 \pm 1.3) \cdot 10^{-1}$	$(2.4 \pm 3.0) \cdot 10^{-1}$	0.86
199.05	315.48		$(1.08 \pm 0.41) \cdot 10^{1}$	$(0.8 \pm 4.2) \cdot 10^{-2}$	$(1.00 \pm 0.51) \cdot 10^{-1}$	$(2.4 \pm 1.2) \cdot 10^{-1}$	1.33

Based on the counts in the pre-defined phase regions and also based on the amplitudes of the fits, the P1/P2 ratio is calculated in each energy bin. For the two highest-energy bins, the fits are not successful, so these two bins are discarded for the P1/P2 ratio. The result is presented in Figure 6.5. Both approaches deliver a declining P1/P2 ratio with increasing energy which is in agreement with previous findings such as [6, 55]. Further, it can be seen that the fit-based P1/P2 ratio is higher than the counts-based P1/P2 ratio in most energy bins. As the significances in both cases deliver similar results though, this might indicate that the fit amplitudes are overestimating the P1 height or underestimating the P2 height. In fact, it can be seen in Figure 6.3 and Figure 6.4 that the P1 height is slightly overestimated in the energy bins between 50 GeV and 125 GeV. Hence, it is concluded that the counts-based approach for the P1/P2 ratio is more accurate than the fit-based version.

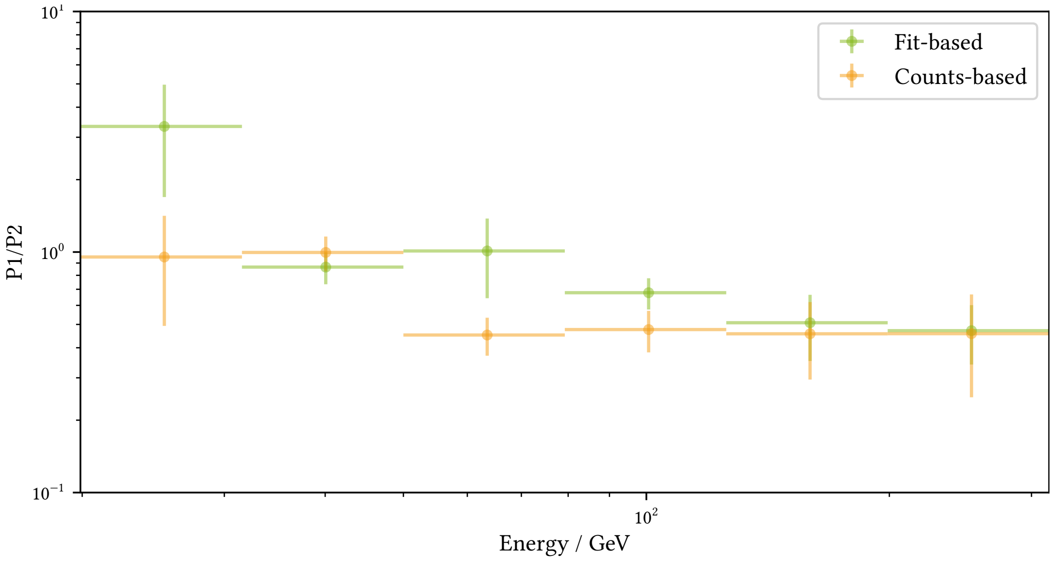

Figure 6.5: Crab Pulsar P1/P2 ratio in dependence of the energy in the Sum-Trigger-II analysis.

6.2.4 Spectra

The phase-resolved spectrum is calculated with `Gammapy` for each phase region, using a forward-folding algorithm estimating the flux points based on an assumed spectral shape.

The spectral bins are chosen as the reconstructed energy bins. Depending on the phase range, the SED calculation is done in different energy ranges. For P1, and P2, the SED calculation is performed from 19.90 GeV to 792.45 GeV since above this regime, no significant pulsed signal is observed anymore. For the other phase ranges, the SED calculations are done from 19.90 GeV to 500.00 GeV. It has to be noted that, as already discussed in Section 6.2.3, the lowest energy bin between ~20 GeV and ~30 GeV is at the edge of the trigger threshold and hence its results have to be interpreted with care. The choice of the maximum energy for the SED calculation is necessary because statistical fluctuations can produce flux points and could hence influence the fit. Especially due to the low test statistic value threshold for the flux points, this is crucial to obtain reliable results. In the following, only the continuous presence of flux points up to a certain energy is regarded as the detection of pulsed emission up to this energy. All higher-energy flux points, especially if not multiple flux points in a row are found, are interpreted as statistical fluctuation.

The MAGIC flux points are visualized with the fit result and the *Fermi*-LAT results. For P1, P2, and the bridge, also a reference spectrum (see Table 6.2) is shown.

The results are shown in Figure 6.6 for the phase regions around P1, in Figure 6.7 for the phase regions around the bridge, and in Figure 6.8 for the phase ranges around P2. The results of the fit parameters are presented in Table 6.8. A list of the flux point values can be found in Appendix D. First of all, it is striking that the MAGIC results for all phase ranges are consistent with the *Fermi*-LAT results. Only for P2 and T2, this analysis delivers flux points that lie slightly above upper limits by *Fermi*-LAT.[9] For P2 this is in an energy range in which both flux points and upper limits occur, indicating that this is the edge of the *Fermi*-LAT sensitivity and hence the results are not contradicting. For T2, the flux points of this analysis show huge uncertainty and only two flux points can be calculated in the two lowest-energy bins. Especially the lowest-energy bin is at the edge of MAGIC's sensitivity and hence its flux might be overestimated. Further, for T2 one flux point above 300 GeV is found. As neither upper limits nor flux points can be calculated for the adjacent energy bins, this flux point is most likely a statistical fluctuation and does not carry physical information. The results for P1, P2, and $\mathrm{BE_n}$ are in good agreement with previous MAGIC results. For P1 and P2, the results found in this analysis agree well with the results from [55] but constrain the spectral parameters further, as can be seen by the lower uncertainties of the power law fit results. Here it is noteworthy that the power law spectral models describe the flux well also above 200 GeV, while the reference curves were calculated only on data between 25 GeV and 200 GeV. In this analysis, P1 can be observed up to ~300 GeV, and pulsed emission from P2 can be reconstructed up to ~500 GeV. Beyond these energies, only statistical fluctuations and no clear pulsed signal can be found.

The results for $\mathrm{BE_n}$ are also in agreement with previous MAGIC results and further constrain the spectrum parameters significantly.

---

[9] Here it is noteworthy that the MAGIC and *Fermi*-LAT thresholds for upper limits are difficult to compare as the results of both experiments rely on different statistical methods.

For the leading and trailing regions, the spectrum can only be calculated in the low-energy regime up to 125 GeV. This is likely due to the fact that more photons are detected in the low-energy regime and the data does not contain enough statistics to calculate the spectra up to higher energies.

For some phase ranges, such as T2, the fit parameters underlie high uncertainties as they base on only few flux points.

Table 6.8: Phase-range-wise spectral fits for the Sum-Trigger-II analysis. Please note that the listed values are fit results before re-weighting the spectrum for the phase interval width.

Name	Start	Stop	E_0/GeV	$F_0/\mathrm{TeV}^{-1}\,\mathrm{cm}^{-2}\,\mathrm{s}^{-1}$	Γ	E_d/GeV
L1	0.950	0.983	100.0	$(6 \pm 4) \cdot 10^{-12}$	4.2 ± 0.6	33.97
P1	0.983	0.026	59.86	$(3.69 \pm 0.31) \cdot 10^{-10}$	3.59 ± 0.14	47.63
T1	0.026	0.040	100.0	$(4 \pm 4) \cdot 10^{-12}$	4.2 ± 0.7	32.62
DB	0.040	0.140	100.0	$(4.1 \pm 1.2) \cdot 10^{-11}$	3.75 ± 0.27	43.03
BE	0.140	0.250	100.0	$(4.1 \pm 1.5) \cdot 10^{-11}$	3.6 ± 0.4	46.07
BF	0.250	0.320	100.0	$(1.8 \pm 1.4) \cdot 10^{-11}$	3.8 ± 0.8	40.48
L2	0.320	0.377	100.0	$(1.6 \pm 0.7) \cdot 10^{-11}$	4.3 ± 0.4	32.41
P2	0.377	0.422	70.33	$(3.92 \pm 0.19) \cdot 10^{-10}$	3.12 ± 0.07	68.27
T2	0.422	0.455	100.0	$(0.8 \pm 2.9) \cdot 10^{-13}$	7.1 ± 1.9	14.03

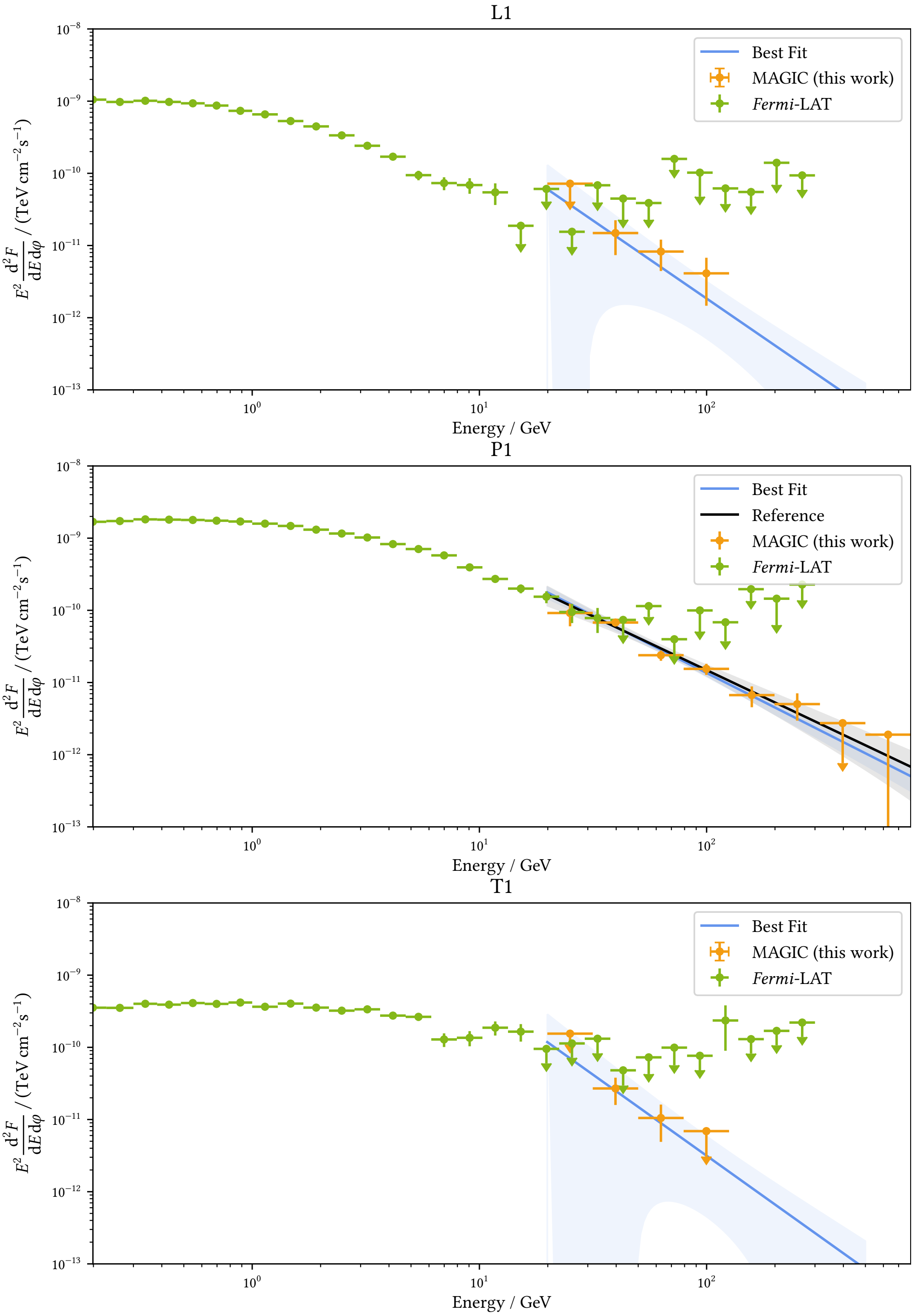

Figure 6.6: Phase-resolved Crab Pulsar spectra for the phase ranges around P1 in the Sum-Trigger-II analysis. The $1\,\sigma$ uncertainty around the best fit and reference curves is shadowed in the corresponding color. The P1 reference is taken from [55].

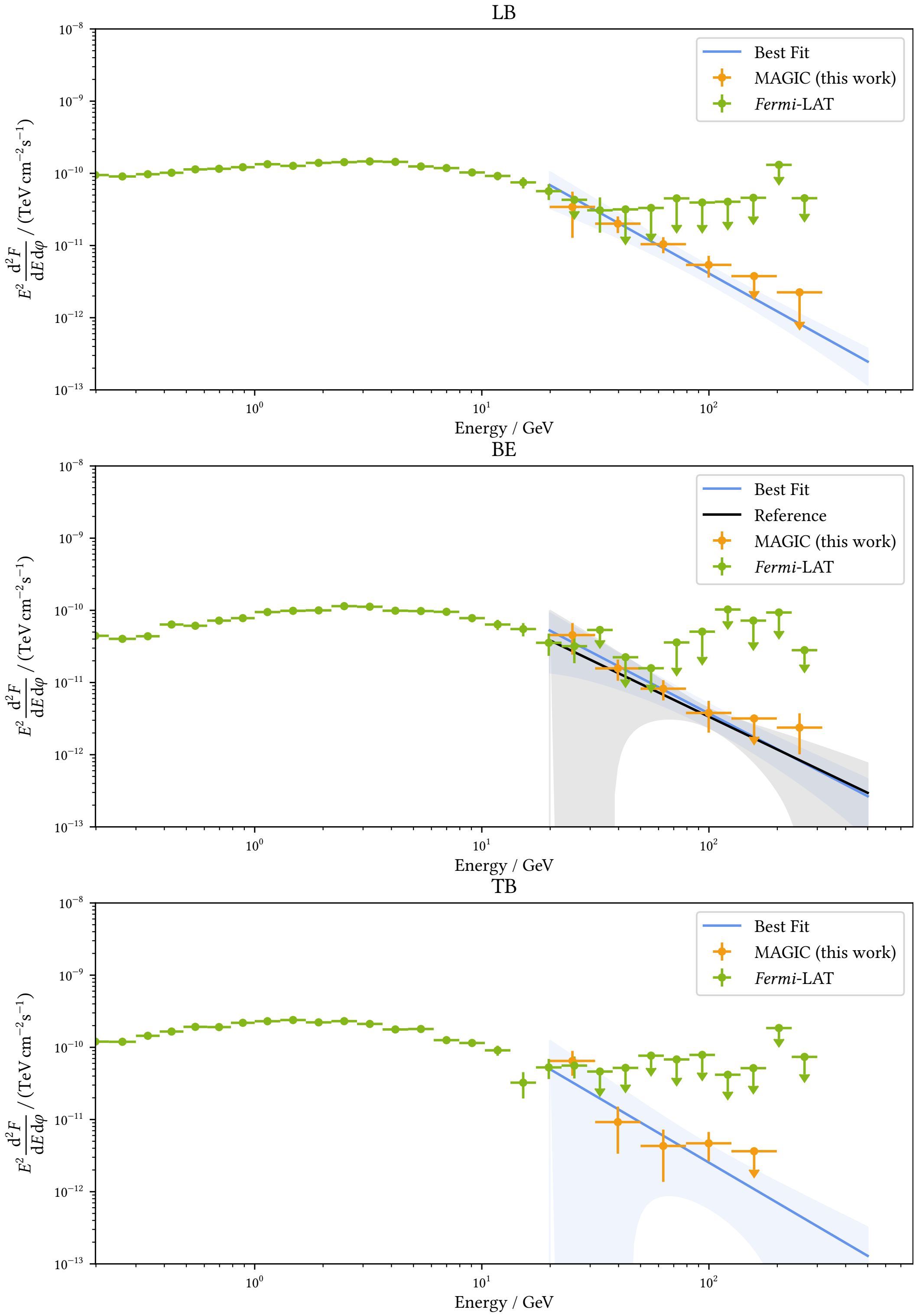

Figure 6.7: Phase-resolved Crab Pulsar spectra for the phase ranges around the bridge in the Sum-Trigger-II analysis. The $\mathrm{BE_n}$ reference is taken from [23].

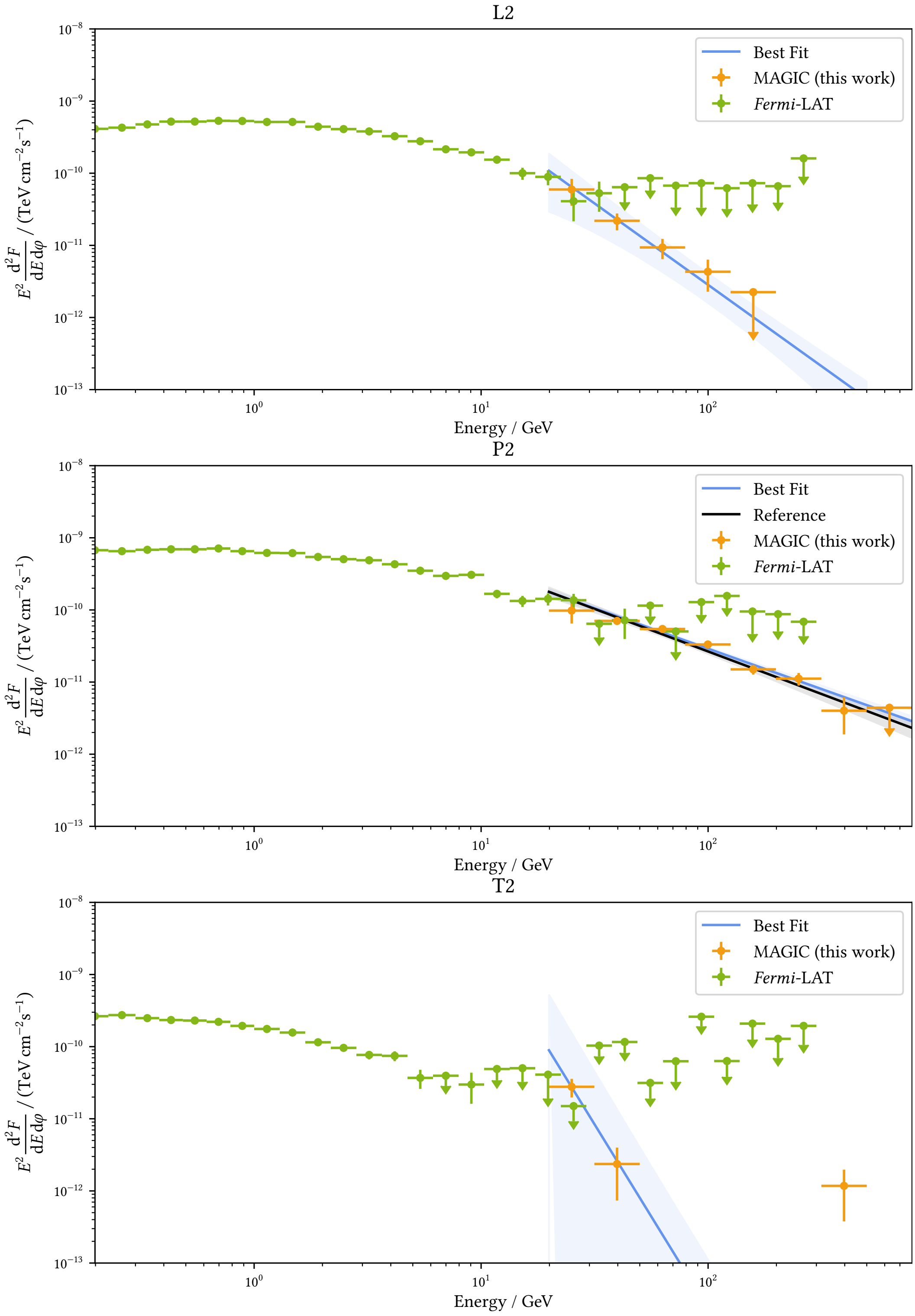

Figure 6.8: Phase-resolved Crab Pulsar spectra for the phase ranges around P2 in the Sum-Trigger-II analysis. The P2 reference is taken from [55].

The phase-resolved integrated flux is calculated below 792.45 GeV for the pre-defined phase ranges as well as in equally sized phase range bins of 0.025 phases. The results are presented in Figure 6.9. A similar shape as in the phasograms can be seen, showing two strong peaks P1 and P2 and an excess signal between both peaks. Please note that in the Off phases, the flux cannot be computed reliably because this is the Off data in the pulsar analysis. Further, please note that the flux points are re-weighted by their inverse phase range width.

The presented flux shows a similar distribution as the phasograms, clearly showing two peaks with increased emission. An integrated flux of $(3.44 \pm 0.27) \cdot 10^{-9}\,1/(\mathrm{cm}^2\,\mathrm{s})$ for P1 and $(4.19 \pm 0.20) \cdot 10^{-9}\,1/(\mathrm{cm}^2\,\mathrm{s})$ for P2 is found. The fluxes in the bridge region between P1 and P2 lie in the order of magnitude of $5 \cdot 10^{-10}\,1/(\mathrm{cm}^2\,\mathrm{s})$ to $2 \cdot 10^{-9}\,1/(\mathrm{cm}^2\,\mathrm{s})$.

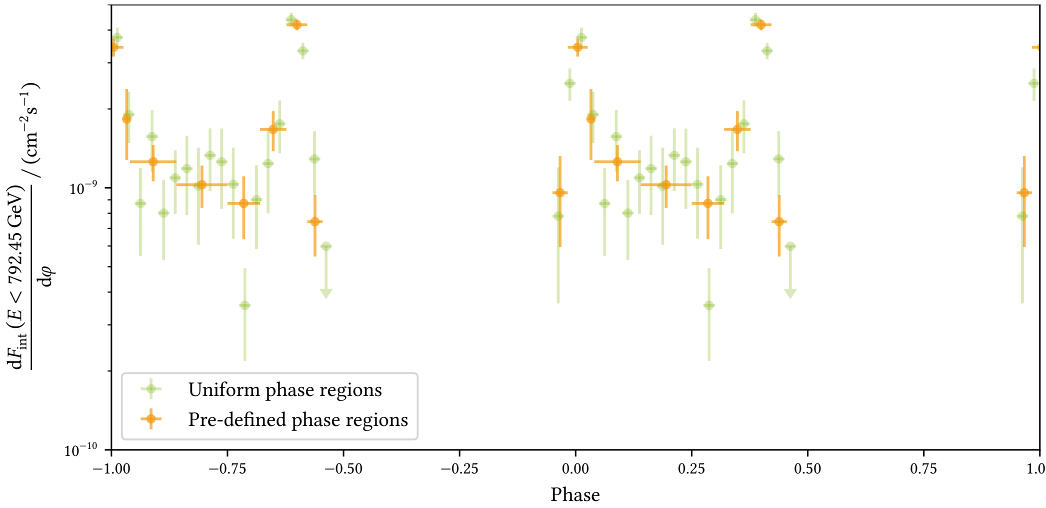

Figure 6.9: Phase-resolved integrated flux below 792.45 GeV for the Crab Pulsar in the Sum-Trigger-II analysis.

6.2.5 Light Curves

Phase-resolved light curves for P1 and P2 with the integrated flux below 792.45 GeV are produced in order to investigate the time-dependent behavior of the pulsed signal. As the statistics on a run-wise basis are too low to deliver reliable results in this case, a night-wise binning is chosen.[10] As visible in Figure 6.10, the integrated flux of both P1 and P2 is at the edge of what can be detected within this analysis, and in addition to some data points, many upper limits are found. The flux is however stable over the entire time range, suggesting that there is no day-scale variability in the integrated flux of the pulses P1 and P2. The variability on shorter time scales cannot be investigated reliably due to a lack of statistics.

---

[10] Still, many upper limits are found but as wider bins are not reasonable due to the uneven distribution of observation time, the night-wise binning is the best choice.

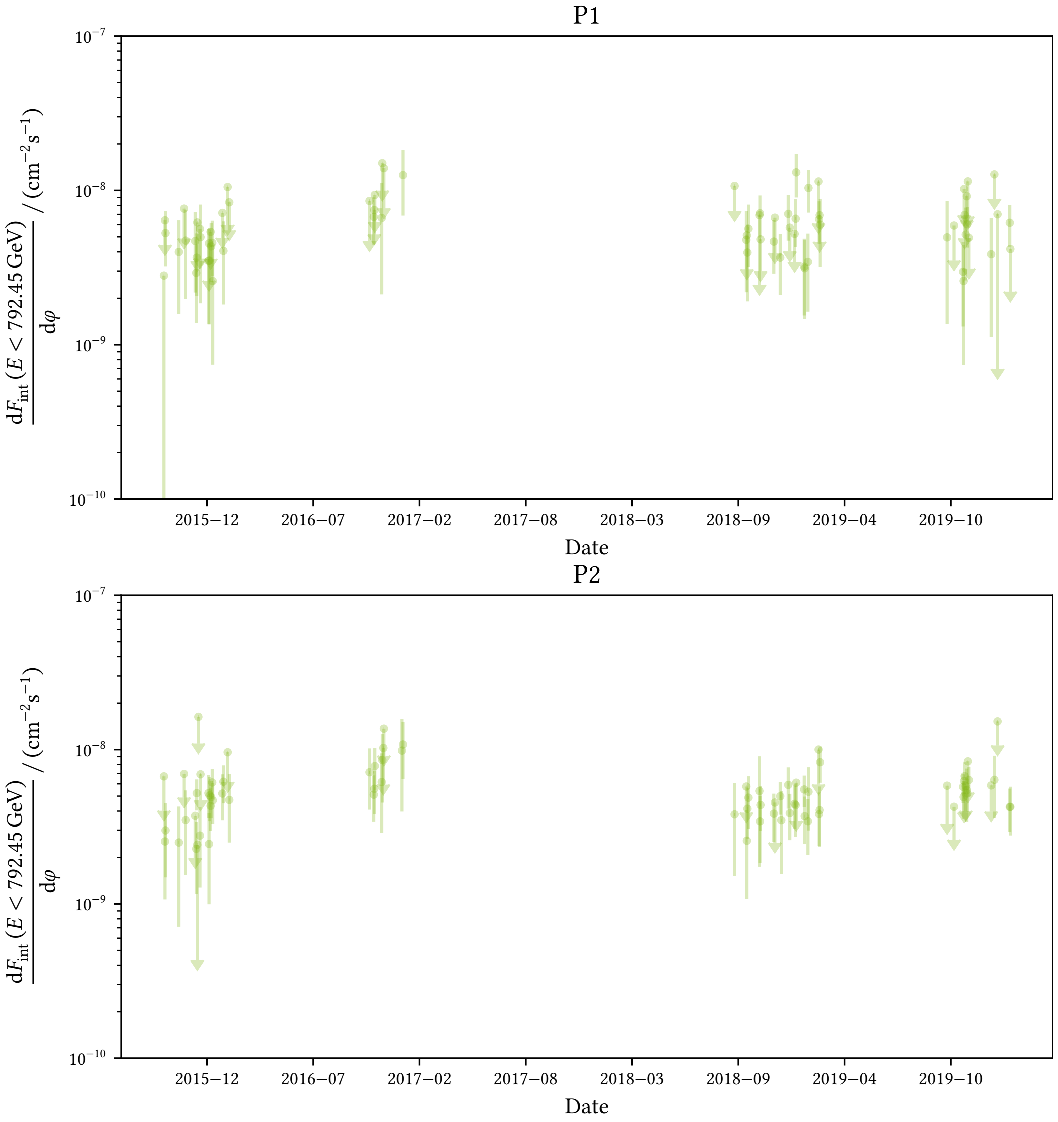

Figure 6.10: Phase-resolved light curves for P1 and P2 with night-wise binning in the Sum-Trigger-II analysis.

6.3 Standard Trigger Analysis

To complement the information extracted from the Sum-Trigger-II data, also an analysis of Standard Trigger data is performed. There is much more data taken with Standard Trigger and hence it can give better insights into energy regimes in which both triggers have a similar performance, i.e. at few hundreds of GeV. For the Standard Trigger analysis, in contrast to the Sum-Trigger-II analysis, all zd ranges are taken into account and also a dedicated VHZ analysis is done. Higher zd angles are associated with a higher energy threshold but also with a higher sensitivity of the telescopes in the high-energy regime. Hence, with the VHZ data, the highest-energy pulsed signal can be investigated.

The analysis is divided into two sub-analyses: One analysis for the standard zd range from 5° to 62° zd, presented in Section 6.3.1, and one dedicated VHZ analysis for zd angles between 62° and 80° zd, presented in Section 6.3.2. The reason for this split lies in the data analysis: The data up to 62° zd is analyzed with the standard MC data only, while for the data above 62° zd, the high-energy MC extension is used additionally.

6.3.1 Zenith Distance 5° to 62°

The zd range from 5° to 62° zd is considered the standard range in which the telescopes operate most of the time. For the analysis of this data, no MC extension has to be used and hence it is grouped as one analysis in this work. In the last twelve years, MAGIC has collected hundreds of hours of Crab Nebula data. In this chapter, a long-term analysis of twelve years of good-quality Crab Pulsar data is shown. Firstly, the data selection and the data processing are described. Afterward, the results for the long-term phasogram and the spectra are shown. For this analysis, the phase-resolved integrated flux is not calculated as apart from P1 and P2, almost all phase ranges only deliver upper limits. Further, no phase-resolved light curves can be calculated as they also mostly deliver upper limits due to the worse sensitivity of the Standard Trigger in the low-energy regime. A Crab Nebula validation for this dataset can be found in Appendix E.2.1.

Data Selection

Only data taken under dark conditions without moonlight is used due to data availability reasons.[11] Further, the moon influences the data quality and affects especially the low-energy regime, which is of special interest for pulsar analyses. In this analysis, only data after the major upgrade of the MAGIC telescopes is used to ensure data of similar quality. The data is composed of two datasets:

Old Preprocessed Data: Data taken in the early stereo phase of MAGIC between February 2012 and November 2014. This data is taken from previous MAGIC analyses and was provided on `melibea` level. Hence, no exact statements concerning the data processing can be made for this dataset. It covers the MAGIC stereo time range not

---

[11] The pre-processed data is available on `superstar` level permanently, while calibrated data, which is necessary for the analysis of moon data, is stored on tapes and has to be requested in advance.

yet accessible to `autoMAGIC`.[12]

Long-term `autoMAGIC` Data: Data taken between November 2014 and March 2024. The data is processed with `autoMAGIC` starting on standard `superstar` files.

In the `autoMAGIC` analysis, some data is explicitly excluded, either based on the observation dates or based on certain observation conditions:

Mono Data: In the time period from 2022-09-04 to 2022-12-14, the telescopes could only observe in mono mode. Since `autoMAGIC` does not support the mono analysis, this data is discarded.

Bad Telescope Performance: The data recorded between December 2022 and the beginning of March 2023 show a bad telescope performance that could not be resolved with a dedicated MC production. Although different configurations were tested, none of them led to a significant improvement in the performance of the analysis, and the Crab Nebula flux is underestimated by about 20 %. Hence, all the data in the period of time from 2022-12-15 to 2023-03-10 is excluded from this analysis.

Moon Filter: From October 2014 to October 2016, data with a physical moon filter placed in front of the camera was taken. This filter leads to a low DC even though moon data is taken. As `autoMAGIC` distinguishes moon data from dark data based on the M1 DC, this data has to be excluded manually as it would have to be processed with a special analysis that is not implemented in `autoMAGIC`.

Further, a very strict cut on the weather parameters is applied to the Crab Nebula data since this is essential for a good performance in the low-energy regime. With the Standard Trigger, the Crab Nebula is sometimes observed under hazy conditions (since it is one of the brightest gamma-ray sources in the sky and so it still can be observed under these conditions). This leads to more noise, especially in the low-energy regime which can obscure the pulsed emission, so the strict cuts on the observation conditions are essential for the pulsar analysis. For the atmospheric transmission, a minimum of 90 % is required and in case no transmission value is available for the run, a maximum cloudiness of 10 % is required. A list of all the cuts applied to the data can be found in Table 6.9. The total amount of data surviving the cuts is 359.97 h, whereas 117.20 h originate from the old preprocessed data and 242.77 h originate from the `autoMAGIC` data.

Data Processing

The old preprocessed data between 2012 and 2014 are converted to `DL3` with `DL3 Converter` version 0.1.15, with energy-dependent hadronness and θ^2 cuts with 90 % MC efficiency. The energy axes are defined between 5 GeV and 50 TeV with 20 bins for the reconstructed energy and 25 bins for the true energy.

The data from November 2014 to March 2024 is processed with `autoMAGIC` with the configuration file shown in Appendix G.2. The same hadronness and θ^2 cuts are applied and

---

[12] The MC data before November 2014 is also available but stored in a different directory structure. Reading out this structure is not yet implemented in `autoMAGIC` and not trivial since no standardized directory structure was used at that time.

Table 6.9: Cuts used for the data selection in the Standard Trigger analysis between 5° and 62° zd.

Parameter Name	Cut Value
start date	2012-02-01
stop date	2024-03-31
transmission (On data)	0.9
transmission (Off data)	0.8
maximum cloudiness (On data)	10
maximum cloudiness (Off data)	20
minimum zd	5°
maximum zd	62°
minimum duration	300 s
minimum DC	0 nA
maximum DC	2200 nA
MOLA threshold (Off data)	$2\,\sigma$

the energy axes are set the same as in the old dataset from 2012 to 2014. The analysis for this dataset is done with MARS version 3-1-0, `DL3 Converter` version 0.1.15, and `autoMAGIC` version 0.8.

The pulsar timing is done with `magicpulsar` based on the ephemerides described in Appendix B. For the data taken between the 2nd and 4th of February 2013, no pulsar ephemeris is available due to a glitch, so this data is excluded from the analysis.

Phasogram

A joint phasogram for the Standard Trigger in the zd range between 5° and 62° is produced for energies above 50 GeV using energy-dependent hadronness and θ^2 cuts, as shown in Figure 6.11. The phasogram shows significant pulsed emission with Li&Ma significances of $S_{\mathrm{P1}} = 9.70\,\sigma$ for P1 and $S_{\mathrm{P2}} = 15.62\,\sigma$ for P2. The joint P1+P2 significance is found to be $S_{\mathrm{P1+P2}} = 17.03\,\sigma$. For the bridge, only a hint of signal can be found for both the wide bridge definition ($S_{\mathrm{BE_w}} = 3.55\,\sigma$) and the narrow definition ($S_{\mathrm{BE_n}} = 2.34\,\sigma$).

The statistical tests for periodicity deliver a significance of $S_Z = 15.88\,\sigma$ for the Z_n^2-test and $S_H = 17.22\,\sigma$ for the H-test which agrees with the observation of a strong periodic signal. The counts and significances for the phase ranges of interest are listed in Table 6.10 together with the results of the energy-dependent phasogram results. All results of the Z_n^2 and H-test are listed in Table 6.11.

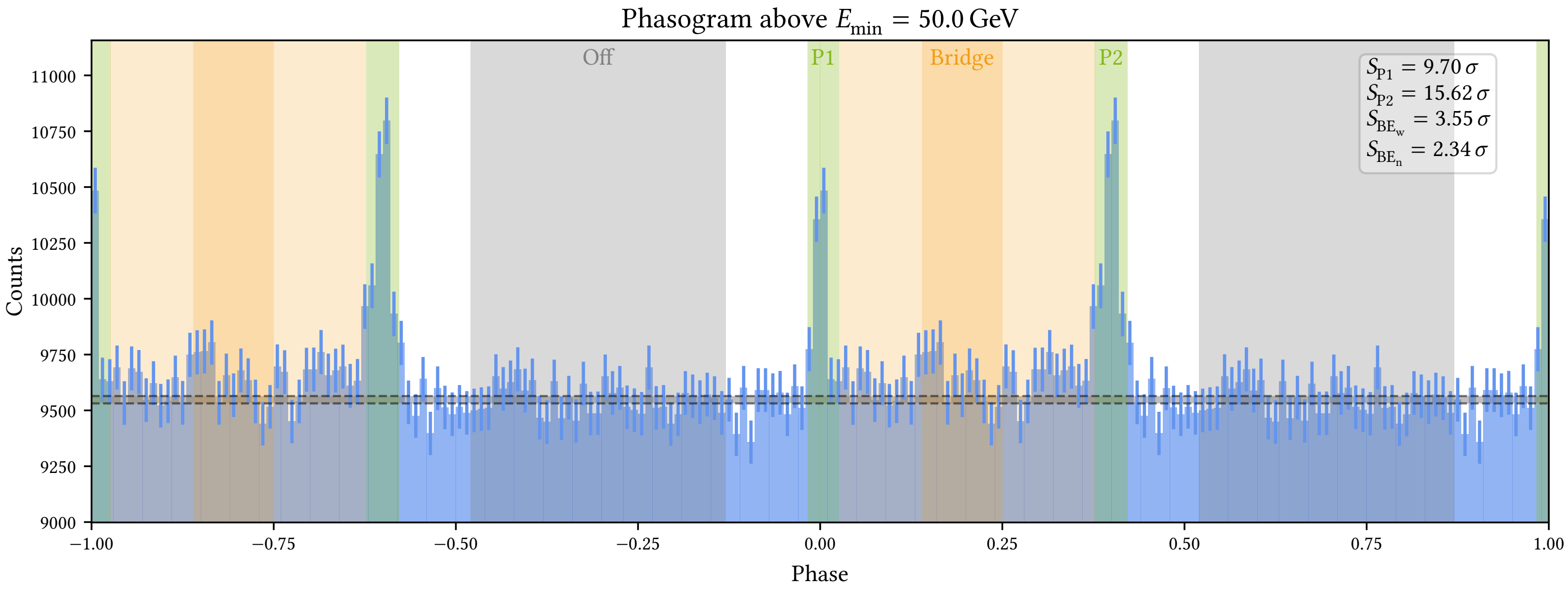

Figure 6.11: Phasogram of the Crab Pulsar above 50 GeV in the Standard Trigger analysis. The entire orange area illustrates the wide definition of the bridge $\mathrm{BE_w}$, whereas the dark orange part of this area depicts the narrow definition of the bridge $\mathrm{BE_n}$. The mean background counts extracted from the Off region are shown as a grey horizontal band.

In the energy range between 50 GeV and 1990 GeV, energy-dependent phasograms in the reconstructed energy bins are produced. Beyond this energy range, no pulsed emission is found in the dataset (as shown with a phasogram above 1 TeV in Appendix C). The energy-dependent phasograms are shown in Figure 6.12 and Figure 6.13. The Li&Ma significance results are listed in Table 6.10 and the results of the Z_n^2 and H-test are listed in Table 6.11.

P1 can only be significantly detected in the three lowest energy bins up to ~200 GeV and a hint of P1 is found in the fourth energy bin up to ~300 GeV. Above those energies, no significant excess signal for P1 is found. P2 is clearly visible up to ~500 GeV but beyond, no significant pulse is visible. The bridge cannot be detected significantly in any of the energy bins. In the two lowest energy bins (below ~125 GeV), a hint of the bridge can be found but in the higher energies, only statistical fluctuations are found.

The triple Gaussian (Equation (6.2)) is fitted to the phasogram in each energy bin up to ~800 GeV. For the higher energies, too much statistical fluctuation is found in the data and hence, the fit cannot be done properly. The fit parameters and the FWHM calculated with Equation (6.3) are presented in Table 6.12 and the resulting functions are shown in red in the phasograms in Figure 6.12 and Figure 6.13.

Firstly, it stands out that in all phasograms, the fitted widths for P1 and P2 are smaller than the width of the pre-defined phase regions. For both P1 and P2, the tendency of a decrease in the pulse width with increasing energy can be observed. For both, it can mostly be observed in the energy range from ~50 GeV to ~300 GeV. The pulse widths in this energy range are in the same order of magnitude as in the Sum-Trigger-II analysis and deliver similar values for the estimated maximum size of the emission region of 150 km to 300 km under the assumption that the emission region allows for a causal relationship. Above these energies, the fitted Gaussians get wider but this is most likely due to a lack of statistics. The position of the peaks is stable over the entire energy range in which they can be detected. Only in the highest energy bin, an excess signal can be found in the phase region around P1 but shifted slightly to a lower phase and in the phase region around P2 but slightly shifted to a higher phase. The fact that in the energy bin below, no pulsed signal can be observed, suggests that this excess is induced by a statistical fluctuation. Since also a peak in the Off region of nearly the same height is visible in the phasogram, the signal is interpreted as noise instead of as shifted peaks. For the bridge, there are large uncertainties in the fit parameters which can be explained by the little excess signal for the bridge in this dataset. Further, the Gaussian function as a model for the bridge is not ideal to describe the bridge, as already discussed in Section 6.2.

The fit-based Li&Ma significances shown in Table 6.12 deviate from the significances based on the pre-defined phase ranges as follows: For P1, the fit-based significances are higher in the low-energy regime up to ~300 GeV where P1 is clearly visible. For P2, a similar trend can be observed. This indicates that the pre-defined phase region for the peaks could be chosen slightly narrower in this analysis.

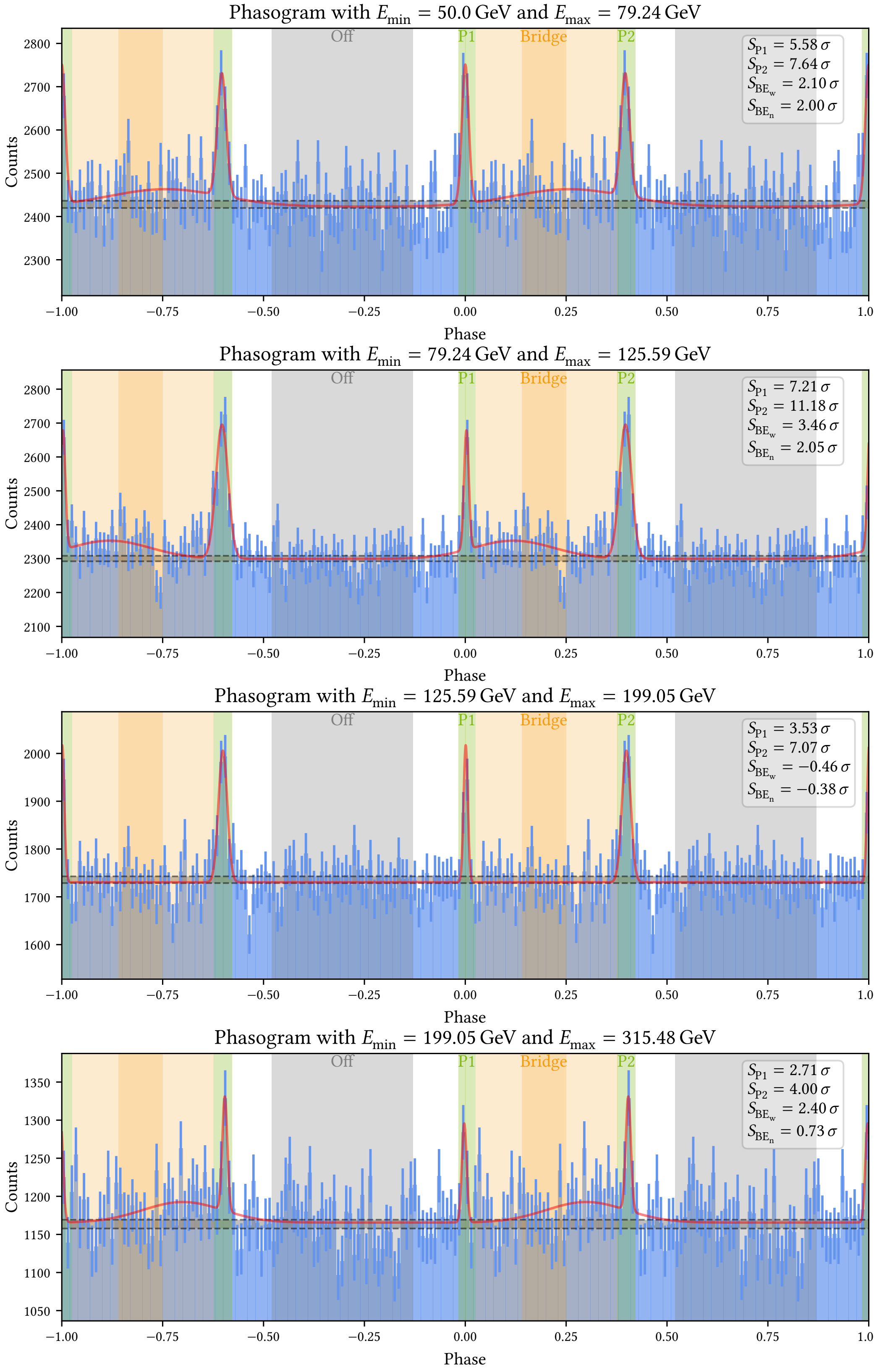

Figure 6.12: Energy bin-wise phasograms for the Standard Trigger analysis. The triple Gaussian fit is shown in red.

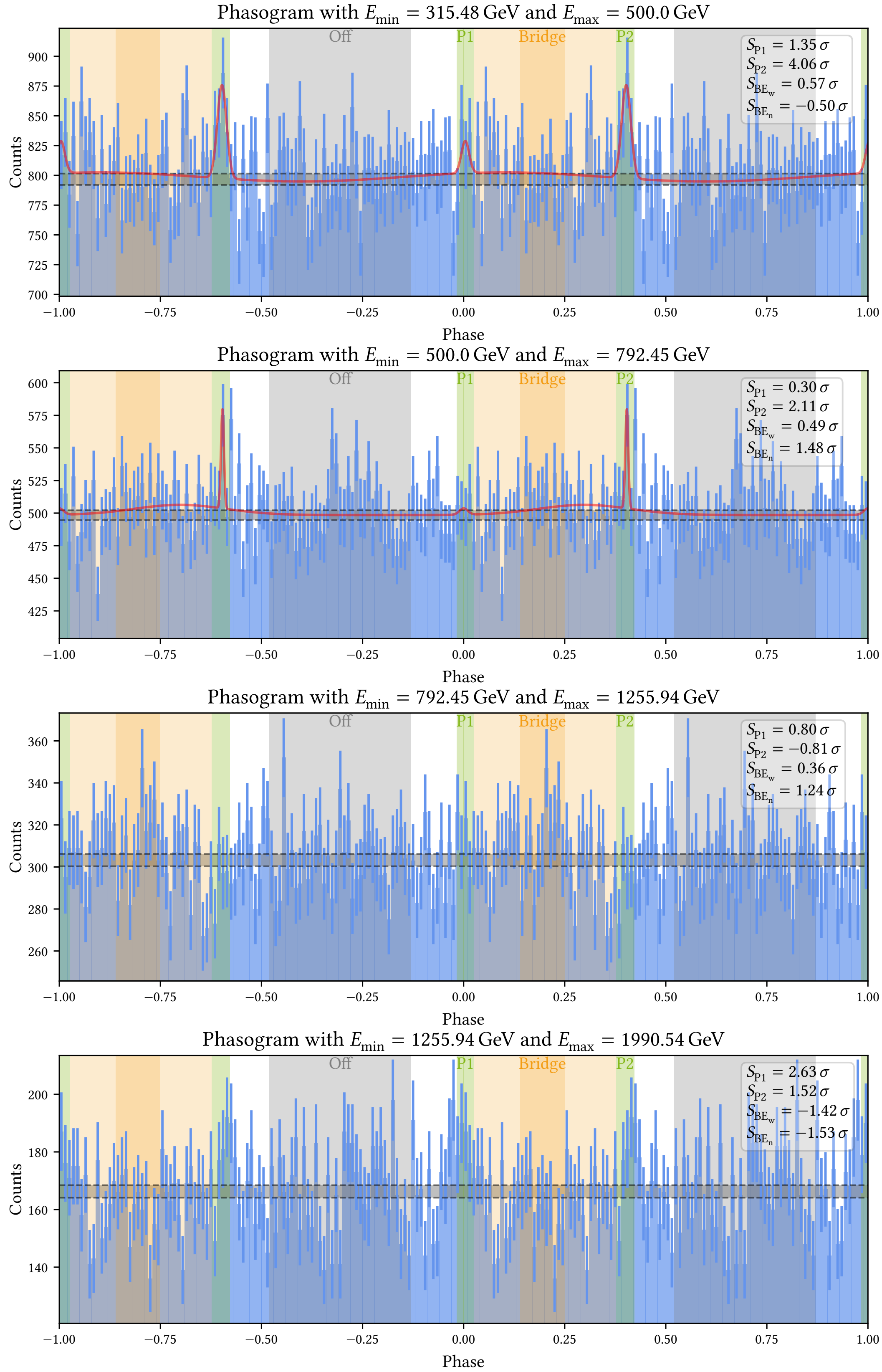

Figure 6.13: Energy bin-wise phasograms for the Standard Trigger analysis (continuation). The triple Gaussian fit is shown in red.

Table 6.10: Li&Ma Significances and counts for the energy-dependent phasograms for the Standard Trigger analysis. The corresponding values for the weighting factor α are $\alpha_{\mathrm{P1}} = 0.123$ for P1, $\alpha_{\mathrm{P2}} = 0.129$ for P2, and $\alpha_{\mathrm{BE_w}} = 1.003$ and $\alpha_{\mathrm{BE_n}} = 0.314$ for the bridge.

E_{min}/GeV	E_{max}/GeV	N_{Off}	N_{P1}	N_{P2}	$N_{\mathrm{BE_w}}$	$N_{\mathrm{BE_n}}$	S_{P1}/σ	S_{P2}/σ	$S_{\mathrm{P1+P2}}/\sigma$	$S_{\mathrm{BE_w}}/\sigma$	$S_{\mathrm{BE_n}}/\sigma$
50.00	-	334173	43158	46456	338044	105896	9.70	15.62	17.03	3.53	2.34
50.00	79.24	84980	11051	11786	86094	27084	5.58	7.64	8.87	2.10	2.00
79.24	125.59	80508	10662	11585	82137	25677	7.21	11.18	12.36	3.46	2.05
125.59	199.05	60753	7790	8485	60767	19033	3.53	7.07	7.14	-0.46	-0.38
199.05	315.48	40723	5208	5547	41528	12893	2.71	4.00	4.51	2.40	0.73
315.48	500.00	27885	3510	3847	28099	8710	1.35	4.06	3.66	0.57	-0.50
500.00	792.45	17444	2158	2350	17586	5609	0.30	2.11	1.64	0.49	1.48
792.45	1255.94	10615	1335	1333	10698	3419	0.80	-0.81	-0.02	0.36	1.24
1255.94	1990.54	5820	791	793	5684	1755	2.63	1.52	2.78	-1.42	-1.53

Table 6.11: Statistical test results for the energy-dependent phasograms for the Standard Trigger analysis.

E_{min}/GeV	E_{max}/GeV	Z_n^2	p_Z	S_Z/σ	n_Z	H	p_H	S_H/σ	n_H
50.00	-	325.63	$4.57 \cdot 10^{-57}$	15.88	10	379.99	$9.73 \cdot 10^{-67}$	17.22	20
50.00	79.24	91.45	$4.14 \cdot 10^{-11}$	6.50	10	73.13	$1.98 \cdot 10^{-13}$	7.26	13
79.24	125.59	186.52	$5.12 \cdot 10^{-29}$	11.12	10	181.80	$2.62 \cdot 10^{-32}$	11.78	17
125.59	199.05	86.67	$2.81 \cdot 10^{-10}$	6.20	10	60.09	$3.64 \cdot 10^{-11}$	6.51	13
199.05	315.48	40.76	$4.00 \cdot 10^{-3}$	2.65	10	14.13	$3.51 \cdot 10^{-3}$	2.70	3
315.48	500.00	17.82	$5.99 \cdot 10^{-1}$	-0.25	10	0.90	$6.97 \cdot 10^{-1}$	-0.52	1
500.00	792.45	26.61	$1.47 \cdot 10^{-1}$	1.05	10	5.61	$1.06 \cdot 10^{-1}$	1.25	4
792.45	1255.94	17.76	$6.03 \cdot 10^{-1}$	-0.26	10	0.99	$6.73 \cdot 10^{-1}$	-0.45	2
1255.94	1990.54	38.31	$8.12 \cdot 10^{-3}$	2.40	10	12.53	$6.67 \cdot 10^{-3}$	2.47	7

Table 6.12: Results of the triple Gaussian fit to the energy-dependent phasograms for P1, P2, and the bridge. The background is only listed once for P1 and is the same for P2 and the bridge.

$E_{\mathrm{min}}/\mathrm{GeV}$	$E_{\mathrm{max}}/\mathrm{GeV}$	N_{bkg}	A	μ	σ	FWHM	S_{LiMa}/σ
				P1			
50.00	79.24	$(2.4228 \pm 0.0069) \cdot 10^{3}$	$(3.21 \pm 0.35) \cdot 10^{2}$	$(0.0 \pm 1.0) \cdot 10^{-3}$	$(8.5 \pm 1.1) \cdot 10^{-3}$	$(2.01 \pm 0.27) \cdot 10^{-2}$	7.51
79.24	125.59	$(2.2994 \pm 0.0052) \cdot 10^{3}$	$(3.52 \pm 0.44) \cdot 10^{2}$	$(2.8 \pm 1.0) \cdot 10^{-3}$	$(5.90 \pm 0.93) \cdot 10^{-3}$	$(1.39 \pm 0.22) \cdot 10^{-2}$	8.0
125.59	199.05	$(1.73 \pm 0.25) \cdot 10^{3}$	$(2.9 \pm 1.1) \cdot 10^{2}$	$(1.04 \pm 0.98) \cdot 10^{-3}$	$(5.2 \pm 2.1) \cdot 10^{-3}$	$(1.22 \pm 0.50) \cdot 10^{-2}$	5.83
199.05	315.48	$(1.1655 \pm 0.0036) \cdot 10^{3}$	$(1.30 \pm 0.32) \cdot 10^{2}$	$(9.974 \pm 0.019) \cdot 10^{-1}$	$(5.9 \pm 1.8) \cdot 10^{-3}$	$(1.39 \pm 0.43) \cdot 10^{-2}$	1.34
315.48	500.00	$(7.9 \pm 7.1) \cdot 10^{2}$	$(2.7 \pm 1.9) \cdot 10^{1}$	$(4.0 \pm 7.6) \cdot 10^{-3}$	$(9.7 \pm 7.8) \cdot 10^{-3}$	$(2.3 \pm 1.8) \cdot 10^{-2}$	1.2
500.00	792.45	$(4.985 \pm 0.025) \cdot 10^{2}$	$(0.5 \pm 1.4) \cdot 10^{1}$	1.000 ± 0.035	$(1.0 \pm 3.5) \cdot 10^{-2}$	$(2.5 \pm 8.3) \cdot 10^{-2}$	-0.62
				P2			
50.00	79.24		$(2.84 \pm 0.31) \cdot 10^{2}$	$(3.966 \pm 0.013) \cdot 10^{-1}$	$(1.08 \pm 0.14) \cdot 10^{-2}$	$(2.54 \pm 0.33) \cdot 10^{-2}$	7.8
79.24	125.59		$(3.95 \pm 0.25) \cdot 10^{2}$	$(3.971 \pm 0.011) \cdot 10^{-1}$	$(1.51 \pm 0.11) \cdot 10^{-2}$	$(3.56 \pm 0.27) \cdot 10^{-2}$	11.71
125.59	199.05		$(2.75 \pm 0.22) \cdot 10^{2}$	$(3.9919 \pm 0.0098) \cdot 10^{-1}$	$(1.09 \pm 0.10) \cdot 10^{-2}$	$(2.57 \pm 0.24) \cdot 10^{-2}$	8.06
199.05	315.48		$(1.50 \pm 0.25) \cdot 10^{2}$	$(4.040 \pm 0.016) \cdot 10^{-1}$	$(6.3 \pm 1.2) \cdot 10^{-3}$	$(1.49 \pm 0.28) \cdot 10^{-2}$	4.51
315.48	500.00		$(7.8 \pm 1.7) \cdot 10^{1}$	$(4.022 \pm 0.029) \cdot 10^{-1}$	$(1.15 \pm 0.30) \cdot 10^{-2}$	$(2.71 \pm 0.71) \cdot 10^{-2}$	3.76
500.00	792.45		$(0.8 \pm 1.3) \cdot 10^{2}$	$(4.04 \pm 0.13) \cdot 10^{-1}$	$(3.7 \pm 6.7) \cdot 10^{-3}$	$(0.9 \pm 1.6) \cdot 10^{-2}$	3.13
				BE			
50.00	79.24		$(4.03 \pm 0.99) \cdot 10^{1}$	$(2.58 \pm 0.38) \cdot 10^{-1}$	$(1.41 \pm 0.51) \cdot 10^{-1}$	$(3.3 \pm 1.2) \cdot 10^{-1}$	4.1
79.24	125.59		$(5.4 \pm 1.1) \cdot 10^{1}$	$(1.19 \pm 0.23) \cdot 10^{-1}$	$(1.00 \pm 0.26) \cdot 10^{-1}$	$(2.35 \pm 0.61) \cdot 10^{-1}$	4.47
125.59	199.05		$(0.0 \pm 2.0) \cdot 10^{2}$	$(2.99 \pm 0.01) \cdot 10^{-1}$	$(4.99 \pm 0.01) \cdot 10^{-1}$	1.176 ± 0.002	0.62
199.05	315.48		$(2.70 \pm 0.74) \cdot 10^{1}$	$(3.00 \pm 0.32) \cdot 10^{-1}$	$(1.00 \pm 0.36) \cdot 10^{-1}$	$(2.35 \pm 0.84) \cdot 10^{-1}$	3.64
315.48	500.00		$(0.2 \pm 6.8) \cdot 10^{2}$	$(1.0 \pm 1.3) \cdot 10^{-1}$	0.3 ± 5.1	$(0.1 \pm 1.2) \cdot 10^{1}$	1.18
500.00	792.45		7.8 ± 4.7	$(2.98 \pm 0.75) \cdot 10^{-1}$	$(1.14 \pm 0.88) \cdot 10^{-1}$	$(2.7 \pm 2.1) \cdot 10^{-1}$	2.04

The P1/P2 ratio is calculated both based on the counts in the pre-defined phase regions and based on the amplitudes of the fits in the reconstructed energy bins up to ∼800 GeV. The results are presented in Figure 6.14. Both methods deliver a declining P1/P2 ratio with increasing energy whereas the ratio is systematically higher in the fit-based P1/P2 ratio. The declining P1/P2 ratio with increasing energy is compatible with previous MAGIC and *Fermi*-LAT results, e.g. as presented in [1, 55]. Further, it is compatible with the Sum-Trigger-II findings from the last section. As already discussed in Section 6.2, the difference in the P1/P2 ratio based on the different methods is most likely caused by uncertainties in the amplitude fit. In some energy bins, it can be seen by eye that the fitted amplitude over- or underestimates the amplitude of the phasogram peak, whereas P1 is mostly overestimated. Hence, also the P1/P2 ratio is overestimated by this method.

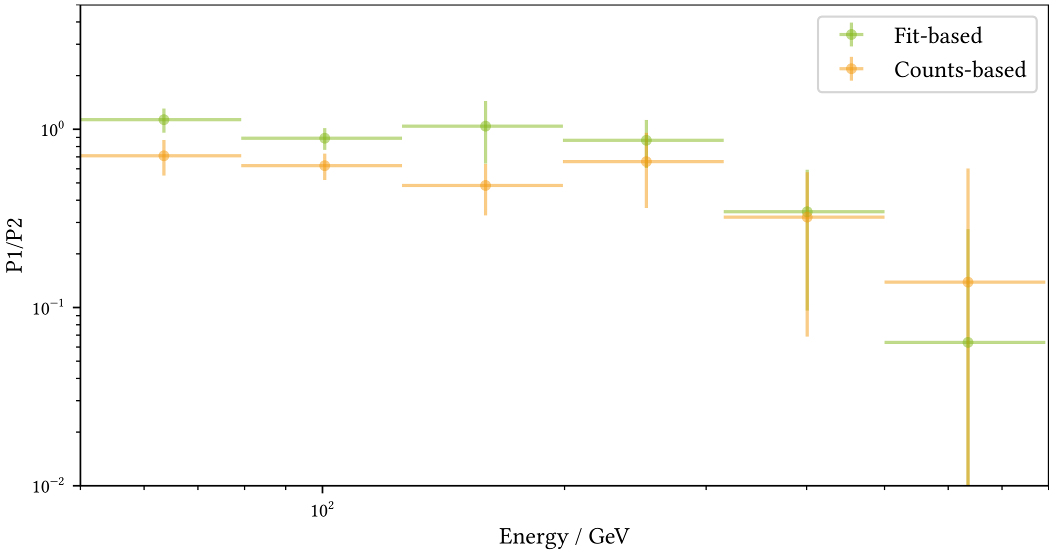

Figure 6.14: Crab Pulsar P1/P2 ratio in dependence of the energy for the Standard Trigger analysis.

Spectra

The phase-resolved spectra for P1, P2, and BE_n are calculated with `Gammapy`. For the other phase regions, the computations are not reasonable due to the lower statistics in the low-energy regime. Again, the spectral bins are chosen as the reconstructed energy bins. For P1 and P2, the calculations are performed in the energy range from 50 GeV to 1990 GeV while for BE, the calculations are done in the energy range from 50 GeV to 500 GeV. Please note that the reference spectra for P1 and P2 are taken from [30] here as this reference is based on Standard Trigger data and relies on a larger energy range than the Sum-Trigger-II reference.

The results are shown in Figure 6.15. A list of the flux point values can be found in Appendix D. In general, the spectra agree with the reference spectra within their uncertainties. Both the P1 and P2 spectra are steeper than the reference spectrum and the spectral index is more similar to the one obtained in the Sum-Trigger-II analysis. The computed flux however lies around the reference curve, while the low-energy flux points lie above and the high-energy flux point lie below the reference curve. The bridge spectrum is underestimated in all energy bins. This is most likely due to the low bridge excess in this dataset that is also seen in the phasogram in Figure 6.11.

The spectra suggest pulsed emission up to ~300 GeV for P1, up to ~125 GeV for BE_n and up to ~800 GeV for P2. In the P1 and P2 spectra, flux points beyond the first upper limit are observed but they are interpreted as statistical fluctuation.

In this analysis, the TeV pulsed emission discovered in [30] cannot be observed. The most probable reason for the different results is the data selection. In the analysis presented in this work, the data selection is optimized for low-energy events, enabling the possibility to calculate flux points starting at 50 GeV. It shows pulsed emission for P2 from 50 GeV to ~800 GeV. The analysis presented in [30], in contrast, focuses more on the high-energy regime and shows pulsed emission for P2 from ~70 GeV to ~1.5 TeV. Further, the energy bins are not the same in both analyses which can affect the excess signal. In this analysis, for example, the pulse observed in the energy range between ~1.25 TeV and ~2 TeV is interpreted as statistical fluctuation, whereas with a different binning, it might contribute to the energy bin up to ~1.5 TeV.

Further, the hadronness and θ^2 cuts are optimized differently. In this analysis, the standard energy-dependent optimization of the hadronness and θ^2 cuts is applied. In the analysis presented in [30] however, a special optimization algorithm dedicated to excess signal (the pulses) in front of a bright source (the Crab Nebula) is applied, which might deliver a better signal-to-background ratio. This algorithm is however not yet implemented in the `DL3 Converter` and can hence not be tested for the dataset used in this analysis. For future analyses, it could be beneficial to compare both optimization algorithms and to investigate their impact on the results.

Another reason for the differences could lie not in the analysis, but in the emission mechanism of the Crab Pulsar itself: The phase-resolved SEDs of the Crab Pulsar are generally assumed constant, which might not correspond to their true nature. The pulsed signal could be variable, e.g. due to morphological changes in the pulsar magnetosphere. In the X-ray regime, the inner Crab Nebula is found to be a highly dynamic region showing time-dependent arcs with increased emission [51]. These arcs might lead to differences in the optical depth that might affect how the gamma photons can escape this environment. In case of an energy-dependent optical depth, this could even influence the spectral index of the resulting spectrum. This behavior could be investigated by calculating the integrated flux in each energy bin in dependence of the time.

Table 6.13: Phase-range-wise spectral fits for the Standard Trigger analysis. Please note that the listed values are fit results before re-weighting the spectrum for the phase interval width.

Name	Start	Stop	E_0/GeV	$F_0/\mathrm{TeV}^{-1}\,\mathrm{cm}^{-2}\,\mathrm{s}^{-1}$	Γ	E_d/GeV
P1	0.983	0.026	150.0	$(1.17 \pm 0.17) \cdot 10^{-11}$	3.45 ± 0.20	86.56
BE	0.140	0.250	100.0	$(1.3 \pm 1.1) \cdot 10^{-11}$	4.6 ± 1.1	52.66
P2	0.377	0.422	150.0	$(2.11 \pm 0.16) \cdot 10^{-11}$	3.26 ± 0.11	98.69

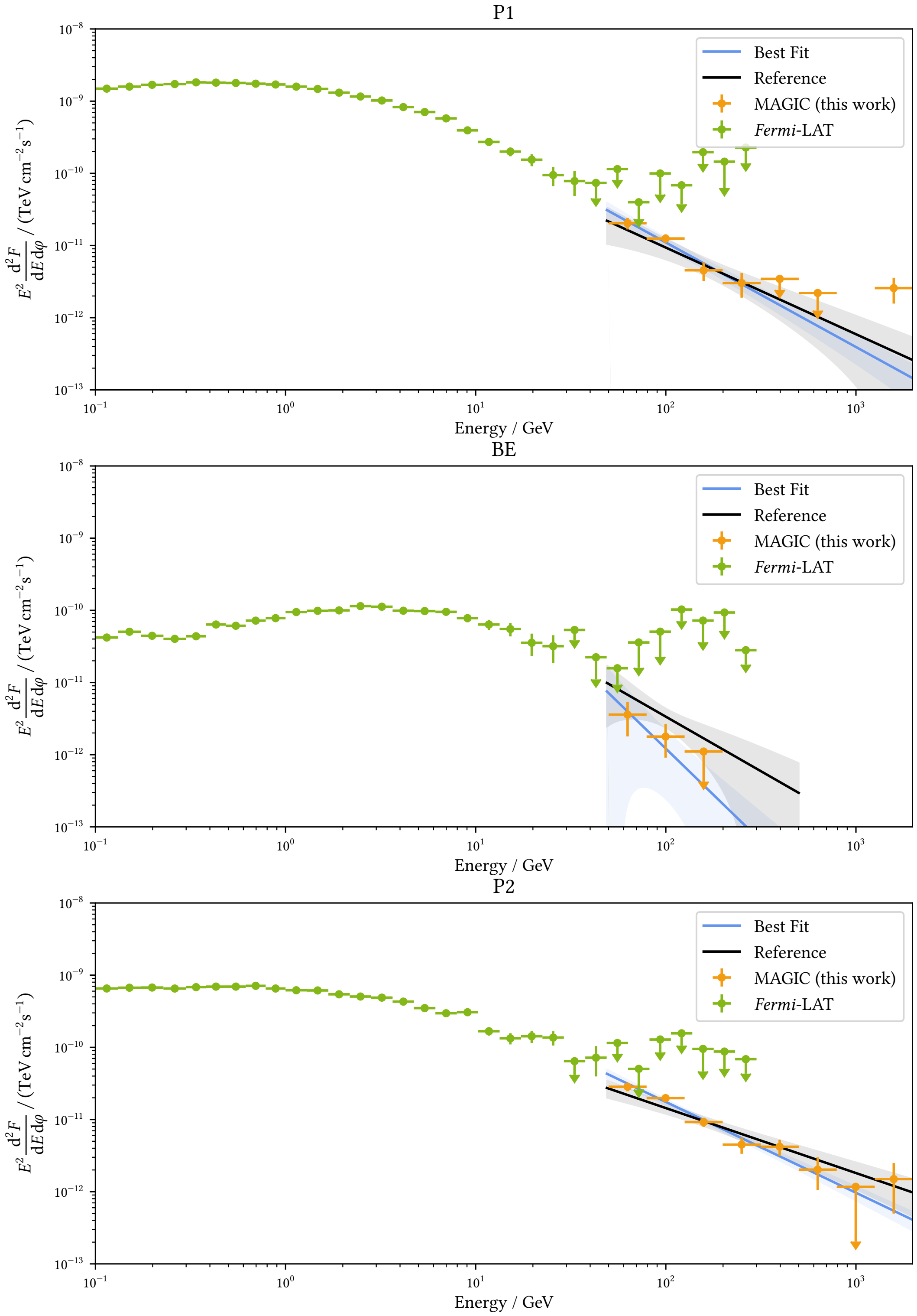

Figure 6.15: Phase-resolved Crab Pulsar spectra for P1, P2, and BE_n in the Standard Trigger analysis. P1 and P2 references taken from [30] and bridge reference taken from [23].

6.3.2 Zenith Distance 62° to 80°

Recent studies of the Vela Pulsar have shown that pulsed emission up to tens of TeV is possible [70]. In order to investigate the pulsed emission above few TeV, a pulsar analysis based on VHZ data is done. For VHZ data, the sensitivity of the MAGIC telescopes is boosted above ∼10 TeV so that better insights into pulsed emission in this energy region could be gained (if it exists). The new implementations in `autoMAGIC` and especially the newly implemented possibility to use the high-energy MC extension enable the possibility to gain long-term VHZ results with comparably little effort. The pulsar-analysis-related results are shown in the following. The corresponding Crab Nebula validation analysis is presented in Appendix E.2.2.

Data Selection and Data Processing

For the analysis, all available VHZ dark data accessible for `autoMAGIC` i.e. the ST.03.06 and later MC periods are processed with `autoMAGIC`. The same periods as described in Section 6.3.1 are excluded. Further, the observations with moon filter are excluded explicitly. The cuts listed in table Table 6.14 are applied, whereas the cuts for the Off data are chosen less strict since in general, MAGIC takes only little data in this zenith range and especially the availability of Off data is worse than in the lower zd regime. The same strict weather cuts as in the previous chapter are chosen. A total of 93.15 hours of data survive the cuts.

The hadronness and θ^2 cut are calculated in each reconstructed energy bin for a MC efficiency of 95 %. The phase information is added to the `DL3` files using `magicpulsar`. The data from the 29th of March 2017 has to be excluded from the analysis due to a pulsar glitch. For this night, no pulsar model is available so that the phase information cannot be calculated.

Table 6.14: Cuts used for the data selection in the VHZ analysis.

Parameter Name	Cut Value
start date	2014-11-24
stop date	2024-03-31
transmission (On data)	0.9
transmission (Off data)	0.6
maximum cloudiness (On data)	10
maximum cloudiness (Off data)	30
minimum zd	62°
maximum zd	80°
minimum duration	300 s
minimum DC	0 nA
maximum DC	2200 nA
MOLA threshold (Off data)	3 σ

Phasogram

A phasogram with the energy-dependent hadronness and θ^2 cuts above 50 GeV is produced, as shown in Figure 6.16. The Li&Ma significances are listed in Table 6.15. It can be seen that no pulsed emission can be found for P1, P2, and the bridge. The significances are all below 0, showing no excess signal is found in the corresponding phase ranges. Also the Z_n^2 and H tests do not find pulsed signal: The significances are $S_Z = 0.66$ and $S_H = -0.27$ while the p-values are $p_Z = 0.26\,\sigma$ and $p_H = 0.61\,\sigma$, showing that this phasogram is well described by the Null Hypothesis of a uniform distribution.

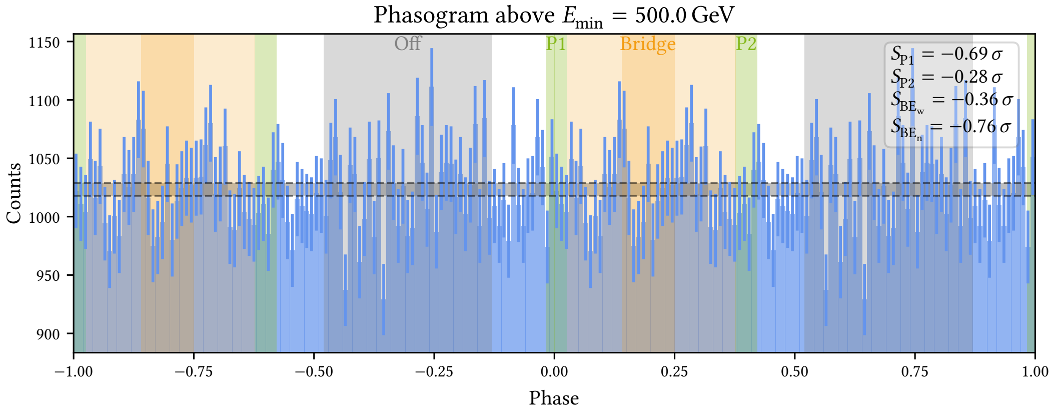

Figure 6.16: Phasogram of the Crab Pulsar above 500 GeV based on the VHZ Standard Trigger data.

Table 6.15: Li&Ma significances for the VHZ data above 500 GeV. The number of Off counts is $N_{\text{Off}} = 35817$.

Name	α	N	S_{LiMa}/σ
P1	0.123	4352	-0.69
P2	0.129	4585	-0.28
BE_w	1.003	35823	-0.36
BE_n	0.314	11165	-0.76

The calculation of spectra for P1, P2, and the bridge is not possible as there are not enough excess counts in all of the phase ranges. The upper limit values are either not calculable or deliver negative results, which corresponds to a statistical but unphysical solution. These findings are in agreement with the negative Li&Ma significances for those phase regions.

6.4 Comparison of the Sum-Trigger-II and Standard Trigger Results

Depending on the trigger the data was acquired with, the results show differences that are addressed in this chapter. Therefore, a comparison of the phasogram above 50 GeV is done and the phase-resolved spectra for P1, P2, and $\mathrm{BE_n}$ are compared.

The phasogram above 50 GeV is shown in Figure 6.17. Please note that the energy range between 20 GeV and 50 GeV that is accessible only with the Sum-Trigger-II is not exploited here for comparability. Further, please note that ~120 h of Sum-Trigger-II data are compared to ~360 h of Standard Trigger data. Although three times as much standard data is used, the total number of events is only higher by approximately 40 %. Further, it is striking that, even though fewer Sum-Trigger-II events are evaluated, the Li&Ma significances for the pulsed signal are higher for P2 and the bridge. The reason for this lies in the higher low-energy sensitivity of the Sum-Trigger-II. While the Sum-Trigger-II triggers more low-energy events that contain pulsed emission, the Standard Trigger records more higher energetic events beyond the energy regime in which strong pulsed emission can be measured.

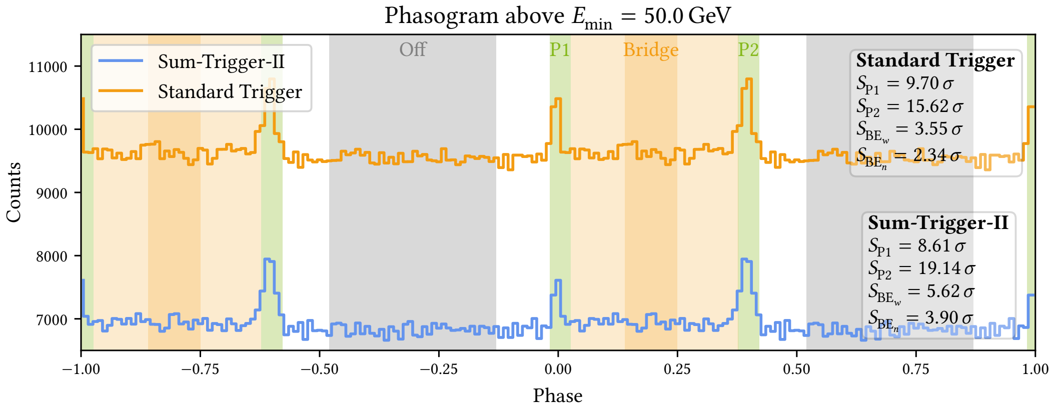

Figure 6.17: Comparison of the Crab Pulsar phasograms in the Sum-Trigger-II and Standard Trigger analyses above 50 GeV.

A comparison of the counts-based P1/P2 ratios can be found in Figure 6.18. As the fit-based P1/P2 ratio is found to be less reliable in the previous sections, these results are not compared here. While in the two lowest energy bins, results can only be obtained with the Sum-Trigger-II data, the results in the two highest energy bins can only be obtained with the Standard Trigger data. In the energy range both analyses deliver P1/P2 ratios in, the results are mostly in agreement within their uncertainties whereas the Sum-Trigger-II P1/P2 ratio is slightly lower than the Standard Trigger P1/P2 ratio.

The phase-resolved spectra for both triggers for P1, P2, and $\mathrm{BE_n}$ as well as the Standard Trigger and Sum-Trigger-II reference curves are shown in Figure 6.19. It is striking that the Standard Trigger fluxes are systematically lower than the Sum-Trigger-II fluxes. This difference is especially large for the bridge emission but also reaches a factor of around 2 for

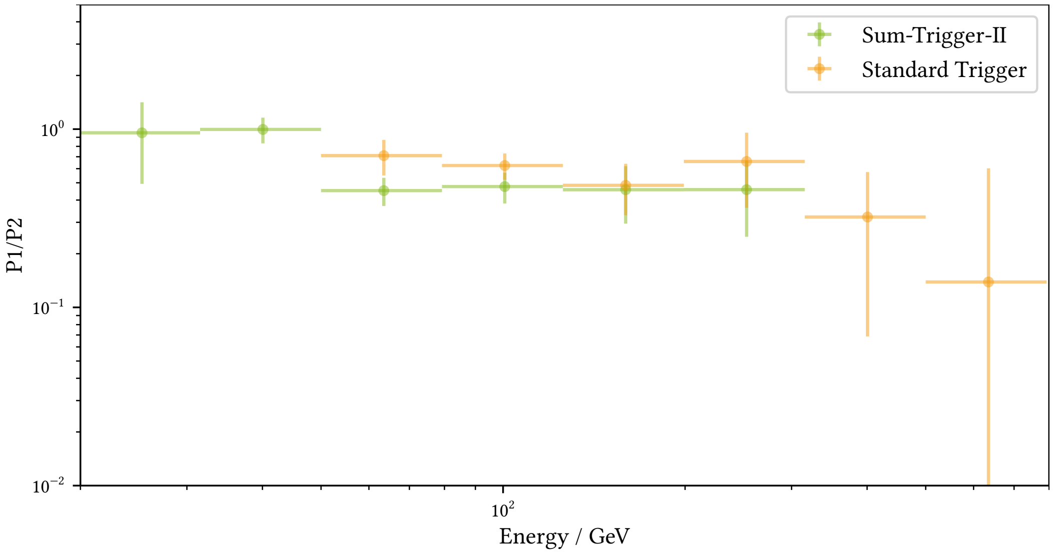

Figure 6.18: Comparison of the energy-dependent P1/P2 ratio in the Sum-Trigger-II and Standard Trigger analyses.

P2. The lower flux for the Standard Trigger data is also visible in the reference spectra. For energies below 100 GeV, the P2 reference curves deviate by more than a factor of two, which is mostly due to the different spectral indices of 2.9 ± 0.2 for the Standard Trigger reference and 3.18 ± 0.11 for the Sum-Trigger-II reference. The analyses suggest spectral indices of 3.26 ± 0.11 in the Standard Trigger analysis and 3.12 ± 0.07 in the Sum-Trigger-II analysis which are both compatible with the Sum-Trigger-II reference value but deviate from the Standard Trigger reference. At this point, please keep in mind that the systematic effects are not yet considered in the uncertainties of the reference spectra and might be different for the two trigger systems.

The differences in the flux values for the two triggers hint at a systematic in the telescope response that does not correctly reflect the trigger system. This difference is also seen in the Crab Nebula checks presented in Appendix E. While the spectrum for the Crab Nebula has the tendency to be underestimated by the Standard Trigger analysis (see Figure E.4), it has the tendency to be overestimated in the Sum-Trigger-II analysis in the energy range below ~1 TeV (see Figure E.1). This systematic in the telescope response could be induced by the Sum-Trigger-II MC data. As described in Section 6.2, this analysis is the first large analysis with the standard (i. e. not tailored to a specific source) Sum-Trigger-II MC data and hence, the telescope characterization might be imprecise. Another reason could be the lack of statistics in the Standard Trigger MC data below ~200 GeV. Since no low-energy MC extension was used, the amount of simulated low-energy events might be too low which might bias the analysis. This reason could however only explain a deviation up to 200 GeV as this is the maximum energy of the additional events added in the low-energy extension and the deviations in the data are still visible beyond 200 GeV.

Another potential reason could be the different observation dates of the data used in both analyses. As discussed before, the Crab Pulsar could emit a variable flux and hence deliver different results for data taken in different periods of time. This behavior could be studied by calculating the integrated flux in each energy bin in dependency of the time. This could however prove to be difficult in the VHE regime due to insufficient statistics. Further, this approach is considered less likely than a systematic effect in the analysis, as the tendency of an underestimation of the flux in the Standard Trigger analysis and an overestimation of the flux in the Sum-Trigger-II analysis can also be seen in the Crab Nebula flux which is known to be stable in the VHE gamma regime [9, 21, 27]. It has to be highlighted, however, that the difference in the phase-resolved SEDs is not only seen in this work, but is also shown by the reference spectra from previous MAGIC analyses. An in-depth investigation of the origin of these differences should be performed in the future.

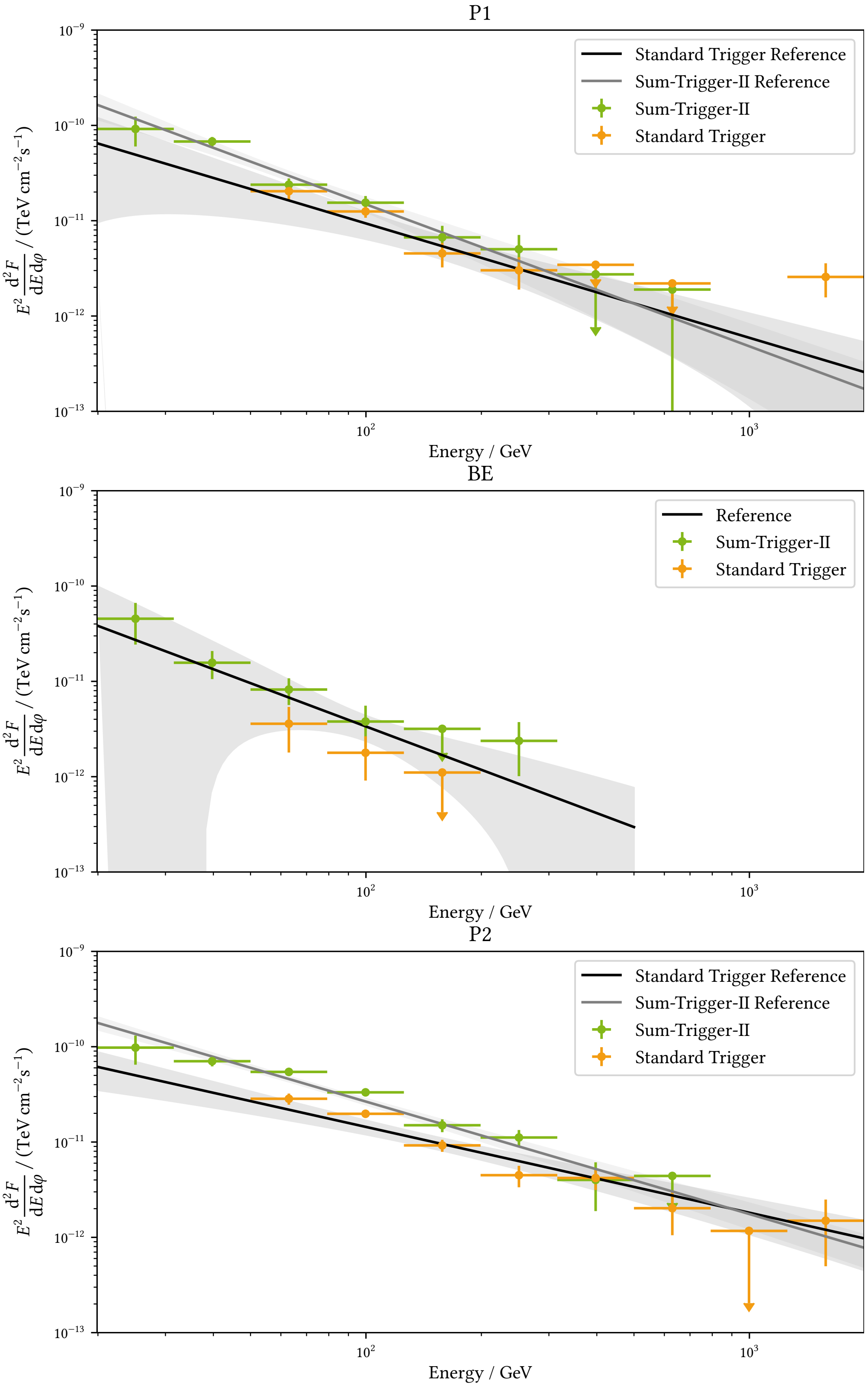

Figure 6.19: Comparison of the Sum-Trigger-II and Standard Trigger spectra for P1, P2, and $\mathrm{BE_n}$.

6.5 Joint Analysis

Although in the last section it was shown that the analyses have a deviating performance, a joint phasogram and joint spectra for P1, P2, and the bridge are computed to exploit the improved statistics of the joint dataset. For this, the Standard Trigger data in the zd range from 5° to 62° and the entire Sum-Trigger-II dataset are joined after the cuts are applied. As no pulsed signal is observed in the VHZ dataset and hence it would only add additional noise, this dataset is not used in the joint analysis.

The joint phasogram is shown in Figure 6.20. The Li&Ma significances reach values of $S_{\mathrm{P1}} = 15.47\,\sigma$ for P1 and $S_{\mathrm{P2}} = 24.30\,\sigma$ for P2, corresponding to the most significant detection of the Crab Pulsar peaks by an IACT to date. The joint P1+P2 significance amounts to $S_{\mathrm{P1+P2}} = 26.73\,\sigma$. The significances for the bridge are $S_{\mathrm{BE_w}} = 8.85\,\sigma$ and $S_{\mathrm{BE_n}} = 5.73\,\sigma$ which is only slightly higher than in the Sum-Trigger-II analysis. This is in agreement with the little excess for the bridge in the Standard Trigger dataset. The Z_n^2 and H-test show strong period signal of $S_Z = 26.32\,\sigma$ and $S_H = 27.07\,\sigma$.

Joint phase-resolved spectra for P1, P2, and $\mathrm{BE_n}$ are presented in Figure 6.21. The corresponding flux point values are listed in Appendix D and the joint best fit parameters can be found in Table 6.16. For P1 and P2, both the Sum-Trigger-II reference and the Standard Trigger reference curve are shown. It can be seen that the joint spectra of P1 and P2 are closer to the Sum-Trigger-II reference curve than to the Standard Trigger reference curve. Despite the increased amount of statistics, the SEDs for P1 and P2 cannot be extended to higher energies than in the Standard Trigger analysis. Still, for P2, a spectrum spanning almost two decades in energy is achieved. In the two highest energy bins above ~800 GeV, only upper limits can be calculated, underlining the interpretation of the highest energy flux point in the Standard Trigger analysis as statistical fluctuation. The highest energy flux point in P1 shows larger uncertainty in this SED than in the one computed only from Standard Trigger data, which also underlines its interpretation as statistical fluctuation. The bridge spectrum in this analysis is significantly steeper than the reference spectrum but still compatible within the uncertainties.

Table 6.16: Phase-range-wise spectral fits for the joint Sum-Trigger-II and Standard Trigger analysis. Please note that the listed values are fit results before re-weighting the spectrum for the phase interval width.

Name	Start	Stop	E_0/GeV	$F_0/\mathrm{TeV^{-1}\,cm^{-2}\,s^{-1}}$	Γ	E_d/GeV
P1	0.983	0.026	59.86	$(3.24 \pm 0.20) \cdot 10^{-10}$	3.60 ± 0.11	59.65
BE	0.140	0.250	100.0	$(2.3 \pm 0.7) \cdot 10^{-11}$	4.09 ± 0.32	42.20
P2	0.377	0.422	70.33	$(3.10 \pm 0.12) \cdot 10^{-10}$	3.29 ± 0.06	76.81

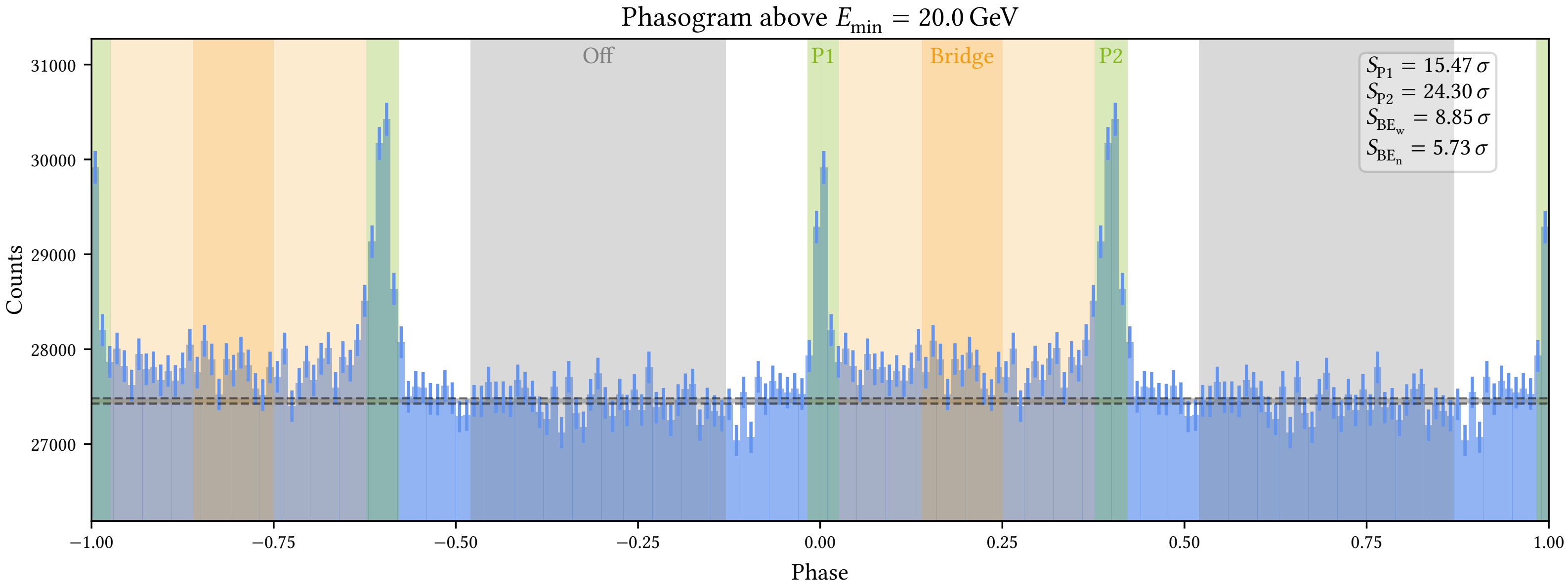

Figure 6.20: Phasogram of the Crab Pulsar in the Sum-Trigger-II and Standard Trigger joint analysis above 20 GeV.

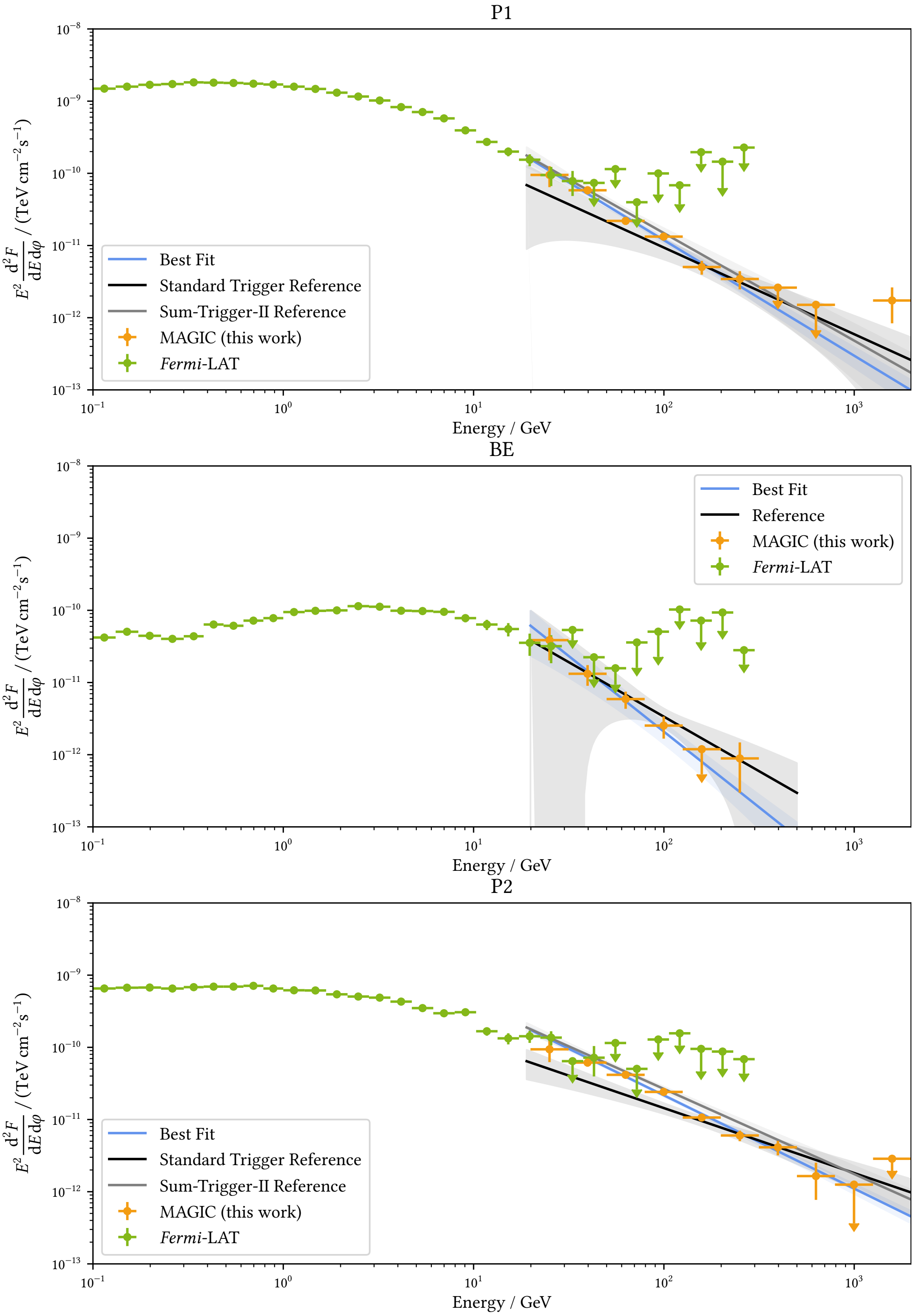

Figure 6.21: Phase-resolved Crab Pulsar spectra for P1, P2, and BE$_n$ in the joint Sum-Trigger-II and Standard Trigger analysis.

7

Dragonfly Pulsar Analysis

> All It Takes Is A Little Push.
>
> ---
>
> The Joker
> The Dark Knight

In this chapter, a low-energy analysis of the MAGIC Sum-Trigger-II Dragonfly data is presented. A pulsar analysis of this exact same data is already presented in [161] but in that analysis, the low-energy regime is not fully exploited as a standard analysis with the sum cleaning and the standard MC simulations is applied to the Sum-Trigger-II data. Consequently, the analysis cannot take advantage of the low-energy threshold that the Sum-Trigger-II provides. The energy threshold of the standard analysis lies between 50 GeV and 100 GeV.[1] In this analysis however, the MaTaJu cleaning algorithm and dedicated Sum-Trigger-II MC simulations are used to exploit the lowest possible energies. Since the pulsation of Dragonfly is expected to be in the lowest energy band that MAGIC can measure, it is reasonable to redo the analysis with the described improvements to reach down to energies as low as 20 GeV. In the following, firstly, the data selection and processing is described and afterward, the phasogram is presented. The Crab Nebula validation for this analysis can be found in Appendix E.3.

7.1 Data Selection and Data Processing

For the Dragonfly analysis, Sum-Trigger-II data recorded between July 5th and November 22nd 2014 is used. This data is in the MC periods ST.03.03 and ST.03.05. For this analysis, the ST.03.03 and ST.03.05 Sum-Trigger MC simulations and the corresponding low-energy extension were produced by me. The same quality cuts as used in the Sum-Trigger-II Crab Pulsar analysis described in Section 6.2 are used here. A list of the cuts can be found in Table 7.1.

As the MaTaJu cleaning is applied in the analysis, a start on raw data is necessary. This poses some difficulties to the analysis: MAGIC stores raw data for five years in a way so that it can still be accessed without huge effort.[2] The Dragonfly data is much older than

---

[1] The cuts that are applied in the standard analysis are quite conservative. Since the exact cuts that were used are not listed in [161], the energy threshold of this analysis cannot be estimated in detail. In any case, the energy threshold of a standard analysis is much higher than the energy threshold in a MaTaJu analysis.

[2] After five years, the tapes on which the data is stored are removed from the tape robot and hence it would require much human effort to find the right tapes and store the data on the server again.

this and hence not available on the PIC server anymore but could be retrieved from a local copy. For some nights however, severe problems occurred for the data processing. All the data taken in November (two nights in total) are incomplete and for almost all runs, data from one telescope is missing. Hence, the data has to be excluded from the analysis since a stereo reconstruction would only be possible for few subruns and it is doubtful that single patchy subruns still contain reliable physics information. Further, for the data on the 5th, 6th, and 8th of June 2014, the subsystem reports are corrupted so that `merpp` fails to join the calibrated output files and the subsystem reports. Hence, also this data cannot be processed to higher data levels.

Table 7.1: Cuts used for the data selection in the Dragonfly analysis.

Parameter Name	Cut Value
start date	2014-07-05
stop date	2014-08-05
transmission (On data)	0.9
transmission (Off data)	0.8
maximum cloudiness (On data)	10
maximum cloudiness (Off data)	20
minimum zd	0°
maximum zd	35°
minimum DC	0 nA
maximum DC	2200 nA
MOLA threshold (Off data)	$3\,\sigma$

The remaining 94 runs, summing up to a total observation time of 27.3 h are processed with `autoMAGIC`. A list of all the successfully processed runs can be found in Appendix F.3. The Off data selection for this dataset poses some problems due to the limited raw data availability. There is no raw Sum-Trigger-II Off data available neither in the PIC nor on local servers of collaboration members that could be used. Hence, the only possible solution is to take the Off data from a MC period with parameters as similar as possible. For this analysis, Off data from the ST.03.11 period is taken since in this period, enough Sum-Trigger-II Off data is available and the values of the `mirror fraction` deviate by less than 10 % from the ones of the ST.03.03 period.[3] The values for the axis deviation differ more which does not affect this particular analysis largely since for the low-energy analysis, very loose cuts are chosen for the directional information.

---

[3] The values for the `mirror fraction` range from 0.48 to 0.68 for M1 and from 0.54 to 0.72 for M2. The `axis deviation` ranges from 3 to 8 for M1 and from 0 to 6 for M2. The values for ST.03.03 and ST.03.11 are the closest match for periods in which Sum-Trigger-II Off data is available: The M1 `mirror fractions` are 0.60 for ST.03.03 and 0.655 for ST.03.11 while the M2 `mirror fractions` are 0.66 for ST.03.03 and 0.72 for ST.03.11. The `axis deviations` for M1 are 3.0 for ST.03.03 and 3.5 for ST.03.11, and for M2 1.0 in ST.03.03 and 5.0 in ST.03.11. Even though the periods show a deviating telescope performance, the Off data from ST.03.11 is used as this is the only easy approach in the absence of Sum-Trigger-II Off data in ST.03.03.

The data is processed to `DL3` with MARS version 3.1.0, `DL3 Converter` version 0.1.15, and `autoMAGIC` version 0.8 using the configuration file shown in Appendix G.3. For the hadronness and θ^2, MC efficiency cuts of 0.9 and 0.75, respectively, are chosen. Afterward, the pulsar timing is done with `magicpulsar`, using ephemerides provided by *Fermi* [109, 160], which are further described in Appendix B.

7.2 Phasogram

Based on the phased `DL3` files, the phasogram shown in Figure 7.1 is produced with `Gammapy` version 1.2 using energy-dependent hadronness and θ^2 cuts. The region definitions are taken from [4] and listed in Table 7.2. The Li&Ma significances are calculated based on the counts in the phase regions and are also shown in Table 7.2.

The phasogram is produced in the energy range from 20 GeV to 1 TeV[4] and shows no significant excess throughout the phase range. The Li&Ma significances are all below 0, indicating no detection of pulsed emission from P1, P2, and the bridge. The Z_n^2 and H-test deliver significances of $S_Z = -1.15\,\sigma$ and $S_H = -0.52\,\sigma$ and p-values of $p_Z = 0.87$ and $p_H = 0.70$, which also shows that no pulsed signal can be found in this dataset.

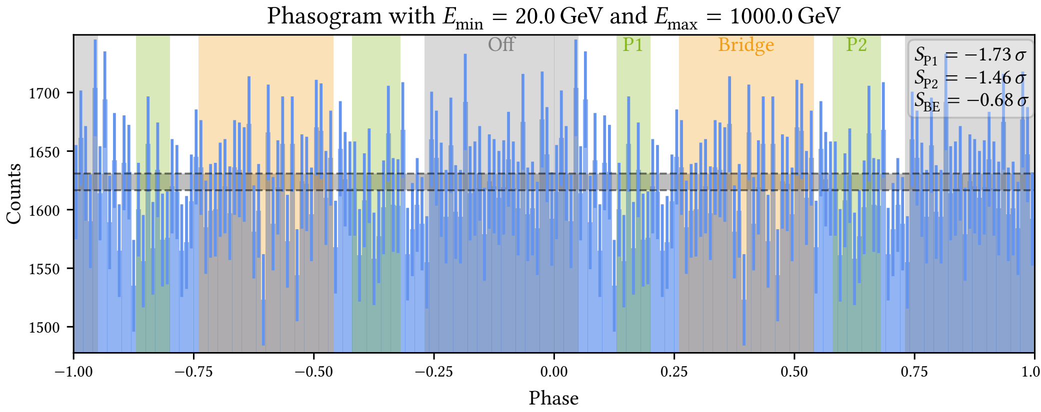

Figure 7.1: Phasogram of the Dragonfly Pulsar between 20 GeV and 1 TeV.

The calculation of the spectra for P1, P2, and the bridge only delivers negative upper limits. These values arise from negative excess signal and do not contain physics information. These results are in agreement with the negative significances shown before.

---

[4] The choice of the energy range is always a tradeoff between enough statistics and a narrow enough energy range to not obscure the pulsed emission in a certain energy bin with noise from other energy ranges. As the dataset for the Dragonfly analysis is comparably small, the energy range is chosen up to 1 TeV although only in the lowest energy regime pulsed emission is expected.

Table 7.2: Phase range definitions for the Dragonfly analysis and their significances in this analysis.

Name	Phase Range	α	N	S_{LiMa}/σ
P1	0.13 - 0.20	0.219	11163	-1.73
Bridge	0.26 - 0.54	0.875	45265	-0.68
P2	0.58 - 0.68	0.313	16025	-1.46
Off	0.73 - 0.05	-	51959	-

8

Conclusions

> Every great story deserves a great ending.
>
> Christopher Nolan

In this work, a long-term analysis of more than 500 h of MAGIC Crab Pulsar data taken with the Standard Trigger and the Sum-Trigger-II, spanning 12 years, is presented. This is the first `DL3` pulsar analysis of the MAGIC experiment, and it was completely automatized with the user-friendly and collaboration-wide available analysis pipeline developed in the scope of this thesis. Large parts of the efforts of this work were made to set up an analysis pipeline that can process massive datasets with little human interaction, allowing for the possibility to perform the most extensive MAGIC pulsar analysis to date. In addition, it allows for performing coherent long-term analyses with unified and reproducible settings, while utilizing the new standard data format `DL3`. The new high-level pipeline is independent of the previously used workflow for pulsar analyses in MAGIC and can serve as a means to cross-check the existing results.

As the main work of the thesis at hand, a total of 120 h of Sum-Trigger-II data are analyzed with the automatized pipeline, which corresponds to the most extensive MAGIC Sum-Trigger-II analysis of the Crab Pulsar to date. Strong pulsed emission with a significance of $S_{\mathrm{P1}} = 12.32\,\sigma$ for P1, $S_{\mathrm{P2}} = 19.13\,\sigma$ for P2, and $S_{\mathrm{BE}_w} = 8.38\,\sigma$ for the bridge is found. The joint P1+P2 significance amounts to $S_{\mathrm{P1+P2}} = 21.14\,\sigma$. Energy-dependent phasograms show a narrow P1 above ~50 GeV and a narrow P2 above ~80 GeV. A rough estimate for the diameter of the emission region of 150 km to 300 km can be derived from the peak width, which corresponds to 5% to 10% of the light cylinder diameter of the Crab Pulsar. With the results obtained in this thesis, the most common theoretical models of different pulsar emission mechanisms can be checked. The narrow peaks and hence the small emission region disfavors models explaining the pulsed emission by widely opened pulsar beams, such as the slot gap and outer gap model. Further, the polar gap model can be ruled out due to the high-energy gamma-ray emission in the order of magnitude of hundreds of GeV. The model agreeing best with the pulsed emission found in this work is the equatorial current sheet, which is also widely favored as model for the gamma-ray pulsar emission [144]. Phase-resolved spectra are calculated not only for P1, P2, and the bridge, but also for the leading and trailing components of all three features starting from energies of only 20 GeV. All the results are in good agreement with the *Fermi*-LAT results. Further, the peaks P1 and P2 can be detected up to few hundreds of GeV. The integrated, pulsar-phase-dependent flux is calculated, resulting in a similar distribution as seen in the phasogram with two clear peaks. The integrated flux delivers values of $\mathrm{d}F_{\mathrm{int,\ P1}}/\mathrm{d}\varphi = (3.44 \pm 0.27) \cdot 10^{-9}\,1/(\mathrm{cm}^2\,\mathrm{s})$ for P1 and $\mathrm{d}F_{\mathrm{int,\ P2}}/\mathrm{d}\varphi = (4.19 \pm 0.20) \cdot 10^{-9}\,1/(\mathrm{cm}^2\,\mathrm{s})$ for P2. Phase-resolved light curves for P1 and P2 show a stable flux for the pulsed emission over the observed nights.

In addition to the Sum-Trigger-II data, 360 h of good-quality Standard Trigger data are analyzed, leading to the most extensive Standard Trigger Crab Pulsar analysis to date. The Standard Trigger proves to be less sensitive to the low-energy signals of pulsars than the Sum-Trigger-II and delivers significances of $S_{\mathrm{P1}} = 9.74\,\sigma$ for P1, $S_{\mathrm{P2}} = 15.60\,\sigma$ for P2, and $S_{\mathrm{BE}_w} = 3.54\,\sigma$ for the bridge. Phase-resolved spectra are calculated for P1, P2, and the bridge. For P2, pulsed emission can be detected up to ~800 GeV, which is lower than the pulsed TeV emission that is presented in [30] based on a smaller dataset of Standard Trigger Crab data. Further, the spectral index for P2 is found to be steeper in this work, which is consistent with the cut-off at a lower energy. A reason for the discrepancy could be the different data selection, as the lower energy limit in this work is lower than in the publication. A physical cause could also be responsible for the discrepancy: The data were taken at different time periods, so source variability could explain this discrepancy. To test this assumption, both analyses would have to be repeated with an identical dataset. The analysis of more than 90 h of good-quality Standard Trigger VHZ data is performed to investigate the high-energy regime further. This analysis delivers no significant pulsed signal.

Differences between the energy spectra calculated with Sum-Trigger-II and Standard Trigger data are found and discussed. The Standard Trigger flux points are systematically lower than the Sum-Trigger-II analysis results, hinting at a systematic over or underestimation of the telescope performance in one of both analyses. This behavior is not only seen in the results of this thesis but also in the reference spectra, taken from previous MAGIC analyses. As the Standard Trigger simulations have been tested and improved over the years, but the Sum-Trigger-II simulations are relatively new and have not yet been adequately verified, it is reasonable to assume that the Sum-Trigger-II simulations should be checked more closely in the future. Again, a variability in the phase-resolved SEDs that might be induced by a change of the optical index in the inner Crab Nebula region, that is known to be highly dynamic from X-ray observations, cannot be ruled out. This could be investigated by testing whether the energy-bin-wise flux in dependence of the time is constant.

Despite the performance differences, a joint analysis of the Standard Trigger and Sum-Trigger-II data is performed to exploit all available information. It delivers significances of $S_{\mathrm{P1}} = 15.49\,\sigma$ for P1, $S_{\mathrm{P2}} = 24.28\,\sigma$ for P2, and $S_{\mathrm{BE}_\mathrm{w}} = 8.85\,\sigma$. The joint P1+P2 significance is $S_{\mathrm{P1+P2}} = 26.73\,\sigma$. These findings represent the most significant detection of pulsed signal from the Crab Pulsar by an IACT to date. Despite the increased statistics, the spectra are not detected up to higher energies in the joint analysis.

An analysis searching for pulsed emission in 27 h of Dragonfly Sum-Trigger-II data delivers no significant excess in the phase ranges in which the pulses are expected.

In the future, the pipeline developed in this work could be used for further analyses such as studies of Lorentz Invariance Violation (LIV) in pulsars (as e.g. presented in [16]) or a re-processing of the MAGIC Geminga Pulsar results [11] based on `DL3` data. Since the high level pipeline makes use of the standard format `DL3`, it could also be used for other experiments. Further, with the newly implemented MaTaJu analysis of Standard Trigger data and the automatized pulsar analysis pipeline, a search for archival MAGIC sources that have been identified as pulsars by *Fermi*-LAT could be performed, similar to the work done in [174] for VERITAS. New implementations for more advanced analyses such as the implementation of more complex data selection algorithms also taking into account the trigger rates could be implemented. Further, the source-background-optimized algorithm for the energy-dependent calculation of the hadronness and θ^2 could improve the performance of the pulsar analysis.

Generally, the future of pulsar research with IACTs will be shaped by the CTA, the new generation and by far biggest system of Cherenkov telescopes, which will observe the night sky with tens of telescopes in three different sizes at two sites. The Large Size Telescope (LST)-1 prototype has already proven its capabilities to detect low-energy pulsed emission of the Crab Pulsar [6]. The LST 2, 3, and 4 are currently under construction and about to begin observations soon. All four LSTs together will be more sensitive than the MAGIC telescopes, especially in the lower GeV range, and will launch a new era of ground-based gamma-ray pulsar astronomy.

A

Technical Details

A.1 Technical Details of `autoMAGIC`

The basic idea of `autoMAGIC` and a simplification of its workflow were already presented in Section 3.6. This chapter dives deeper into the technical structure of `autoMAGIC` and its workflow. The details of the general implementation were already described in [113, 155] and are repeated here for convenience only. Some of the described features and workflows however were implemented later and are firstly described here.

The core concept of `autoMAGIC` is the database, so understanding the database is crucial for understanding the idea behind `autoMAGIC`. All important analysis-related information is stored in multiple tables. In the `autoMAGIC` database there are currently about 80 tables which can be roughly divided into three categories:

- Job tables are used to keep track of the jobs that are processed by `autoMAGIC`. There is one dedicated job table for each MARS executable. They contain columns for each changing parameter in the analysis chain and ensure that each job in the database is unique.
- Data tables list the data based on which the analyses are performed, including observation parameters and paths to the files. On the one hand, this information is used as the pool of observations `autoMAGIC` can select observations from and on the other hand, it is used for selection data based on certain values of certain parameters.
- Logic tables are used to structure the database and to ensure not to store too much redundant information in the database.

All the data stored in the database tables can be linked by using relationships that can associate objects from one table to another in multiple ways. For example in the `autoMAGIC` database, the job table `jobs_star_superstar` lists the jobs for the MARS executables `star` and `superstar`. It has a relationship to the logic `states` table which specifies the different states a job can have in the workflow so that for each job individually, the database can keep track of whether this job has already been processed and if it was successful. Further, the `jobs_star_superstar` has a relationship to the data table `runs` which contains information of (amongst others) the observation parameters. Explaining the entire database structure would go way beyond the scope of this chapter. For more examples of the database structure I refer the interested reader to [113, 155].

The database lays the basis for the `autoMAGIC` workflow. Before `autoMAGIC` can be used, the database has to be filled with the data that is needed for the analysis. For this, scripts are set into place that can add the MAGIC data and also the MC data into the database.

For this, the user can choose between different data levels. The data can be filled based on calibrated files or based on `superstar` files, whereas the latter one is the currently preferred option.

Once the database is filled, the analysis can be performed based on a configuration file. The configuration file contains entries for the analysis target object and time range, as well as about the analysis parameters. Among the most important parameters are the quality cuts for the selection, which are set separately for the On and Off data. In the analysis configuration file, many more settings can be adjusted, such as the image cleaning algorithm, the view cone of the analysis and the hadronness and θ^2 cuts or their MC efficiencies. A full overview of all configuration file options would go beyond the scope of this chapter, so the interested reader is referred to the `autoMAGIC` Gitlab: `https://gitlab.pic.es/magic/automatic_analysis`.

Differently than described in [155], the job creation is now implemented as "bottom-to-top", meaning that for all possible runs, firstly the low-level jobs are created and, based on them, the higher-level jobs. This is a design decision that was taken for a more uniform workflow for analyses for dedicated sources and the massive data processing. The workflow is as follows: Firstly, the data suitable to the settings in the configuration file is searched in the database. Then, while iterating over all found runs, the jobs for the MARS wrappers are created. Before creating a new job, in each step it is checked if a job with the exact same settings is already existing in the database and in case it is, this job is returned instead of creating a new one.

As soon as the jobs are created, they can be submitted to the cluster. `autoMAGIC` automatically checks the jobs for their dependencies and firstly submits the low-level MARS jobs and waits with the submission of the higher analysis steps until the jobs for the lower steps are finished. For each job, a program wrapping the respective MARS executable is executed on a node of the PIC cluster. It handles the data transfer from the server to the working node, runs the MARS executable, handles the data transfer of the resulting files to the PIC file system and manages the communication with the database.

When the data processing has finished, a tarball of the resulting `DL3` files is created, containing not only the results but also meta information for the observation conditions of the runs, which can be useful for a data selection in `Gammapy`.

A.2 Technical Details of `magicpulsar`

`magicpulsar` is a pipeline that I developed as an alternative for `tempo2` for MAGIC. The basics are explained in Section 5.6. This chapter dives deeper into the internal processes of `magicpulsar` and explains the similarities and differences to `tempo2`. So far, MAGIC has only done pulsar analyses with the long-term standard program `tempo2`. In the last years however, the data format `DL3` has developed to become a standard format in gamma-ray astronomy which can be analyzed with open-source science tools such as `Gammapy`. This is an important step towards open science, which cannot be done with `tempo2` because it is not compatible with python and therefore cannot be included into the high level analysis pipeline. `PINT` represents a more modern alternative and is over huge parts a re-implementation of `tempo2` in python. One of the biggest differences of `tempo2` and `PINT` is the time system they use: While `tempo2` standardly computes the SSB arrival times in TCB, `PINT` does it in TDB per default. The resulting differences are however small compared to the timing accuracy reached by IACTs. `magicpulsar` is an important step for MAGIC towards pulsar analyses on a current standard data format and my analyses are the first MAGIC `DL3` pulsar analyses.

`magicpulsar` uses the MAGIC `DL3` files and an ephemerides file containing all the available ephemerides for the source as input. From the MAGIC `DL3` files, for each run, the TOAs are extracted and stored in a separate timing file that contains information about the TOA and its uncertainty, the telescope, and the observation frequency (this is mostly relevant for radio astronomy). It is in a specific `tempo2` format which is also the preferred format for inputs for `PINT`. The parameters and their values for an analysis of MAGIC data are:

- Filename/Identifier: magic
- Observing Frequency: 0.0
- Arrival Time (MJD): TOA of this specific event
- Uncertainty (µs): 0.0
- Telescope Code: magic

For the analysis of MAGIC data, only the TOAs are important. These have to be known with a very high accuracy which can cause problems when representing the numbers in computers.

From the ephemerides file, ephemeris files in the `tempo2` format (see also Appendix B) are extracted that are each only valid for one month. Afterward, the core-step of the pulsar timing is done with the python package `PINT`: For each timing file, `magicpulsar` searches the suiting ephemeris file that is valid on the observation date and hands both to `PINT`, which then calculates the pulsar phases for each event in the `DL3` file. `magicpulsar` then stores them in an additional column called `PHASE` in the `DL3` files.

Thereafter, `magicpulsar` produces some of the most commonly used plots for pulsar analyses, performing a `Gammapy` analysis and plotting the results. This is just for convenience of the user and rather thought to have a first look into the data instead of refining the analysis. Still, it represents an automatized pulsar analysis workflow that can reliably deliver reproducible results. `magicpulsar` is working completely automatically, once a configuration file has been filled by the user and given to `magicpulsar`. An example of a `magicpulsar` configuration and an explanation of its parameters can be found below.

```
[target]
source_name = "CrabNebula"                    # name of target source

[directories]
output_dir = "/path/to/your/output/directory" # path to output directory
fits_file_dir = "/path/to/your/DL3/Files"     # path to folder with the DL3 files
ephemeris = "/path/to/your/ehpemeris"         # path to all.gro ephemeris file

[cuts]
E_max = 200                      # Maximum energy for Pulsar analysis in GeV
E_min = 25                       # Minimum energy for Pulsar analysis in GeV
zenith_min = 5                   # Minimum zd for Pulsar analysis in degree
zenith_max = 50                  # Maximum zd for Pulsar analysis in degree
E_min_nebula = 50                # Minimum energy for Crab Nebula Check in GeV
E_max_nebula = 10000             # Maximum energy for Crab Nebula Check in GeV
E_min_nebula_lc = 300            # Minimum energy for LC in Crab Check in GeV
E_max_nebula_lc = 50000          # Maximum energy for LC in Crab Check in GeV

[phase_ranges]
num_on_phase_ranges = 2          # Number of pulses
on_phase_1 = [0.983,  0.026]     # Values for the first on phase range
on_phase_2 = [0.377, 0.422]      # Values for the second on phase range

num_off_phase_ranges = 1         # Number of Off phase ranges
off_phase_1= [0.52, 0.87]        # Values for the first Off phase range

[phasogram]
phasogram_bins = 100             # Number of bins for the phasogram

[spectrum]
n_bins_spectrum = 6              # Number of energy bins for spectrum calculations
ts_threshold_ul = 2              # TS threshold to define the use of an upper limit

e_true_min = 5                   # Minimum for Gammapy true energy axis in GeV
e_true_max = 50000               # Maximum for Gammapy true energy axis in GeV
e_true_n_bins = 25               # Number of bins for Gammapy true energy axis

e_reco_min = 5                   # Minimum for Gammapy rec. energy axis in GeV
e_reco_max = 50000               # Maximum for Gammapy rec. energy axis in GeV
e_reco_n_bins = 20               # Number of bins for Gammapy rec. energy axis

model_index_P1 = 3.49             # Model index for P1 power law
model_amplitude_P1 = 3.83e-10     # Model amplitude P1 power law in cm-2 s-1 TeV-1
model_reference_energy_P1 = 59.86 # Model reference energy for P1 power law in GeV

model_index_P2 = 3.18             # Model index for P2 power law
model_amplitude_P2 = 3.66e-10     # Model amplitude P2 power law in cm-2 s-1 TeV-1
model_reference_energy_P2 = 70.33 # Model reference energy for P2 power law in GeV
```

Only the first four inputs of this file are important for the pulsar timing itself. The rest of the parameters are for the `Gammapy` pulsar analysis that is done afterward automatically to give the user some quick results of the analysis.

`magicpulsar` is already used by other scientists in MAGIC for example for LIV studies based on the Crab Pulsar and for pulsar analyses of Boomerang.

B

Pulsar Ephemerides - A Detailed Overview

As described in Section 5.3, the pulsar ephemerides are crucial for the pulsar timing. This section gives some more technical information about the ephemerides that were used in this work. The parameters provided in a pulsar ephemeris are explained and a list of all the used ephemerides is given. Firstly, it should be noted, that the following explanations refer to ephemerides in the `tempo2` format, which is a long-time standard in pulsar astronomy. There are numerous parameters that can occur in `tempo2` ephemerides but here only the ones that were used in this analysis are going to be explained. A complete overview can be found in [94].

The pulsar ephemerides rely on other ephemerides such as planet ephemerides and time ephemerides. The planet ephemerides describe the positions of the planets in the solar system at different times. Further, a time ephemeris can be specified which accounts for the time shift from TDB to TCB. The time ephemeris however is only important for backward compatibility with `tempo`.

A full list of the pulsar ephemeris parameters that are relevant for this work are shown in Table B.1.

The Crab Pulsar ephemerides used in this work were taken from the Jodrell Bank observatory [117]. The values of the parameters that are not changing in the ephemerides of the Crab Pulsar are shown in Table B.2. The values that do change are listed in tables B.3 and B.4.

The Dragonfly ephemerides used in this work were taken from *Fermi* [109, 160]. For Dragonfly, only one ephemeris for the whole time range is provided. Its parameters are listed in Table B.5 and Table B.6.

Table B.1: Parameters used in a pulsar ephemeris and their explanation [94].

Parameter Name	Explanation
`PSRJ`	pulsar name
`RAJ`	right ascension of pulsar position
`DECJ`	declination of pulsar position
`F0`	pulsar frequency in Hertz
`F1`	first derivative of pulsar frequency/$\dot{f}$
`F2`	second derivative of pulsar frequency/ $\ddot{f}$
`TRES`	*RMS* timing residual
`PEPOCH`	time reference for the ephemeris
`POSEPOCH`	epoch of position measurement
`START`	starting time of validity in Modified Julian Date (MJD)
`FINISH`	ending time of validity in MJD
`TZRMJD`	reference TOA calculated as the first site-arrival-time
`TZRFRQ`	frequency of the arrival time corresponding to `TZRMJD`
`TZRSITE`	telescope site code corresponding to `TZRMJD`
`EPHEM`	name of solar system ephemeris to use
`CLK`	time system to use
`UNITS`	type of unit system to use
`PLANET_SHAPIRO`	account for Shapiro delay induced by planets
`CORRECT_TROPOSPHERE`	account for tropospheric delays
`T2CMETHOD`	method for transforming from terrestrial to celestial frame
`TIMEEPH`	time ephemeris to use
`MODE`	fitting with (`1`) or without (`0`) errors
`DILATEFREQ`	apply gravitational redshift and time dilation
`NE_SW`	electron density at 1AU due to solar wind
`NITS`	number of iterations for fit
`NTOA`	number of TOAs used in fitting
`CHI2R`	reduced χ^2-value calculated in fitting
`WAVEEPOCH`	reference time for wave solution
`WAVE_OM`	frequency of sinusoid for wave solution
`WAVE`N	amplitude of sine and cosine for the Nth harmonic for wave solution
`GLEP_`N	glitch epoch (i. e. time)
`GLPH_`N	glitch phase change
`GLF0_`N	glitch permanent pulse frequency change
`GLF1_`N	glitch permanent change of $\dot{f}$
`GLF0D_`N	glitch pulse frequency change
`GLTD_`N	glitch decay time
`DMEPOCH`	dispersion measure epoch (i. e. time)
`DM`	dispersion measure

Table B.2: Values for the fixed parameters in the Crab Pulsar ephemerides used in this work.

Parameter Name	Value
`PSRJ`	J0534+2200
`RAJ`	05:34:31.972
`DECJ`	22:00:52.07
`TZRSITE`	COE
`EPHEM`	DE200
`CLK`	TT(TAI)
`UNITS`	TDB
`PLANET_SHAPIRO`	Y
`CORRECT_TROPOSPHERE`	N
`T2CMETHOD`	IAU2000B
`TIMEEPH`	FB90

Table B.3: Values for the variable parameters in the Crab Pulsar ephemerides used in this work. Data provided by the Jodrell Bank Observatory [117].

START/MJD	FINISH/MJD	PEPOCH/MJD	F0/Hz	F1/10^{-10}Hz/s	F2/10^{-20}Hz/s^2	TRES
57693	57707	57700.000000275	29.6483329395181	-3.68982	6.83D-20	0.5
57707	57723	57715.000000295	29.6478547478211	-3.68972	-3.89D-20	0.6
57723	57754	57738.000000232	29.6471215546085	-3.68942	1.55D-20	0.3
57754	57785	57769.000000296	29.6461334246826	-3.68912	1.92D-20	0.6
57785	57813	57799.000000331	29.6451772653663	-3.68880	5.88D-21	0.7
57813	57839	57826.000000007	29.6443168004937	-3.68842	-1.41D-20	0.7
57844	57874	57859.000000247	29.6432651976707	-3.68812	2.16D-20	0.5
57874	57905	57890.000000376	29.6422774075712	-3.68787	2.50D-20	0.8
57905	57935	57920.000000069	29.6413215497439	-3.68754	2.10D-20	0.7
57935	57966	57950.000000157	29.6403657801965	-3.68730	5.71D-21	0.6
57966	57997	57981.000000289	29.6393782215064	-3.68701	9.29D-21	0.6
57997	58027	58012.000000349	29.6383907543430	-3.68657	1.16D-20	0.8
58027	58058	58042.000000104	29.6374352087644	-3.68636	1.93D-20	0.3
58058	58063	58060.000000217	29.6368619250180	-3.68612	6.46D-20	0.1
58065	58071	58068.000000228	29.6366215666433	-3.69981	-8.10D-18	0.5
58071	58089	58080.000000333	29.6362370758467	-3.70847	2.94D-19	0.5
58088	58120	58104.000000331	29.6354688451327	-3.70141	2.81D-19	1.0
58119	58150	58134.000000229	29.6345101986328	-3.69604	1.76D-19	0.4
58150	58178	58164.000000327	29.6335526353020	-3.69318	9.27D-20	0.6
58178	58209	58194.000000208	29.6325956451232	-3.69147	3.44D-20	0.3
58209	58238	58224.000000223	29.6316390101744	-3.69007	3.16D-20	0.6
58239	58270	58255.000000322	29.6306508393765	-3.68916	4.60D-20	0.2
58270	58300	58285.000000004	29.6296947140166	-3.68847	2.63D-20	0.4
58300	58318	58309.000000366	29.6289299031711	-3.68799	7.36D-20	0.3
58331	58358	58344.000000326	29.6278147472534	-3.68753	-1.13D-20	0.3
58365	58392	58378.000000199	29.6267315838432	-3.68701	2.10D-20	0.3
58392	58423	58407.000000281	29.6258078517314	-3.68657	-2.79D-21	0.9
58423	58453	58438.000000100	29.6248204878992	-3.68618	3.65D-20	0.9
58453	58484	58469.000000271	29.6238332381965	-3.68564	3.43D-20	2.5
58484	58515	58499.000000114	29.6228779361748	-3.68537	2.56D-20	1.3
58515	58543	58529.000000129	29.6219227053512	-3.68514	2.83D-20	0.9
58543	58574	58559.000000089	29.6209675809012	-3.68472	-2.62D-21	0.4
58574	58604	58589.000000322	29.6200125167767	-3.68445	1.02D-20	0.6
58604	58635	58620.000000266	29.6190257177678	-3.68408	1.85D-20	0.4
58635	58665	58650.000000083	29.6180708240333	-3.68399	1.42D-20	0.4
58666	58688	58677.000000362	29.6172114790437	-3.68351	-5.23D-21	0.4
58688	58696	58692.000000099	29.6167349675319	-3.69077	6.05D-19	0.2
58696	58710	58703.000000284	29.6163844951404	-3.68565	2.49D-19	0.3
58710	58727	58718.000000273	29.6159069639062	-3.68419	3.97D-20	0.2
58727	58757	58742.000000368	29.6151430651158	-3.68361	2.06D-20	0.2
58757	58788	58772.000000156	29.6141883316381	-3.68312	3.55D-20	0.5
58788	58818	58803.000000022	29.6132019114108	-3.68282	1.40D-21	0.4
58818	58849	58833.000000106	29.6122473527479	-3.68259	-3.61D-21	0.3
58849	58880	58864.000000389	29.6112610422545	-3.68217	9.61D-21	0.3
58880	58909	58895.000000365	29.6102748364423	-3.68195	2.21D-20	0.7
58909	58925	58917.000000232	29.6095749979898	-3.68174	4.38D-20	0.6
58975	59001	58988.000000154	29.6073167263017	-3.68084	1.42D-20	0.6
59001	59031	59016.000000077	29.6064262753055	-3.68065	9.38D-21	1.2
59031	59062	59046.000000387	29.6054722908124	-3.68032	2.20D-20	0.6
59062	59093	59077.000000328	29.6044865933749	-3.68015	8.13D-21	0.4
59093	59123	59108.000000236	29.6035009439794	-3.67982	2.13D-20	0.8
59123	59154	59138.000000292	29.6025471817658	-3.67952	-7.05D-21	0.6
59154	59184	59169.000000169	29.6015617032843	-3.67917	-7.12D-21	0.6
59184	59215	59200.000000029	29.6005763187534	-3.67884	1.68D-20	1.1
59215	59246	59230.000000177	29.5996228160771	-3.67858	-5.16D-21	0.9
59246	59274	59260.000000046	29.5986693695511	-3.67823	9.01D-21	0.8
59274	59305	59290.000000263	29.5977160074804	-3.67789	1.80D-20	1.0

Table B.4: Values for the variable parameters in the Crab Pulsar ephemerides used in this work (continuation). Data provided by the Jodrell Bank Observatory [117].

`START`/MJD	`FINISH`/MJD	`PEPOCH`/MJD	`F0`/Hz	`F1`/10^{-10}Hz/s	`F2`/10^{-20}Hz/s^2	`TRES`
59305	59335	59320.000000290	29.5967627249085	-3.67768	1.80D-20	0.9
59335	59366	59351.000000099	29.5957777450822	-3.67735	3.90D-20	1.0
59366	59396	59381.000000173	29.5948246221018	-3.67701	1.32D-20	0.5
59396	59427	59411.000000151	29.5938715705564	-3.67686	1.48D-20	0.6
59427	59458	59442.000000144	29.5928868231300	-3.67646	1.80D-20	0.9
59458	59488	59473.000000092	29.5919021679669	-3.67619	7.90D-22	0.9
59488	59519	59503.000000292	29.5909493239813	-3.67590	2.84D-20	0.4
59519	59549	59534.000000218	29.5899648200545	-3.67556	2.45D-20	0.4
59549	59580	59565.000000309	29.5889804045828	-3.67527	7.30D-22	0.6
59580	59611	59596.000000333	29.5879960750662	-3.67484	1.18D-20	0.6
59611	59639	59625.000000269	29.5870753201810	-3.67470	8.04D-21	0.8
59639	59670	59655.000000371	29.5861228784729	-3.67431	2.67D-20	4.0
59670	59700	59685.000000327	29.5851705307104	-3.67418	4.36D-20	0.6
59700	59731	59715.000000086	29.5842182671596	-3.67374	2.09D-20	0.5
59731	59761	59746.000000256	29.5832343419117	-3.67344	1.53D-20	0.6
59761	59792	59776.000000349	29.5822822110006	-3.67321	1.96D-20	0.5
59792	59823	59807.000000207	29.5812984322474	-3.67279	8.55D-21	0.5
59823	59852	59837.000000096	29.5803464746885	-3.67250	-3.17D-21	0.8
59853	59884	59868.000000325	29.5793628480444	-3.67225	1.25D-20	0.3
59884	59914	59899.000000224	29.5783793115904	-3.67198	1.11D-21	0.4
59914	59945	59930.000000190	29.5773958567167	-3.67162	7.45D-22	0.6
59945	59976	59960.000000287	29.5764442134408	-3.67134	8.38D-21	0.8
59976	60004	59990.000000265	29.5754926607871	-3.67090	3.78D-21	0.7
60004	60035	60020.000000132	29.5745411845952	-3.67074	1.38D-20	0.3
60035	60065	60050.000000321	29.5735897827538	-3.67033	1.64D-20	0.4
60065	60096	60081.000000163	29.5726067404384	-3.67015	3.63D-20	0.4
60096	60126	60111.000000183	29.5716555178458	-3.66962	1.12D-20	0.6
60126	60156	60141.000000097	29.5707043679803	-3.66945	9.34D-21	0.5
60157	60188	60172.000000355	29.5697215629818	-3.66921	3.79D-21	0.7
60188	60216	60202.000000363	29.5687705364372	-3.66890	1.16D-20	0.3

Table B.5: Values for the parameters in the Dragonfly Pulsar ephemerides used in this work, provided by *Fermi* [109, 160].

Parameter Name	Entry
`PSRJ`	J2021+3651
`RAJ`	20:21:05.4300000 0.03000000000000000000
`DECJ`	+36:51:04.63000 0.50000000000000000000
`F0`	9.6386857801018948171 0.00000054299408028356
`F1`	-8.8602882446373247162e-12 2.9014565310494818264e-17
`F2`	3.0483723798362894126e-22 1.3359699446731969803e-24
`TRES`	374.993
`PEPOCH`	55634.999806324581591
`POSEPOCH`	54093.999830218091212
`START`	54682.659438135486639
`FINISH`	58678.658949854236639
`TZRMJD`	56423.514753536169671
`TZRFRQ`	1520
`TZRSITE`	jbdfb
`EPHEM`	DE405
`CLK`	TT(TAI)
`UNITS`	TDB
`PLANET_SHAPIRO`	N
`CORRECT_TROPOSPHERE`	N
`T2CMETHOD`	TEMPO
`TIMEEPH`	FB90
`EPHVER`	5
`MODE`	1
`DILATEFREQ`	N
`NE_SW`	9.961
`NITS`	1
`NTOA`	1889
`CHI2R`	1.1356 1808
`WAVEEPOCH`	55635
`WAVE_OM`	0.0014301418903258 0
`WAVE1`	0.0040982757342922 0.00095972904271565
`WAVE2`	0.0084158442164021 -0.37151423399669
`WAVE3`	0.04748178826579 0.10083784827922
`WAVE4`	0.0018106368416641 -0.0078109805517133
`WAVE5`	0.0091987121527224 -0.023059199919278
`WAVE6`	0.023994514559903 -0.0049426399820394
`WAVE7`	-0.0098614972945421 0.026087573256011
`WAVE8`	-0.025722840441142 0.0051453070632718
`WAVE9`	0.0054687616804734 -0.020785410761386
`WAVE10`	0.013220770488573 0.0042283014040311

Table B.6: Values for the parameters in the Dragonfly Pulsar ephemerides used in this work, provided by *Fermi* [109, 160] (continuation).

Parameter Name	Entry
`WAVE11`	-0.0053812877850165 0.020896510693821
`WAVE12`	-0.016344685498859 -0.0069106567533776
`WAVE13`	0.005985055718634 -0.016233235472724
`WAVE14`	0.01270355572336 0.0073866556447336
`WAVE15`	-0.0078787721745351 0.01230671234568
`WAVE16`	-0.0097361804162498 -0.0087141732025372
`WAVE17`	0.0093132804484898 -0.0085296591486608
`WAVE18`	0.0077353205373744 0.0087443643010954
`WAVE19`	-0.008189245060075 0.0048006817842797
`WAVE20`	-0.0036533485259612 -0.0073662647421068
`WAVE21`	0.0077069320592379 -0.0023540141334555
`WAVE22`	0.0022366027449656 0.0055106765812134
`WAVE23`	-0.0061067916610728 0.00076053543376864
`WAVE24`	-0.00017371635205208 -0.0051042667441144
`WAVE25`	0.0044131791620981 0.0002654767736565
`WAVE26`	-0.00058851103908086 0.0029476267935376
`WAVE27`	-0.0028354983272778 -0.00080988877585079
`WAVE28`	0.0010163242872666 -0.0023794539864898
`WAVE29`	0.0019142523545376 0.00095634477662259
`WAVE30`	-0.0012354485604344 0.0014414038285552
`WAVE31`	-0.00095915635388228 -0.00093590848033492
`WAVE32`	0.00083287628220793 -0.00051297743153969
`WAVE33`	0.00057344418072358 0.00069423882871578
`WAVE34`	-0.00077673847433786 0.00027645357775456
`WAVE35`	-0.00010644930672805 -0.00021686288956962
`WAVE36`	0.00040614072396384 4.5572150411639e-05
`WAVE37`	-0.00014242780370508 0.00023923136170539
`WAVE38`	-0.00023325847949828 2.4862976680751e-05
`WAVE39`	-1.1514797101918e-05 2.5501686586002e-05
`WAVE40`	6.2205177185838e-05 -1.5243543032556e-05
`GLEP_1`	55110.637497316944064
`GLEP_2`	57209.424802965026174
`GLPH_1`	0.9067692095246242534
`GLPH_2`	0.35927508834514709779
`GLF0_1`	2.1402469590136394831e-05
`GLF0_2`	2.9379467574466383112e-05
`GLF1_1`	-5.3709326656042174809e-14
`GLF1_2`	-5.569503309527592219e-14
`GLF0D_1`	1.4964079122589356824e-07
`GLF0D_2`	2.1613038275136446666e-07
`GLTD_1`	9.8416921261240783991
`GLTD_2`	20.721946040018927704
`DMEPOCH`	54710.00
`DM`	367.5 1.0

C

High-Energy Phasograms

In this chapter, the high-energy phasograms for the Sum-Trigger-II and Standard Trigger analysis are presented. The phasogram generated from Sum-Trigger-II data above 1 TeV is shown in Figure C.1. It shows negative significances for P1, P2, and the bridge, indicating no pulsed signal is found beyond 1 TeV. The Standard Trigger phasogram above 1 TeV is shown in Figure C.2. Here, weak excess signal of $1.74\,\sigma$ for P1 and $1.23\,\sigma$ for P2 can be found. This weak excess originates most likely from statistical fluctuations, as shown by the Z_n^2 and H-test with significance of $-0.09\,\sigma$ and $-1.51\,\sigma$, respectively.

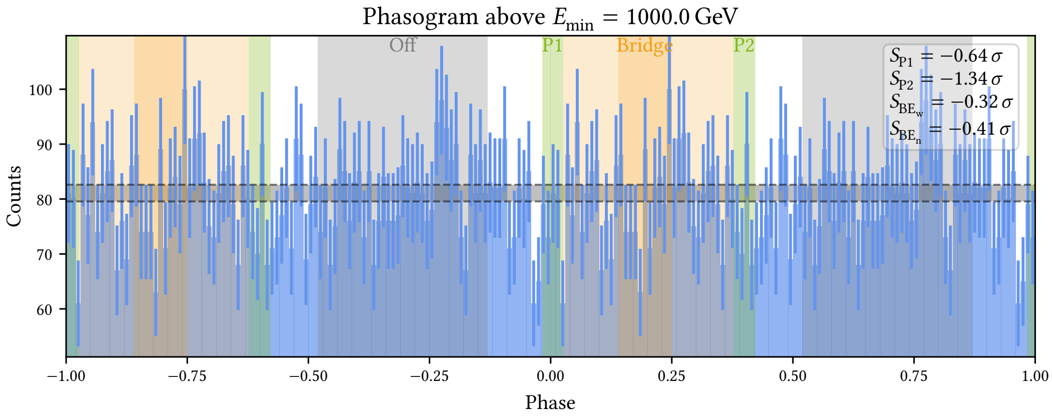

Figure C.1: Phasogram of the Crab Pulsar in the Sum-Trigger-II analysis above 1 TeV.

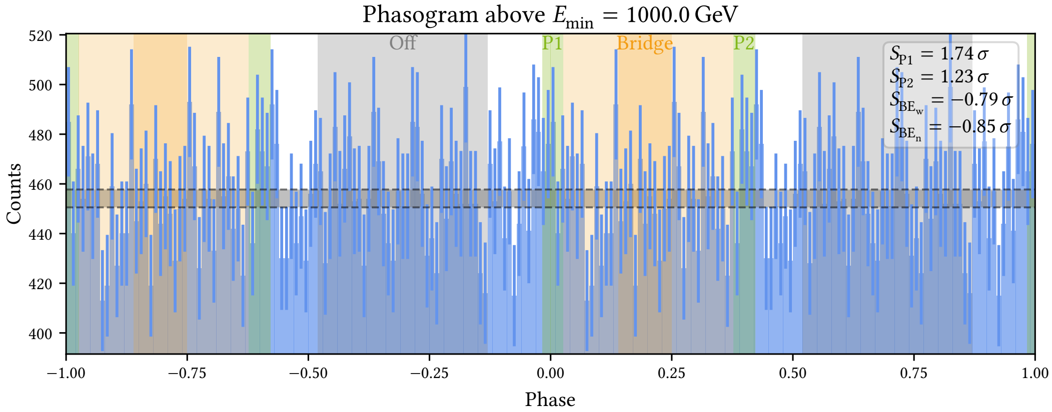

Figure C.2: Phasogram of the Crab Pulsar in the Standard Trigger analysis above 1 TeV.

D
Flux Point Tables

In this chapter, the flux point values for the Sum-Trigger-II analysis, the Standard Trigger analysis, and the joint analysis are listed. The energy-bin-wise and phase-range-wise values of the SED are listed together with the upper limit value and the test statistic value. The column “Upper Limit Bool” shows if the corresponding value is considered an upper limit or a flux point in this work, based on the value of the test statistic. Please note that, as described in Section 6.1, the test statistic threshold for an upper limit is set to a comparably low value of 2, corresponding to $\sqrt{2}\,\sigma$ flux points. Based on the test statistic values in the tables below, also other upper limit thresholds could be set.

The values for the Sum-Trigger-II flux points can be found in Table D.1, Table D.2, and Table D.3. The Standard Trigger flux points are listed in Table D.4 and the joint flux points are shown in Table D.5. The “nan” entries could not be calculated.

Table D.1: Flux point values in the Sum-Trigger-II analysis. The rescaled flux point values as well as the upper limit values are given. When the “UL Bool” entry is True, the upper limit value applies.

E_{min}/GeV	E_{max}/GeV	Rescaling Factor	$E^2 \frac{\mathrm{d}F}{\mathrm{d}E}$ / (TeV cm^{-1} s^{-1})	UL/(TeV cm^{-1} s^{-1})	TS value	UL Bool
L1						
19.91	31.55	30.3	$(0.9 \pm 3.1) \cdot 10^{-11}$	$7.19 \cdot 10^{-11}$	0.08	True
31.55	50.00	30.3	$(1.49 \pm 0.75) \cdot 10^{-11}$	$3.00 \cdot 10^{-11}$	3.95	False
50.00	79.24	30.3	$(8.2 \pm 3.8) \cdot 10^{-12}$	$1.59 \cdot 10^{-11}$	4.75	False
79.24	125.59	30.3	$(4.1 \pm 2.7) \cdot 10^{-12}$	nan	2.46	False
125.59	199.05	30.3	$(-4.9 \pm 2.1) \cdot 10^{-12}$	$-7.52 \cdot 10^{-13}$	5.54	True
199.05	315.48	30.3	$(-2.3 \pm 2.0) \cdot 10^{-12}$	nan	1.28	True
315.48	500.00	30.3	$(-0.8 \pm 2.1) \cdot 10^{-12}$	nan	0.15	True
P1						
19.91	31.55	23.26	$(9.2 \pm 3.2) \cdot 10^{-11}$	$1.56 \cdot 10^{-10}$	8.53	False
31.55	50.00	23.26	$(6.78 \pm 0.78) \cdot 10^{-11}$	$8.35 \cdot 10^{-11}$	77.63	False
50.00	79.24	23.26	$(2.39 \pm 0.39) \cdot 10^{-11}$	$3.17 \cdot 10^{-11}$	38.82	False
79.24	125.59	23.26	$(1.55 \pm 0.27) \cdot 10^{-11}$	$2.09 \cdot 10^{-11}$	33.97	False
125.59	199.05	23.26	$(6.7 \pm 2.1) \cdot 10^{-12}$	$1.10 \cdot 10^{-11}$	10.04	False
199.05	315.48	23.26	$(5.0 \pm 2.1) \cdot 10^{-12}$	$9.21 \cdot 10^{-12}$	6.12	False
315.48	500.00	23.26	$(-1.3 \pm 2.0) \cdot 10^{-12}$	$2.74 \cdot 10^{-12}$	0.42	True
500.00	792.45	23.26	$(-2.2 \pm 2.0) \cdot 10^{-12}$	$1.90 \cdot 10^{-12}$	1.19	True
T1						
19.91	31.55	71.43	$(6.2 \pm 4.6) \cdot 10^{-11}$	$1.55 \cdot 10^{-10}$	1.80	True
31.55	50.00	71.43	$(2.7 \pm 1.1) \cdot 10^{-11}$	$4.92 \cdot 10^{-11}$	6.04	False
50.00	79.24	71.43	$(1.05 \pm 0.56) \cdot 10^{-11}$	$2.18 \cdot 10^{-11}$	3.57	False
79.24	125.59	71.43	$(-0.9 \pm 3.8) \cdot 10^{-12}$	$6.91 \cdot 10^{-12}$	0.05	True
125.59	199.05	71.43	$(4.0 \pm 3.2) \cdot 10^{-12}$	nan	1.62	True
199.05	315.48	71.43	$(1.1 \pm 3.0) \cdot 10^{-12}$	nan	0.15	True
315.48	500.00	71.43	$(-1.6 \pm 3.0) \cdot 10^{-12}$	nan	0.27	True

Table D.2: Flux point values in the Sum-Trigger-II analysis (continuation). The rescaled flux point values as well as the upper limit values are given. When the "UL Bool" entry is True, the upper limit value applies.

E_{min}/GeV	E_{max}/GeV	Rescaling Factor	$E^2 \frac{\mathrm{d}F}{\mathrm{d}E}$ / (TeV cm^{-1} s^{-1})	UL/(TeV cm^{-1} s^{-1})	TS Value	UL Bool
			LB			
19.91	31.55	10.00	$(3.4 \pm 2.1) \cdot 10^{-11}$	$7.73 \cdot 10^{-11}$	2.56	False
31.55	50.00	10.00	$(2.01 \pm 0.52) \cdot 10^{-11}$	$3.05 \cdot 10^{-11}$	14.96	False
50.00	79.24	10.00	$(1.04 \pm 0.26) \cdot 10^{-11}$	$1.57 \cdot 10^{-11}$	16.11	False
79.24	125.59	10.00	$(5.4 \pm 1.8) \cdot 10^{-12}$	$9.02 \cdot 10^{-12}$	9.04	False
125.59	199.05	10.00	$(0.9 \pm 1.4) \cdot 10^{-12}$	$3.77 \cdot 10^{-12}$	0.39	True
199.05	315.48	10.00	$(-0.5 \pm 1.4) \cdot 10^{-12}$	$2.25 \cdot 10^{-12}$	0.14	True
315.48	500.00	10.00	$(-0.7 \pm 1.4) \cdot 10^{-12}$	nan	0.30	True
			BE			
19.91	31.55	9.09	$(4.5 \pm 2.1) \cdot 10^{-11}$	$8.78 \cdot 10^{-11}$	4.65	False
31.55	50.00	9.09	$(1.57 \pm 0.51) \cdot 10^{-11}$	$2.60 \cdot 10^{-11}$	9.41	False
50.00	79.24	9.09	$(8.2 \pm 2.6) \cdot 10^{-12}$	$1.34 \cdot 10^{-11}$	10.30	False
79.24	125.59	9.09	$(3.8 \pm 1.8) \cdot 10^{-12}$	$7.34 \cdot 10^{-12}$	4.63	False
125.59	199.05	9.09	$(0.3 \pm 1.4) \cdot 10^{-12}$	$3.18 \cdot 10^{-12}$	0.07	True
199.05	315.48	9.09	$(2.4 \pm 1.4) \cdot 10^{-12}$	nan	3.07	False
315.48	500.00	9.09	$(1.5 \pm 1.4) \cdot 10^{-12}$	nan	1.28	True
			TB			
19.91	31.55	14.29	$(6.5 \pm 2.4) \cdot 10^{-11}$	$1.14 \cdot 10^{-10}$	7.17	False
31.55	50.00	14.29	$(9.2 \pm 5.9) \cdot 10^{-12}$	$2.10 \cdot 10^{-11}$	2.50	False
50.00	79.24	14.29	$(4.3 \pm 2.9) \cdot 10^{-12}$	$1.02 \cdot 10^{-11}$	2.16	False
79.24	125.59	14.29	$(4.7 \pm 2.0) \cdot 10^{-12}$	$8.80 \cdot 10^{-12}$	5.35	False
125.59	199.05	14.29	$(0.4 \pm 1.6) \cdot 10^{-12}$	$3.64 \cdot 10^{-12}$	0.05	True
199.05	315.48	14.29	$(1.8 \pm 1.6) \cdot 10^{-12}$	nan	1.26	True
315.48	500.00	14.29	$(0.2 \pm 1.6) \cdot 10^{-12}$	nan	0.02	True

Table D.3: Flux point values in the Sum-Trigger-II analysis (continuation). The rescaled flux point values as well as the upper limit values are given. When the "UL Bool" entry is True, the upper limit value applies.

E_{min}/GeV	E_{max}/GeV	Rescaling Factor	$E^2\,\frac{\mathrm{d}F}{\mathrm{d}E}$ / (TeV cm^{-1} s^{-1})	UL/(TeV cm^{-1} s^{-1})	TS Value	UL Bool
L2						
19.91	31.55	17.54	$(5.9 \pm 2.4) \cdot 10^{-11}$	$1.08 \cdot 10^{-10}$	6.15	False
31.55	50.00	17.54	$(2.19 \pm 0.58) \cdot 10^{-11}$	$3.34 \cdot 10^{-11}$	14.66	False
50.00	79.24	17.54	$(9.4 \pm 2.9) \cdot 10^{-12}$	$1.52 \cdot 10^{-11}$	10.39	False
79.24	125.59	17.54	$(4.3 \pm 2.0) \cdot 10^{-12}$	$8.40 \cdot 10^{-12}$	4.55	False
125.59	199.05	17.54	$(-1.0 \pm 1.6) \cdot 10^{-12}$	$2.25 \cdot 10^{-12}$	0.39	True
199.05	315.48	17.54	$(-1.1 \pm 1.6) \cdot 10^{-12}$	nan	0.49	True
315.48	500.00	17.54	$(-2.4 \pm 1.6) \cdot 10^{-12}$	nan	2.39	True
P2						
19.91	31.55	22.22	$(9.8 \pm 3.3) \cdot 10^{-11}$	$1.64 \cdot 10^{-10}$	8.86	False
31.55	50.00	22.22	$(7.04 \pm 0.83) \cdot 10^{-11}$	$8.70 \cdot 10^{-11}$	74.64	False
50.00	79.24	22.22	$(5.44 \pm 0.42) \cdot 10^{-11}$	$6.29 \cdot 10^{-11}$	176.98	False
79.24	125.59	22.22	$(3.32 \pm 0.29) \cdot 10^{-11}$	$3.91 \cdot 10^{-11}$	138.17	False
125.59	199.05	22.22	$(1.50 \pm 0.23) \cdot 10^{-11}$	$1.97 \cdot 10^{-11}$	44.97	False
199.05	315.48	22.22	$(1.12 \pm 0.22) \cdot 10^{-11}$	$1.56 \cdot 10^{-11}$	27.12	False
315.48	500.00	22.22	$(4.0 \pm 2.1) \cdot 10^{-12}$	$8.32 \cdot 10^{-12}$	3.69	False
500.00	792.45	22.22	$(0.1 \pm 2.1) \cdot 10^{-12}$	$4.41 \cdot 10^{-12}$	0.00	True
T2						
19.91	31.55	30.30	$(2.78 \pm 0.80) \cdot 10^{-11}$	$4.39 \cdot 10^{-11}$	12.24	False
31.55	50.00	30.30	$(2.4 \pm 1.6) \cdot 10^{-12}$	$5.63 \cdot 10^{-12}$	2.12	False
50.00	79.24	30.30	$(7.9 \pm 9.7) \cdot 10^{-13}$	nan	0.68	True
79.24	125.59	30.30	$(-6.2 \pm 6.5) \cdot 10^{-13}$	nan	0.91	True
125.59	199.05	30.30	$(3.5 \pm 5.9) \cdot 10^{-13}$	nan	0.37	True
199.05	315.48	30.30	$(-1.1 \pm 6.6) \cdot 10^{-13}$	nan	0.03	True
315.48	500.00	30.30	$(1.17 \pm 0.80) \cdot 10^{-12}$	nan	2.26	False

Table D.4: Flux point values in the Standard Trigger analysis. The rescaled flux point values as well as the upper limit values are given. When the “UL Bool” entry is True, the upper limit value applies.

E_{min}/GeV	E_{max}/GeV	Rescaling Factor	$E^2\,\frac{\mathrm{d}F}{\mathrm{d}E}$ / (TeV cm^{-1} s^{-1})	UL/(TeV cm^{-1} s^{-1})	TS Value	UL Bool
			P1			
50.00	79.24	23.26	$(2.04 \pm 0.37) \cdot 10^{-11}$	$2.79 \cdot 10^{-11}$	31.12	False
79.24	125.59	23.26	$(1.25 \pm 0.18) \cdot 10^{-11}$	$1.61 \cdot 10^{-11}$	52.06	False
125.59	199.05	23.26	$(4.5 \pm 1.3) \cdot 10^{-12}$	$7.17 \cdot 10^{-12}$	12.48	False
199.05	315.48	23.26	$(3.0 \pm 1.1) \cdot 10^{-12}$	$5.28 \cdot 10^{-12}$	7.36	False
315.48	500.00	23.26	$(1.4 \pm 1.0) \cdot 10^{-12}$	$3.45 \cdot 10^{-12}$	1.82	True
500.00	792.45	23.26	$(2.8 \pm 9.5) \cdot 10^{-13}$	$2.20 \cdot 10^{-12}$	0.09	True
792.45	1255.9	23.26	$(7.7 \pm 9.7) \cdot 10^{-13}$	nan	0.65	True
1255.94	1990.5	23.26	$(2.6 \pm 1.0) \cdot 10^{-12}$	nan	6.92	False
			P2			
50.00	79.24	22.22	$(2.84 \pm 0.38) \cdot 10^{-11}$	$3.61 \cdot 10^{-11}$	58.28	False
79.24	125.59	22.22	$(1.98 \pm 0.18) \cdot 10^{-11}$	$2.34 \cdot 10^{-11}$	124.93	False
125.59	199.05	22.22	$(9.2 \pm 1.3) \cdot 10^{-12}$	$1.19 \cdot 10^{-11}$	49.93	False
199.05	315.48	22.22	$(4.5 \pm 1.1) \cdot 10^{-12}$	$6.78 \cdot 10^{-12}$	16.04	False
315.48	500.00	22.22	$(4.2 \pm 1.1) \cdot 10^{-12}$	$6.32 \cdot 10^{-12}$	16.49	False
500.00	792.45	22.22	$(2.02 \pm 0.97) \cdot 10^{-12}$	$3.98 \cdot 10^{-12}$	4.46	False
792.45	1255.94	22.22	$(-7.9 \pm 9.6) \cdot 10^{-13}$	$1.17 \cdot 10^{-12}$	0.66	True
1255.94	1990.54	22.22	$(1.5 \pm 1.0) \cdot 10^{-12}$	nan	2.32	False
			BE			
50.00	79.24	9.09	$(3.6 \pm 1.8) \cdot 10^{-12}$	$7.21 \cdot 10^{-12}$	4.00	False
79.24	125.59	9.09	$(1.78 \pm 0.87) \cdot 10^{-12}$	$3.53 \cdot 10^{-12}$	4.20	False
125.59	199.05	9.09	$(-2.6 \pm 6.8) \cdot 10^{-13}$	$1.11 \cdot 10^{-12}$	0.15	True
199.05	315.48	9.09	$(4.3 \pm 6.0) \cdot 10^{-13}$	nan	0.53	True
315.48	500.00	9.09	$(-2.7 \pm 5.4) \cdot 10^{-13}$	nan	0.25	True

Table D.5: Flux point values in the joint analysis. The rescaled flux point values as well as the upper limit values are given. When the "UL Bool" entry is True, the upper limit value applies.

E_{min}/GeV	E_{max}/GeV	Rescaling Factor	$E^2\,\frac{\mathrm{d}F}{\mathrm{d}E}$ / (TeV cm^{-1} s^{-1})	UL/(TeV cm^{-1} s^{-1})	TS Value	UL Bool
P1						
19.91	31.55	23.26	$(9.5 \pm 3.1) \cdot 10^{-11}$	$1.57 \cdot 10^{-10}$	9.76	False
31.55	50.00	23.26	$(5.83 \pm 0.72) \cdot 10^{-11}$	$7.26 \cdot 10^{-11}$	67.98	False
50.00	79.24	23.26	$(2.19 \pm 0.27) \cdot 10^{-11}$	$2.73 \cdot 10^{-11}$	69.76	False
79.24	125.59	23.26	$(1.33 \pm 0.15) \cdot 10^{-11}$	$1.62 \cdot 10^{-11}$	86.01	False
125.59	199.05	23.26	$(5.0 \pm 1.1) \cdot 10^{-12}$	$7.24 \cdot 10^{-12}$	21.81	False
199.05	315.48	23.26	$(3.44 \pm 0.97) \cdot 10^{-12}$	$5.40 \cdot 10^{-12}$	12.90	False
315.48	500.00	23.26	$(8.0 \pm 8.9) \cdot 10^{-13}$	$2.61 \cdot 10^{-12}$	0.82	True
500.00	792.45	23.26	$(-1.9 \pm 8.4) \cdot 10^{-13}$	$1.51 \cdot 10^{-12}$	0.05	True
792.45	1255.94	23.26	$(4.4 \pm 8.7) \cdot 10^{-13}$	nan	0.26	True
1255.94	1990.54	23.26	$(1.73 \pm 0.90) \cdot 10^{-12}$	nan	3.88	False
P2						
19.91	31.55	22.22	$(9.4 \pm 3.1) \cdot 10^{-11}$	$1.57 \cdot 10^{-10}$	9.06	False
31.55	50.00	22.22	$(6.15 \pm 0.74) \cdot 10^{-11}$	$7.64 \cdot 10^{-11}$	70.39	False
50.00	79.24	22.22	$(4.16 \pm 0.28) \cdot 10^{-11}$	$4.73 \cdot 10^{-11}$	229.62	False
79.24	125.59	22.22	$(2.41 \pm 0.15) \cdot 10^{-11}$	$2.72 \cdot 10^{-11}$	259.62	False
125.59	199.05	22.22	$(1.07 \pm 0.11) \cdot 10^{-11}$	$1.30 \cdot 10^{-11}$	90.98	False
199.05	315.48	22.22	$(6.0 \pm 1.0) \cdot 10^{-12}$	$8.04 \cdot 10^{-12}$	37.13	False
315.48	500.00	22.22	$(4.12 \pm 0.94) \cdot 10^{-12}$	$6.01 \cdot 10^{-12}$	20.16	False
500.00	792.45	22.22	$(1.65 \pm 0.88) \cdot 10^{-12}$	$3.42 \cdot 10^{-12}$	3.61	False
792.45	1255.94	22.22	$(-5.5 \pm 8.9) \cdot 10^{-13}$	$1.25 \cdot 10^{-12}$	0.38	True
1255.94	1990.54	22.22	$(1.00 \pm 0.91) \cdot 10^{-12}$	$2.86 \cdot 10^{-12}$	1.22	True
BE						
19.91	31.55	9.09	$(3.9 \pm 1.8) \cdot 10^{-11}$	$7.57 \cdot 10^{-11}$	4.41	False
31.55	50.00	9.09	$(1.32 \pm 0.42) \cdot 10^{-11}$	$2.17 \cdot 10^{-11}$	9.86	False
50.00	79.24	9.09	$(5.9 \pm 1.6) \cdot 10^{-12}$	$9.05 \cdot 10^{-12}$	14.09	False
79.24	125.59	9.09	$(2.53 \pm 0.86) \cdot 10^{-12}$	$4.26 \cdot 10^{-12}$	8.70	False
125.59	199.05	9.09	$(-1.3 \pm 6.6) \cdot 10^{-13}$	$1.19 \cdot 10^{-12}$	0.04	True
199.05	315.48	9.09	$(8.9 \pm 5.9) \cdot 10^{-13}$	nan	2.28	False
315.48	500.00	9.09	$(0.4 \pm 5.5) \cdot 10^{-13}$	nan	0.01	True

Crab Nebula Checks

The data analysis chain for IACTs is complex and makes use of ensemble learning methods for the gamma-hadron estimation, energy reconstruction, and direction reconstruction. To test the performance of these trained models, it is common standard to perform an analysis of the Crab Nebula (the gamma-ray standard candle) and to check its performance. As long as the analysis can reconstruct the Crab Nebula flux, it is considered reliable. A light curve and a spectrum of the Crab Nebula are computed for each MC period.[1] Please note that in some MC periods, no Crab Nebula data is contained in the corresponding dataset and hence, no Crab Nebula check can be performed.

The spectral energy distribution of the Crab Nebula follows a log-parabola model

$$F(E) = F_0 \left(\frac{E}{E_0}\right)^{-\alpha-\beta\log_{10}\left(\frac{E}{E_0}\right)} \tag{E.1}$$

where $F(E)$ is the flux, F_0 is the amplitude, E_0 is the reference energy and, α and β are parameters describing the curvature of the function. As reference flux, the two models listed in Table E.1 are used.

Table E.1: Reference spectra for the Crab Nebula spectrum.

E_0/GeV	F_0/TeV^{-1} cm^{-2} s^{-1}	α	β	Reference
300	$(6.0 \pm 0.2) \cdot 10^{-10}$	2.31 ± 0.06	0.26 ± 0.07	[19]
1000	$(3.39 \pm 0.09) \cdot 10^{-11}$	2.51 ± 0.02	0.21 ± 0.03	[20]

As also done in the pulsar analyses, the spectral calculations are done with a fixed spectral index of 2 which is common in the field of gamma astronomy (and especially established by *Fermi*-LAT [181]), but not the standard for `Gammapy` calculations. For this, the forward-folding algorithm is executed in each energy bin based on a power law spectral model with index 2.

E.1 Crab Sum-Trigger-II Analysis

A joint Crab Nebula spectrum is shown in Figure E.1. In general, the SED is in agreement with the reference curves. In the energy range between 200 GeV and 1 TeV it tends to slightly

---

[1] To test the performance of each single RF, it would have to be done for each zd range the MC data is produced in. For clarity, the Crab Nebula checks are done in each MC period joint over the entire zd range of the dataset here.

overestimate the flux whereas above 2 TeV it slightly underestimates the Crab Nebula flux.

In Figure E.2, the period wise SEDs are shown. They show a similar behavior as the joint Crab Nebula spectrum. For ST.03.07, the entire spectrum is overestimated by around 10-20 %. Further, it stands out that the second-highest energy flux point delivers a very low flux for ST.03.07, ST.03.10, and ST.03.11. This most likely arises from statistical fluctuations but could also be linked to a bad MC performance in the high energies. As the high-energy regime above 1 TeV is not of much interest in Sum-Trigger-II observations, this does not affect the results of the analyses usually done with Sum-Trigger-II data.

In Figure E.3, light curves of the Crab Nebula with the integrated flux above 300 GeV are shown. They are displayed both with a run-wise and a night-wise binning. The results show flux points clustered around the reference values taken from [20] and [21]. Only for data in the end of 2016, in some nights, the flux is significantly overestimated. This is however in agreement with the overestimated ST.03.07 spectrum.

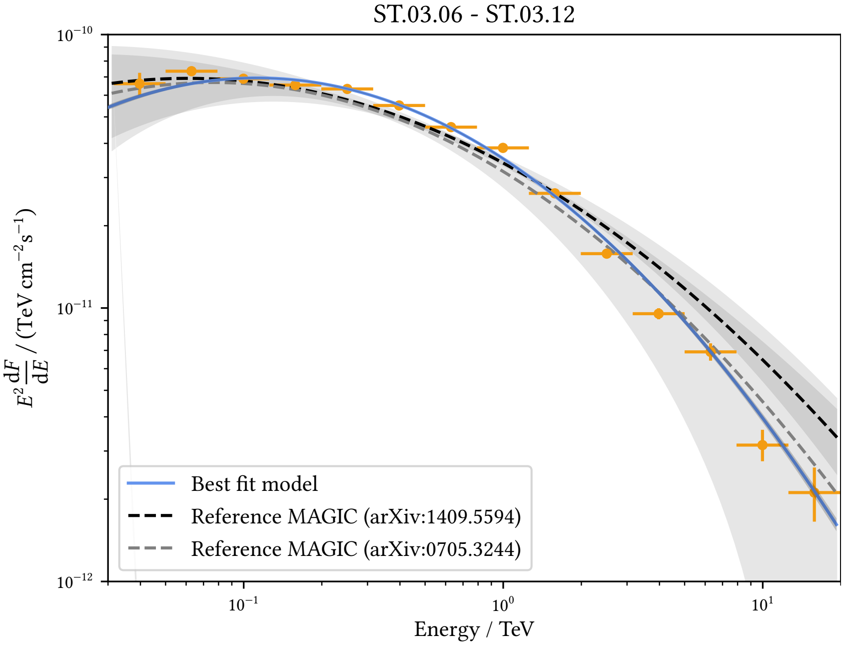

Figure E.1: Joint SED of the Crab Nebula check for the Sum-Trigger-II data.

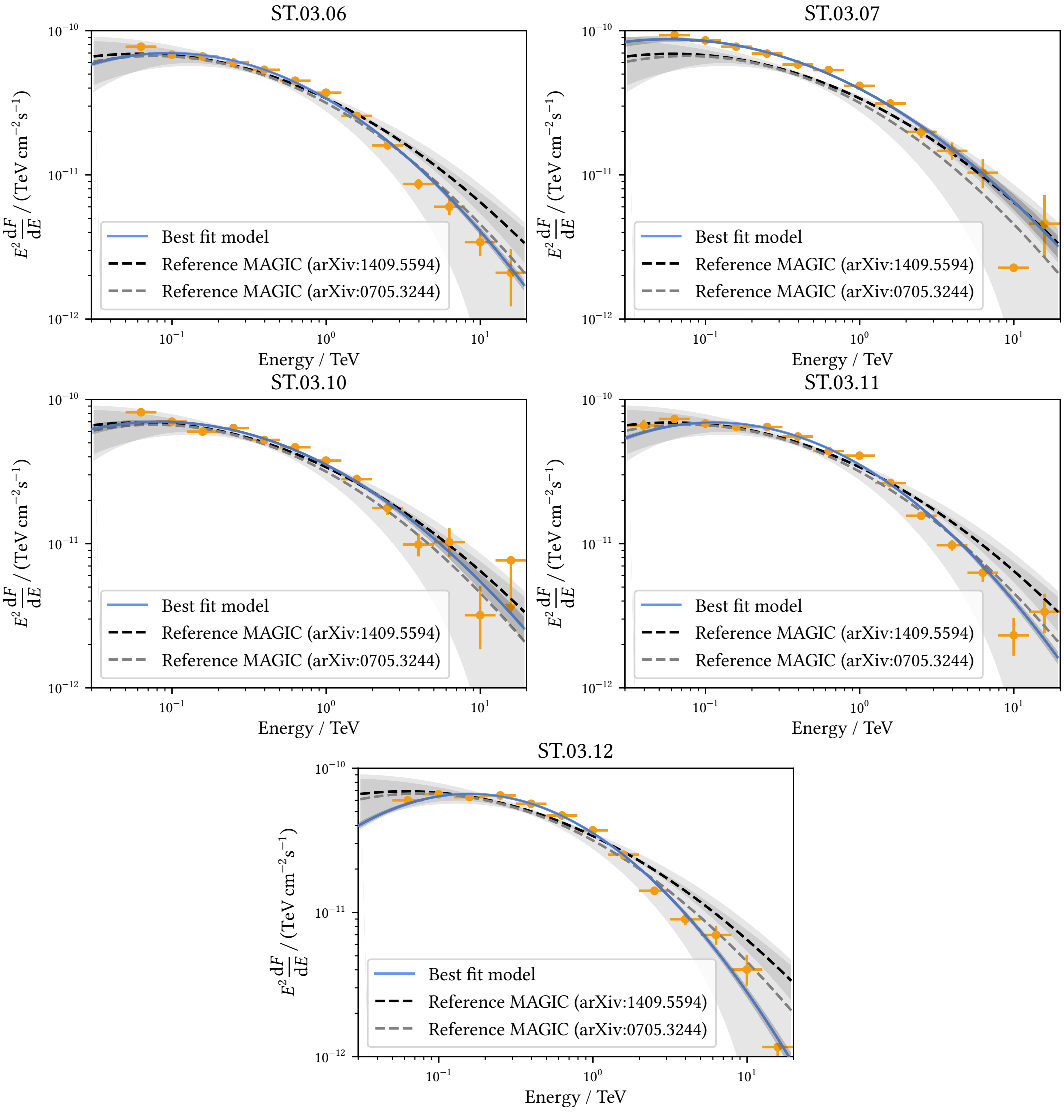

Figure E.2: MC period-wise Crab Nebula checks for the Sum-Trigger-II analysis.

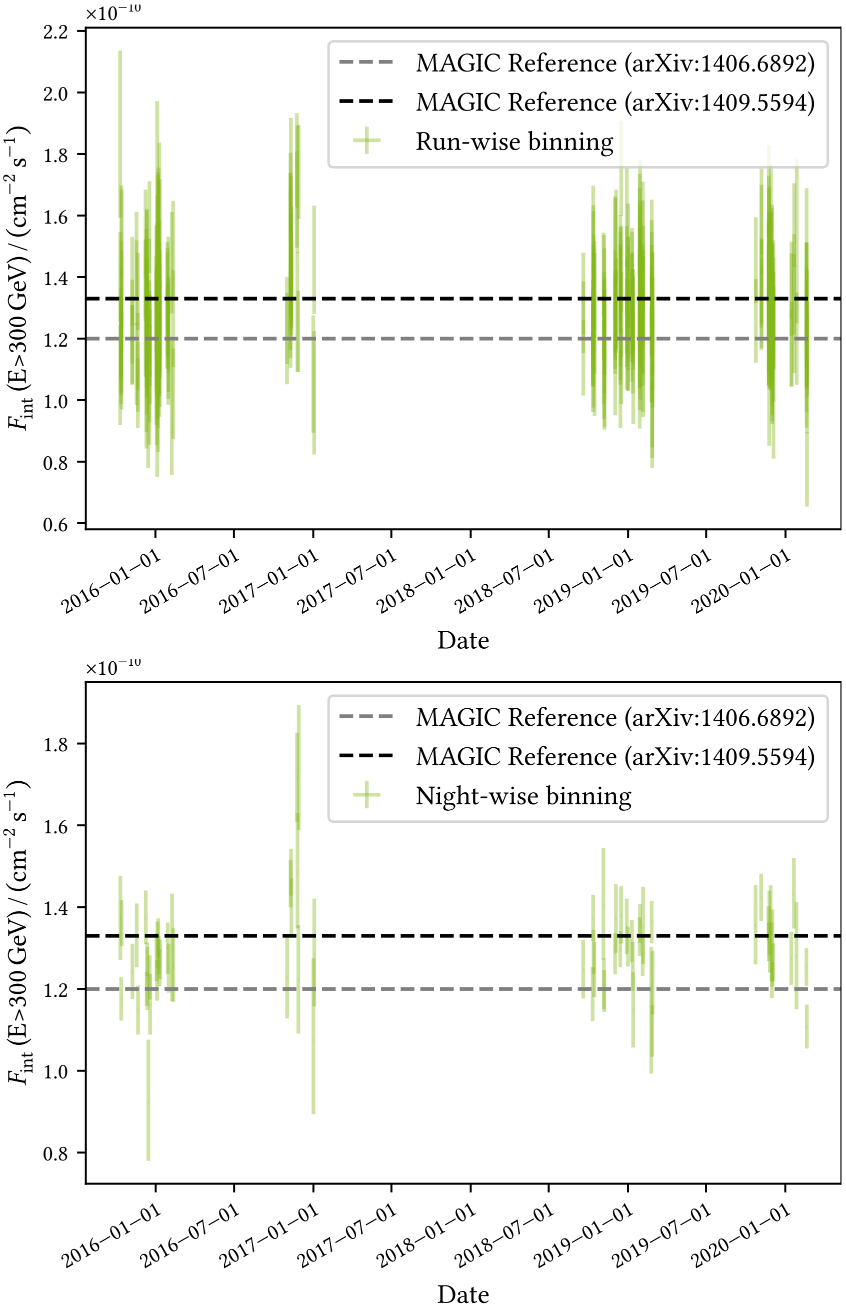

Figure E.3: Light curves of the Crab Nebula check for the Sum-Trigger-II data.

E.2 Crab Standard Trigger Analysis

The Crab Nebula check for the Crab Pulsar Standard Trigger analysis is split into two subsets: A Crab Nebula check for the 5° to 62° zd analysis and a Crab Nebula check for the VHZ analysis.

The Crab Pulsar analysis with Standard Trigger data spreads over multiple MC periods and several zd ranges which sums up to more than 50 RFs that are produced for the analysis. Hence, joining the corresponding zd range for each analysis and only producing the MC period wise Crab Nebula SEDs is reasonable.

E.2.1 Crab 5° to 62° Zenith Distance

In Figure E.4, the joint SED of the Crab Nebula for the 5° to 62° zd Standard Trigger analysis is shown. It is in agreement with the MAGIC reference but slightly underestimates the flux in the entire energy range. The MC period-wise SEDs for a joint zd from 5° to 62° are shown in Figure E.5 and Figure E.6. For some periods, such as ST.03.01, St.03.05, ST.03.13, ST.03.15, ST.03.16, and ST.03.17, the flux is underestimated by around 20 %, especially in the low-energy regime. These are however mostly short MC periods or periods that lie mostly in summer time when the Crab Nebula is not observable or only observable in high-zd observations.

Light curves with the integrated flux above 300 GeV are shown in Figure E.7. In general, the flux points are clustered around the reference curves. However, some flux points significantly underestimate the flux. Though, they are not excluded from the analysis in order not to bias the analysis. With increasing time, a tendency towards a lower flux can be seen, which could indicate a worsening telescope performance with increasing age.

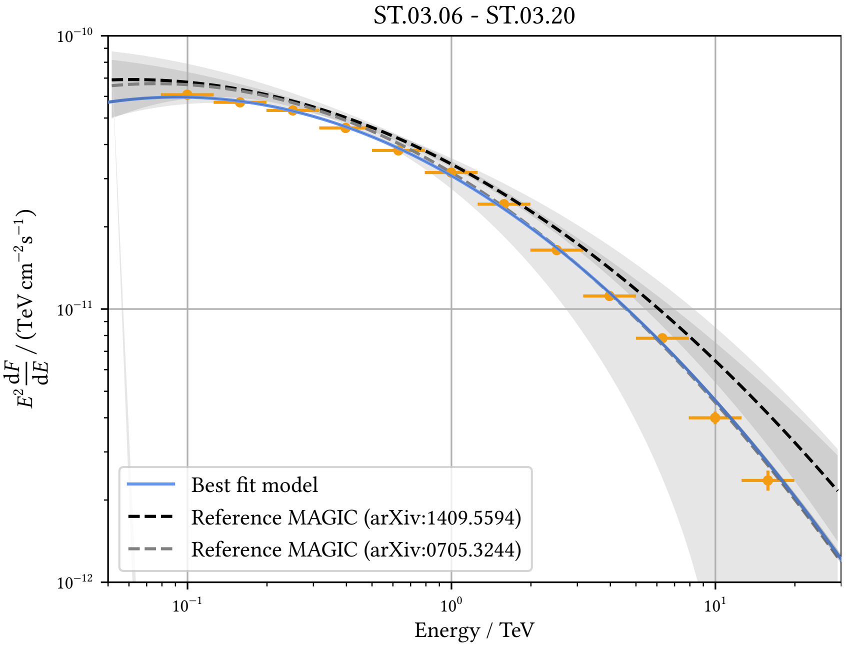

Figure E.4: Spectrum of the Crab Nebula check for the Standard Trigger data.

E.2.2 Crab 62° to 80° Zenith Distance

The Crab Nebula check for the VHZ Standard Trigger analysis is done period wise but joint for the zd range from 62° to 80°.

The joint SED for all VHZ data is shown in Figure E.8. As can be seen, the threshold lies much higher for these observations. Starting from 1 TeV, the reconstructed SED is in good agreement with the MAGIC reference curves.

The period-wise SEDs are presented in Figure E.9 and mostly show a decent performance. For all periods except ST.03.06, the best fit model deviates significantly from the reference models. This behavior is caused by the absence of low-energy flux points which are crucial for obtaining the curvature of the fit. The computed flux points however (which are independent from the best fit model) are clustered around the reference curves in all MC periods.

The light curves in Figure E.10 show the integrated flux above 300 GeV. For many nights, only upper limits can be produced which is not surprising considering the higher energy threshold of the VHZ observations. Still, the flux points that can be produced are clustered around the reference curves. Some upper limits significantly below the reference flux can be seen that are most likely due to malfunctioning runs that are not cut out in the data selection.

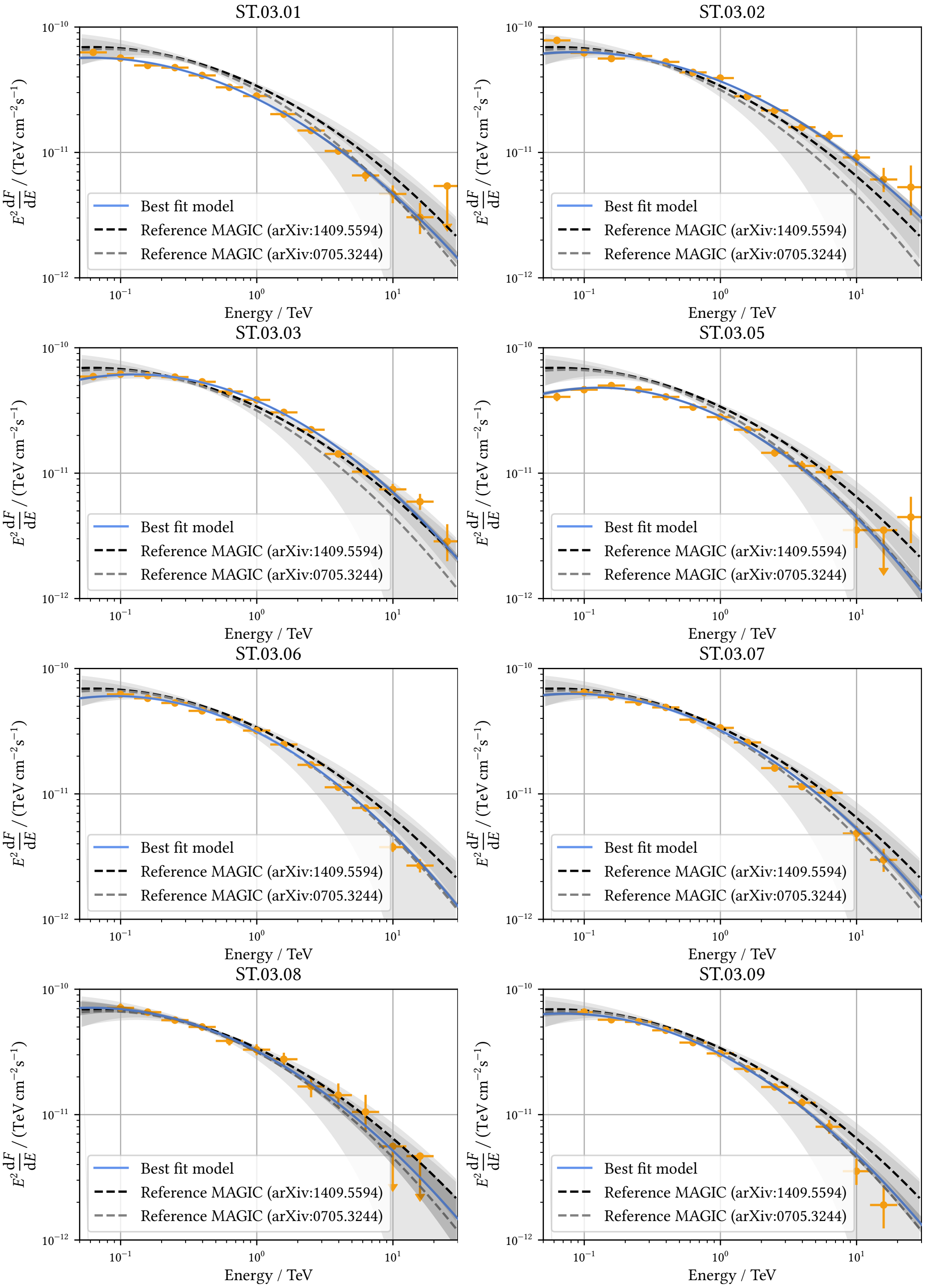

Figure E.5: MC period-wise Crab Nebula checks for the Standard Trigger Crab Pulsar analysis.

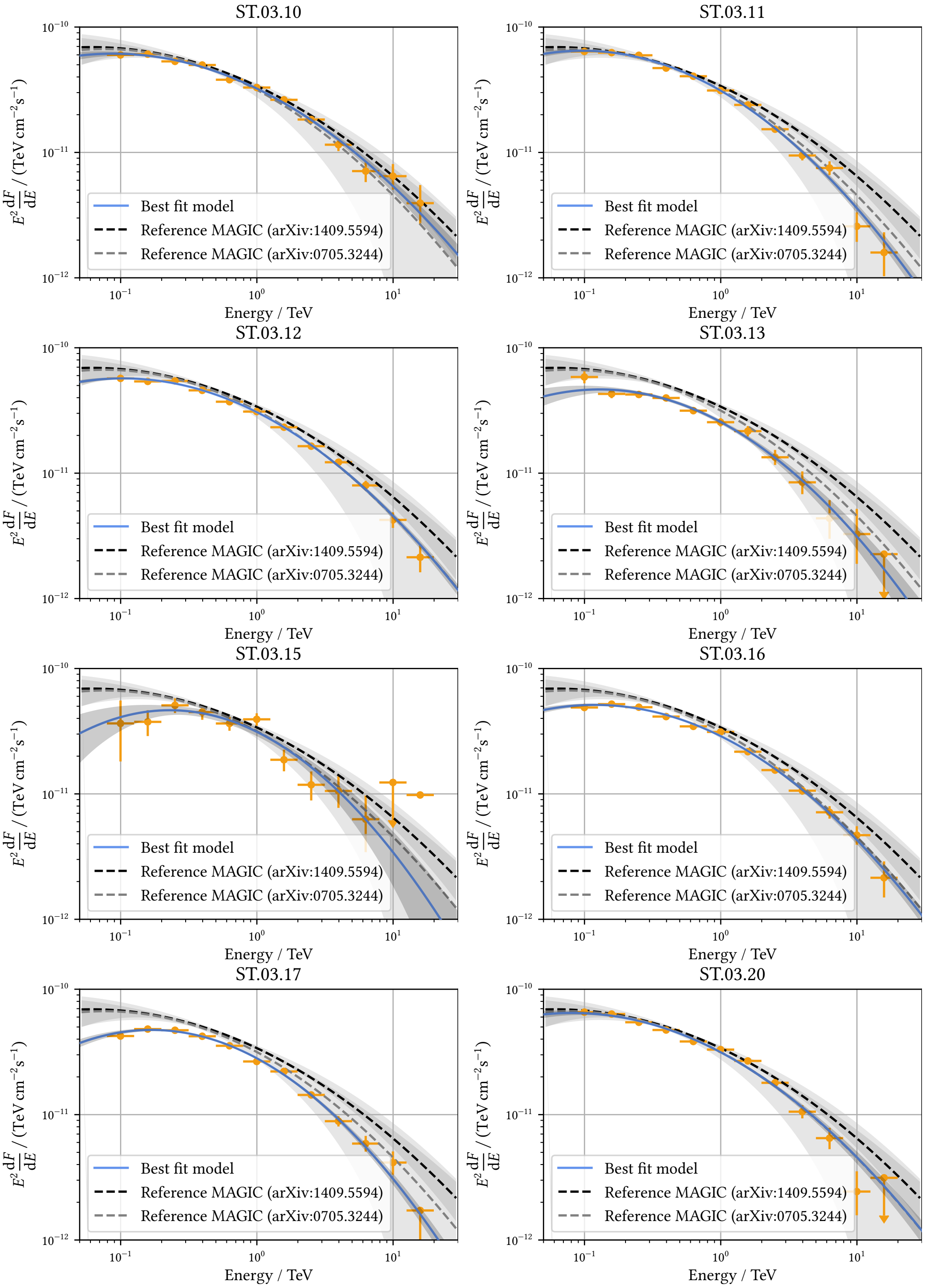

Figure E.6: MC period-wise Crab Nebula checks for the Standard Trigger Crab Pulsar analysis (continuation).

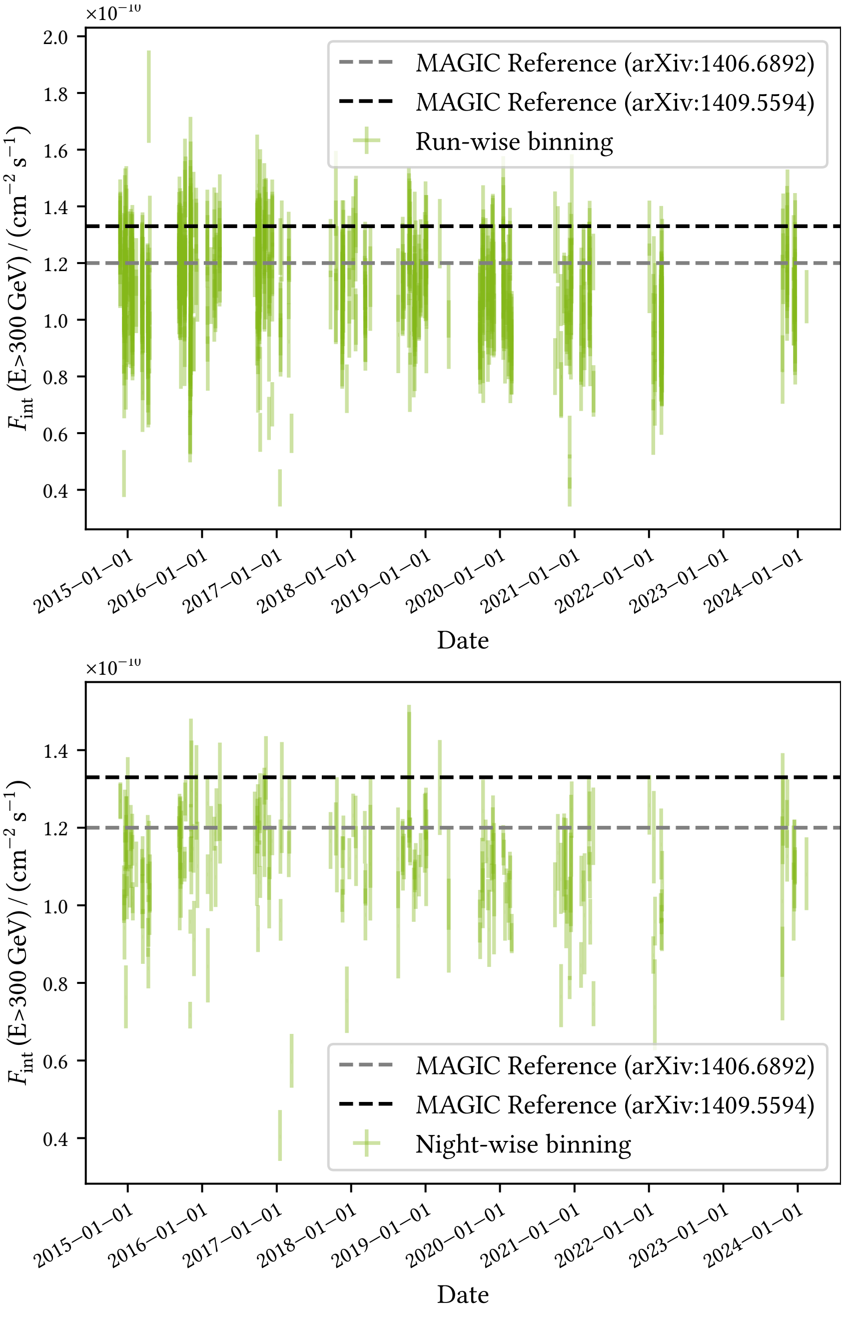

Figure E.7: Light curve of the Crab Nebula check for the Standard Trigger data.

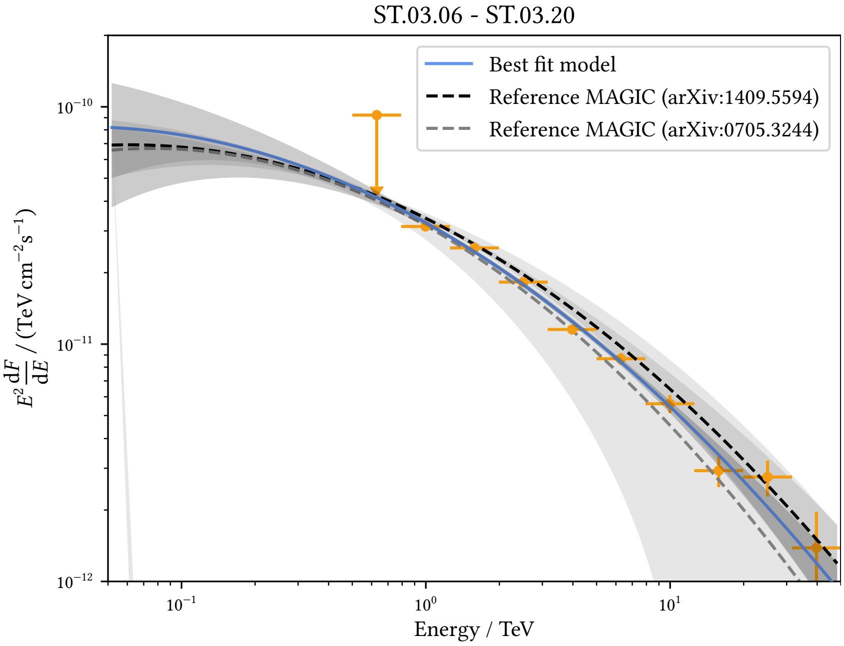

Figure E.8: Spectrum of the Crab Nebula check for the VHZ Standard Trigger data.

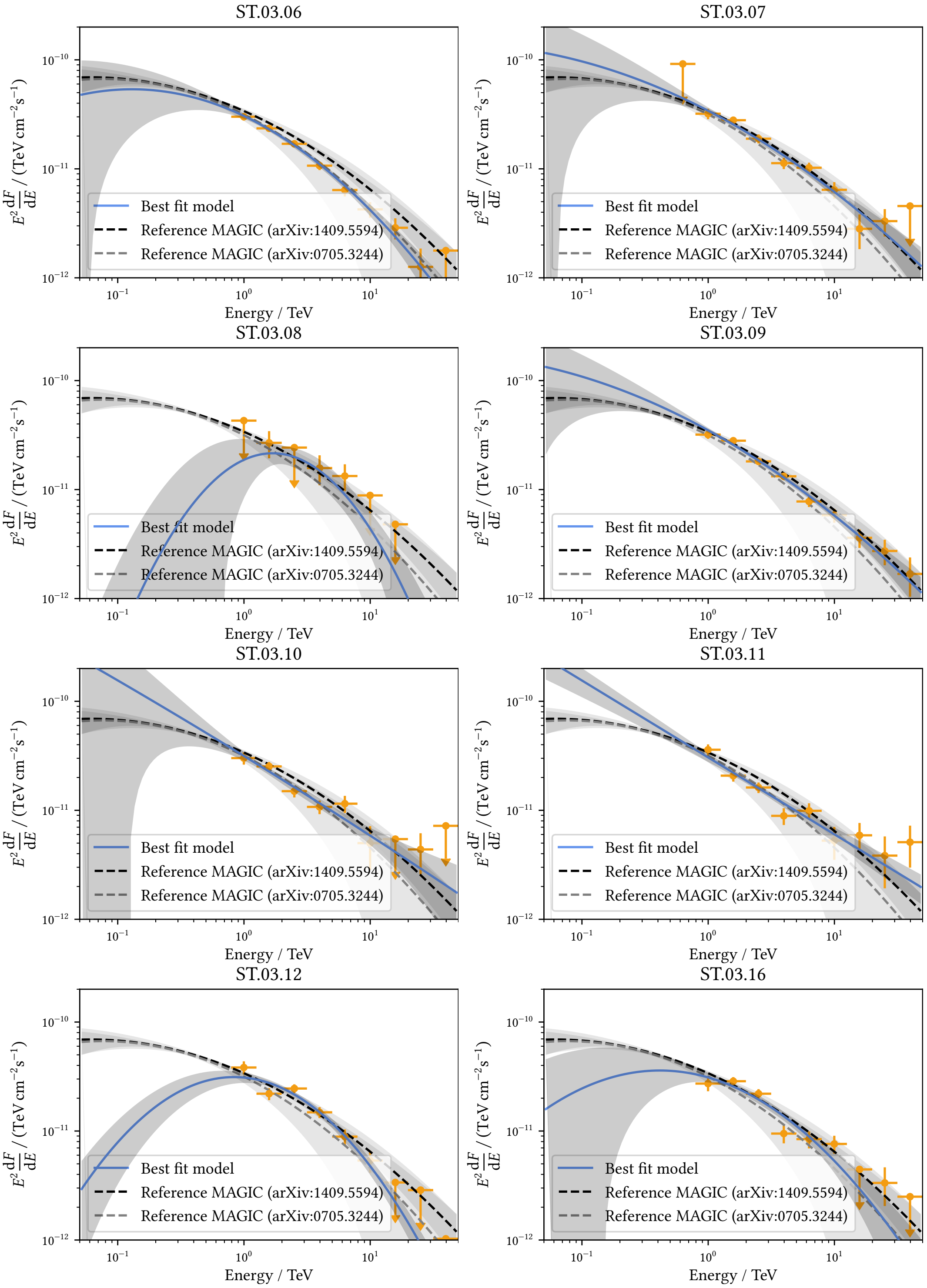

Figure E.9: MC period-wise Crab Nebula checks for the VHZ Standard Trigger Crab Pulsar analysis.

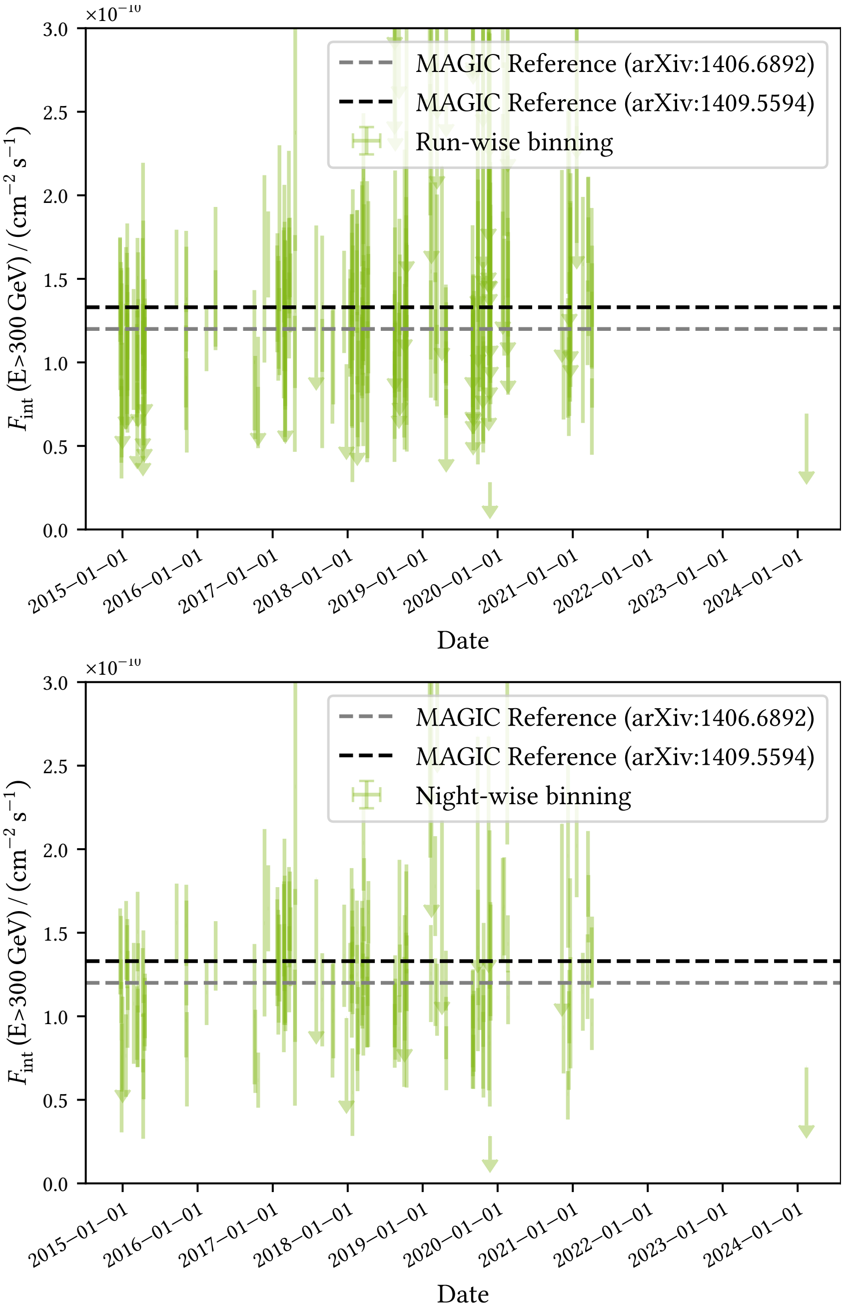

Figure E.10: Light curve of the Crab Nebula check for the VHZ Standard Trigger data.

E.3 Dragonfly Sum-Trigger-II Analysis

For the Crab Nebula check of the RF used in the Dragonfly Sum-Trigger-II data (produced from ST.03.03 MC data and ST.03.11 Off data), Sum-Trigger-II Crab Nebula data from ST.03.11 in the zd range from 5° to 35° is used, as for ST.03.03, no Sum-Trigger-II Crab Nebula data is available. The selected Crab Nebula data are processed with the Dragonfly mixed MC period RF and with the ST.03.03 MC test sample. The Crab Nebula spectrum is shown in Figure E.11. Despite the non-standard selection of Off data and Crab Nebula data for the check, the SED is in agreement with the reference curves. The light curves (note that the Crab Nebula data is taken from ST.03.11) are shown in Figure E.12. They show a stable flux over the entire time range and flux points clustered around the reference curves.

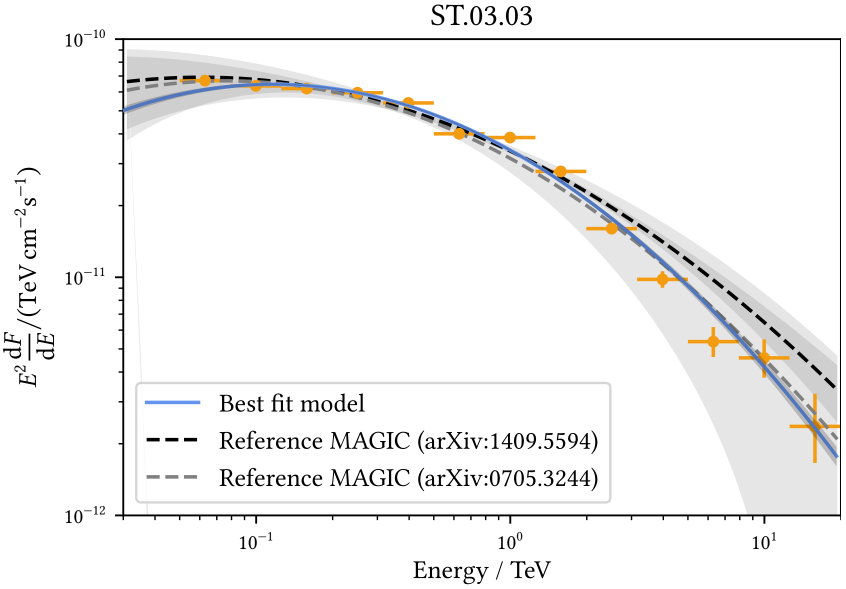

Figure E.11: SED of the Crab Nebula check for the Dragonfly Sum-Trigger-II data. Please note that the Crab Nebula data is taken from ST.03.11 to test the RF for ST.03.03.

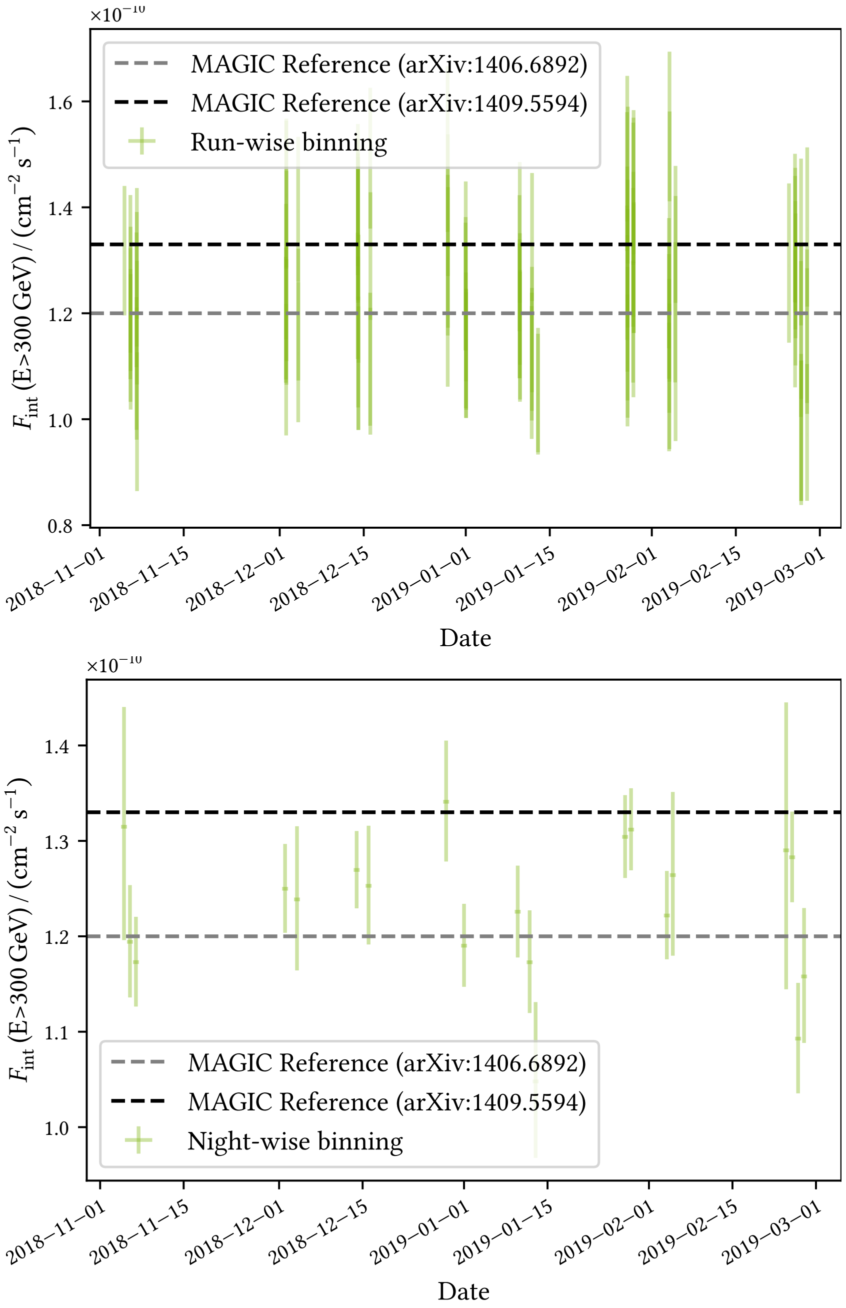

Figure E.12: Light curve of the Crab Nebula check for the Dragonfly Sum-Trigger-II data. Please note that the Crab Nebula data is taken from ST.03.11 to test the RF for ST.03.03.

Data Lists

F.1 Sum-Trigger-II Crab Analysis

The tables Table F.1 and Table F.2 list all the runs that are used in the Sum-Trigger-II analysis of the Crab Pulsar.

Table F.1: List of Sum-Trigger-II Crab Nebula runs used for the corresponding analysis.

Date	Run Number	Date	Run Number	Date	Run Number	Date	Run Number
2015-10-11	5047182	2015-12-13	5049356	2016-01-08	5050233	2016-11-10	5058305
	5047185		5049357	2016-01-10	5050274	2016-11-11	5058341
	5047186		5049358		5050275		5058342
2015-10-13	5047270	2015-12-15	5049455		5050276		5058343
	5047271	2015-12-18	5049556		5050277		5058344
	5047272		5049557		5050278	2016-11-24	5058578
	5047273		5049558		5050279		5058579
	5047274		5049559		5050280	2016-11-25	5058649
	5047275		5049560		5050281		5058650
2015-10-14	5047314		5049561		5050282	2016-11-27	5058702
	5047315		5049562	2016-01-11	5050321		5058703
	5047316	2015-12-19	5049612		5050322	2016-11-28	5058732
	5047317		5049613		5050323	2017-01-01	5059496
	5047318		5049614		5050324	2017-01-03	5059573
	5047319	2016-01-03	5049989		5050325		5059574
	5047320		5049990		5050326	2018-09-19	5075426
2015-11-08	5047964		5049991		5050327		5075427
	5047965		5049992		5050328		5075428
	5047966		5049993		5050329	2018-10-11	5075885
	5047967	2016-01-04	5050043	2016-01-29	5050895		5075886
2015-11-18	5048500		5050044		5050896		5075887
	5048501		5050047		5050897		5075888
	5048502		5050048		5050900		5075889
	5048503		5050049		5050901		5075890
2015-11-21	5048626		5050050	2016-01-31	5050926	2018-10-12	5075930
	5048627		5050051		5050927		5075931
	5048628		5050052		5050928		5075932
	5048629	2016-01-05	5050094		5050929		5075933
2015-12-09	5049115		5050095		5050930		5075934
	5049116		5050098		5050931		5075935
	5049117		5050099		5050932	2018-10-13	5075975
	5049118		5050100	2016-02-08	5051151		5075976
2015-12-11	5049236	2016-01-05	5050101		5051152		5075977
	5049237		5050102	2016-02-11	5051266		5075978
	5049238		5050103		5051267		5075979
	5049239	2016-01-07	5050170		5051268		5075980
	5049240		5050171		5051269	2018-10-15	5076070
	5049241		5050172	2016-11-01	5058065		5076071
	5049242		5050173		5058066		5076072
	5049243		5050174	2016-11-09	5058257		5076073
	5049244		5050175		5058258	2018-11-05	5076459
	5049245		5050176		5058259	2018-11-06	5076496
2015-12-12	5049292		5050177		5058260		5076497
	5049293		5050178		5058261		5076498
	5049294	2016-01-08	5050225		5058262		5076499
	5049295		5050226		5058263		5076500
	5049296		5050227	2016-11-10	5058299		5076501
	5049297		5050228		5058300	2018-11-07	5076547
	5049298		5050229		5058301		5076548
	5049299		5050230		5058302		5076549
	5049300		5050231		5058303		5076550
	5049301		5050232		5058304		5076551

Table F.2: List of Sum-Trigger-II Crab Nebula runs used for the corresponding analysis (continuation).

Date	Run Number	Date	Run Number	Date	Run Number	Date	Run Number
2018-11-07	5076552	2019-01-10	5078708	2019-02-27	5080197	2019-12-01	5087140
	5076553	2019-01-12	5078709		5080198		5087141
2018-12-02	5077151	2019-01-13	5078758	2019-10-24	5086170		5087142
	5077152		5078759		5086171		5087143
	5077155	2019-01-28	5079147	2019-11-06	5086507		5087144
	5077156		5079148		5086508		5087145
	5077157		5079149		5086509		5087147
	5077158		5079150		5086510		5087148
	5077159		5079151		5086511	2019-12-02	5087185
	5077160		5079152		5086512		5087186
	5077161		5079153	2019-11-23	5086757		5087187
2018-12-04	5077247		5079154		5086758	2019-12-04	5087273
	5077248		5079157		5086759		5087274
	5077249		5079158		5086760		5087275
	5077250	2019-01-29	5079198		5086761		5087276
2018-12-14	5077652		5079199		5086762		5087277
	5077653		5079200		5086763		5087278
	5077654		5079201		5086764		5087279
	5077655		5079202		5086765		5087280
	5077656		5079203		5086766		5087281
	5077657		5079204		5086767	2019-12-22	5087560
	5077658		5079205		5086768		5087561
	5077659		5079206	2019-11-24	5086808		5087562
	5077660	2019-02-04	5079454		5086809	2019-12-23	5087615
	5077661		5079455		5086810		5087616
2018-12-16	5077747		5079456		5086811	2020-01-15	5088351
	5077748		5079459		5086812		5088352
	5077749		5079463		5086813		5088353
	5077750		5079464		5086814		5088354
2018-12-29	5078026		5079465		5086815	2020-01-21	5088612
	5078027		5079466		5086816		5088613
	5078028		5079469	2019-11-25	5086863		5088614
	5078029	2019-02-05	5079509		5086864	2020-01-27	5088711
	5078030		5079510		5086865		5088712
2019-01-01	5078173		5079513	2019-11-26	5086905	2020-02-19	5089317
	5078174		5079514		5086906		5089318
	5078175	2019-02-24	5080047		5086908		5089319
	5078176	2019-02-25	5080095		5086909		5089320
	5078177		5080096		5086910		5089321
	5078178		5080097		5086911		5089322
	5078179		5080098		5086914		5089323
	5078180		5080099	2019-11-28	5087008		5089324
2019-01-10	5078609		5080100		5087010		5089325
	5078610		5080101		5087011		5089326
	5078611	2019-02-26	5080141		5087012		5089327
	5078612		5080142		5087013	2020-02-20	5089363
	5078613		5080143	2019-11-30	5087092		5089364
	5078614		5080144		5087093		5089365
	5078615		5080145		5087094		5089366
	5078705		5080146		5087095		5089367
	5078706	2019-02-27	5080195	2019-12-01	5087138		5089368
	5078707		5080196		5087139		

F.2 Standard Trigger Crab Analysis

In this chapter, the nights of observations used in this work are listed. As more than a thousand runs are used, the following tables only contain a list of the nights but not of the runs. Only the nights with data surviving the cuts are shown.

F.2.1 Zenith Distance 5° to 62°

The nights with observations surviving the cuts for the 5° to 62° zd analysis are listed in Table F.3.

F.2.2 Zenith Distance 62° to 80°

The nights with observations surviving the cuts for the 62° to 80° zd analysis are listed in Table F.4.

Table F.3: Standard Trigger observation nights used in the 5° to 62° zd analysis.

2012-11-12	2014-02-25	2015-04-10	2016-10-01	2018-10-18	2020-11-10
2012-11-13	2014-02-26	2015-04-11	2016-10-08	2018-11-04	2020-11-11
2012-12-05	2014-02-27	2015-04-12	2016-10-09	2018-11-08	2020-11-18
2012-12-07	2014-03-01	2015-04-13	2016-10-10	2018-11-09	2020-11-19
2012-12-10	2014-03-02	2015-04-15	2016-10-11	2018-11-11	2020-11-21
2012-12-14	2014-03-04	2015-04-18	2016-10-12	2018-11-14	2020-11-25
2012-12-15	2014-03-06	2015-04-19	2016-10-30	2018-11-30	2020-12-08
2012-12-16	2014-03-19	2015-04-20	2016-11-01	2018-12-08	2020-12-09
2012-12-17	2014-03-20	2015-09-09	2016-11-02	2018-12-28	2020-12-13
2013-01-08	2014-03-21	2015-09-10	2016-11-08	2019-01-01	2020-12-14
2013-01-09	2014-03-23	2015-09-12	2016-11-09	2019-01-03	2020-12-15
2013-01-10	2014-03-24	2015-09-13	2016-11-24	2019-01-04	2020-12-16
2013-01-11	2014-09-01	2015-09-14	2016-11-25	2019-01-05	2020-12-18
2013-01-12	2014-09-27	2015-09-15	2016-11-28	2019-01-06	2021-02-02
2013-01-13	2014-10-02	2015-09-16	2016-12-10	2019-03-12	2021-02-03
2013-01-14	2014-10-05	2015-09-17	2017-01-17	2019-04-24	2021-02-14
2013-01-15	2014-10-18	2015-09-19	2017-01-19	2019-04-25	2021-02-19
2013-01-17	2014-10-22	2015-09-21	2017-01-20	2019-09-24	2021-03-12
2013-01-19	2014-11-04	2015-09-22	2017-01-26	2019-09-25	2021-03-14
2013-01-31	2014-11-25	2015-10-07	2017-03-01	2019-09-26	2021-03-16
2013-02-01	2014-11-26	2015-10-08	2017-03-04	2019-10-05	2021-03-18
2013-02-07	2014-12-13	2015-10-09	2017-03-15	2019-10-07	2021-03-19
2013-02-08	2014-12-14	2015-10-12	2017-09-22	2019-10-09	2021-04-03
2013-02-09	2014-12-15	2015-11-03	2017-10-18	2019-10-10	2021-04-04
2013-02-10	2014-12-16	2015-11-04	2017-10-23	2019-10-11	2022-01-03
2013-02-11	2014-12-18	2015-11-05	2017-11-18	2019-10-23	2022-01-22
2013-02-12	2014-12-19	2015-11-06	2017-11-19	2019-11-03	2022-01-25
2013-02-15	2014-12-20	2015-11-07	2017-11-20	2019-11-04	2022-01-30
2013-02-16	2014-12-21	2015-11-08	2017-11-23	2019-11-09	2022-01-31
2013-02-28	2014-12-23	2015-11-09	2017-11-24	2019-11-21	2022-02-28
2013-03-12	2014-12-24	2015-11-10	2017-12-10	2019-11-22	2022-03-02
2013-09-05	2014-12-25	2015-11-20	2017-12-11	2019-11-23	2022-03-03
2013-09-09	2014-12-26	2015-11-22	2017-12-23	2019-11-27	2022-03-04
2013-10-05	2014-12-27	2015-12-03	2018-01-11	2019-11-28	2022-03-05
2013-10-10	2014-12-28	2015-12-04	2018-01-23	2019-12-01	2022-03-06
2013-10-31	2015-01-01	2015-12-09	2018-01-25	2019-12-03	2022-03-07
2013-11-01	2015-01-11	2016-01-27	2018-03-09	2019-12-04	2023-10-17
2013-11-07	2015-01-16	2016-01-28	2018-03-11	2020-01-17	2023-10-18
2013-11-12	2015-01-17	2016-01-29	2018-03-12	2020-01-18	2023-10-19
2013-11-13	2015-01-18	2016-02-14	2018-03-13	2020-01-21	2023-10-21
2013-11-29	2015-01-23	2016-03-01	2018-04-05	2020-01-26	2023-11-09
2013-12-05	2015-01-24	2016-03-07	2018-04-06	2020-02-02	2023-11-10
2013-12-23	2015-01-25	2016-03-11	2018-08-19	2020-02-12	2023-11-11
2013-12-24	2015-01-26	2016-03-27	2018-08-20	2020-02-17	2023-12-11
2014-01-02	2015-02-12	2016-03-28	2018-09-10	2020-02-19	2023-12-12
2014-01-05	2015-03-12	2016-03-29	2018-09-11	2020-02-21	2023-12-15
2014-01-22	2015-03-13	2016-09-15	2018-09-12	2020-02-27	2023-12-16
2014-01-28	2015-03-14	2016-09-26	2018-09-17	2020-02-28	2023-12-18
2014-02-03	2015-03-15	2016-09-27	2018-10-11	2020-09-27	2023-12-19
2014-02-04	2015-03-16	2016-09-28	2018-10-12	2020-10-11	2024-02-13
2014-02-06	2015-03-18	2016-09-29	2018-10-13	2020-10-26	
2014-02-22	2015-04-09	2016-09-30	2018-10-16	2020-10-27	

Table F.4: Standard Trigger observation nights used in the 62° to 80° zd analysis.

2014-12-20
2014-12-24
2014-12-25
2014-12-26
2014-12-27
2014-12-28
2015-01-01
2015-01-17
2015-01-18
2015-01-23
2015-01-24
2015-01-25
2015-01-26
2015-02-24
2015-03-12
2015-03-14
2015-03-15
2015-03-16
2015-03-18
2015-04-09
2015-04-10
2015-04-11
2015-04-12
2015-04-13
2015-04-18
2015-04-19
2015-04-20
2015-09-21
2015-11-06
2015-11-07
2015-11-08
2015-11-10
2016-02-14
2016-03-29
2016-10-04
2016-10-08
2016-10-22
2016-11-22
2016-12-10
2017-01-23
2017-01-24
2017-01-28
2017-01-30
2017-02-03
2017-02-24
2017-02-25
2017-02-26
2017-02-27
2017-02-28
2017-03-02
2017-03-03
2017-03-04
2017-03-21
2017-03-22
2017-03-23
2017-03-26
2017-04-19
2017-04-20
2017-04-21
2017-08-01
2017-08-30
2017-10-19
2017-10-23
2017-12-15
2017-12-26
2018-01-13
2018-01-20
2018-01-21
2018-01-22
2018-01-23
2018-01-24
2018-01-25
2018-01-26
2018-02-15
2018-02-16
2018-02-17
2018-02-18
2018-02-22
2018-03-11
2018-03-12
2018-03-13
2018-03-14
2018-03-17
2018-03-18
2018-03-19
2018-03-20
2018-03-22
2018-04-05
2018-04-06
2018-04-08
2018-04-11
2018-04-12
2018-08-17
2018-08-18
2018-08-19
2018-08-20
2018-08-21
2018-09-07
2018-09-08
2018-09-09
2018-09-10
2018-09-11
2018-09-12
2018-10-03
2018-10-04
2018-10-05
2018-10-06
2018-10-12
2018-10-13
2018-10-14
2018-10-15
2018-10-16
2019-02-04
2019-02-07
2019-02-10
2019-02-13
2019-02-27
2019-03-01
2019-03-03
2019-03-04
2019-03-12
2019-03-13
2019-04-05
2019-04-07
2019-04-08
2019-04-09
2019-04-24
2019-04-25
2019-04-26
2019-09-01
2019-09-02
2019-09-03
2019-09-04
2019-09-05
2019-09-07
2019-09-26
2019-09-27
2019-09-28
2019-10-06
2019-10-22
2019-10-23
2019-10-24
2019-10-25
2019-11-18
2019-11-19
2019-11-23
2019-11-24
2019-11-25
2019-11-27
2019-11-28
2020-01-26
2020-02-02
2020-02-17
2020-02-18
2020-02-20
2020-02-21
2020-11-09
2020-11-17
2020-12-08
2020-12-09
2020-12-13
2020-12-15
2020-12-19
2020-12-21
2021-01-20
2021-02-19
2021-03-14
2021-03-16
2021-03-18
2021-04-03
2021-04-04
2021-04-05
2024-02-13

F.3 Sum-Trigger-II Dragonfly Analysis

All the runs used in the analysis of Dragonfly Sum-Trigger-II data are listed in Table F.5. Only the runs surviving the cuts are shown.

Table F.5: Sum-Trigger-II runs of Dragonfly used for the analysis.

Date	Run Number	Date	Run Number	Date	Run Number
2014-07-22	5036621	2014-07-27	5036796	2014-08-02	5037006
	5036622		5036797		5037007
	5036623		5036798		5037010
2014-07-23	5036655		5036799		5037011
	5036656		5036800		5037012
	5036657		5036801		5037013
	5036658	2014-07-28	5036834		5037014
	5036659		5036835	2014-08-03	5037044
	5036660		5036836		5037046
2014-07-24	5036690		5036837		5037048
	5036691		5036838		5037049
	5036692		5036839		5037050
	5036695		5036840		5037051
	5036696		5036841		5037052
	5036697		5036842	2014-08-04	5037083
	5036698	2014-07-29	5036873		5037084
2014-07-25	5036727	2014-07-30	5036899		5037085
	5036728		5036900		5037086
	5036729		5036901		5037087
	5036730		5036902		5037088
	5036731		5036903		5037089
	5036732		5036904		5037090
	5036733		5036905	2014-08-05	5037121
	5036734		5036906		5037124
	5036735		5036907		5037125
2014-07-26	5036761	2014-07-31	5036933		5037126
	5036762		5036935		5037127
	5036763		5036936		
	5036764		5036937		
	5036765		5036938		
	5036766		5036939		
	5036767		5036940		
	5036768		5036941		
	5036769				

G

Analysis Configuration Files

G.1 Crab Sum-Trigger-II Analysis

In the following, the `autoMAGIC` configuration file used for the Sum-Trigger-II MaTaJu Crab Pulsar analysis is presented. Please note that this is only the configuration file for the analysis starting on superstar level. Multiple separate MaTaJu productions were done to process the additional off data up to superstar level that are not shown here. Further, three analyses for the three different source names in the data `CrabNebula`, `Crab`, and `CrabNebula-0` were done.

```
mars_version = "Mars-V3-0-1"

[target]
source_name = "CrabNebula"
start_date = 2014-11-24
stop_date = 2020-02-22

[data_selection]
L1Table = "L1_3NN"
L3Table = "L3T_SUMSUM_100_SYNC"
transmission_9km_min_off = 0.8
transmission_9km_min = 0.9
transmission_9km_max = 1.2
zd_min = 5
zd_max = 35
dc_min = 0
dc_max = 2200
hv_setting = "NominalHV"
mola_threshold = 3
cloudiness_max_off = 20
cloudiness_max_on = 10
use_broken_lidar_data = true
calibrated_version_M1 = "current"
calibrated_version_M2 = "current"
force_take_pic_archive_mataju_files = false
mataju_start_data_level = "superstar"

[sorcerer]
ignore_mars_version_of_calibrated_file = true

[star]
cleaning_method = "mataju"
cl_lv1 = false
cl_lv2 = false
noise_lv_mean = false
noise_lv_rms = false
store_star_output = false
```

```
[superstar]
ignore_mars_version_of_superstar_file = true

[RF]
cleaning_survival_rate = 0.5
force_rf = true
only_one_RF = false
max_underpopulated_bins_RF_check = 25
check_off_data_for_current_calibrated_version = false
energy_estimation_method = "RFenStereo"
use_egal_off_if_not_enough_gal_off = true

[mc_parameters]
corsika_versions = ["mmcs699"]
view_cone = "ringwobble"
dont_care_view_cone = false
mc_trigger_type = "SUMT"
extension = "lowE"
max_number_lowe_mc_runs = 3000
ignore_mars_version_of_selectmc_file = false

[melibea]
use_lidar_correction = true
forced_coach_job_ids = false
force_diffuse_mcs = false

[magicDL3]
dl3_converter_version = "v0.1.12"
irf_type = "point-like"
az_bins = 1
hadronness_cut_from_efficiency = true
theta2_cut_from_efficiency = true
hadronness_cut = 0.3
theta2_cut = 0.02
quantile_hadronness_cut = 0.9
quantile_theta2_cut = 0.75

[Mataju]
bright_star_exclude_radius = 100
```

G.2 Crab Standard Trigger Analysis

In the following, the `autoMAGIC` configuration files used for the Standard Trigger analyses are presented. The first configuration file is used for the analysis for zd angles in a range of 5° to 62° while the second configuration file is used for the analysis for zd angles in the range of 62° to 80°. Different configuration files are necessary because for the VHZ analysis the high-energy MC extension is used. Further, the transmission cuts for the off data are lowered because much less off data is available in the VHZ range.

G.2.1 5° to 62° Zenith Distance

```
mars_version = 'Mars-V3-1-0'

[target]
source_name = "CrabNebula"
start_date = 2014-11-24
stop_date = 2024-03-31

[data_selection]
L1Table = ""
L3Table = ""
transmission_9km_min_off = 0.8
transmission_9km_min = 0.9
transmission_9km_max = 1.2
zd_min = 5
zd_max = 62
dc_min = 0
dc_max = 2200
hv_setting = "NominalHV"
mola_threshold = 2
cloudiness_max_off = 20
cloudiness_max_on = 10
use_broken_lidar_data = true
calibrated_version_M1 = "current"
calibrated_version_M2 = "current"

[star]
cleaning_method = "sum"
cl_lv1 = false
cl_lv2 = false
noise_lv_mean = false
noise_lv_rms = false
switch_off_starguider = true
store_star_output = false

[superstar]
ignore_mars_version_of_superstar_file = true

[RF]
cleaning_survival_rate = 0.5
force_rf = true
only_one_RF = false
max_underpopulated_bins_RF_check = 25
check_off_data_for_current_calibrated_version = true
energy_estimation_method = "RFenStereo"

[mc_parameters]
corsika_versions = ["mmcs699", "mmcs6500"]
```

```
view_cone = "ringwobble"
dont_care_view_cone = true
mc_trigger_type = "standard"
extension = ""
ignore_mars_version_of_selectmc_file=false

[melibea]
use_lidar_correction = true
forced_coach_job_ids = false
force_diffuse_mcs = false

[magicDL3]
dl3_converter_version = "v0.1.15"
irf_type = "point-like"
az_bins = 1
hadronness_cut_from_efficiency = true
theta2_cut_from_efficiency = true
hadronness_cut = 0.3
theta2_cut = 0.02
quantile_hadronness_cut = 0.9
quantile_theta2_cut = 0.9
```

G.2.2 62° to 80° Zenith Distance

```
mars_version = 'Mars-V3-1-0'

[target]
source_name = "CrabNebula"
start_date = 2014-11-24
stop_date = 2024-03-31

[data_selection]
L1Table = ""
L3Table = ""
transmission_9km_min_off = 0.6
transmission_9km_min = 0.9
transmission_9km_max = 1.2
zd_min = 62
zd_max = 80
dc_min = 0
dc_max = 2200
hv_setting = "NominalHV"
mola_threshold = 3
cloudiness_max_off = 30
cloudiness_max_on = 10
use_broken_lidar_data = true
calibrated_version_M1 = "current"
calibrated_version_M2 = "current"

[star]
cleaning_method = "sum"
cl_lv1 = false
cl_lv2 = false
noise_lv_mean = false
noise_lv_rms = false
switch_off_starguider = true
store_star_output = false

[superstar]
ignore_mars_version_of_superstar_file = true

[RF]
cleaning_survival_rate = 0.5
force_rf = true
only_one_RF = false
max_underpopulated_bins_RF_check = 25
check_off_data_for_current_calibrated_version = true
energy_estimation_method = "RFenStereo"

[mc_parameters]
corsika_versions = ["mmcs699", "mmcs6500"]
view_cone = "ringwobble"
dont_care_view_cone = true
mc_trigger_type = "standard"
extension = "highE"
ignore_mars_version_of_selectmc_file=false

[melibea]
use_lidar_correction = true
forced_coach_job_ids = false
force_diffuse_mcs = false

[magicDL3]
dl3_converter_version = "v0.1.15"
```

```
irf_type = "point-like"
az_bins = 1
hadronness_cut_from_efficiency = true
theta2_cut_from_efficiency = true
hadronness_cut = 0.3
theta2_cut = 0.02
quantile_hadronness_cut = 0.95
quantile_theta2_cut = 0.95
```

G.3 Dragonfly Analysis

This chapter shows the `autoMAGIC` configuration file used for the Dragonfly analysis. The option `force_off_analysis_period` was implemented in `autoMAGIC` specifically for this analysis.

```
mars_version = "Mars-V3-1-0"

[target]
source_name = "Dragonfly"
start_date = 2014-07-05
stop_date = 2014-08-05

[data_selection]
L1Table = "L1_3NN"
L3Table = "L3T_SUMSUM_100_SYNC"
transmission_9km_min_off = 0.8
transmission_9km_min = 0.9
transmission_9km_max = 1.2
zd_min = 5
zd_max = 35
dc_min = 0
dc_max = 2200
hv_setting = "NominalHV"
mola_threshold = 3
cloudiness_max_off = 20
cloudiness_max_on = 10
use_broken_lidar_data = true
calibrated_version_M1 = "current"
calibrated_version_M2 = "current"
force_take_pic_archive_mataju_files = false
mataju_start_data_level = "superstar"

[sorcerer]
ignore_mars_version_of_calibrated_file = true

[star]
cleaning_method = "mataju"
cl_lv1 = false
cl_lv2 = false
noise_lv_mean = false
noise_lv_rms = false
store_star_output = false
switch_off_starguider = true

[superstar]
ignore_mars_version_of_superstar_file = true

[RF]
cleaning_survival_rate = 0.5
force_rf = true
only_one_RF = true
max_underpopulated_bins_RF_check = 25
check_off_data_for_current_calibrated_version = false
energy_estimation_method = "RFenStereo"
use_egal_off_if_not_enough_gal_off = true

[mc_parameters]
corsika_versions = ["mmcs699"]
view_cone = "ringwobble"
dont_care_view_cone = false
```

```
mc_trigger_type = "SUMT"
extension = "lowE"
max_number_lowe_mc_runs = 4000
force_off_analysis_period = "ST0311"
ignore_mars_version_of_selectmc_file = false

[melibea]
use_lidar_correction = true
forced_coach_job_ids = false
force_diffuse_mcs = false

[flute]
binning = "run-wise"
run_fold = true
hadronness_cut_from_efficiency = true
theta2_cut_from_efficiency = false
hadronness_cut = 0.3
theta2_cut = 0.02
quantile_hadronness_cut = 0.9
quantile_theta2_cut = 0.9

[magicDL3]
dl3_converter_version = "v0.1.15"
irf_type = "point-like"
az_bins = 1
hadronness_cut_from_efficiency = true
theta2_cut_from_efficiency = true
hadronness_cut = 0.3
theta2_cut = 0.02
quantile_hadronness_cut = 0.9
quantile_theta2_cut = 0.75

[Mataju]
bright_star_exclude_radius = 100
```

Bibliography

1. A. A. Abdo et al. (Fermi Collaboration). “Fermi Large Area Telescope Observations of the Crab Pulsar and Nebula”. *The Astrophysical Journal* 708:2, 2009, pages 1254–1267. ISSN: 1538-4357.
   DOI: 10.1088/0004-637x/708/2/1254. arXiv: 0911.2412 [astro-ph.HE]
2. A. A. Abdo et al. (Fermi Collaboration). “Fermi Observations of TeV-Selected Active Galactic Nuclei”. *The Astrophysical Journal* 707:2, 2009, pages 1310–1333. ISSN: 1538-4357.
   DOI: 10.1088/0004-637x/707/2/1310. arXiv: 0910.4881 [astro-ph.HE]
3. A. A. Abdo et al. (Fermi Collaboration). “Fermi observations of high-energy gamma-ray emission from GRB 080916C”. *Science* 323:5922, 2009, pages 1688–1693.
   DOI: 10.1126/science.1169101. arXiv: 0907.0714 [astro-ph.HE]
4. A. A. Abdo et al. (Fermi Collaboration). “Pulsed gamma-rays from PSR J2021+ 3651 with the Fermi Large Area Telescope”. *The Astrophysical Journal* 700:2, 2009, page 1059.
   DOI: 10.1088/0004-637X/700/2/1059. arXiv: 0905.4400 [astro-ph.HE]
5. S. Abdollahi et al. (Fermi Collaboration). “Fermi Large Area Telescope Fourth Source Catalog”. *The Astrophysical Journal Supplement Series* 247:1, page 33.
   DOI: 10.3847/1538-4365/ab6bcb
6. K. Abe et al. (LST Collaboration). “A detailed study of the very-high-energy Crab pulsar emission with the LST-1”. *Astronomy and Astrophysics*.
   Note: Submitted on March 20 2024. Accepted on June 28 2024.
7. S. Abe et al. (LST Collaboration). “Observations of the Crab Nebula and Pulsar with the Large-Sized Telescope Prototype of the Cherenkov Telescope Array”. *The Astrophysical Journal* 956:2, 2023, page 80.
   DOI: 10.3847/1538-4357/ace89d. arXiv: 2306.12960 [astro-ph.HE]
8. S. Abe et al. (MAGIC Collaboration). “Standardised formats and open-source analysis tools for the MAGIC telescopes data”. *JHEAP*.
   Note: Submitted on June 10 2024. Publication in 2024 expected.
9. A. Abramowski et al. (H.E.S.S Collaboration). “H.E.S.S observations of the Crab during its March 2013 GeV gamma-ray flare”. *Astronomy & Astrophysics* 562, 2014, page L4.
   DOI: 10.1051/0004-6361/201323013. arXiv: 1311.3187 [astro-ph.HE]

10. V. A. Acciari et al. (MAGIC Collaboration). "MAGIC very large zenith angle observations of the Crab Nebula up to 100 TeV". *Astronomy & Astrophysics* 635, 2020, A158.
DOI: 10.1051/0004-6361/201936899. arXiv: 2001.09566 [astro-ph.HE]

11. V. A. Acciari et al. (MAGIC Collaboration). "Detection of the Geminga pulsar with MAGIC hints at a power-law tail emission beyond 15 GeV". *Astronomy & Astrophysics* 643, 2020, page L14.
DOI: 10.1051/0004-6361/202039131. arXiv: 2011.10412 [astro-ph.HE]

12. F. Acero et al. (Fermi Collaboration). "Fermi large area telescope third source catalog". *The Astrophysical Journal Supplement Series* 218:2, 2015, page 23.
DOI: 10.1088/0067-0049/218/2/23. arXiv: 1501.02003 [astro-ph.HE]

13. M. Ackermann et al. (Fermi Collaboration). "The first Fermi-LAT gamma-ray burst catalog". *The Astrophysical Journal Supplement Series* 209:1, 2013, page 11.
DOI: 10.1088/0067-0049/209/1/11. arXiv: 1303.2908 [astro-ph.HE]

14. F. Aharonian et al. (H.E.S.S Collaboration). "First detection of a VHE gamma-ray spectral maximum from a cosmic source: H.E.S.S discovery of the Vela X nebula". *Astronomy & Astrophysics* 448:2, 2006, pages L43–L47.
DOI: 10.1051/0004-6361:200600014. arXiv: astro-ph/0601575 [astro-ph]

15. F. Aharonian et al. (H.E.S.S Collaboration). "Observations of the Crab nebula with H.E.S.S". *Astronomy & Astrophysics* 457:3, 2006, pages 899–915.
DOI: 10.1051/0004-6361:20065351. arXiv: astro-ph/0607333 [astro-ph.HE]

16. M. L. Ahnen et al. (MAGIC Collaboration). "Constraining Lorentz invariance violation using the Crab Pulsar emission observed up to TeV energies by MAGIC". *The Astrophysical Journal Supplement Series* 232:1, 2017, page 9.
DOI: 10.3847/1538-4365/aa8404. arXiv: 1709.00346 [astro-ph.HE]

17. J. Albert et al. (MAGIC Collaboration). "FADC signal reconstruction for the MAGIC telescope". *Nuclear Instruments and Methods in Physics Research Section A: Accelerators, Spectrometers, Detectors and Associated Equipment* 594:3, 2008, pages 407–419.
DOI: 10.1016/j.nima.2008.06.043. arXiv: astro-ph/0612385 [astro-ph]

18. J. Albert et al. (MAGIC Collaboration). "Implementation of the random forest method for the imaging atmospheric Cherenkov telescope MAGIC". *Nuclear Instruments and Methods in Physics Research Section A: Accelerators, Spectrometers, Detectors and Associated Equipment* 588:3, 2008, pages 424–432.
DOI: 10.1016/j.nima.2007.11.068. arXiv: 0709.3719 [astro-ph]

19. J. Albert et al. (MAGIC Collaboration). "VHE γ-Ray Observation of the Crab Nebula and its Pulsar with the MAGIC Telescope". *The Astrophysical Journal* 674:2, 2008, page 1037.
DOI: 10.1086/525270. arXiv: 0705.3244 [astro-ph]

20. J. Aleksić et al. (MAGIC Collaboration). “The major upgrade of the MAGIC telescopes, Part II: A performance study using observations of the Crab Nebula”. *Astroparticle Physics* 72, 2016, pages 76–94.
DOI: `10.1016/j.astropartphys.2015.02.005`. arXiv: `1409.5594` `[astro-ph.IM]`
21. J. Aleksić et al. (MAGIC Collaboration). “Measurement of the Crab Nebula spectrum over three decades in energy with the MAGIC telescopes”. *Journal of High Energy Astrophysics* 5, 2015, pages 30–38.
DOI: `10.1016/j.jheap.2015.01.002`. arXiv: `1406.6892` `[astro-ph.HE]`
22. J. Aleksić and J. Rico (MAGIC Collaboration). *FITS format for MAGIC data.* Technical report TDAS 09-05. 2009.
`https://magic.mpp.mpg.de/backend/tdas-notes`.
Note: Internal MAGIC document
23. J. Aleksić et al. (MAGIC Collaboration). “Detection of bridge emission above 50 GeV from the Crab pulsar with the MAGIC telescopes”. *Astronomy & Astrophysics* 565, 2014, page L12.
DOI: `10.1051/0004-6361/201423664`. arXiv: `1402.4219` `[astro-ph.HE]`
24. J. Aleksić et al. (MAGIC Collaboration). “Observations of the Crab Pulsar between 25 and 100 GeV with the MAGIC I Telescope”. *The Astrophysical Journal* 742:1, 2011, page 43.
DOI: `10.1088/0004-637X/742/1/43`. arXiv: `1108.5391` `[astro-ph.HE]`
25. J. Aleksić et al. (MAGIC Collaboration). “Phase-resolved energy spectra of the Crab pulsar in the range of 50–400 GeV measured with the MAGIC telescopes”. *Astronomy & Astrophysics* 540, 2012, page A69.
DOI: `10.1051/0004-6361/201118166`. arXiv: `1109.6124` `[astro-ph.HE]`
26. J. Aleksić et al. (MAGIC Collaboration). “The major upgrade of the MAGIC telescopes, Part I: The hardware improvements and the commissioning of the system”. *Astroparticle Physics* 72, 2016, pages 61–75.
DOI: `10.1016/j.astropartphys.2015.04.004`. arXiv: `1409.6073` `[astro-ph.IM]`
27. E. Aliu et al. (VERITAS Collaboration). “A search for enhanced very high energy gamma-ray emission from the 2013 March Crab Nebula flare”. *The Astrophysical Journal Letters* 781:1, 2013, page L11.
DOI: `10.1088/2041-8205/781/1/L11`. arXiv: `1309.5949` `[astro-ph.HE]`
28. E. Aliu et al. (VERITAS Collaboration). “Detection of Pulsed Gamma Rays Above 100 GeV from the Crab Pulsar”. *Science* 334:6052, 2011, pages 69–72.
DOI: `10.1126/science.1208192`. arXiv: `arXiv:1108.3797` `[astro-ph.HE]`
29. H. Anderhub et al. (MAGIC Collaboration). “Observation of pulsed γ-Rays above 25 GeV from the Crab Pulsar with MAGIC”. *Science* 322:5905, 2008, pages 1221–1224.
DOI: `10.1126/science.1164718`. arXiv: `0809.2998` `[astro-ph]`

30. S. Ansoldi et al. (MAGIC Collaboration). “Teraelectronvolt pulsed emission from the Crab Pulsar detected by MAGIC”. *Astronomy & Astrophysics* 585, 2016, A133.
DOI: 10.1051/0004-6361/201526853. arXiv: 1510.07048 [astro-ph.HE]

31. M. Arakawa et al. (Fermi Collaboration). “Detection of Small Flares from the Crab Nebula with Fermi-LAT”. *The Astrophysical Journal* 897:1, 2020, page 33.
DOI: 10.3847/1538-4357/ab9368. arXiv: 2005.07958 [astro-ph.HE]

32. A. Archer et al. (VERITAS Collaboration). “A Search for Pulsed Very High-energy Gamma-Rays from 13 Young Pulsars in Archival VERITAS Data”. *The Astrophysical Journal* 876:2, 2019, page 95.
DOI: 10.3847/1538-4357/ab14f4. arXiv: 1904.09329 [astro-ph.HE]

33. J. Arons. “Pair creation above pulsar polar caps-Geometrical structure and energetics of slot gaps”. *The Astrophysical Journal* 266, 1983, pages 215–241.
DOI: 10.1086/160771

34. J. Arons. “The Slot Gap Model of Pulsars”. *Symposium - International Astronomical Union* 95, 1981, pages 69–85.
DOI: 10.1017/S0074180900092706

35. J. Arons and E. T. Scharlemann. “Pair formation above pulsar polar caps-Structure of the low altitude acceleration zone”. *The Astrophysical Journal* 231, 1979, pages 854–879.
DOI: 10.1086/157250

36. W. B. Ashworth. “John Bevis and His ”Uranographia” (ca. 1750)”. *Proceedings of the American Philosophical Society* 125:1, 1981, pages 52–73.
http://www.jstor.org/stable/986187 visited on 2024-06-01

37. W. B. Atwood et al. “The Large Area Telescope on the Fermi Gamma-Ray Space Telescope Mission”. *The Astrophysical Journal* 697:2, 2009, pages 1071–1102.
DOI: 10.1088/0004-637X/697/2/1071. arXiv: 0902.1089 [astro-ph.IM]

38. M. Bachetti et al. “Extending the Z_n^2 and H Statistics to Generic Pulsed Profiles”. *The Astrophysical Journal* 909:1, 2021, page 33.
DOI: 10.3847/1538-4357/abda4a

39. C. Baixeras et al. (MAGIC Collaboration). “Commissioning and first tests of the MAGIC telescope”. *Nuclear Instruments and Methods in Physics Research Section A: Accelerators, Spectrometers, Detectors and Associated Equipment* 518:1-2, 2004, pages 188–192.
DOI: 10.1016/j.nima.2003.10.057

40. M. G. Baring. “High-energy emission from pulsars: the polar cap scenario”. *Advances in Space Research* 33:4, 2004, pages 552–560. ISSN: 0273-1177.
DOI: 10.1016/j.asr.2003.08.020. arXiv: astro-ph/0308296 [astro-ph].
Note: High-Energy Studies of Supernova Remnants and Neutron Stars

41. A. Basu, D. Bhattacharya, and B. C. Joshi. “Absolute time calibration of LAXPC aboard AstroSat”. *Journal of Astrophysics and Astronomy* 42, 2021, pages 1–7

42. M. Bayer. “SQLAlchemy”. In: *The Architecture of Open Source Applications Volume II: Structure, Scale, and a Few More Fearless Hacks*. Ed. by A. Brown and G. Wilson. aosabook.org, 2012.
`http://aosabook.org/en/sqlalchemy.html`

43. M. Bayer. *Alembic version 1.13.1 Documentation*. Version 1.13.1.
`https://alembic.sqlalchemy.org/en/latest/` visited on 2024-06-22

44. J. Bevis. “Atlas Celeste (Uranographia Britannica)”, 1750

45. M. F. Bietenholz et al. “The Expansion of the Crab Nebula”. *The Astrophysical Journal Letters* 373, 1991, page L59.
DOI: `10.1086/186051`

46. R. Blandford and S. A. Teukolsky. “Arrival-time analysis for a pulsar in a binary system.” *The Astrophysical Journal* 205, 1976, pages 580–591.
DOI: `10.1086/154315`

47. R. Bock et al. “Methods for multidimensional event classification: a case study using images from a Cherenkov gamma-ray telescope”. *Nuclear Instruments and Methods in Physics Research Section A: Accelerators, Spectrometers, Detectors and Associated Equipment* 516:2-3, 2004, pages 511–528.
DOI: `10.1016/j.nima.2003.08.157`

48. K. Brazier. “Confidence intervals from the Rayleigh test”. *Monthly Notices of the Royal Astronomical Society* 268:3, 1994, pages 709–712

49. R. Brun and F. Rademakers. *ROOT - An Object-Oriented Data Analysis Framework*. 1997.
DOI: `10.5281/zenodo.848818`. `www:%20https://root.cern/download/lj.ps.gz`.
Note: Paper published in the Linux Journal, Issue 51, July 1998.

50. R. Buccheri et al. “Search for pulsed gamma-ray emission from radio pulsars in the COS-B data”. *Astronomy & Astrophysics* 128, 1983, pages 245–251

51. R. Bühler and R. Blandford. “The surprising Crab pulsar and its nebula: a review”. *Reports on Progress in Physics* 77:6, 2014, page 066901.
DOI: `10.1088/0034-4885/77/6/066901`. arXiv: `1309.7046 [astro-ph.HE]`

52. A. Burtovoi et al. “Prospects for the detection of high-energy (E> 25 GeV) Fermi pulsars with the Cherenkov Telescope Array”. *Monthly Notices of the Royal Astronomical Society* 471:1, 2017, pages 431–446.
DOI: `10.1093/mnras/stx1582`. arXiv: `1706.07228 [astro-ph.HE]`

53. Z. Cao, F. Aharonian, et al. (LHAASO Collaboration). “Peta-electron volt gamma-ray emission from the Crab Nebula”. *Science* 373:6553, 2021, pages 425–430.
DOI: `10.1126/science.abg5137`. arXiv: `2111.06545 [astro-ph.HE]`

54. Z. Cao, F. Aharonian, et al. (LHAASO Collaboration). "Ultrahigh-energy photons up to 1.4 petaelectronvolts from 12 gamma-ray galactic sources". *Nature* 594:7861, 2021, pages 33–36.
DOI: `10.1038/s41586-021-03498-z`

55. G. Ceribella. "Insights into the 10-100 GeV gamma-ray emission of pulsars from extensive observations of MAGIC". PhD thesis. Technische Universität München, 2021.
`https://www.mpp.mpg.de/~ceribell/0000_GCeribella_Doktorarbeit__hyper.pdf`

56. B. Cerutti et al. "Particle acceleration in axisymmetric pulsar current sheets". *Monthly Notices of the Royal Astronomical Society* 448:1, 2015, pages 606–619.
DOI: `10.1093/mnras/stv042`. arXiv: `1410.3757 [astro-ph.HE]`

57. K. Cheng, C. Ho, and M. Ruderman. "Energetic radiation from rapidly spinning pulsars. I-Outer magnetosphere gaps. II-VELA and Crab". *Astrophysical Journal* 300, 1986, pages 500–539.
DOI: `10.1086/163830`

58. E. F. Codd. "A Relational Model of Data for Large Shared Data Banks". *Communications of the ACM* 13:6, 1970, pages 377–387.
DOI: `10.1145/362384.362685`

59. P. Colin et al. (MAGIC Collaboration). "Performance of the MAGIC telescopes in stereoscopic mode". In: *Proceedings of the 31st International Cosmic Ray Conference, ICRC2009*. 2009.
DOI: `10.48550/arXiv.0907.0960`. arXiv: `0907.0960 [astro-ph.IM]`

60. J. Cortina et al. (MAGIC Collaboration). "Technical performance of the MAGIC telescopes". In: *Proceedings of the 31st International Cosmic Ray Conference, ICRC2009*. 2009.
DOI: `10.48550/arXiv.0907.1211`. arXiv: `0907.1211 [astro-ph.IM]`

61. C. J. Date. *A Guide to the SQL Standard*. Addison-Wesley Longman Publishing Co., Inc., 1989. ISBN: 978-0-201-50209-1

62. J. K. Daugherty and A. K. Harding. "Gamma ray pulsars: emission from extended polar cap cascades". *The Astrophysical Journal* 458, 1996, page 278.
DOI: `10.1086/176811`. arXiv: `astro-ph/9508155 [astro-ph]`

63. F. Dazzi et al. (MAGIC Collaboration). "The Stereoscopic Analog Trigger of the MAGIC Telescopes". *IEEE Transactions on Nuclear Science* 68:7, 2021, pages 1473–1486.
DOI: `10.1109/TNS.2021.3079262`

64. F. Dazzi et al. (MAGIC Collaboration). "Performance studies of the new stereoscopic Sum-Trigger-II of MAGIC after one year of operation". In: *Proceedings of the 34th International Cosmic Ray Conference, ICRC 2015*. 2015.
DOI: `10.48550/arXiv.1508.05255`. arXiv: `1508.05255 [astro-ph.IM]`

65. A. De Angelis and M. Pimenta. *Introduction to particle and astroparticle physics. Multimessenger astronomy and its particle physics foundations.* Springer, 2018.
DOI: 10.1007/978-3-319-78181-5

66. O. De Jager and I. Büsching. “The H-test probability distribution revisited: improved sensitivity”. *Astronomy & Astrophysics* 517, 2010, page L9.
DOI: 10.1051/0004-6361/201014362. arXiv: 1005.4867 [astro-ph.HE]

67. C. Deil et al. *Data formats for gamma-ray astronomy - version 0.3.* 2022.
DOI: 10.5281/zenodo.7304668. https://gamma-astro-data-formats.readthedocs.io/en/v0.3

68. C. Deil et al. “Gammapy - A prototype for the CTA science tools”. In: *Proceedings of the 35th International Cosmic Ray Conference, ICRC 2017.* 2017.
arXiv: 1709.01751 [astro-ph.IM]

69. C. Deil et al. “Open high-level data formats and software for gamma-ray astronomy”. In: *Proceedings, 6th International Meeting on High Energy Gamma-Ray Astronomy.* 2016.
DOI: 10.1063/1.4969003. arXiv: 1610.01884 [astro-ph.IM]

70. “Discovery of a radiation component from the Vela pulsar reaching 20 teraelectronvolts”. *Nature astronomy* 7:11, 2023, pages 1341–1350.
DOI: 10.1038/s41550-023-02052-3. arXiv: 2310.06181 [astro-ph.HE]

71. E. Domingo-Santamaria et al. (MAGIC Collaboration). “The DISP analysis method for point-like or extended gamma source searches / studies with the MAGIC telescope”. In: *Proceedings of the 29th International Cosmic Ray Conference, ICRC 2005.* 2005.
DOI: 10.48550/arXiv.astro-ph/0508274. arXiv: astro-ph/0508274 [astro-ph]

72. A. Donath and T. G. D. T. (https://gammapy.org/team.html). *Gammapy: a Python package for gamma-ray astronomy.* 2023.
DOI: 10.25080/gerudo-f2bc6f59-028

73. Donath, Axel et al. “Gammapy: A Python package for gamma-ray astronomy”. *Astronomy & Astrophysics* 678, 2023, A157.
DOI: 10.1051/0004-6361/202346488. arXiv: 2308.13584 [astro-ph.IM]

74. S. W. Ellingson et al. “Observations of crab giant pulses in 20–84 MHz using LWA1”. *The Astrophysical Journal* 768:2, 2013, page 136.
DOI: 10.1088/0004-637X/768/2/136. arXiv: 1304.0812 [astro-ph.HE]

75. J. M. Fierro et al. “Phase-resolved Studies of the High-Energy Gamma-Ray Emission from the Crab, Geminga, and Vela Pulsars”. *The Astrophysical Journal* 494:2, 1998, page 734.
DOI: 10.1086/305219. arXiv: astro-ph/9709123 [astro-ph]

76. FITS Working Group. *Definition of the Flexible Image Transport System(FITS). Version 4.0.* 2016.
https://fits.gsfc.nasa.gov/fits_standard.html

77. V. P. Fomin et al. “New methods of atmospheric Cherenkov imaging for gamma-ray astronomy. I. The false source method”. *Astroparticle Physics* 2:2, 1994, pages 137–150.
DOI: `10.1016/0927-6505(94)90036-1`

78. J. R. García et al. (MAGIC Collaboration). “Status of the new Sum-Trigger system for the MAGIC telescopes”. *arXiv e-prints*, 2014.
DOI: `10.48550/arXiv.1404.4219`. arXiv: `1404.4219 [astro-ph.IM]`

79. M. Gaug et al. (MAGIC Collaboration). “Calibration of the MAGIC Telescope”. *Part 3: MAGIC Detector and Analysis Details*, 2005, page 33

80. M. Gaug et al. (MAGIC Collaboration). *Atmospheric Monitoring for the MAGIC Telescopes*. 2014.
arXiv: `1403.5083 [astro-ph.IM]`

81. I. A. Grenier and A. K. Harding. “Gamma-ray pulsars: A gold mine”. *Comptes Rendus Physique* 16:6-7, 2015, pages 641–660.
DOI: `10.1016/j.crhy.2015.08.013`. arXiv: `1509.08823 [astro-ph.HE]`

82. B. Guinot. “Is the International Atomic Time TAI a coordinate time or a proper time?” *Celestial mechanics* 38:2, 1986, pages 155–161

83. D. Haefner et al. (MAGIC Collaboration). “New improved Sum-Trigger system for the MAGIC telescopes”. In: *Proceedings of the 32nd International Cosmic Ray Conference, ICRC 2011*. 2011.
DOI: `10.7529/ICRC2011/V09/1326`. arXiv: `1111.1299 [astro-ph.IM]`

84. J. Halpern et al. “Discovery of high-energy gamma-ray pulsations from PSR J2021+ 3651 with AGILE”. *The Astrophysical Journal* 688:1, 2008, page L33.
DOI: `10.1086/594117`. arXiv: `0810.0008 [astro-ph]`

85. A. K. Harding. “Pulsar emission physics: The first fifty years”. *Proceedings of the International Astronomical Union* 13:S337, 2017, pages 52–57.
DOI: `doi:10.1017/S1743921318000509`. arXiv: `1712.02409 [astro-ph.HE]`

86. C. R. Harris et al. “Array programming with NumPy”. *Nature* 585, 2020, pages 357–362.
DOI: `10.1038/s41586-020-2649-2`. arXiv: `2006.10256 [cs.MS]`

87. D. Heck et al. *CORSIKA: A Monte Carlo Code to Simulate Extensive Air Showers*. Technical report FZKA 6019. Forschungszentrum Karlsruhe, 1998

88. D. Heck and T. Pierog. *Extensive Air Shower Simulation with CORSIKA: A User’s Guide*. Version 7.7500. 2023.
`https://www.iap.kit.edu/corsika/70.php`.
Note: Only the most recent version of the documentation can be accessed without password.

89. W. Heitler. *The quantum theory of radiation*. 2nd ed. Oxford University Press, 1944.
`https://archive.org/details/in.ernet.dli.2015.37198`

90. V. F. Hess. "Über Beobachtungen der durchdringenden Strahlung bei sieben Freiballonfahrten". *Phys. Zeit* 13, 1912, pages 1084–1091.
http://inspirehep.net/record/1623161/files/HessArticle.pdf.
Note: German, English translation available at https://arxiv.org/abs/1808.02927.

91. J. Hessels et al. "Observations of PSR J2021+3651 and its X-ray Pulsar Wind Nebula G75.2+0.1". *The Astrophysical Journal* 612:1, 2004, page 389.
DOI: 10.1086/422408. arXiv: astro-ph/0403632 [astro-ph]

92. A. Hewish et al. "Observation of a Rapidly Pulsating Radio Source". *Nature* 217:5130, 1968, pages 709–713.
DOI: 10.1038/217709a0

93. A. M. Hillas. "Cerenkov light images of EAS produced by primary gamma rays and by Nuclei". In: *Proceedings of the 19th International Cosmic Ray Conference, ICRC 1985*. Vol. 3. 1985

94. G. Hobbs et al. *Tempo2 User Manual*. Jodrell Bank Centre for Astrophysics, University of Manchester.
https://www.jb.man.ac.uk/research/pulsar/Resources/tempo2_manual.pdf visited on 2024-06-22

95. G. Hobbs, R. Edwards, and R. Manchester. "TEMPO2, a new pulsar-timing package–I. An overview". *Monthly Notices of the Royal Astronomical Society* 369:2, 2006, pages 655–672.
DOI: 10.1111/j.1365-2966.2006.10302.x. arXiv: astro-ph/0603381 [astro-ph]

96. D. Hoffleit and W. Warren Jr. *The Bright Star Catalog, 5th Revised Edition*. 1991.
http://cdsarc.u-strasbg.fr/viz-bin/Cat?V/50

97. M. Holler et al. (H.E.S.S Collaboration). "Observations of the Crab Nebula with H.E.S.S phase II". In: *Proceedings of the 34th International Cosmic Ray Conference, ICRC 2015*. 2015.
DOI: 10.48550/arXiv.1509.02902. arXiv: 1509.02902 [astro-ph.HE]

98. HTCondor Team. *HTCondor*. 2024.
DOI: 10.5281/zenodo.2579447

99. E. P. Hubble. "Novae or Temporary Stars". *Leaflet of the Astronomical Society of the Pacific* 1:14, 1928, page 55

100. International Astronomical Union. *Sixteenth General Assembly Grenoble 1976*. 1976.
https://www.iau.org/static/resolutions/IAU1976_French.pdf visited on 2024-01-30

101. K. G. Jones. "Messier's Nebulae and Star Clusters". *Journal for the History of Astronomy, Vol. 1, p. 82* 1, 1970, page 82.
http://naedine.astrolab.ru/sites/default/files/books/jones.pdf

102. V. Kalogera and G. Baym. "The maximum mass of a neutron star". *The Astrophysical Journal* 470:1, 1996, page L61

103. D. Kaplan et al. *nanograv/PINT: 0.9.6*. Version 0.9.6. 2023.
DOI: 10.5281/zenodo.8072376

104. G. H. Kaplan. "The IAU resolutions on astronomical reference systems, time scales, and Earth rotation models", 2006.
DOI: 10.48550/arXiv.astro-ph/0602086. arXiv: astro-ph/0602086 [astro-ph.HE]

105. A. Kirichenko et al. "Optical observations of PSR J2021+ 3651 in the Dragonfly Nebula with the GTC". *The Astrophysical Journal* 802:1, 2015, page 17.
DOI: 10.1088/0004-637X/802/1/17. arXiv: 1501.04594 [astro-ph.SR]

106. A. Knierim. *aknierim/TikZ_assortment: Assortment of TikZ graphics/source code*. Version v1.1. 2024.
DOI: 10.5281/zenodo.11045574. https://doi.org/10.5281/zenodo.11045574

107. K. Kosack et al. *cta-observatory/ctapipe*. 2021.
DOI: 10.5281/zenodo.3372210

108. R. Kothes. "Pulsar Wind Nebulae". In: *Modelling Pulsar Wind Nebulae*. Ed. by D. F. Torres. Springer International Publishing, Cham, 2017, pages 4–12.
DOI: 10.1007/978-3-319-63031-1_1

109. *LAT Third Catalog of Gamma-ray Pulsars*. 2023.
https://fermi.gsfc.nasa.gov/ssc/data/access/lat/3rd_PSR_catalog/3PC_HTML/J2021+3651.html

110. S. Lesage et al. (Fermi Collaboration). "Fermi-GBM Discovery of GRB 221009A: An Extraordinarily Bright GRB from Onset to Afterglow". *The Astrophysical Journal Letters* 952:2, 2023, page L42.
DOI: 10.3847/2041-8213/ace5b4. arXiv: 2303.14172 [astro-ph.HE]

111. R. W. Lessard et al. "A new analysis method for reconstructing the arrival direction of TeV gamma rays using a single imaging atmospheric Cherenkov telescope". *Astroparticle Physics* 15:1, 2001, pages 1–18.
DOI: 10.1016/s0927-6505(00)00133-x. arXiv: astro-ph/0005468 [astro-ph]

112. T.-P. Li and Y.-Q. Ma. "Analysis methods for results in gamma-ray astronomy". *The Astrophysical Journal* 272, 1983, pages 317–324.
DOI: 10.1086/161295

113. L. M. Linhoff. "Multiwavelength Analysis of the TeV-RadioGalaxy 3C 84/NGC 1275". PhD thesis. TU Dortmund University, 2021.
DOI: 10.17877/DE290R-22408

114. S. Lombardi et al. (MAGIC Collaboration). "Advanced stereoscopic gamma-ray shower analysis with the MAGIC telescopes". In: *Proceedings of the 32nd International Cosmic Ray Conference, ICRC2011*. 2011.
DOI: 10.48550/arXiv.1109.6195. arXiv: 1109.6195 [astro-ph.IM]

115. M. Lopez et al. (MAGIC Collaboration). *Detection of the crab pulsar with MAGIC*. 2009.
DOI: 10.48550/arXiv.0907.0832. arXiv: 0907.0832 [astro-ph.HE]

116. J. Luo et al. "PINT: a modern software package for pulsar timing". *The Astrophysical Journal* 911:1, 2021, page 45.
DOI: `10.3847/1538-4357/abe62f`. arXiv: `2012.00074 [astro-ph.IM]`

117. A. Lyne, R. Pritchard, and F. Graham Smith. "23 years of Crab pulsar rotational history". *Monthly Notices of the Royal Astronomical Society* 265:4, 1993, pages 1003–1012.
`http://www.jb.man.ac.uk/~pulsar/crab.html`

118. A. Lyne, F. Graham-Smith, and B. Stappers. In: *Pulsar Astronomy*. 5th ed. Cambridge Astrophysics. Cambridge University Press, 2022.
DOI: `10.1017/9781108861656`

119. Y. E. Lyubarskii. "A model for the energetic emission from pulsars." *Astronomy & Astrophysics* 311, 1996, pages 172–178

120. R. Manchester. "Millisecond pulsars, their evolution and applications". *Journal of Astrophysics and Astronomy* 38:3, 2017, page 42.
DOI: `10.1007/s12036-017-9469-2`. arXiv: `1709.09434 [astro-ph.HE]`

121. K. Meagher (VERITAS Collaboration). "Six years of VERITAS observations of the Crab Nebula". *Proceedings of the 34th International Cosmic Ray Conference, ICRC 2015*, 2015.
DOI: `10.48550/arXiv.1508.06442`. arXiv: `1508.06442 [astro-ph.HE]`

122. C. Meegan et al. (Fermi Collaboration). "The Fermi Gamma-ray Burst Monitor". *The Astrophysical Journal* 702:1, 2009, pages 791–804.
DOI: `10.1088/0004-637X/702/1/791`. arXiv: `0908.0450 [astro-ph.IM]`

123. C. Messier. "Tables des Nebuleuses, ainsi que des amas d'Etoiles, que l'on decouvre parmi les Etoiles fixes sur l'horizon de Paris; observes a l'Observatoire de la Marine". *Memoires de l'Academie des Sciences*, 1771

124. Meyer, M., Horns, D., and Zechlin, H.-S. "The Crab Nebula as a standard candle in very high-energy astrophysics". *Astronomy & Astrophysics* 523, 2010, A2.
DOI: `10.1051/0004-6361/201014108`. arXiv: `1008.4524 [astro-ph.HE]`

125. R. Mirzoyan. "On the calibration accuracy of light sensors in atmospheric Cherenkov fluorescence and neutrino experiments". In: *Proceedings of the 25th International Cosmic Ray Conference, ICRC 1997*. Vol. 7. 1997, page 265

126. A. Moralejo et al. (MAGIC Collaboration). "MARS, the MAGIC analysis and reconstruction software". In: *Proceedings of the 31st International Cosmic Ray Conference, ICRC2009*. 2009.
DOI: `10.48550/arXiv.0907.0943`. arXiv: `0907.0943 [astro-ph.IM]`

127. T. D. Moyer. "Transformation from proper time on Earth to coordinate time in solar system barycentric space-time frame of reference: Part 1". *Celestial Mechanics* 23:1, 1981, pages 33–56.
DOI: `10.1007/BF01228543`

128. P. V. R. Murthy and A. W. Wolfendale. “Ultra high energy gamma-rays”. In: *Gamma-ray Astronomy*. 2nd ed. Cambridge Astrophysics. Cambridge University Press, 1993, pages 173–232.
DOI: 10.1017/CBO9780511564840.007

129. A. G. Muslimov and A. K. Harding. “Extended acceleration in slot gaps and pulsar high-energy emission”. *The Astrophysical Journal* 588:1, 2003, page 430.
DOI: 10.1086/368162. arXiv: astro-ph/0301023 [astro-ph]

130. A. G. Muslimov and A. K. Harding. “High-altitude particle acceleration and radiation in pulsar slot gaps”. *The Astrophysical Journal* 606:2, 2004, page 1143.
DOI: 10.1086/383079. arXiv: astro-ph/0402462 [astro-ph]

131. M. de Naurois. “L’astronomie γ de très haute énergie. Ouverture d’une nouvelle fenêtre astronomique sur l’Univers non thermique”. PhD thesis. Université Paris VI, 2012.
https://inis.iaea.org/collection/NCLCollectionStore/_Public/49/048/49048989.pdf

132. C. Nigro et al. “Towards open and reproducible multi-instrument analysis in gamma-ray astronomy”. *Astronomy&Astrophysics* 625, 2019, page A10. ISSN: 1432-0746.
DOI: 10.1051/0004-6361/201834938. arXiv: 1903.06621 [astro-ph.HE]

133. C. Nigro. *MAGIC DL3 converter*.
https://gitlab.pic.es/magic_dl3/magic_dl3 visited on 2024-06-22.
Note: MAGIC internal

134. C. Nigro, T. Hassan, and L. Olivera-Nieto. “Evolution of Data Formats in Very-High-Energy Gamma-Ray Astronomy”. *Universe* 7:10, 2021, page 374.
DOI: 10.3390/universe7100374. arXiv: 2109.14661 [astro-ph.HE]

135. P. Nolan et al. (EGRET Collaboration). “EGRET observations of pulsars”. *Astronomy and Astrophysics Supplement* 120, 1996, pages 61–64.
DOI: 10.48550/arXiv.astro-ph/9607079. arXiv: astro-ph/9607079 [astro-ph]

136. F. Pacini. “Energy emission from a neutron star”. *Nature* 216:5115, 1967, pages 567–568.
DOI: 10.1038/216567a0

137. G. Panfilo and F. Arias. “The Coordinated Universal Time (UTC)”. *Metrologia* 56:4, 2019, page 042001.
DOI: 10.1088/1681-7575/ab1e68

138. D. W. Pankenier. “Notes on translations of the East Asian records relating to the supernova of AD 1054”. *Journal of Astronomical History and Heritage* 9:1, 2006, pages 77–82.
https://ui.adsabs.harvard.edu/abs/2006JAHH....9...77P/abstract

139. R. Paoletti et al. (MAGIC Collaboration). “The trigger system of the MAGIC telescope”. *IEEE transactions on nuclear science* 54:2, 2007, pages 404–409.
DOI: 10.1109/TNS.2007.892649

140. C. Pethick and D. Ravenhall. “Matter at large neutron excess and the physics of neutron-star crusts”. *Annual Review of Nuclear and Particle Science* 45:1, 1995, pages 429–484.
DOI: 10.1146/annurev.ns.45.120195.002241

141. G. Petit. “A new realization of Terrestrial Time”. In: *Proceedings of the 35th Annual Precise Time and Time Interval Systems and Applications Meeting*. 2003, pages 307–318

142. G. Petit. “Comparision of ”Old” and ”New” Concepts: Coordinate Times and Time Transformations”. *Daniel Gambis, Dennis D. McCarthy, Gérard Petit, Jim Ray, Bernd Richter, Markus Rothacher, E. Myles Standish and Jan Vondrak*, 2002, page 19

143. J. Pétri. “Theory of pulsar magnetosphere and wind”. *Journal of Plasma Physics* 82:5, 2016, page 635820502.
DOI: 10.1017/S0022377816000763. arXiv: 1608.04895 [astro-ph.HE]

144. A. Philippov and M. Kramer. “Pulsar magnetospheres and their radiation”. *Annual Review of Astronomy and Astrophysics* 60, 2022, pages 495–558.
DOI: 10.1146/annurev-astro-052920-112338

145. H. Pletsch et al. (Fermi Collaboration). “Discovery of nine gamma-ray pulsars in Fermi Large Area Telescope data using a new blind search method”. *The Astrophysical Journal* 744:2, 2011, page 105.
DOI: 10.1088/0004-637X/724/2/1044. arXiv: 1111.0523 [astro-ph.HE]

146. A. M. Price-Whelan et al. (Astropy Collaboration). “The Astropy Project: Building an Open-science Project and Status of the v2.0 Core Package”. *The Astronomical Journal* 156:3, 2018, page 123.
DOI: 10.3847/1538-3881/aabc4f. arXiv: 1801.02634 [astro-ph.IM]

147. V. Radhakrishnan. “Fifteen Months of Pulsar Astronomy”. *Publications of the Astronomical Society of Australia* 1:6, 1969, pages 254–263.
DOI: 10.1017/S1323358000011826

148. M. Rissi et al. (MAGIC Collaboration). “A new sum trigger to provide a lower energy threshold for the MAGIC telescope”. *IEEE Transactions on Nuclear Science* 56:6, 2009, pages 3840–3843.
DOI: 10.1109/TNS.2009.2030802

149. M. S. Roberts et al. “PSR J2021+ 3651: A young radio pulsar coincident with an unidentified EGRET γ-ray source”. *The Astrophysical Journal* 577:1, 2002, page L19.
DOI: 10.1086/344082. arXiv: astro-ph/0206443 [astro-ph]

150. T. P. Robitaille et al. (Astropy Collaboration). “Astropy: A community Python package for astronomy”. *Astronomy & Astrophysics* 558, 2013, page A33.
DOI: 10.1051/0004-6361/201322068. arXiv: 1307.6212 [astro-ph.IM]

151. A. H. Rots et al. “Representations of time coordinates in FITS-Time and relative dimension in space”. *Astronomy & Astrophysics* 574, 2015, page A36.
DOI: `10.1051/0004-6361/201424653`

152. M. Ruderman and P. G. Sutherland. “Theory of pulsars-Polar caps, sparks, and coherent microwave radiation”. *The Astrophysical Journal* 196, 1975, pages 51–72.
DOI: `10.1086/153393`

153. T. Y. Saito and J. Sitarek (MAGIC Collaboration). *Improvement of the θ^2 analysis by using the Random Forest method in the DISP estimation*. Technical report TDAS 09-01. 2009.
`https://magic.mpp.mpg.de/backend/tdas-notes`.
Note: Internal MAGIC document

154. F. Schmuckermaier et al. (MAGIC Collaboration). “Correcting MAGIC Telescope data taken under non-optimal atmospheric conditions with an elastic LIDAR”. In: *Journal of Physics Conference Series*. Vol. 2398. Journal of Physics Conference Series. 2022, 012011, page 012011.
DOI: `10.1088/1742-6596/2398/1/012011`. arXiv: `2302.12072 [astro-ph.IM]`

155. J. L. Schubert. *Automatization of the Reduction of MAGIC Sum-Trigger-II Data*. Master’s thesis. 2021.
Note: Unpublished

156. M. Servillat et al. *FAIR high level data for Cherenkov astronomy*. 2022.
DOI: `10.48550/arXiv.2201.03247`. arXiv: `2201.03247 [cs.IT]`

157. M. Shayduk et al. *New Image Cleaning Method for the MAGIC Telescope*. Technical report. MAGIC, 2005.
`https://magic.mpp.mpg.de/backend/tdas-notes`.
Note: Internal MAGIC document

158. M. Shayduk et al. (MAGIC Collaboration). “A New Image Cleaning Method for the MAGIC Telescope”. In: *Proceedings of the 29th International Cosmic Ray Conference, ICRC 2005*. Vol. 5. 2005, page 223

159. P. Slane. “Pulsar wind nebulae”, 2017. Ed. by A. W. Alsabti and P. Murdin, page 2159.
DOI: `10.1007/978-3-319-21846-5_95`. arXiv: `1406.6892 [astro-ph.HE]`

160. D. A. Smith et al. (Fermi Collaboration). “The Third Fermi Large Area Telescope Catalog of Gamma-Ray Pulsars”. *The Astrophysical Journal* 958:2, 2023, page 191.
DOI: `10.3847/1538-4357/acee67`. arXiv: `2307.11132 [astro-ph.HE]`

161. I. Šnidarić. “Very high energy gamma-ray emission from pulsars and pulsars wind nebulae observed by MAGIC telescopes”. PhD thesis. University of Zagreb, 2023.
`http://fulir.irb.hr/8010/1/IS_PhD_thesis.pdf`

162. D. Sobczyńska. *Mmcs from CORSIKA 6.014*. Technical report TDAS 02-10. MAGIC, 2002.
Note: Internal MAGIC document

163. P. Sommers and J. W. Elbert. "Ultra-high-energy gamma-ray astronomy using atmospheric Cerenkov detectors at large zenith angles". *Journal of Physics G Nuclear Physics* 13:4, 1987, pages 553–566.
DOI: `10.1088/0305-4616/13/4/019`

164. D. H. Staelin and E. C. Reifenstein III. "Pulsating radio sources near the Crab Nebula". *Science* 162:3861, 1968, pages 1481–1483.
DOI: `10.1126/science.162.3861.1481`

165. M. Stonebraker, L. A. Rowe, and M. Hirohama. "The implementation of POSTGRES". *IEEE transactions on knowledge and data engineering* 2:1, 1990, pages 125–142.
DOI: `10.1109/69.50912`

166. E. Striani et al. (Fermi Collaboration). "Variable gamma-ray emission from the Crab Nebula: Short flares and long 'waves'". *The Astrophysical Journal* 765:1, 2013, page 52.
DOI: `10.1088/0004-637X/765/1/52`. arXiv: `1302.4342 [astro-ph.HE]`

167. P. Sturrock. "A model of pulsars". *Astrophysical Journal* 164, 1971, page 529.
DOI: `10.1086/150865`

168. M. Su et al. (Fermi Collaboration). "Giant gamma-ray bubbles from Fermi-LAT: active galactic nucleus activity or bipolar galactic wind?" *The Astrophysical Journal* 724:2, 2010, page 1044.
DOI: `10.1088/0004-637X/724/2/1044`. arXiv: `1005.5480 [astro-ph.HE]`

169. J. Takata, S. Shibata, and K. Hirotani. "A pulsar outer gap model with trans-field structure". *Monthly Notices of the Royal Astronomical Society* 354:4, 2004, pages 1120–1132.
DOI: `10.1111/j.1365-2966.2004.08270.x`. arXiv: `astro-ph/0408044 [astro-ph]`

170. M. Tavani et al. (AGILE Collaboration). "Discovery of Powerful Gamma-Ray Flares from the Crab Nebula". *Science* 331:6018, 2011, page 736.
DOI: `10.1126/science.1200083`. arXiv: `1101.2311 [astro-ph.HE]`

171. D. Tescaro et al. (MAGIC Collaboration). "The MAGIC telescopes DAQ software and the on-the-fly online analysis client". In: *Proceedings of the 33rd International Cosmic Ray Conference, ICRC2013*. 2013.
DOI: `10.48550/arXiv.1310.1565`. arXiv: `1310.1565 [astro-ph.IM]`

172. D. Thain, T. Tannenbaum, and M. Livny. "Distributed computing in practice: the Condor experience". *Concurrency and computation: practice and experience* 17:2-4, 2005, pages 323–356

173. V. Trimble. "The distance to the Crab nebula and NP 0532". *Publications of the Astronomical Society of the Pacific* 85:507, 1973, page 579.
DOI: `10.1086/129507`

174. J. Tyler. "A search for Fermi LAT pulsars in archival VERITAS data". PhD thesis. McGill University (Canada), 2019

175. G. Van Rossum and F. L. Drake. *Python 3 Reference Manual*. CreateSpace, Scotts Valley, CA, 2009. ISBN: 1441412697

176. P. Virtanen et al. "SciPy 1.0: fundamental algorithms for scientific computing in Python". *Nature Methods*, 2020.
DOI: `10.1038/s41592-019-0686-2`. arXiv: `1907.10121` [`cs.MS`]

177. S. v. d. Walt, S. C. Colbert, and G. Varoquaux. "The NumPy array: a structure for efficient numerical computation". *Computing in Science & Engineering* 13:2, 2011, pages 22–30.
DOI: `10.1109/MCSE.2011.37`. arXiv: `1102.1523` [`cs.MS`]

178. T. C. Weekes et al. (WHIPPLE Collaboration). "Observation of tev gamma-rays from the crab nebula using the atmospheric cherenkov imaging technique". *Astrophysical Journal* 342, 1989, pages 379–395.
DOI: `10.1086/167599`

179. D. C. Wells and E. W. Greisen. "FITS –- a flexible image transport system". In: *Image Processing in Astronomy*. 1979, page 445

180. J. Woo et al. "Hard X-Ray Observation and Multiwavelength Study of the PeVatron Candidate Pulsar Wind Nebula "Dragonfly"". *The Astrophysical Journal* 954:1, 2023, page 9.
DOI: `10.3847/1538-4357/acdd5e`. arXiv: `2306.07347` [`astro-ph.HE`]

181. M. Wood et al. (Fermi Collaboration). *Fermipy: An open-source Python package for analysis of Fermi-LAT Data*. 2017.
DOI: `10.48550/arXiv.1707.09551`. arXiv: `1707.09551` [`astro-ph.IM`]

182. X-ray: NASA/CXC/SAO; Optical: NASA/STScI; Infrared: NASA-JPL-Caltech. *Crab Nebula: A Crab Walks Through Time*. 2018.
`https://chandra.harvard.edu/photo/2018/crab/` visited on 2024-06-22

183. X-ray: NASA/CXC/SAO; Optical: NASA/STScI; Infrared: NASA/JPL/-Caltech; Radio: NSF/NRAO/VLA; Ultraviolet: ESA/XMM-Newton. *Crab Nebula: Observatories Combine to Crack Open the Crab Nebula*. 2017.
`https://chandra.harvard.edu/photo/2017/crab/` visited on 2024-06-22

184. M. Xinjie and T. Yi. "The current sheets in the magnetosphere of a pulsar". *Astrophysics and space science* 132, 1987, pages 201–206.
DOI: `10.1007/BF00637795`

185. R. Zanin. "Crab Observational Status: Nebulae, Pulsations, and Flares". In: *Modelling Pulsar Wind Nebulae*. Ed. by D. F. Torres. Springer International Publishing, Cham, 2017, pages 101–133.
DOI: `10.1007/978-3-319-63031-1_6`

186. R. Zanin et al. (MAGIC Collaboration). “MARS, the MAGIC analysis and reconstruction software”. In: *Proceedings of the 33rd International Cosmic Ray Conference, ICRC2013*. 2013

187. J. Zar. “Probabilities of Rayleigh’s Test Statistics for Circular Data”. *Behavior Research Methods & Instrumentation* 6, 1974, pages 450–450.
DOI: 10.3758/BF03200403

188. D. Zarić et al. (MAGIC Collaboration). “MAGIC observations of Dragonfly Nebula at TeV Energies using the Very Large Zenith Angle Technique”. *Proceedings of the 36th International Cosmic Ray Conference, ICRC2019* ICRC2019, 2019, page 827.
DOI: 10.22323/1.358.0827. arXiv: 1909.05107 [astro-ph.HE]

189. C. Zhang et al. “Study of measured pulsar masses and their possible conclusions”. *Astronomy & Astrophysics* 527, 2011, page A83.
DOI: 10.1051/0004-6361/201015532. arXiv: 1010.5429 [astro-ph.HE]

190. S. Zhou et al. “Pulsar Glitches: A Review”. *Universe* 8:12, 2022, page 641.
DOI: 10.48550/arXiv.2211.13885. arXiv: 2211.13885 [astro-ph.HE]

List of Figures

List of Tables

Glossary

AGILE Astro-Rivelatore Gamma a Immagini Leggero. 9

AGN Active Galactic Nucleus. 37

CDF Comulative Density Function. 54

`CORSIKA` Cosmic Ray Simulations for Kascade. 20

CTA Cherenkov Telescope Array. 9, 34, 111

DC Dark Current. 63, 64, 83, 84, 95, 106

DRS4 Domino Ring Sampler 4. 18

EAS Extensive Air Shower. 13, 15, 17, 38

FITS Flexible Image Transport System. 34

FoV Field of View. 37, 40, 42, 43, 45

FWHM Full Width at Half Maximum. 61, 68, 69, 73, 86, 90

GADF Gamma Astronomy Data Format. 33

GRB Gamma-Ray Burst. 12, 37

GTC Gran Telescopio Canarias. 16

H. E. S. S. High Energy Stereoscopic System. 5, 9

IACT Imaging Air Cherenkov Telescope. 1, 2, 5, 9, 10, 12–15, 17, 18, 23, 25, 28, 29, 34, 37, 38, 63, 101, 110, 111, 115, 133

IRF Instrument Response Function. 21, 23, 28–30, 33

ISF Inverse Survival Function. 54

KIT Karlsruhe Institute of Technology. 20

LAT Large Area Telescope. 1, 11, 12, 59, 61–63, 75, 91, 109, 111, 133

LHAASO Large High Altitude Air Shower Observatory. 9

LIDAR Light Detection and Ranging. 15, 16

LIV Lorentz Invariance Violation. 111, 116

LST Large Size Telescope. 111

LUT Look Up Table. 33

MAGIC Major Atmospheric Gamma-Ray Imaging Cherenkov. 1–3, 9, 10, 12, 15–17, 20, 22, 31–35, 37, 38, 41, 43, 46, 48–50, 55, 57, 59, 61, 62, 64, 68, 75, 82, 91, 95, 99, 105, 109–111, 113, 115, 116, 137, 138, 181, 183

MARS MAGIC Analysis and Reconstruction Software. 31–33, 35, 45, 65, 84, 107, 113, 114

MC Monte Carlo. 17, 20–22, 28, 31, 33, 43, 45–48, 63–65, 82, 83, 95, 98, 105–107, 113, 114, 133–135, 137–140, 143, 145, 157, 182, 183

MJD Modified Julian Date. 118, 120, 121

`MMCS` MAGIC Monte Carlo Software. 20

MOLA MAGIC Online Analysis. 33, 63, 64, 84, 95, 106

MWL Multi Wavelength. 8, 10–12, 181

NN Nearest Neighbors. 25, 38, 41, 42, 181

NSB Night Sky Background. 37, 40, 41

PCA Principal Component Analysis. 25, 26

p. e. photo electrons. 18, 23, 24, 26, 31, 41, 42, 46, 47

PIC Port d'Informació Científica. 35, 46, 63, 106, 114

`PINT` `PINT` is not `tempo3`. 49, 54–56, 115

PMT Photo Multiplier Tube. 15, 17, 18, 23, 24, 37, 40, 41, 63

PSF Point Spread Function. 29, 30

PWN Pulsar Wind Nebula. 3, 8, 9, 12

RF Random Forest. 20, 21, 28, 33, 46, 48, 133, 137, 145, 146

RMS Root Mean Square. 23, 24, 118

SED Spectral Energy Distribution. 30, 61, 75, 92, 99, 101, 110, 127, 133, 134, 137, 138, 145, 182

SNR supernova remnant. 8, 9

SQL Structured Query Language. 35

SSB Solar System Barycenter. 49–52, 115

TAI Temps Atomique International. 50

TCB Barycentric Coordinate Time. 50, 54, 115, 117

TDB Barycentric Dynamical Time. 50, 54, 115, 117

TOA Time Of Arrival. 31, 49–52, 55, 56, 58, 115, 118

TT Terrestial Time. 50

UTC Coordinated Universal Time. 50

UV Ultra Violet. 10

VERITAS Very Energetic Radiation Imaging Telescope Array System. 9, 10, 12, 63, 111

VHE Very High Energy. 2, 5, 8–11, 13, 23, 49, 52, 57–59, 61, 99

VHZ Very High Zenith. 48, 57, 82, 95, 96, 101, 110, 137, 138, 142–144, 157, 182, 183

zd zenith distance. 2, 38, 55, 64, 82, 84, 95, 101, 106, 133, 137, 138, 145, 150–152, 157, 183, 184

Acknowledgements

> True Inspiration is Impossible to Fake.
>
> Arthur
> Inception

An dieser Stelle möchte ich gerne einigen Leuten danken, ohne die diese Promotion für mich nicht möglich gewesen wäre. Zunächst gilt mein großer Dank Dominik Elsässer für das Erstgutachten und die Betreuung dieser Arbeit. Du hast damals in der Astroteilchenphysik Vorlesung mein Interesse für die Gammaastronomie entfacht und damit meinen Weg maßgeblich beeinflusst. Außerdem möchte ich mich bei Wolfgang Rhode für die Mitbetreuung und die mir während der Promotion eröffneten Möglichkeiten danken. Vielen herzlichen Dank auch an Chris Delitzsch für die Zweitbegutachtung dieser Arbeit.

Vielen Dank Andrea für dein Engangement, um den Lehrstuhl am Laufen zu halten und für die wunderbaren zerstreuenden Gespräche zwischendurch. Mit dir werden die bürokratischen Hürden zu ein bisschen Papierkram nebenbei!

Thank you Giovanni Ceribella for supporting me with all your knowledge on the pulsar analysis. It is quite a complex topic and without all your expertise I would have had a far more challenging (and probably far longer) time doing all this. Thank you for all the zoom and in person meetings that we had and for all the time you took to answer my questions.

Vielen Dank an das Büro 155 in allen Besetzungsvariationen. Es war mir eine Freude mit euch zu arbeiten (oder an einigen Tagen auch eher weniger zu arbeiten und eher zu quatschen)! Ich konnte sowohl fachlich als auch persönlich super viel aus unseren SMARTen Gesprächen mitnehmen. Auch wenn zwischendurch eine Sanduhr notwendig war, bin ich mir sicher, dass ich unsere Bürogespräche in Zukunft vermissen werde.

Besonders danken möchte ich Lena und Simone für die gemeinsame Arbeit an `autoMAGIC`. Es ist ein cooles Projekt bei dem ich super viel lernen konnte und es erspart einem einfach echt viele graue Haare, die einem MARS sonst beschert hätte. Auch das Lästern über PIC Probleme war immer eine (wenn auch leider nicht allzu seltene) Freude!

Danke Ali für die vielen gemeinsamen Pausen und Spaziergänge, die immer eine willkommene Ablenkung von nervigen Problemen waren. Danke für alle deine Ratschläge und Denkanstöße für Entscheidungen in allen Lebenslagen. Ich würde auch jeder Zeit wieder mit dir den Roque hochwandern!

Danke Simone für das Aufrechterhalten des Thrill-Levels! Danke für die offenen Gespäche und die neuen Perspektiven, die du mir aufgezeigt hast.

Danke Stefan für alle die kleineren und größeren Programmierfragen, die du mir beantwortet hast und für den (hin und wieder höchst notwendigen) emotionalen Beistand für die Monte Carlos! Ich freue mich schon wenn wir das nächste mal alle mit Hamilton am Strand beglücken können.

Danke an die gesamte Astroteilchenphysik Arbeitsgruppe in Dortmund für die gute Zusammenarbeit und das angenehme Arbeitsumfeld! Es ist schön zu erleben, wie einen ein Miteinander viel mehr voran bringt als ein Gegeneinander und es ist toll, dass das in Dortmund auch so gelebt wird. Danke für die coolen Dienstreisen mit Euch und für alles, was ich von Euch lernen konnte.

Special thanks go also to the working group at the Max Planck Institute for Physics in Munich who welcomed me very warmly for my research stay. It was a great experience to spend some time in such an international working group with so diverse people. I loved all your social activities and that they are open to everyone!

Vielen Dank Simone und Janina für die etlichen Hochschulsportkurse, die wir zusammen besucht haben. Es war mir stets eine Freude und ein toller Ausgleich.

Danke Maria für deine super tollen Hochschulsportkurse, die mich während der Pandemiezeit und auch meistens im Winter aus meinem Motivationstief wieder rausgeholt und mir neue Energie gegeben haben. Egal ob nun physisch in Dortmund oder als online Kurs zu Hause oder in München.

Vielen Dank auch an den Verein Vorhang auf Holzwickede für die tollen Gelegenheiten, die ihr mir gegeben habt, um mich selbst zu entfalten und in meiner Freizeit einen tollen Ausgleich zur Arbeit zu finden.

Vielen Dank an alle, die diese Arbeit korrekturgelesen haben oder mich an anderer Stelle sehr voran gebracht haben: Danke Ali, Simone, Stefan, Max, David, Lucas, Karo, Maxie, Janina, Leonie, Kati, Tristan und alle Anderen, die ich in dieser Aufzählung vergessen habe.

Danke an meinen Physiklehrer Christoph Förster dank dem ich meine Begeisterung für die Physik schon in der Schulzeit entdeckt habe und ohne den ich diese Laufbahn vermutlich niemals eingeschlagen hätte.

Danke Maxie für die vielen durchgemachten Nächte mit Burgern oder Lasagne und die gemeinsamen Reisen. Danke für deine Lebensweisheiten und deinen schonungslosen Pragmatismus.

Mein tiefster Dank gilt meiner Familie, die mich in allen Lebenslagen unterstützt und mir in jeder Situation mit einem guten Rat zur Seite stehen kann. Ich weiß, Ihr seid immer für mich da und werdet es auch immer sein. Danke, dass Ihr mir immer wieder neue Perspektiven schenkt, immer ein offenes Ohr zum Zuhören bereithaltet und dass ihr mich auf meinem Weg begleitet.

Danke David für alles was ich von dir lernen, mit dir erleben und mit dir teilen darf.